www.scirp.org/journal/jbise

Scientific Research

JBiSE

ISSN: 1937-6871

Volume 3 Number 4 April 2010

Journal of Biomedical Science and Engineering

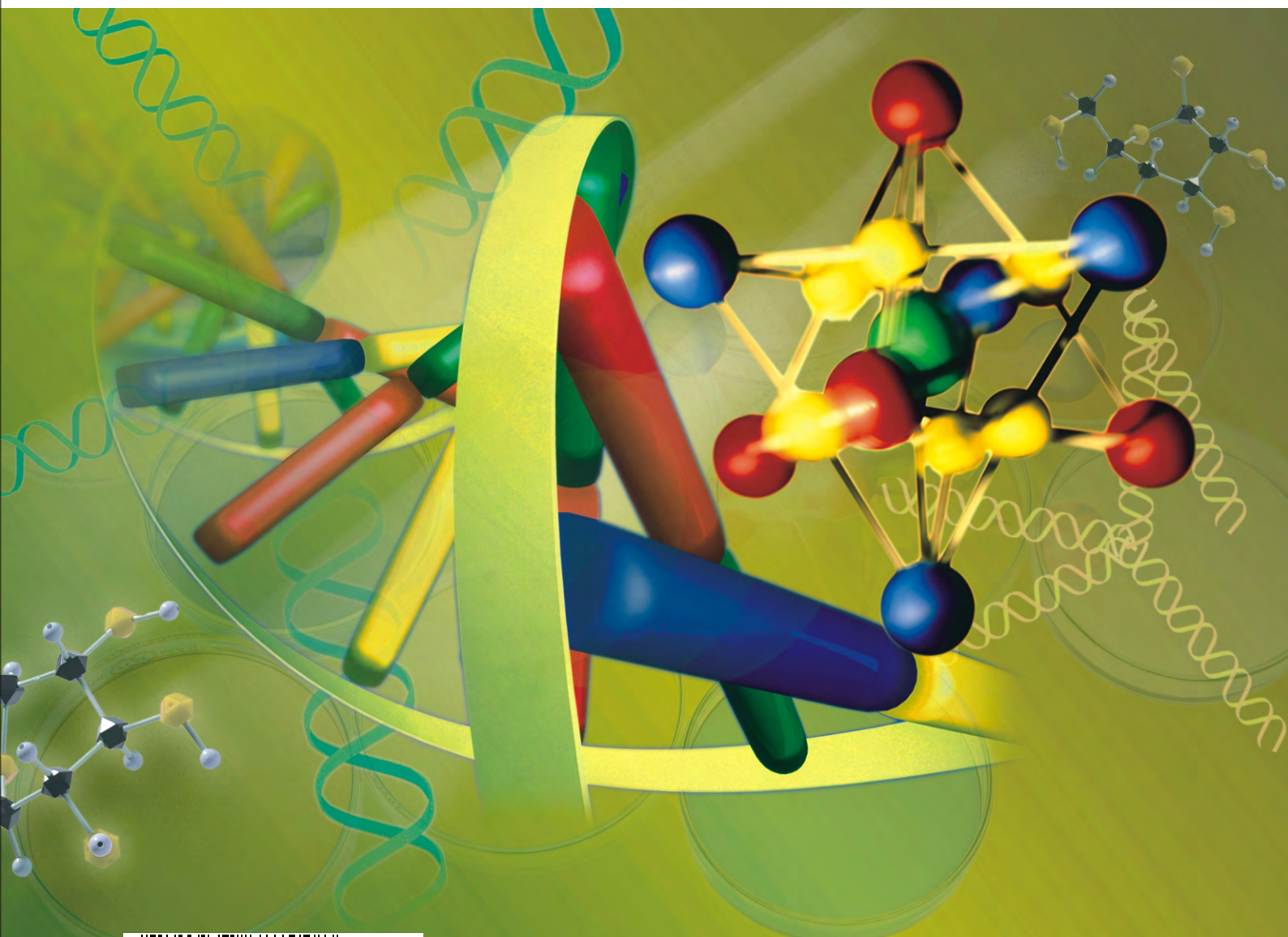

9 771937 687008 04

Journal Editorial Board

ISSN 1937-6871 (Print) ISSN 1937-688X (Online)
http://www.scirp.org/journal/jbise

TABLE OF CONTENTS

Volume 3, Number 4, April 2010

Journal of Biomedical Science and Engineering (JBiSE)

Journal Information

SUBSCRIPTIONS

The *Journal of Biomedical Science and Engineering* (Online at Scientific Research Publishing, www.SciRP.org) is published monthly by Scientific Research Publishing, Inc., USA.

Subscription rates:

Print: $50 per issue.
To subscribe, please contact Journals Subscriptions Department, E-mail: sub@scirp.org

SERVICES

Advertisements
Advertisement Sales Department, E-mail: service@scirp.org

Reprints (minimum quantity 100 copies)
Reprints Co-ordinator, Scientific Research Publishing, Inc., USA.
E-mail: sub@scirp.org

COPYRIGHT

PRODUCTION INFORMATION

For manuscripts that have been accepted for publication, please contact:
E-mail: jbise@scirp.org

J. Biomedical Science and Engineering, 2010, 3, 331-339 **JBiSE**
doi:10.4236/jbise.2010.34046 Published Online April 2010 (http://www.SciRP.org/journal/jbise/).

Statistical analysis of conformational properties of periodic dinucleotide steps in nucleosomes

Xi Yang[1], Hong Yan[1,2]

[1]Department of Electronic Engineering, City University of Hong Kong, Hong Kong, China;
[2]School of Electrical and Information Engineering, University of Sydney, Sydney, Australia.
Email: xiyang3@student.cityu.edu.hk

Received 15 January 2010; revised 25 January 2010; accepted 27 January 2010.

ABSTRACT

Deformability of DNA is important for its superhelical folding in the nucleosome and has long been thought to be facilitated by periodic occurrences of certain dinucleotides along the sequences, with the period close to 10.5 bases. This study statistically examines the conformational properties of dinucleotides containing the 10.5 - base periodicity and those without that periodicity through scanning all nucleosome structures provided in PDB. By categorizing performances on the distribution of step parameter values, averaged net values, standard deviations and deformability based on step conformational energies, we give a detailed description as to the deformation preferences correlated with the periodicity for the 10 unique types of dinucleotides and summarize the possible roles of various steps in how they facilitate DNA bending. The results show that the structural properties of dinucleotide steps are influenced to various extents by the periodicity in nucleosomes and some periodic steps have shown a clear tendency to take specific bending or shearing patterns.

Keywords: Deformability of DNA; Nucleosome; Dinucleotides; 10.5-Base Periodicity; Deformation Preferences; Flexibility; DNA Bending

1. INTRODUCTION

Numerous studies of nucleosome positioning have demonstrated that the arrangement of nucleosomes on DNA is nonrandom. The periodic occurrences of certain base pairs or motifs have been proven to be ubiquitous in nucleosomes [1-5]. The periodicity of dinucleotide steps can be considered as an important signal for nucleosome identification, and it is widely considered to be closely related to the superhelical structure of nucleosomal DNA [6-9]. On the other hand, the stereochemical characteristics of DNA fragments decide their individual behaviors of deformation when being located at certain sites along the DNA sequence [1,10-13]. Anisotropic deformation along a superhelical path implies some dimers may play the role of "hinge" and others facilitate "hinges" adhering to the histone octamer core or just simply follow the "hinge" wrapping around the core. From this point of view, there exist some base steps that are geometrically more significant than others, which are mainly reflected by the special structural parameter settings of these important "building blocks".

Although in previous studies, various methods, such as molecular dynamics simulations, energy surface calculation and deformability statistics based on dimer energy function, have already been used to decipher the conformational roles of the ten independent types of dinucleotides [11,13,14], statistics which focus on a large number of nucleosome samples whose crystal structures are experimentally determined is still scarce. Here, we choose 35 crystal structures of nucleosomes published in Protein Data Bank (PDB) as the subject of the statistical survey. The aim of our research is to observe the overall conformational patterns measured by the distribution and variability of base pair step parameters and step conformation energies and build interrelationships between periodicity and deformability of base-pair steps.

2. MATERIALS AND METHODS

2.1. Crystal Structure and Dinucleotide Step Parameters

There are 35 crystal structures of nucleosomes available in the Protein Date Bank (PDB) currently. All of them belong to the typical complex between histone core particle (H3, H4, H2A and H2B) and DNA sequence which is organized into a superhelix around the core. The PDB ID of the 35 histone-DNA complexes are 1AOI, 1EQZ, 1F66, 1ID3, 1KX3, 1KX4, 1KX5, 1M1A, 1M18, 1M19, 1P3A, 1P3B, 1P3F, 1P3G, 1P3I, 1P3K, 1P3L, 1P3M, 1P3O, 1P3P, 1P34, 1S32, 1U35,

1ZBB, 1ZLA, 2CV5, 2F8N, 2FJ7, 2NQB, 2NZD, 2PYO, 3B6F, 3B6G, 3C1B and 3C1C. The software 3DNA [15] is used to calculate the six step parameters of nucleosome DNA: Shift, Slide, Rise, Roll, Tilt and Twist.

2.2. Periodicity and Deformability of Dinucleotide Steps

The periodic occurrence of dinucleotides observed in nucleosomes has long been thought to be closely related with the sequence-dependent helical anisotropy of DNA. AA/TT was firstly thought to be a step with intrinsic curvature characteristic when it is periodically repeated [16]. Correctly phased repeats (10.5 bp) of AG/CT, CG, GA/TC and GC can also cause appreciable curvature [10]. The 10.5 bp periodicity, which is widely acknowledged to be closely related to superhelix structure, tends to be 11 bp in bacteria and 10 bp in archaea and eukaryotes [17] and even for the same type of dinucleotides in the same nucleosome, being located at different places of the core DNA sequence, such as at the two ends or in the middle section, can make the periodicity fluctuate slightly [18].

In order to take the diversity of periodicity into account, the 10 ~ 11 bp are comprehensively considered as the separation standard, that is, any step having been separated with another step of the same type by 10 ~ 11 bp will be recognized as a periodic step and marked with "1", while if the distance between the neighbouring steps of the same type goes beyond or is not up to this standard, they will be marked with "0". The ten types of steps collected from 35 nucleosomes are separated into the corresponding "0" and "1" groups accordingly.

In the above method for extracting the periodic dinucleotides, we consider only one period. That is, any neighbouring occurrence of the same type of dinucleotides with a distance of 10 ~ 11 bp will be considered a desired periodic pattern. More sophisticated methods, such as the matched mirror position filter (MMPF) [19], can be used to take several periods and their relations into account in a long DNA sequence. In this paper, since we deal with short nucleosome sequences from the PDB, there are not many long periodic patterns. Thus, we detect one-period patterns only. Noise and bias in these patterns and related parameter values can be reasonably assumed to be random and should not affect the overall distribution.

2.3. Separation of the Groups in Plots

Statistical analysis on the structural characteristics of the "0" and "1" groups is made by producing the value distribution histograms of the six base pair step parameters. By categorizing the distribution trends, we can give a detailed description as to the deformation preferences of dinucleotide steps in terms of angular and translational parameters and summarize the possible roles of the significant steps which facilitate DNA bending.

2.4. Calculation of Deformability based on Step Conformational Energy

The conformational energies reflect the fluctuations and correlations of structural parameters and also describe the deformability of dinucleotides at the global level rather than in one dimension. The conformational energy for each base-pair step is estimated by the function based on the fluctuations of step parameters from their equilibrium values [14]

$$E_i = \frac{1}{2}\Delta\Theta^T F \Delta\Theta$$

All the dinucleotides collected from the 35 nucleosomes are considered as a set of experimental observations, and parameter values averaged over this dataset represent the equilibrium geometrical states of steps. Thus the deviation matrix $\Delta\Theta$ and its transpose $\Delta\Theta^T$ can be obtained: $\Delta\Theta = (\Delta\theta_1, \ldots, \Delta\theta_6)$ and $\Delta\theta_i = \theta_i - \theta_i°$ (i = 1 ,…, 6). The covariance matrix of the step parameters M calculated over the same set of DNA structures is used to deduce the dimmer stiffness matrix F: $M = kTF^{-1}$ [13]. For simplicity, the Boltzmann's constant k and absolute temperature T is recognized as unity and set to 1 because the relative deformability of steps is not influenced by the value of kT, and in this sense, the calculation result is a kind of energy score rather than the real energy unit in joule.

3. RESULTS AND DISCUSSION

3.1. Frequency Distribution of Step Parameter Values

The number of CG steps is especially limited in all the 35 nucleosomes. 1KX4 is a special one in which four CGs are found. For 25 nucleosomes there are only two CGs in each sequence with an interval of 7 ~ 8 bp while for the remaining 9 nucleosomes, no CG can be found at all. This explains why all the CG steps in the 35 nucleosomes are categorized into the CG0 group.

The values of Shift, Slide, Roll and Tilt distribute over both negative and positive ranges. Twist predominantly takes a positive value with two exceptions: –138.4º and –179.1º of TC/GA occurring in 1S32 and 3C1C respectively. Rise is generally considered as the most conserved parameter not only at each step type but also between the types in order to keep the hydrophobic interaction between two base pairs when a dinucleotide conformation changes [20,21]. It is also the case in nucleosomes since the averaged Rise values for the 10 types of steps are restricted into 3.2 ~ 3.5 Å with very small SD values. However, there still exist a

few steps with negative Rise values as well as values exceeding 6 Å. Finally, for all the 10 unique steps, their "0" groups have very similar distributions with their respective "1" groups on the parameter Rise, Tilt and Twist, and hence the "0" versus "1" differences in terms of the value distribution pattern on these three parameters are not discussed here.

For the value of Shift, AA/TT, AC/GT, AG/CT, AT, CA/TG and TA have no significantly different distribution patterns between the 0 and 1 groups and the overall preferences of value signs of these steps are not obvious in the distribution plots. But for GA/TC, GC and GG/CC (**Figures 1(a)** to **1(c)**), the "0" and "1" distinction that "1" group tends to assume extreme values in both directions, does exist. In comparison with the relatively evenly distributed values of GG/CC0, GG/ CC1 group has two modes around 1Å and –1 Å meaning that most GG/CC steps in compliance with the 10~11 bp periodicity tend to take large Shift value, and GC follows in the same way. Although the peak of GA/TC1 distribution does not occupy values as large as GG/CC1 or GC1, the "1" group of GA/TC still shows clear preferences of taking non-zero Shift values. In addition, most CG steps tend to take positive Shift values.

For the values of Slide, AA/TT, AC/GT, AT, CA/TG, GA/TC and TA have no significantly different distribution patterns between the 0 and 1 group. On the other hand, AG/CT, GC and GG/CC have very similar Slide value distribution modes: "1" groups mainly distribute over the positive Slide range while their "0" groups span a relatively wider range towards both directions (**Figures 1(d)** to **1(f)**). With very few exceptions, CG dinucleotides predominantly take positive Slide values.

For the value of Roll, the "0" groups of AA/TT, AC/GT, CA/TG, GA/TC and GG/CC have similar distribution patterns with their corresponding "1" groups. On the other hand, AG/CT, AT, GC and TA show relatively prominent differences in their respective "0" versus "1" groups (**Figures 1(g)** to **1(j)**). Particularly, the Roll values of "1" group in AG/CT mainly fall into the negative range while most Roll values in the "0" group have a positive sign. The "1" group of GC also chiefly takes a negative Roll value but its "0" group has a more even distribution towards both positive and negative directions. The distribution patterns of "0" and "1" groups in AT and TA, in which the majority in the "1" groups are positive and "0" groups subtly incline to negative, seems to be the opposite of AG/CT and GC.

3.2. Average and Standard Deviation of the Absolute Values of Parameters

Table 1 summarizes the average values and standard deviations of the absolute values of base-pair parameters for the 10 unique sequential base-pair steps in their "1" and "0" groups. Calculations on absolute values of the parameters ignore the effects of rotational and translational direction and only take the degree of deformation into consideration. The performances on the average degree of deformation in terms of net rotational and translational parameters can be divided into the following four kinds: 1) GC: steps with periodicity have larger net values than those without periodicity on five of six parameters. 2) TA, AG/CT and GG/CC: steps with periodicity have larger net values on four of six parameters. 3) CA/TG and AC/GT: steps with periodicity exceed those without periodicity only on three of six parameters, in other words, in terms of three parameters, steps having no periodicity have greater net values than steps with periodicity. 4) AA/TT, GA/TC and AT: steps without periodicity exceed those with periodicity on five of six parameters which is exactly contrary to 1). It might also be noted that CG has remarkable average values of Shift, Slide and Twist. The averaged net Roll and SD values of the GG/CC0 group are significantly higher than those of the GG/CC1 group. Similarly, the GA/TC0 group has much larger averaged net Tilt value and SD than the GA/TC1 group.

3.3. Helical Parameters Reflect Structural Features of Dinucleotide Steps with Periodicity

In our studies, the statistical result of the value distribution frequency of the "0" and "1" groups of the 10 independent dinucleotide steps indicates that apparent differences between dinucleotides with periodicity and those without periodicity exist mainly in three helical parameters: Shift, Slide and Roll. They can be recognized as key parameters that drive the structural variability of periodic steps from others of the same type but without periodicity. Our finding supports Suzuki and Tolstorukov's theories [9,21] that Roll and Slide are the most important media by which particular dinucleotides exert their deformation properties on the overall structure of naked DNA or nucleosomes, and moreover, for types like AG/CT, GC, GG/CC, AT and TA in nucleosomes, their regular occurrences with the 10.5 bp periodicity along the DNA sequence endow these two parameters with unusual values and distribution trends. Indeed, Twist is an especially important parameter for describing dinucleotides' local behavior of "kinks". "Kinks" have impacts on the overall stretching of DNA sequence and to some extent influence dinucleotide periodicity. However, our results show that differences on Twist between the periodic and the non-periodic are not that obvious. Shift, which used to be excluded from the collection of key parameters, is in our conclusion another essential indicator of periodicity-dependent conformational attrib-

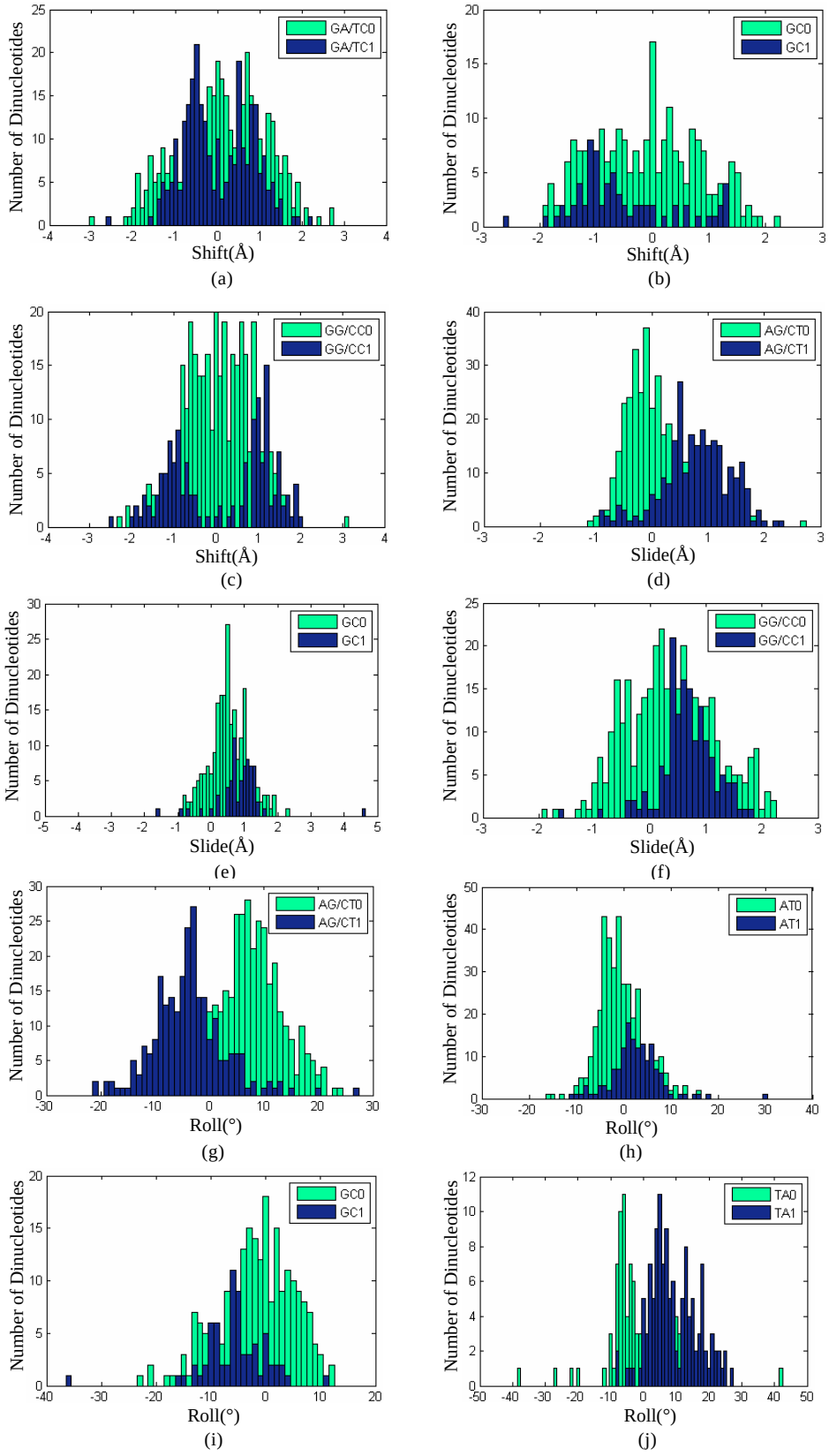

Figure 1. Frequency distribution of step parameter values.

Table 1. Average and standard deviation of the absolute values of base-pair parameters for the "0" and "1" groups of the 10 dinucleotide steps.

Step	N	Shift (Å)	Slide (Å)	Rise (Å)	Roll (°)	Tilt (°)	Twist (°)
CA/TG0	497	$0.62_{0.47}$	**‡ $0.95_{0.80}$**	$3.55_{0.45}$	*** $11.4_{7.5}$**	**‡ $4.0_{3.5}$**	**‡ $37.4_{6.9}$**
CA/TG1	468	$0.56_{0.48}$	***‡ $1.41_{0.92}$**	$3.41_{0.59}$	$9.1_{12.3}$	**‡ $5.4_{14.3}$**	***‡ $41.1_{10.6}$**
CG0	56	$0.79_{0.46}$	$1.38_{0.42}$	$3.44_{0.22}$	$4.9_{3.5}$	$3.4_{2.7}$	$40.9_{4.4}$
CG1	0						
TA0	108	**‡ $0.39_{0.38}$**	**‡ $0.47_{0.53}$**	$3.55_{0.47}$	**‡ $8.4_{7.1}$**	**‡ $3.8_{3.9}$**	$38.5_{5.8}$
TA1	124	**‡ $0.54_{0.54}$**	**‡ $0.49_{0.38}$**	$3.41_{0.40}$	**‡ $9.7_{6.7}$**	**‡ $4.8_{4.0}$**	$35.6_{5.3}$
AA/TT0	630	$0.44_{0.35}$	$0.34_{0.30}$	$3.36_{0.54}$	**‡ $5.4_{4.6}$**	$3.8_{3.2}$	$36.2_{6.1}$
AA/TT1	355	$0.41_{0.32}$	$0.33_{0.30}$	$3.34_{0.40}$	**‡ $6.9_{5.3}$**	$3.3_{3.1}$	$35.0_{5.7}$
GA/TC0	371	$0.83_{0.60}$	$0.69_{0.61}$	**‡ $3.33_{0.65}$**	$6.5_{4.9}$	*** $7.7_{19.6}$**	$36.7_{14.3}$
GA/TC1	262	$0.68_{0.40}$	$0.36_{0.26}$	**‡ $3.39_{0.55}$**	$4.4_{3.0}$	$4.2_{3.4}$	$35.9_{5.5}$
AG/CT0	351	**‡ $0.70_{0.49}$**	**‡ $0.43_{0.38}$**	**‡ $3.39_{0.30}$**	$8.2_{5.1}$	$4.4_{3.8}$	**‡ $33.3_{4.2}$**
AG/CT1	249	**‡ $0.89_{0.55}$**	**‡ $0.86_{0.48}$**	**‡ $3.41_{0.46}$**	$6.1_{4.6}$	$3.9_{3.2}$	**‡ $37.0_{5.6}$**
GG/CC0	348	**‡ $0.66_{0.47}$**	**‡ $0.69_{0.52}$**	$3.34_{0.59}$	$10.1_{9.2}$	**‡ $4.5_{4.6}$**	**‡ $33.2_{7.0}$**
GG/CC1	144	***‡ $1.11_{0.42}$**	**‡ $0.72_{0.39}$**	$3.24_{0.36}$	$4.9_{4.2}$	**‡ $5.8_{4.2}$**	**‡ $33.5_{5.0}$**
AT0	381	$0.45_{0.37}$	$0.74_{0.33}$	$3.19_{0.36}$	**‡ $3.7_{3.0}$**	$3.2_{2.6}$	$32.0_{4.8}$
AT1	144	$0.41_{0.36}$	$0.61_{0.29}$	$3.11_{0.27}$	**‡ $4.3_{4.0}$**	$2.9_{2.5}$	$28.3_{3.7}$
GC0	224	**‡ $0.78_{0.54}$**	**‡ $0.62_{0.43}$**	**‡ $3.35_{0.46}$**	**‡ $5.4_{4.4}$**	$4.8_{4.2}$	**‡ $36.8_{4.7}$**
GC1	68	**‡ $0.93_{0.47}$**	**‡ $0.95_{0.56}$**	***‡ $3.61_{0.56}$**	**‡ $6.6_{5.2}$**	$3.8_{3.1}$	**‡ $37.6_{8.1}$**
AC/GT0	263	**‡ $0.52_{0.38}$**	**‡ $0.59_{0.39}$**	$3.30_{0.45}$	**‡ $4.8_{3.2}$**	$4.1_{4.2}$	$31.3_{5.3}$
AC/GT1	196	**‡ $0.54_{0.43}$**	**‡ $0.67_{0.35}$**	$3.17_{0.46}$	**‡ $5.9_{3.7}$**	$4.1_{3.2}$	$29.5_{5.5}$

Absolute value of every step on each parameter is calculated, and then the mean parameter value and standard deviation for each group are calculated.
Number of subscript represents standard deviation.
* Maximum mean value for each parameter selected from all groups.
‡ Situation in which the mean value of the "1" group on one parameter is higher than that of "0" group.

utes of dinucleotides. Despite the fact that the mean Shift values are very small for all groups, the standard deviations are fairly considerable which means Shift values vary greatly even within each type and within each group, and this phenomenon of small mean values but large SD can be explained by the fact that the large positive values and large net negative values cancel each other out. Statistics on the value range and averaged absolute value support this interpretation as well and prove that in the case of nucleosomes, Shift distance is nearly comparable to Slide in respect of deformation degree and value variability.

3.4. Deformability of Steps

The six structural parameters are in fact interdependent and the one-dimensional study is quite limited in characterizing the flexibility of various dinucleotide steps. The step conformational energies incorporate these structural features and well outline the deformability of the periodic and the non-periodic dinucleotides. For a certain type of dinucleotide in each nucleosome, the representative energy score for the "0" or "1" group of this type is defined as the average product of energy values of all the steps in this group. A complete list of dinucleotide energy scores calculated in this way over the 35 nucleosomes is given in Appendix. For dinucleotides of AA/TT, AT, AG/CT, CA/TG and GC type, the number of periodic groups having higher energy scores than the corresponding non-periodic groups is close to or approximately the same with that of non-periodic groups having higher energy scores than periodic groups of the same type among all the nucleosome samples. In a statistical sense the observed deformabilities of periodic dinucleotides of these types are almost identical with their non-periodic counterparts. It is also found that in most of the 35 nucleosome cases the GA/TC0 and GG/CC0 groups have greater energy scores than corresponding GA/TC1 and GG/CC1 groups, with the proportions up to 88.5% and 79.4% of the total samples respectively. On the contrary, the quantity of nucleosomes in which the energy scores of AC/GT1 and TA1 groups exceed those of AC/GT0 and TA0 groups accounts for 80% and 87.8% of the total number of nucleosomes respectively. It is concluded that periodic GA/TC and GG/CC steps have greater deformability than their non-periodic counterparts while periodic AC/GT and TA steps appear more rigid than the non-periodic AC/GT and TA steps.

4. SUMMARY

AA/TT steps belong to the type whose conformational settings are not very susceptible to the 10.5 periodicity. In the parameter value frequency histogram, AA/TT steps with periodicity have no clear differences from those without periodicity. The mean absolute values, value variabilities for the periodic and non-periodic steps are also very close to each other. Although statistics on step conformational energy reveals that the probability of the non-peiodic group requiring higher amount of energy to deform is higher than that of the periodic group requiring higher energy, it is still not predominant enough to discriminate the non-periodic group from the periodic group. The above results may suggest that the periodicity of AA/TT steps, on the whole, does not produce particular effects on their conformation features. AA/TT or A-tracts are most likely to play the role of exerting context influences on their neighbor dinucleotides and occupy specific positions to facilitate the bending of DNA around the histone core [22,23].

AC/GT can also be categorized into the periodicity-unsusceptible type. The relations and comparisons of the six parameters between periodic AC/GT and non-periodic AC/GT on value frequency plots, averaged net values and their standard deviations are quite similar to that of AA/TT. Compared with the non-periodic ones, to some extent periodic AC/GT steps are more rigid.

AG/CT steps can be characterized as very susceptible to the 10.5 periodicity. Firstly, there are obvious differences in the plots of value occurrences on Slide and Roll between the 10.5 bp-periodic AG/CT steps and the non-periodic ones. Secondly, periodic AG/CT steps have clearly different performances from non-periodic ones on averaged net values and value standard deviations, further testifying that the structural feature of AG/CT in terms of some parameters is correlated with periodic step occurrences in the DNA sequence.

AT steps have limited structural susceptibility to the 10.5 periodicity. On the frequency plots of parameter values, periodic steps are different from non-periodic steps on the parameter Roll, but non-periodic AT steps exceed periodic ones on five of the six parameters in the measurement of the mean net values. It can be concluded that the 10.5 periodicity is a structural feature of AT but may not necessarily contribute to sharp deformation in nucleosomes.

CA/TG steps are also susceptible to the 10.5 periodicity. Although the periodic group does not show any apparent differences from the non-periodic group on distribution plots of value occurrences and averaged values, the periodic group has much larger standard deviations than the non-periodic group. This implies that the 10.5 periodicity expressed in CA/TG steps have very large parameter value variability. CA/TG is acknowledged by most reports as being the most flexible steps that may act as "hinge" fitting the duplex to the protein surface due to its great structural variability and low energy consumption for bending [9,10,14,20,24].

CG steps are all marked as non-periodic, but notably they have distinct preferences of parameter value occurrences. Most CG steps take negative Shift and Roll values and positive Slide values. CG also has a large averaged net value on Twist which is only slightly lower than CA/TG1, while the corresponding standard deviation for net Twist values is much smaller than that of CA/TG1. It means that CG steps uniformly have a large degree of Twist.

GA/TC steps also have a certain degree of structural susceptibility to the 10.5 periodicity. Compared with non-periodic ones, GA/TC steps with 10.5 bp periodicity display a slightly different value distribution on Shift and obviously more deformability than the non-periodic ones.

The GC step is another kind of dinucleotides particularly sensitive to the 10.5 periodicity. Periodic GC steps have clearly distinguishing distribution patterns from non-periodic steps on value occurrences statistical plots of Shift, Roll and Slide. The periodic group also has larger averaged net values and standard deviations than the latter on five of the six parameters.

The GG/CC steps also belong to the periodicity-susceptible type. Steps with 10.5 bp periodicity have different distributions of value occurrences from non-periodic ones on Shift and Slide. The averaged net values of periodic ones are higher than those of non- periodic ones on four of the six parameters. The periodic GG/CC steps also have obviously more deformability than non-periodic ones. However, it still should be noted that the standard deviations of non-periodic GG/CC steps are higher than those of periodic ones on six parameters in case of mean net values, and the non-periodic group has far larger averaged net Roll value and standard deviations than the periodic group. Thus, the influence of periodicity on GG/CC is interpreted as partially reinforcing the deformability while restricting bending and shearing variability.

TA steps have a certain degree of sensitivity to the 10.5 bp periodicity. Differences between periodic ones and non-periodic ones on Roll value distribution frequency plots can be observed but are relatively subtle. The mean net values of periodic steps exceed those of the non-periodic ones on four of the six parameters, and standard deviations on each parameter for the two groups, however, are quite close to each other. The result of energy score calculation also reveals periodic TA steps are more rigid than non-periodic ones. The periodicity, by all counts, has limited influences on TA steps.

To summarize all the above analysis comprehensively, the dinucleotide steps AG/CT, GC and GG/CC are most immediately affected by the 10.5 bp periodicity. Periodic occurrences along the nucleosomal DNA sequence as-

sign them distinct shearing and bending preferences, greater degrees of deformation and variability. Steps CA/TG, GA/TC and TA can be divided into the second category that is modestly influenced by the 10.5 periodicity. Undoubtedly, special conformational trends on some aspects do appear for periodic ones in this category, compared with the first class above, however, trends for the separation of periodic ones from non-periodic ones are not prominent enough or all the separation standards cannot be satisfied at the same time. Steps AA/TT, AC/GT and AT fall into the third category that is least structurally influenced by the 10.5 periodicity, which means that the structural attributes of periodic steps in this category is similar to non-periodic ones. Finally, susceptibility of CG to 10.5 bp periodicity cannot be evaluated because of lack of enough nucleosome samples, but as a YR-type dimer it should have considerable influence on DNA deformation.

5. ACKNOWLEDGEMENT

This work is supported by the Hong Kong Research Grant Council (Project CityU 123408).

REFERENCES

[1] Zhurkin, V.B. (1983) Specific alignment of nucleosomes on DNA correlates with periodic distribution of purine-pyrimidine and pyrimidine-purine dimers. *FEBS Letters*, **158(2)**, 293-297.

[2] Sarchwell, S.C., Drew, H.R. and Travers, A.A. (1986) Sequence periodicities in chicken nucleosome core DNA. *Journal of Molecular Biology*, **191(4)**, 659-675.

[3] Simpson, R.T. (1991) Nucleosome positioning: Occurrence, mechanisms, and functional consequences. *Progress in Nucleic Acid Research and Molecular Biology*, **40**, 143-184.

[4] Peckham, H.E., Thurman, R.E., Fu, Y., Stamatoyannopoulos, J.A., Nobel, W.S., Struhl, K. and Weng, Z. (2007) Nucleosome positioning signals in genomic DNA. *Genome Research*, **17(8)**, 1170-1177.

[5] Salih, F., Salih, B. and Trifonov, E.N. (2008) Sequence structure of hidden 10.4-base repeat in the nucleosomes of C. elegans. *Journal of Biomolecular Structure and Dynamics*, **26(3)**, 273-281.

[6] Trifonov, E.N. (1998) 3-, 10.5-, 200- and 400-base periodicities in genome sequences. *Physica A*, **249(1-4)**, 511-516.

[7] Widom, J. (2001) Role of DNA sequence in nucleosome stability and dynamics. *Quarterly Reviews of Biophysics*, **34**, 269-324.

[8] Segal, E., Fondufe-Mittendorf, Y., Chen, L., Thåström, A., Field, Y., Moore, I.K., Wang, J.Z. and Widom, J. (2006) A genomic code for nucleosome positioning. *Nature*, **442(7104)**, 772-778.

[9] Tolstorukov, M.Y., Colasanti, A.V., McCandlish, D.M., Olson, W.K. and Zhurkin, V.B. (2007) A novel roll-and-slide mechanism of DNA folding in chromatin: Implications for nucleosome positioning. *Journal of Molecular Biology*, **371(3)**, 725-738.

[10] Bolshoy, A., McNamara, P., Harrington, R.E. and Trifonov, E.N. (1991) Curved DNA without A-A: Experimental estimation of all 16 DNA wedge angles. *Proceedings of the National Academy of Sciences*, **88(6)**, 2312-2316.

[11] Packer, M.J., Dauncey, M.P. and Hunter, C.A. (2000) Sequence-dependent DNA structure: Dinucleotide confor mational maps. *Journal of Molecular Biology*, **295(1)**, 71-83.

[12] Bishop, T.C. (2005) Molecular dynamics simulations of a nucleosome and free DNA. *Journal of Biomolecular Structure and Dynamics*, **22(6)**, 673-686.

[13] Fujii, S., Kono, H., Takenaka, S., Go, N. and Sarai, A. (2007) Sequence-dependent DNA deformability studied using molecular dynamics simulations. *Nucleic Acids Research*, **35(18)**, 6063-6074.

[14] Olson, W.K., Gorin, A.A., Lu, X., Hock, L.M. and Zhurkin, V.B. (1998) DNA sequence-dependent deformability deduced from protein-DNA crystal complexes. *Proceedings of the National Academy of Sciences*, **95(19)**, 11163-11168.

[15] Lu, X. and Olson, W.K. (2003) 3DNA: A software package for the analysis, rebuilding and visualization of three-dimensional nucleic acid structures. *Nucleic Acids Research*, **31(17)**, 5108-5121.

[16] Trifonov, E.N. (1980) Sequence-dependent deformational anisotropy of chromatin DNA. *Nucleic Acids Research*, **8(17)**, 4041-4053.

[17] Worning, P., Jensen, L.J., Nelson, K.E., Brunak, S. and Ussery, D.W. (2000) Structural analysis of DNA sequence: Evidence for lateral gene transfer in Thermotoga maritima. *Nucleic Acids Research*, **28(3)**, 706-709.

[18] Liu, H., Wu, J., Xie, J., Yang, X., Lu, Z. and Sun, X. (2008) Characteristics of nucleosome core DNA and their applications in predicting nucleosome positions. *Biophysical Journal*, **94(12)**, 4597-4604.

[19] Wu, Q., Wang J. and Yan, H. (2009) Prediction of nucleosome positions in the yeast genome based on matched mirror position filtering. *Bioinformation*, **3(10)**, 454-459.

[20] Suzuki, M., Yagi, N. and Finch, J.T. (1996) Role of base-backbone and base-base interactions in alternating DNA conformations. *FEBS letters*, **379(2)**, 148-152.

[21] Suzuki, M., Amano, N., Kakinuma, J. and Tateno, M. (1997) Use of a 3D structure data base for understanding sequence-dependent conformational aspects of DNA. *Journal of Molecular Biology*, **274(3)**, 421-435.

[22] Sarai, A., Mazur, J., Nussinov, R. and Jernigan, R.L. (1989) Sequence dependence of DNA conformational flexibility. *Biochemistry*, **28(19)**, 7842-7849.

[23] Young, M.A., Ravishanker, G., Beveridge, D.L. and Berman, H.M. (1995) Analysis of local helix bending in crystal structures of DNA oligonucleotides and DNA-protein complexes. *Biophysical Journal*, **68(6)**, 2454-2468.

[24] Bharanidharan, D. and Gautham, N. (2006) Principle component analysis of DNA oligonucleotide structural data. *Biochemical and Biophysical Research Communications*, **340(4)**, 1229-1237.

Appendix

	aa0	aa1	ac0	ac1	ag0	ag1	at0	at1	ca0	ca1	cg0
1AOI	1.92	2.00	2.43	1.95	3.23	3.50	1.97	2.26	3.37	2.95	
1EQZ	1.85	1.83	1.34	3.01	3.77	2.49	2.43	4.59	3.98	3.57	2.11
1F66	2.26	1.53	2.36	1.39	2.88	2.34	2.18	2.53	3.39	3.54	2.03
1ID3	2.46	1.59	1.86	4.82	2.62	3.86	2.09	1.31	3.89	3.01	4.24
1KX3	1.65	1.52	1.82	3.00	1.90	2.34	5.62	2.53	3.82	3.19	
1KX4	3.05	2.85	2.01	2.71	1.50	3.54	2.41	3.01	6.44	2.68	2.46
1KX5	2.11	2.21	1.30	2.91	2.90	3.50	2.43	2.05	4.12	2.81	
1M18	2.22	1.92	2.64	4.38	3.88	3.85	2.51	2.56	3.17	3.73	3.09
1M19	2.21	1.36	3.88	4.06	4.04	2.86	2.14	1.82	2.68	6.28	3.22
1M1A	1.63	2.29	4.90	3.63	2.77	2.54	1.93	2.47	3.49	4.45	2.59
1P34	2.22	2.30	1.88	2.91	2.02	2.87	1.93	1.70	3.89	3.61	2.26
1P3A	2.41	2.15	1.47	1.78	2.68	2.11	2.17	1.87	3.63	3.89	2.84
1P3B	2.03	1.11	1.48	2.78	2.61	1.95	1.60	1.20	3.04	5.22	2.33
1P3F	1.76	2.16	2.00	2.39	2.62	3.68	2.58	2.58	3.69	4.05	3.82
1P3G	2.02	2.65	1.76	3.26	2.30	3.46	2.08	1.61	3.22	4.22	2.06
1P3I	1.77	1.38	1.83	3.26	3.06	2.15	2.00	2.66	3.64	3.75	2.45
1P3K	2.20	1.32	1.83	2.70	2.76	2.75	2.40	1.54	3.23	2.91	4.07
1P3L	2.34	1.60	2.47	3.12	2.59	1.86	2.67	3.55	4.03	3.95	3.58
1P3M	1.92	2.03	1.97	3.21	2.70	2.53	2.56	1.32	4.15	4.08	3.90
1P3O	1.94	2.52	2.02	2.76	2.98	2.99	1.89	1.70	3.70	4.01	3.00
1P3P	1.85	2.74	2.31	2.36	3.36	2.76	2.14	1.95	3.82	4.20	2.90
1S32	2.25	0.53	1.58	1.23	2.15	2.05	1.85	1.63	3.24	7.79	1.48
1U35	1.76	1.53	7.55	3.66	2.49	4.25	1.90	2.41	3.70	5.64	1.73
1ZBB	2.25	1.96	1.71	3.35	2.25	2.90	2.36	1.87	3.89	2.64	1.30
1ZLA	1.07	0.94	1.08	2.17	1.77	2.38	1.45	1.40	3.67	7.89	2.47
2CV5	1.85	1.81	1.88	2.11	1.93	5.07	2.98	2.41	3.87	3.74	
2F8N	1.72	2.51	3.35	3.86	2.25	6.04	2.01	1.61	3.36	4.75	2.41
2FJ7	2.61	2.86	2.42	2.91	2.96	2.96	3.54	2.00	2.83	3.33	
2NQB	2.11	0.84	1.48	1.96	1.34	1.60	1.59	1.20	2.44	8.94	1.69
2NZD	1.68	1.15	1.39	2.15	1.96	2.42	3.32	1.60	5.55	2.97	
2PYO	2.08	2.40	1.56	2.38	2.28	4.47	2.36	3.12	4.14	2.83	
3B6F	3.09	2.75	0.66	2.07	2.56	2.69	3.22	1.84	2.36	4.09	
3B6G	3.06	1.52	4.54	2.47	2.21	4.01	2.73	3.05	3.91	3.38	
3C1B	2.16	0.63	1.34	1.57	1.29	1.64	1.44	1.14	2.30	8.11	2.25
3C1C	1.55	0.81	2.49	1.71	1.28	2.24	1.71	1.41	3.16	6.88	3.18
AVE.	**2.09**	**1.81**	**2.25**	**2.74**	**2.51**	**2.99**	**2.35**	**2.10**	**3.62**	**4.37**	**2.67**
	aa0>aa1	aa0<aa1	ac0>ac1	ac0<ac1	ag0>ag1	ag0<ag1	at0>at1	at0<at1	ca0>ca1	ca0<ca1	
Number	23	12	7	28	13	22	23	12	15	20	
Percent-age	65.70%	34.30%	20.00%	80.00%	37.10%	62.90%	65.70%	34.30%	42.90%	57.10%	

	ga0	ga1	gc0	gc1	gg0	gg1	ta0	ta1
1AOI	3.86	2.81	4.96	3.10	4.68	4.27	2.41	3.77
1EQZ	3.13	2.30	4.94	2.94	2.66	4.99	2.49	5.07
1F66	5.71	1.48	3.37	2.03	5.88	2.93	1.86	3.13
1ID3	2.64	1.73	2.60	5.44	5.36	4.98	1.65	
1KX3	3.13	1.72	4.72	2.01	4.37	3.66	1.50	5.46
1KX4	3.36	2.19	3.13		3.29		4.38	
1KX5	7.51	1.68	2.97	2.97	2.38	4.00	2.14	2.88
1M18	3.57	2.02	3.64	2.53	3.08	3.85	2.43	2.31
1M19	2.28	2.04	2.36	3.31	2.96	2.35	2.18	3.60
1M1A	2.99	1.93	5.28	2.77	3.22	3.18	2.99	3.09
1P34	4.47	2.83	2.13	2.95	5.32	3.58	2.24	4.14
1P3A	3.83	2.22	3.16	2.35	5.26	4.75	3.52	3.94
1P3B	5.19	2.17	3.20	4.36	6.19	4.16	2.07	2.78
1P3F	3.57	2.00	3.99	2.01	4.73	3.37	1.67	3.70
1P3G	3.23	2.91	1.75	2.25	5.68	4.74	1.92	4.77
1P3I	3.59	2.91	3.43	4.14	6.09	2.87	1.42	4.63
1P3K	3.40	3.28	2.57	4.04	5.65	5.39	2.01	5.76
1P3L	2.59	2.45	2.51	2.57	4.42	4.07	1.22	5.28
1P3M	2.35	2.59	3.45	4.08	4.51	3.50	3.93	4.53
1P3O	2.94	2.29	2.18	3.36	5.87	4.03	1.72	4.38
1P3P	3.13	2.29	4.38	2.55	3.88	2.76	1.72	4.50
1S32	8.72	1.15	1.87	1.98	1.89	2.18	1.12	4.00
1U35	1.52	1.81	2.79		3.33	2.36	0.79	3.34
1ZBB	5.82	0.89	2.55	6.95	2.12	4.07	6.07	2.36
1ZLA	9.07	1.32	2.48	2.05	3.59	2.70	0.75	2.86
2CV5	3.32	2.86	3.94	5.05	3.22	4.65	2.36	2.44
2F8N	2.44	1.76	2.73	4.34	3.38	2.30	6.74	1.97
2FJ7	2.53	4.69	2.93		2.92	3.76	3.66	6.34
2NQB	9.18	1.21	1.74	1.94	4.60	2.54	1.54	1.07
2NZD	2.66	2.63	2.24		8.64	3.65	3.16	2.20
2PYO	6.42	1.69	3.34	3.60	3.20	3.04	2.11	2.19
3B6F	3.42	4.06	2.56	3.01	3.45	2.66	2.77	3.03
3B6G	2.61	1.64	4.10	3.61	2.90	2.60	1.94	2.07
3C1B	9.82	1.73	1.72	1.43	4.83	2.16	1.06	1.49
3C1C	8.98	1.93	2.68	2.24	3.57	2.23	1.46	1.74
AVE.	**4.37**	**2.21**	**3.10**	**3.16**	**4.20**	**3.48**	**2.37**	**3.48**
	ga0>ga1	ga0<ga1	gc0>gc1	gc0<gc1	gg0>gg1	gg0<gg1	ta0>ta1	ta0<ta1
Number	31	4	14	17	27	7	4	29
Percentage	88.60%	11.40%	45.20%	54.80%	79.40%	20.60%	12.10%	87.90%

J. Biomedical Science and Engineering, 2010, 3, 340-350 **JBiSE**
doi:10.4236/jbise.2010.34047 Published Online April 2010 (http://www.SciRP.org/journal/jbise/).

Characterization of the sequence spectrum of DNA based on the appearance frequency of the nucleotide sequences of the genome

——A new method for analysis of genome structure

Masatoshi Nakahara[1], Masaharu Takeda[2]

[1]Department of Computer and Information Sciences, Sojo University, Ikeda, Japan;
[2]Department of Materials and Biological Engineering, Tsuruoka National College of Technology, Tsuruoka, Japan.
Email: mtakeda@tsuruoka-nct.ac.jp

Received 13 January 2010; revised 25 January 2010; accepted 30 January 2010.

ABSTRACT

The nucleotide (base) sequence of the genome might reflect biological information beyond the coding sequences. The appearance frequencies of successive base sequences (key sequences) were calculated for entire genomes. Based on the appearance frequency of the key sequences of the genome, any DNA sequences on the genome could be expressed as a sequence spectrum with the adjoining base sequences, which could be used to study the corresponding biological phenomena. In this paper, we used 64 successive three-base sequences (triplets) as the key sequences, and determined and compared the spectra of specific genes to the chromosome, or specific genes to tRNA genes in *Saccharomyces cerevisiae*, *Schizosaccharomyces pombe* and *Escherichia coli*. Based on these analyses, a gene and its corresponding position on the chromosome showed highly similar spectra with the same fold enlargement (approximately 400-fold) in the *S. cerevisiae*, *S. pombe* and *E. coli* genomes. In addition, the homologous structure of genes that encode proteins was also observed with appropriate tRNA gene(s) in the genome. This analytical method might faithfully reflect the encoded biological information, that is, the conservation of the base sequences was to make sense the conservation of the translated amino acids sequence in the coding region, and might be universally applicable to other genomes, even those that consisted of multiple chromosomes.

Keywords: Appearance Frequency of Triplet in Genome Base Sequence; Self-Similarity; Analytical Method of Genome Structure

1. INTRODUCTION

It was well known that there were structural hierarchies in the genome, such as the chromosome, nucleosome, ORF (open reading frame) and so on [1]. Among them, much attention have been paid to the ORF, and many research projects were being performed from the viewpoint of protein function using methods such as proteome and transcriptome analyses [2-5]. Many studies of entire genome sequences have been reported [6-11], although complete genome base sequences have only been revealed within the last 10 years or so. However, we currently have limited tools to analyze a large-scale molecule such as a whole genome, including pertinent hard-and software. It was very important to investigate the structural features of the entire genome because the four bases could be arranged in a sophisticated fashion in the genome, and in principle the base sequences might be reflected in the conformations of protein, RNA and DNA. In other words, if we could identify a meaningful structure, or an analytical method for analysis of the genome, we could also obtain important information about the functions of protein, RNA and DNA from that structure.

The four bases in genomic DNA were arranged sophisticatedly in all organisms and distinguish the coding-and the non-coding region clearly on the genome. By analyzing the appearance frequency of the bases, it was shown that first, the symmetry [8-11], second, the bias [12-15] and third, the fractality [16-19] could be necessary to generate genome base sequences. We analyzed genome structure based on the appearance frequency of genome base sequences [20]. We have studied many genome sequences down-loaded from databases like NCBI [21], and calculated the appearance frequencies of an optional base sequence (key sequence) in a genome.

Subsequently, we determined the sequence spectra of chromosome, gene and DNA from the key sequence of the genome (chromosome), and analyzed both the coding-and non-coding sequences because the key se-

quences were used throughout the genome in cells. However, in the coding regions in the DNA, the appearance frequencies of the key sequences of an individual gene should vary in the genome because the protein-encoding gene and the adjoining (5'- and 3'-) non-coding base sequences were different. In other words, the appearance frequencies of the base sequences should be different for each gene. Even if the base sequences of the gene were identical, the adjoining base sequences differ, suggesting that each DNA sequence might have an effect on the expression of the gene and function as an informative DNA molecule [20].

Each gene was transcribed to mRNA, and translated to a protein on the ribosome (polyribosome) according to the DNA sequence of each coding region. In other words, the biological information of DNA (base sequence) should be transferred to protein via mRNA (base sequence). That is, the information of the base sequence of DNA was transformed to the amino acid sequence by tRNAs corresponding to the base sequences of the mRNA on the ribosome [22].

However, the coding regions varied in individual genomes and species [23,24]. The non-coding sequences might be necessary to precisely, rapidly, and consistently regulate gene expression [24,25]. In other words, the genome might be a "field" on which the four bases were sophisticatedly arranged into genes that were regulated and expressed to carry out the biological phenomena of life. Therefore, analytical methods to characterize genome structure were needed to understand the encoded biological phenomena.

In this study, we developed an analytical method based on the frequencies of the nucleotide (base) sequences in the whole genome according to the flow of biological information, and focused on the self-similarity in the genomes of *S. cerevisiae* and *S. pombe*, where most of the genes had introns, and *E. coli*, in which most of genes were in operons.

2. MATERIALS AND METHODS

2.1. Sequence Spectrum Method (SSM)

The outline of the proposed method was as follows. The base sequence of interest was sectioned by a small number of bases from the top (5'-end). The sectioned base sequence was called the key sequence. In the case of three successive base sequences (d = 3), the appearance frequencies of the 64 triplets (the genetic codon) were shown in **Table 1** (key sequence at d = 3). The key sequences of the nine successive base sequences (d = 9) was 262,144 sequences (= 4^9, ref. 20). The appearance frequency of the key sequence was counted in the entire genome, and was plotted at the position of the first base of the key sequence as described in the next paragraph of the Materials and Methods. These procedures were carried out for the entire base sequence of interest with one base shift (p = 1). The next step was to average the appearance frequencies so that a recognizable pattern of appearance frequency was obtained for the base sequence. This pattern of the averaged appearance frequency was called the "sequence spectrum". Finally, the homology factor between two sequence spectra was calculated to determine the degree of homology. The exact procedure was explained below in a mathematical way.

Let S be an entire set of base sequences, and B = [b_i] be a partial set of interest in S. A base element was denoted by b_i (I=1, ... , M), and M was the base sequence size of B. The base element b_i become A (adenine), T (thymine), G (guanine) or C (cytosine). The key sequence k_i and the appearance frequency f_i were defined for b_i as follows.

Key sequence k_i: base sequence comprised of sequential base elements b_i~b_{i+d-1} (d : base size of the key sequence)

Appearance frequency f_i: appearance count of k_i in S

The key sequence k_i was compared with the base sequence of the entire set S, and the appearance frequency f_i was increased by one every time the key sequence k_i matches the partial base sequence of the entire set S. This procedure was iterated for all key sequences k_i to obtain f_i (I = 1, ... , M). Consequently, the appearance frequency vector F = [f_i] (I = 1, ... , M) was determined (actually, the appearance frequencies for the last (d-1) base elements of B could not be calculated; however, this was neglected because M >> d-1).

Next, the appearance frequency f_i was averaged as follows:

$$f_{si} = \frac{1}{2m+1}\sum_{j=i-m}^{i+m} f_j$$

where the parameter m was average width. This averaged appearance frequency Fs = [f_{si}] (I = 1, … , M) was called the "sequence spectrum".

The next step was to calculate the homology factor to determine the degree of homology. The homology factor determines the homologous region of a target base sequence with respect to a reference base sequence. In order to derive the homology factor, the mutual correlation function MF was calculated as

$$MF_k(Fsr, Fst) = \frac{1}{\|Fsr\|\|Fst_k\|}\sum_{i=1}^{Mr}(fsr_i - \overline{fsr})*(fst_{i+k} - \overline{fst_k})$$

$$\|Fsr\| = \sqrt{\sum_{i=1}^{Mr}(fsr_i - \overline{fsr})*(fsr_i - \overline{fsr})}$$

$$\|Fst_k\| = \sqrt{\sum_{i=1}^{Mr}(fst_{i+k} - \overline{fst_k})*(fst_{i+k} - \overline{fst_k})}$$

$$\overline{fsr} = \sqrt{\frac{1}{Mr}\sum_{i=1}^{Mr} fsr_i}$$

$$\overline{fst_k} = \sqrt{\frac{1}{Mr}\sum_{i=1}^{Mr} fst_{i+k}}$$

Table 1. Key sequences of the three succssive base sequences*1 in genome*2.

Triplet	Frequency	Triplet	Frequency	Triplet	Frequency	Triplet	Frequency
(a) S. cerevisiae							
AAA	478,677	AAT	359,378	AAG	263,401	AAC	219,288
ATA	302,770	ATT	358,051	ATG	221,867	ATC	214,197
AGA	246,395	AGT	184,087	AGG	138,976	AGC	139,262
ACA	208,942	ACT	183,292	ACG	106,020	ACC	141,084
TAA	271,996	TAT	301,699	TAG	156,650	TAC	172,399
TTA	271,724	TTT	475,621	TTG	279,349	TTC	286,655
TGA	244,596	TGT	207,422	TGG	179,858	TGC	150,406
TCA	245,024	TCT	244,505	TCG	110,351	TCC	154,145
GAA	288,804	GAT	213,000	GAG	136,067	GAC	118,074
GTA	172,583	GTT	218,208	GTG	128,946	GTC	117,316
GGA	154,364	GGT	139,691	GGG	81,268	GGC	95,122
GCA	150,888	GCT	139,012	GCG	67,875	GCC	95,478
CAA	281,266	CAT	222,808	CAG	152,602	CAC	129,575
CTA	155,668	CTT	261,471	CTG	152,121	CTC	135,857
CGA	110,589	CGT	105,859	CGG	70,348	CGC	68,463
CCA	181,394	CCT	138,308	CCG	71,012	CCC	82,880
(b) S. pombe							
AAA	569,684	AAT	409,666	AAG	277,238	AAC	234,759
ATA	310,191	ATT	409,111	ATG	227,572	ATC	207,984
AGA	225,118	AGT	196,340	AGG	128,892	AGC	158,220
ACA	212,145	ACT	193,959	ACG	110,332	ACC	123,580
TAA	334,648	TAT	310,127	TAG	162,059	TAC	183,503
TTA	334,208	TTT	572,331	TTG	296,280	TTC	292,897
TGA	244,964	TGT	213,557	TGG	156,002	TGC	157,500
TCA	245,161	TCT	227,278	TCG	123,339	TCC	149,364
GAA	291,250	GAT	207,564	GAG	134,381	GAC	108,437
GTA	185,292	GTT	236,486	GTG	113,029	GTC	109,314
GGA	148,699	GGT	123,656	GGG	67,242	GGC	75,049
GCA	157,454	GCT	157,621	GCG	64,622	GCC	75,416
CAA	295,764	CAT	227,501	CAG	134,892	CAC	113,317
CTA	160,646	CTT	277,788	CTG	135,142	CTC	134,949
CGA	122,848	CGT	110,569	CGG	62,511	CGC	64,344
CCA	156,714	CCT	129,667	CCG	61,979	CCC	67,351
(c) E. coli							
AAA	108,901	AAT	82,992	AAG	63,364	AAC	82,578
ATA	63,692	ATT	83,395	ATG	76,229	ATC	86,476
AGA	56,618	AGT	49,774	AGG	50,611	AGC	80,848
ACA	58,633	ACT	49,863	ACG	73,263	ACC	74,899
TAA	68,837	TAT	63,279	TAG	27,241	TAC	52,591
TTA	68,824	TTT	109,825	TTG	76,968	TTC	83,846
TGA	83,483	TGT	58,369	TGG	85,132	TGC	95,221
TCA	84,033	TCT	55,469	TCG	71,733	TCC	56,025
GAA	83,490	GAT	86,547	GAG	42,460	GAC	54,737
GTA	52,670	GTT	82,590	GTG	66,108	GTC	54,225
GGA	56,199	GGT	74,291	GGG	47,470	GGC	92,123
GCA	96,010	GCT	80,285	GCG	114,609	GCC	92,961
CAA	76,607	CAT	76,974	CAG	104,785	CAC	66,752
CTA	26,762	CTT	63,653	CTG	102,900	CTC	42,714
CGA	70,934	CGT	73,159	CGG	86,870	CGC	115,673
CCA	86,442	CCT	50,412	CCG	87,031	CCC	47,764

*1; 5'- to 3'-end correspond to the left to the right letter of each triplet.
*2; S. cerevisiae genome is composed of 16 chromosomes plus mtDNA.
S. pombe genome is composed of 3 chromosomes plus mtDNA.

where

Fsr: sequence spectrum of the reference base sequence with base size Mr

Fst: sequence spectrum of the target base sequence with base size Mt (> Mr)

The mutual correlation function MF ranges from –1 to 1, and then the homology factor HF was defined as

$$HF_k\left(Fsr, Fst\right) = \frac{\left(MF_k + 1\right)}{2} * 100[\%]$$

The higher the homology factor, the more homologous the sequence spectra were. The homologous regions of the target base sequence with respect to the reference base sequence were obtained by calculating the homology factors HF_k for all k (k = 0, ... , Mt-Mr), and targeting the regions with higher homology factors.

When the target base sequence was very large, elements of the target sequence spectrum were skipped by the size factor p to reduce the size as follows.

$$fst_i \rightarrow fst_{(i-1)*p+1}$$

For instance, when p = 2

$$fst_1, fst_2, fst_3 \ldots \rightarrow fst_1, fst_3, fst_5 \ldots$$

This operation reduced the size to 1/p.

The base sequences of the genomes were obtained from the databases listed below.

Saccharomyces cerevisiae:
http://www.mips.biochem.mpg.de/

Schizosaccharomyces pombe:
http://www.sanger.ac.uk/

Escherichia coli:
http://bmb.med.miami.edu/Ecogene/ecoWeb/

2.2. Appearance Frequencies of Bases or Base Sequences.

In order to analyze the structure of the base sequence, the most appropriate parameter was considered to be the appearance frequency. For three successive bases (triplets), the appearance frequency was counted for the entire genome by matching the triplet from the start of the base sequence in a genome with one base shift (p = 1) as follows.

Ex. Triplet bases**:** **AAT**
AAT ⟶ (one base shift)
BaseSequence:
5’-ATCG**AAT**CCGT**AAT**TCGGAGTCG**AAT**T-3’
Count of **AAT**: 1 2 3

3. RESULTS

3.1. Sequence Spectrum

Figure 1 showed the sequence spectrum of the F_1F_0-ATPase subunit gene *ATP*1 [26, YBL099W] in *Saccharomyces cerevisiae*. In this figure, the vertical parameter of the sequence spectrum f_{si} was not designated, and it was scaled properly because the shape of the sequence spectrum only makes sense in this manuscript. The horizontal parameter was the base sequence number i (I=1, ... , M), and it was also omitted in the following figures because it was easily derived from the base sequence size M.

Controllable parameters in the sequence spectrum were the base size d of the key sequence, the average width m, and the size factor p (skipped base numbers). The parameter d determines the highest resolution for extracting the structural features of the base sequence. In this report, we used the key sequence as d = 3 (appearance frequency table of triplet, **Table 1**) for numerical experiments of the homologous structure discussed in the following sections.

However, as shown in **Figure 1**, smaller m-values caused a harder zigzag pattern of the sequence spectrum, and eventually it become more difficult to identify the structure of the base sequence (**Figure 1(a)**). Therefore, large m-values were usually used to obtain the overall features of the structure, and smaller m-values were applied to investigate the structure in detail (**Figure 1(b)**). The value of m normally ranges from 1/10 to 1/100 of the base sequence size. In this manuscript, m = 2 for a tRNA, m = 60 for a gene, and m = 8,000 for a chromosome. The size factor p was adjusted to the base sequence size especially when the homology factor between a small reference and a large target was calculated.

The possible appearance frequencies f_i of key sequences k_i were calculated for the entire set S in advance. The appearance frequency table depended on the entire set S, and in general S was the genome of the target species.

3.2. Reverse-Complement Symmetry in the Appearance Frequency Table

Table 1 showed the appearance frequencies (3 successive base sequences = triplet, d = 3) of the key sequence for *Saccharomyces cerevisiae* (a), *Schizosaccharomyces pombe* (b), and *Escherichia coli* (c). This table gave some important features about the genome. In the case of *S. cerevisiae*, first, it was notable that the appearance frequencies of the key sequence and its reverse-complementary key sequence were almost the same. The reverse-complement key sequence was derived from reversing the base order of the original key sequence in *S. cerevisiae*, exchanging A and T, and exchanging G and C. For example, the appearance frequency of 5’-ATT is 358,051 and that of 5’-AAT was 359,378. The difference was less than 1%. The largest difference was about 2% for 5’-GGG (81,268) and 5’-CCC (82,880). This fact is valid regardless of the species, such as *Escherichia coli* (**Table 1(b)**) or *Schizosaccharomyces pombe* (**Table 1(c)**). This reverse-complement symmetry led to the fact that the numbers of A and T were almost equal, and the numbers of G and C were almost equal.

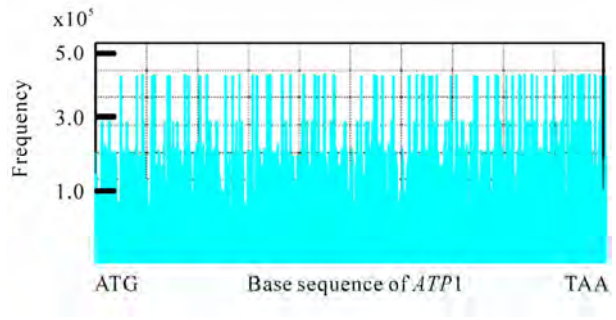

(a) *ATP*1, m = 0

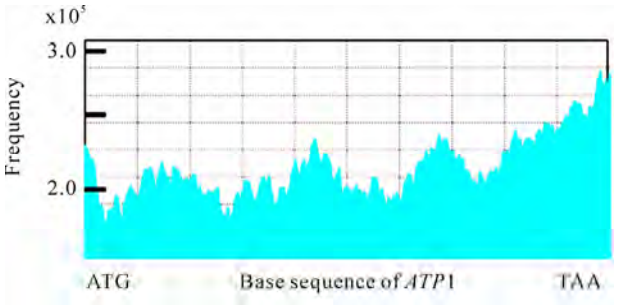

(b) *ATP*1, m = 60

Figure 1. Sequence spectrum of *ATP*1. Sequence spectra of *ATP*1 [26-28] from *Saccharomyces cerevisiae* with different average widths (a) m = 0, and (b) m = 60. The vertical parameter (appearance frequency of the triplet, d = 3) of the sequence spectrum is not designated, and it is scaled properly. The horizontal axis is the base sequence of *ATP*1 (1,638 nt designated as M, ATG = start codon – TAA = stop codon). The skipped base numbers (p) are shown in the figures. The zigzag motif becomes more moderate and the resolution becomes lower as the average width of m becomes larger.

Generally it was well known that the numbers of A and T and the numbers of G and C were the same due to the double helix structure of DNA. However, in this case, this coincidence of base numbers occurred in the genome, so it had nothing to do with the double helix structure. Therefore, the coincidence of base numbers occurred when the base sequence size was very large even in a single strand. Actually this reverse-complement symmetry occurred in each chromosome as well.

On the other hand, it did not occur when the base sequence size was not large enough. For instance, the base sequence size of a single gene was not adequate. The fact that the appearance frequencies of the key sequence and its reverse-complementary key sequence were almost equal implies that there must be a certain amount of symmetry in the genome.

Second, the appearance frequency (in parentheses) for each key sequence was not random, but some of the key sequences had very close appearance frequencies even when they did not have a complementary relationship. For example, in the case of *S. cerevisiae*, the key sequences 5'-AAC (219,288), 5'-ATC (214,197) and 5'-ACA (208,942) had close appearance frequencies of about 210,000, and those of the key sequences 5'-ACG (106,020), 5'-CGA (110,589) and 5'-GAC (110,874) were about 110,000. These different key sequences with close appearance frequencies might have a similar effect on the sequence spectrum. In other words, single-stranded DNA with base-symmetry might be able to make many double-helical stems in a molecule, and the peaks of the sequence spectrum, the "up" of the double-helical stem might have the same effect on the "down" of it. Needless to say, these facts were valid regardless of the species.

3.3. Homologous Structure in Genomes (Enlargement-Reduction of the base Sequence)

*ATP*1 (YBL099W) of *S. cerevisiae* was present on the left arm of chromosome II (37,045-38,679 from the left telomere). **Figure 2** showed the spectra of *ATP*1 (1,638 nt, **Figure 1(b)**), and (a) chromosome II (813,139 nt), respectively. The red arrowhead indicated the position of *ATP*1 on chromosome II [27, 28]. When the spectrum of *ATP*1 (1,638 nt) was skipped 3 bases and the homology analyzed between chromosome II and the skipped-*ATP*1, the red-region (20,401 ~ 60,401 = 40,000 nt) of chromosome II was homologous to the 3 bases-skipped-*ATP*1 (1,341 ~ 1,638 = 297 nt) (**Figure 2(b)**, HF of the red-region of chromosome II to the purple-region of *ATP*1 = 95%).

When *ATP*1 was skipped 10, or 16 bases, the homologous area of *ATP*1 to the red-region of chromosome II was enlarged to 990 nt (**Figure 2(c)**, 648 ~ 1,638), or 1,584 nt (**Figure 2(d)**, 54 ~ 1,638), respectively. That is, the base sequence of the complete *ATP*1 gene had self-similarity to the gene-position on chromosome II. Other genes of *S. cerevisiae* were highly homologous with the gene-position of each chromosome irrespective to the sizes, the order, the direction of transcription and the chromosomes. The fold-enlargement of the gene to each chromosome was calculated as approximately 400-fold (**Table 2(a)**).

The same relationship of the enlargement-reduction of the chromosome-gene was observed in *S. pombe* (eukaryotic cells, **Table 2(b)**) and *E. coli* (prokaryotic cells, **Table 2(c)**). In the case of small intron-containing genes in *S. pombe*, and genes in operons in the *E. coli* genome, the homology condition of the base width was also 100 nt, like that of the *S. cerevisiae* genome. Therefore, the homology pattern in a wide range of organisms might be dependent on the base sequence sizes for the gene analyzed. In any case, in the *S. cerevisiae*, *S. pombe* and *E. coli* genomes, genes and the base sequence near the chromosomal position of the gene had self-similarity with each other in the same ratio, approximately 400-fold. In some preliminary experiments, we observed the self-

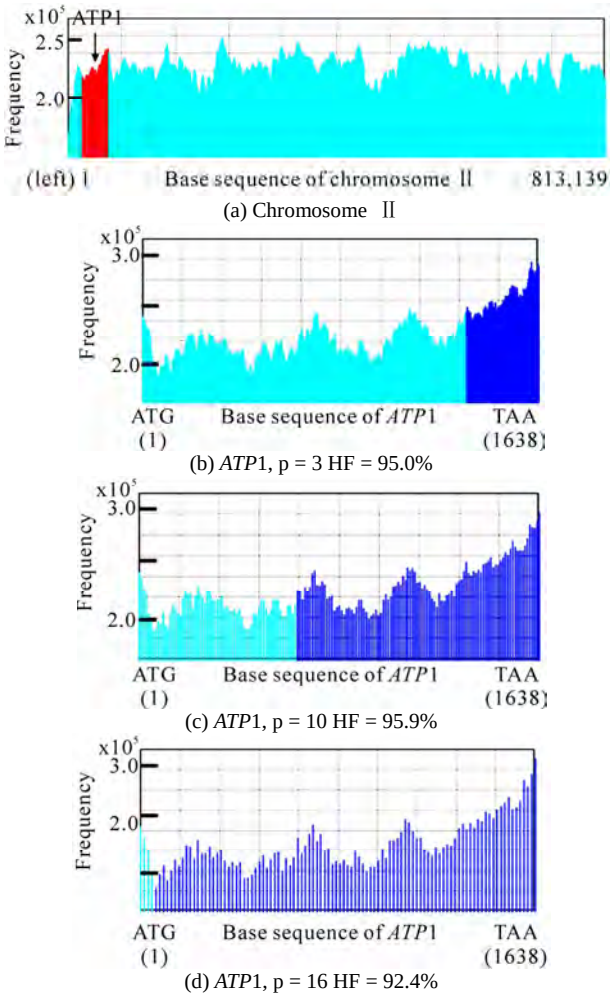

Figure 2. Homology of chromosome II to *ATP*1. (a) *Saccharomyces cerevisiae* chromosome II (813,139 nt, from the left telomere sequence to the right telomere sequence), m = 8,000, d = 3, p = 400. The *ATP*1 gene is located 37,001 bases from the left telomere of chromosome II (arrowhead) [26-28]. The red-region is composed of 40,000 nt (the numbers on the abscissa 20,401 – 60,401). The numbers on the abscissa indicate the base number from the left telomere according to MIPS. (b) *ATP*1 gene (1,638 nt, F_1F_0-ATPase complex α subunit) (26), m = 60, d = 3, p = 3. (c) *ATP*1 (1,638 nt), m = 60, d = 3, p = 10. (d) *ATP*1 (1,638 nt), m = 60, d = 3, p = 16. The homologous region (purple) of *ATP*1 to the red-region was designated the base number of the initiated base "A" (the start codon, ATG) of the coding region of *ATP*1 as 1 [26, 28].

similarity of a gene to the chromosomal position in H. sapiens (for instance, Hs.5174 and chromosome 22; data not shown). This self-similarity might be universal in all species.

3.4. Homologous Structure in tRNAs (Enlargement-Reduction of the Base Sequence)

If a homologous structure was general, it must exist not only in protein-coding genes but also in RNA genes. Actually, the sequence spectrum of each gene was more than 80% similar to the tRNA genes in *S. cerevisiae*, *S. pombe* and *E. coli* (**Table 3**). Most amino acids have plural genetic codons. Each genetic codon had plural tRNA genes on several different chromosomes. How were the plural tRNA genes used properly to construct proteins during the transformation of the biological information in organisms? The genetic codons for glutamate (Glu) were 5'-GAA and 5'-GAG. In *S. cerevisiae*, the nuclear-encoded Glu(GAA)-tRNA genes were 14 on various chromosomes, and all of them were composed of 72 identical nucleotides (bases). Three out of these 14 Glu(GAA)-tRNA genes were present on chromosome V (576,869 bp), located at positions 177,098 ~ 177,169, 354,930 ~ 355,001 and 487,397 ~ 487-326, and were designated Glu (GAA-1), Glu (GAA-2) and Glu (GAA-3), respectively [29-31, **Figure 3** lower panel].

Figure 3 showed that the sequence spectra of these 3 Glu (GAA)-tRNA genes on chromosome V and *ATP*1 [26-28] were depicted. The window length of the tRNA gene was 70 nt in the analysis because Glu (GAA)-tRNA genes were composed of 72 nt (bold-black bar in upper panel). In addition, the Glu (GAA)-tRNA spectra analysis used DNA sequences (112 bp) adjoined to the 5'-, 3'-20 nucleotides (green letters) added to these three Glu (GAA)-tRNA genes (72 bp, black letters). As a result, the homology factors (HF) of *ATP*1 to these three Glu (GAA)-tRNA genes were different; that is, 77.0% for GAA-1, 77.0% for GAA-2 and 88.5% for GAA-3, respectively, although these Glu (GAA)-tRNA genes were all composed of 72 identical nucleotides.

The sequence spectra of *ATP*1 (1,638 nt) and the nuclear-encoded 14 Glu (GAA)-tRNA (72 nt) were fairly homologous. The red area of the Glu (GAA)-tRNA gene was homologous to the homologous area (purple) of the *ATP*1 gene (1,638 bp), and the bracket in **Figure 3** showed the Glu (GAA)-tRNA gene consisting of 72 bp. The homologous area (red) of the Glu (GAA)-tRNA to the *ATP*1 gene overlapped with a part of the adjoining sequences of the tRNA-gene (the homologous region of the tRNA gene with the *ATP*1 gene was also indicated from the red-base to the red base in the lower panel of **Figure 3**). In other words, the sequence spectrum analyses based on the frequencies of the base sequences in the genome indicated that the sequence spectrum of the gene might be influenced by the adjoined DNA sequences. The smaller the base numbers of the DNA sequence, such as for the tRNA-genes, the greater these effects.

In the same way, other nuclear-encoded 11 Glu (GAA)-tRNA genes on several different chromosomes were generally homologous to the *ATP*1 gene on chromosome II, which encoded the subunit of the F_1F_0-ATPase complex [26-28], but their homology factors (HF) varied. The maximum homologous Glu (GAA) tRNA gene was on chromosome IX (HF = 89.2%, position, 370,414-370,485,

Table 2. Self-similarity with a gene to the chromosome.

Gene	nt (*1)	Chromosome (*2)	nt (*3)	intron #	p-value (*4)	HF (%) (*5)
(a) S. cerevisiae						
SEO1	1,779	1, left	230,203	0	17	61.2
FLO1	4,611	1, right		0	46	73.3
ATP1	1,638	2, left	813,139	0	16	92.4
SUP45	1,311	2, right		0	13	72.4
PRD1	2,136	3, left	315,350	0	21	77.7
PHO87	2,769	3, right		0	27	75.2
ATP16	480	4, left	1,531,929	0	4	93
RAD9	3,927	4, right		0	39	74.2
PAU2	360	5, left	576,870	0	3	85.2
GLC7	1,461	5, right		0	14	73.6
EMP47	1,335	6, left	270,148	0	13	81.4
PHO4	939	6, right		0	9	82.8
POX1	2,244	7, left	1,090,936	0	22	80.9
TFC4	3,075	7, right		0	30	69.9
GUT1(STE20)	2,127	8, left	562,638	0	21	61.6
IRE1(NDT80)	3,345	8, right		0	33	80
HOP1	1,815	9, left	439,885	0	17	64.5
MRS1(PAN1)	1,089	9, right		0	10	91.7
CYR1	6,078	10, left	745,440	0	61	79.7
ATP2	1,533	10, right		0	15	75.1
SDH1	1,920	11, left	666,445	0	17	71.1
CCP1((NUP133)	1,083	11, right		0	10	76.2
HSP104	2,724	12, left	1,078,173	0	27	68.4
MAS1	1,386	12, right		0	13	81.2
CYB2(CAT2)	1,773	13, left	924,430	0	17	88.4
HXT2(AAC1)	1,623	13, right		0	16	70.1
RAS2	966	14, left	784,328	0	9	86.1
POP2	1,299	14, right		0	13	75.4
ADH1	1,044	15, left	948,061	0	10	85.2
ADE2	1,713	15, right		0	17	78.8
TBF1(PHO85)	1,686	16, left	948,061	0	16	67.7
PZF1	1,287	16, right		0	12	91.2
(b) S. pombe						
ATP2	1,578	1 (968,783)	5,579,133	0	15	78.6
RPL37	337	1 (1,275,535)		1	3	81.3
RPL37(exon)	270				2	77.5
CDC24	1,823	1 (2,863,965)		6	18	81.3
CDC24(exon)	1,506				15	77.5
ATP1	2,049	1 (5,256,781)		2	20	75
ATP1(exon)	1,611				16	76.1
MEU6	2,083	2 (454,230)	4,539,804	2	20	82.3
MEU6(exon)	1,956				19	82.3
CDC2	1,189	2 (1,500,340)		4	11	76.4
CDC2(exon)	894				8	78.8
ATP16	483	2 (3,046,873)		0	4	90.4
SPO4	1,672	2 (3,827,178)		2	16	85.1
SPO4(exon)	1,290				12	74.6
RAF1	1,917	3 (100,255)	2,455,984	0	19	73
HIF2	1,875	3 (194,552)		3	18	71.9
HIF2(exon)	1,695				16	N.D.(*6)
SRK1	3,932	3 (1,302,900)		1	39	64
SPK1(exon)	1,743				17	69

Gene	nt (*1)	Chromosome (*2)	nt (*3)	intron #	p-value (*4)	HF (%) (*5)
GAF1	2,568	3 (1,666,310)		0	25	76.2
TIF6	1,104	3 (2,223,154)		2	11	86.4
TIF6(exon)	735				7	76
ATP5	838	3 (2,268,884)		2	8	74.8
ATP5(exon)	651				6	93
			(c) E. coli (K12)			
araA	1,503	66,835	4,639,221	0	15	74.5
lacZ	3,075	362,455		0	30	66.3
galE	1,017	790,262		0	10	87.7
trpD	1,596	1,317,813		0	15	77.5
cybB	531	1,488,926		0	5	87.8
galF	894	2,111,458		0	8	88
argA	1,332	2,947,264		0	13	68.9
secY	1,332	3,440,788		0	13	82.8
atpA	1,741	3,916,339		0	17	73.9
purA	1,299	4,402,710		0	12	83

*1, Base numbers of the gene without intron.
*2, Gene position on the chromosome (from the left to the right = S. pombe).
*3, Size (base numbers) of chromosome or genome.
*4, Skipped base numbers of the gene (max.p-value).
*5, Entire gene in the max.p-value-chromosome HF (%) in the homologous region.
*6, not determined.

Table 3. Self-similarity with a protein to tRNA gene.

Gene	size (nt) (*1)	chromosome (*2)	tRNA (*3)	size (nt, *4)	chromosome (*5)	p (*6)
			(S. cerevisiae)			
ATP1	1,638	2	Glu(GAA)	72	12	16
RAS2	936	14	Lys(AAG)	72	6	9
ADH1	1,047	15	Arg(AGG)	72	10	10
TFC4	3,075	7	Ser(TCG)	103	3	30
PAU2	360	5	Ser(AGC)	101	6	3
CYR1	6,078	10	Ser(AGC)	101	6	60
			(S. pombe)			
ATP1	1,611	1	Tyr(TAC)	84	2	16
YPT3	645	1	Arg(AGA)	73	2	6
CDC2	894	2	Ser(TCT)	82	1	8
SPO4	1,290	2	Thr(ACT)	72	3	12
GAF1	2,568	3	Ser(AGC)	95	2	25
TIF6	735	3	Arg(AGA)	73	3	7
			(E. coli)			
galE	1,017	K12 genome	Ser(TCC)	88	K12 genome	10
atpA	1,735		Ser(AGC)	93		17
cybB	531		Ser(TCC)	88		5
lacZ	3,075		Arg(CGT)	77		30

*1; base numbers of gene without intron
*2; Chromosome presented the gene
*3; Homologous tRNA gene.
*4; Size of tRNA gene.
*5; Chromosome presented the tRNA gene.
*6; Skipped base numbers of the gene.

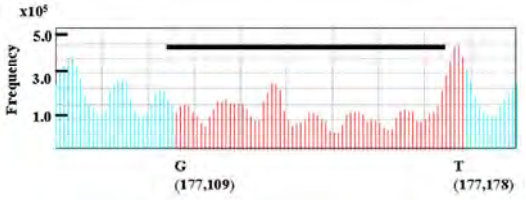

(a) Glu (GAA)-tRNA-1, HF = 77.0%

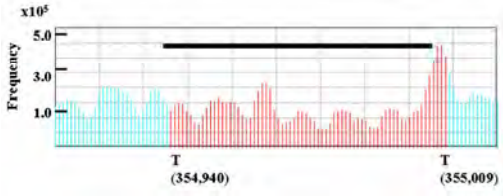

(b) Glu (GAA)-tRNA-2, HF = 77.0%

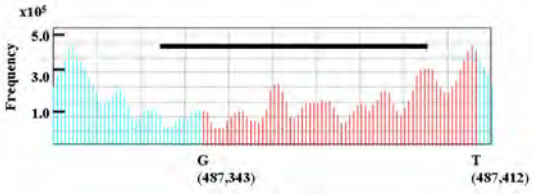

(c) Glu (GAA)-tRNA-3, HF = 88.5%

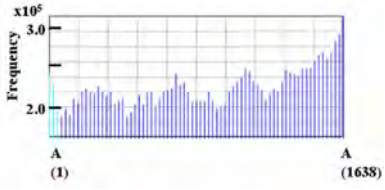

(d) ATP1, M = 1,638, d = 3, p = 23

Upper panel: Sequence spectrum of (a) Glu(GAA-1)-tRNA gene; (b) Glu(GAA-2)-tRNA gene; (c) Glu(GAA-3)-tRNA gene on chromosome V of *S. cerevisiae*; (d) Sequence spectrum of *ATP*1. The bold black line indicates the area of the Glu(GAA)-tRNA gene consisting of 72 bp.

Glu (GAA) tRNA gene on chromosome V.
Chr. V (576,869 bp)

```
177061 atattcatga agaataaggt ttttcaacct actttgatcc gatatagtgt aacggctatc
177121 acatcacgct ttcaccgtgg agaccggggt tcgactcccc gtatcggagt actttttga
177181 tggctacaat cataatttga catacctcat atgaatatga tgtggtagta aattaaatag
```

(a) (GAA-1) 177,098 ~ 177,169 (Watson strand, left to right)

```
354901 ttgagatgca acacatacgt gtattgtaat ccgatatagt gtaacggcta tcacatcacg
354961 ctttcaccgt ggagaccggg gttcgactcc ccgtatcgga gtacttttt gacatcatac
355021 agtgtatgta tggggttagg agccaccttc caacaaagca tcacgctgtc gtatctcaat
```

(b) (GAA-2) 354,930 ~ 355,001 (Watson strand, left to right)

```
487261 ttacacggta aaaaaaatgt tttcaaagct tttgatcgta agcgattgaa aaaatataac
487321 gaatactccg atacggggag tcgaaccccg gtctccacgg tgaaagcgtg atgtgatagc
487381 cgttacacta tatcggatta aattcatgaa ttttttaggg ctccgaatat tgtaaattcg
```

(c) (GAA-3) 487,397 ~ 487,326 (Crick strand, right to left)

Lower panel: The adjoining DNA sequences of each Glu(GAA)-tRNA gene, and the orientation of each tRNA gene. The base sequences of Glu(GAA)-tRNA (72 bp, black letter), adjoining sequences (5'-20 bp, 3'-20 bp, green letter), and the outside sequences that were analyzed are shown in pink letters [29-31]. *ATP*1-homologous region of each Glu(GAA)-tRNA gene from the underlined red base to the underlined red base (70 bp).

Figure 3. Homology of Glu(GAA)-tRNA gene to *ATP*1 gene.

Watson-strand) and the minimum was on chromosome VII (HF = 73.8%, position, 328,586-328,657, Watson-strand). These results indicated that the analyses of such small DNA sequences were deeply affected by the adjoining sequences.

Other protein-encoding genes were highly homologous to the appropriate tRNA genes in the yeast *S. cerevisiae*. Similar homology of protein-encoding genes to appropriate tRNA genes in the same organism was observed for other genes in *S. pombe* and *E. coli* (data not shown). These results showed that the homologous structures spread consistently from a very small gene (tRNA) to a complete chromosome with the same scale regardless the species.

4. DISCUSSION

The results obtained in this study might lead to the development of generation-rules for the base sequence of the genome. The reason why genomes possess homologous structure regardless of the size of the base sequence could be related to the physical hierarchy in the structure of the genome, such as the double helix structure of DNA, nucleosome structure, super helix structure, and so on. The phenomenon in which homologous patterns

appear in various size levels is known as "self-similarity" or "fractal". Therefore, the structure of the genome could be essentially related to the fractal.

During the 1990s, many papers reported that the genome bases should follow the fractal-rule [15-18 etc], and Genome Projects for many species had revealed genomic base sequences in the last 10 years. Therefore, analyses of the concrete biological phenomena based on the structures of genomes should be in progress.

In this paper, the analyses of the sequence spectrum, m = 2 for a tRNA, m = 60 for a protein, and m = 8,000 for a chromosome were used. In the case of the sequence spectrum of protein, m = 10 (average of 20 nt) or m = 60 (average of 120 nt) was easier to use for the analysis of the sequence spectrum when the m-value corresponded to 6 ~ 7, or 40 amino acid residues, respectively [32].

In the case of the chromosome, m was adjusted to 8,000 (average of 16,000 nt = 80 nucleosomes) or 10,000 (average of 20,000 nt = 100 nucleosomes). In any case, the smaller the adjusted m-value is, the higher the resolution of the sequence spectrum. These results suggested that "m" might be reflected in the higher order structure of a molecule, a gene for tRNA, or protein or chromosome, but the detailed biological meaning of the m-value is in progress [33, 34].

In addition, as described previously, each genetic codon had multiple tRNA genes on several different chromosomes. How were the multiple tRNA genes used properly to construct proteins during the transformation of biological information in organisms? In biological processes, the base sequence of DNA was transcribed to mRNA, and then the base sequence of mRNA was transferred to the amino acid sequence by tRNAs. In such cases, the higher homologous structure (HF) of tRNA genes might be one of the distinctions of an appropriated protein. In other words, the base sequence of DNA was reflected in the amino acid sequence through the base sequence of RNA. Therefore, the above method might be applicable to the interactive-sites of DNA, RNA, and protein. In such analyses, the selection of the d- and p-values might be important to obtain the highest resolution of the sequence spectrum corresponding to the structural features of the target DNAs or proteins.

Genomic DNA might be enlarged and reduced because the base sequence of the genomic DNA had fractality; therefore, it had similarity to related sites and was able to prefer a gene over the chromosome. The coding- and non-coding regions of a genome were different with respect to bases as described. As a result, biases of the four bases occurred on genomic DNA [20].

The analyses based on the appearance frequency of the base sequences in a genome should be universally applicable to everything that was expressed by base sequences, not only in *Saccharomyces cerevisiae*, but also *Homo sapiens*, *Escherichia coli* and all genomes; therefore, this method might be applied as a first screen to characterize interaction-sites in biological phenomena.

5. CONCLUSIONS

The results obtained in this study were summarized as follows. 1) Homologous structure exists in the appearance frequency of short base sequences such as triplets over an entire chromosome in the genome, and the 5'- and 3'-adjoining base sequences of the DNA were deeply affected by the homology factor when the target DNA was small in size or located at the boundary, 2) homologous structure was universally observed in a variety of species, 3) the homology of the sequence spectrum of a gene was observed in the appropriate tRNA genes, and the analysis (SSM) of the DNA base sequences might be reflected in that of protein; in other words, 4) the SSM might be reflected as a vehicle of biological information, and a suitable prediction method to identify interacting regions DNA, RNA or protein by the appropriate conditions of "m", "d" and "p", in each gene, or genomic DNA, 5) SSM was faithfully reflected the biological information, therefore, the conservation of the bases sequences of genomic DNA were also conserved the translated amino acids sequence, the protein sequence, in the coding region, 6) SSM could deal consistently with molecules that consists of base sequences.

6. ACKNOWLEDGEMENTS

The authors wish to thank to Dr. Hiroshi Shibata at Sojo University for his comments about the fractal analysis in this research.

REFERENCES

[1] Singer, M. and Berg, P. (1991) Genes & genomes – A changing perspective-. *University Science Books*.

[2] Garrel, J.I. (1997) The yeast proteome handbook. Third edition, Beverly, Proteome Inc.

[3] Velculescu, V.E., Zhang, L., Zhou, W., Vogelstein, J., Basral, M.A., Bassett, D.E.Jr., Hieter, P., Vogelstein, B. and Kinzler, K.W. (1997) Characterization of the yeast transcriptome. *Cell*, **88,** 243-51.

[4] Wan, X.F., VerBerkmoes, N.C., McCue, L.A., Stanek, D., Connlly, H., *et al.* (2004) Transcriptomic and proteomic characterization of the fur modulon in the metal- reducing bacterium Shewanella oneidensis. *The Journal of Bacteriology*, **186,** 8385-8400.

[5] Sakharkar, K.R., Sakharkar, M.K., Culiat, C.T., Chow, V. T. and Pervaiz, S. (2006) Functional and evolutionary analyses on expressed intronless genes in the mouse genome. *FEBS Letters*, **580,** 1472-1478.

[6] Karkas, J.D., Rudner, R. and Chargaff, E. (1968) Separation of *B. subtilis* DNA into complementary strands. II. Template functions and composition as determined by transcription by RNA polymerase. *Proceedings of the National Academy of Sciences of the United States of America*, **60,** 915-920.

[7] Bell, S. J., Fordyke, D. R. (1999) Accounting unit of in DNA. *Journal of Theoretical Biology*, **197,** 51-61.

[8] Abe, T., Kanaya, S., Kinouchi, M., Kudo, Y., Mori, H. *et al*. (1999) Gene classification method based on batch- learning SOM. *Genome Informatics Seris*, **10**, 314-315.

[9] Baisnee, P.-F., Hampson, S. and Baldi, P. (2002) Why are complementary DNA strands symmetric? *Bioinformatics*, **18,** 1021-1033.

[10] Chen, L. and Zhao, H. (2005) Negative correlation between compositional symmetries and local recombination rates. *Bioinformatics*, **21,** 3951-3958.

[11] Albrecht-Buehler, G. (2006) Asymptotically increasing compliance of genomes with Chargaff's second parity rules through inversions and inverted transpositions. *Proceedings of the National Academy of Sciences of the United States of America*, **103,** 17828-17833.

[12] Wilson, J. T., Wilson, L. B., Reddy, V. B., Cavallesco, C., Ghosh, P. K., *et al*. (1980) Nucleotide sequence of the coding portion of human alpha globin messenger RNA. *Journal of Biological Chemistry*, **255,** 2807-2815.

[13] Wada, A., Suyama, A. and Hanai, R. (1991) Phenomenological theory of GC/AT pressure on DNA base composition. *Journal of Molecular Evolution*, **32,** 374-378.

[14] Nakamura, Y., Itoh, T. and Martin, W. (2007) Rate and polarity of gene and fission in Oryza sativa and Arabidopsis thaliana. *Molecular Biology and Evolution*, **24,** 110-121.

[15] Paila, U., Kondam, R. and Ranjan, A. (2008) Genome bias influences amino acid choice: analysis of amino acid substitution and re-compilation matrices exclusive to an AT-biased genome. *Nucleic Acids Research*.

[16] Voss, R.F. (1992) Evolution of long-range fractal correlation and 1/f noise in DNA base sequences. *Physical Review Letters*. **68,** 3805-3809.

[17] Bains, W. (1993) Local self-similarity of sequence in mammalian nuclear DNA is modulated by a 180 bp periodicity. *Journal of Theoretical Biology*, **161,** 13-143.

[18] Weinberger, E.D. and Stadler, P.F. (1993) Why some fitness landscape are fractal. *Journal of Theoretical Biology*, **163,** 255-275.

[19] Lu, X., Sun, Z., Chen, H. and Li, Y. (1998) Characterizing self-similarity in bacteria DNA sequences. *Physical Review E—Statistical*, **58,** 3578-3584.

[20] Takeda, M. and Nakahara, M. (2009) Structural Features of the Nucleotide Sequences of Genomes. *Journal of Computer Aided Chemistry*, **10,** 38-52.

[21] NCBI Genome Data Base (2009) http://www.ncbi.nlm.nih.gov/sites/entrez?db=genome.

[22] Crick, F.H. (1968) The origin of genetic code. *Journal of Molecular Biology*, **38,** 367-379.

[23] International Human Genome Sequencing Consortium. (2001) Initial sequencing and analysis of the human genome. *Nature*, **409,** 860-921.

[24] Mattick, J.S. (2004) RNA regulation: A new genetics? *Nature Reviews Genetics*, **5,** 316-323.

[25] Lynch, M. (2007) The frailty of adaptive hypothesis for the origins of organismal complexity. *Proceedings of the National Academy of Sciences of the United States of America*, **104,** 8597-8604.

[26] Takeda, M., Chen, W.-H., Saltzgaber, J. and Douglas, M.G. (1986) Nuclear genes encoding the yeast mitochondrial ATPase complex-analysis of *ATP*1 coding the F_1-ATPase α–subunit and its assembly-. *Journal of Biological Chemistry*, **261,** 15126-15133.

[27] Takeda, M., Okushiba, T., Hayashida, T. and Gunge, N. (1994) *ATP*1 and *ATP*2, F_1F_0-ATPase α and β subunit genes of *Saccharomyces cerevisiae*, are respectively located on chromosome II and X. *Yeast*, **10,** 1531-1534.

[28] Mewes, H. W., Albermann, K., Bähr, M., Frishmann, D., Gleissner, A., *et al.* (1997) Overview of the yeast genome. *Nature*, **387 (supp),** 7-65.

[29] Dietrich, F. S., Mulligan, J., Hennessy, K., Yelton, M. A., Allen, E., *et al.* (1997) The nucleotide sequence of *Saccharomyces cerevisiae* chromosome V. *Nature*, **387 (supp),** 78-81.

[30] Saccharomyce Genome Database. (2009) (http://www.yeastgenome.org/).

[31] Transfer RNA data base. (2009) (http://gtrnadb.ucsc.edu/).

[32] Matthews, B.W. (1993) Structural and genetic analysis of protein stability. *Annual Review of Biochemistry*, **62,** 139-160.

[33] Kornberg, R.D. (1974) Chromatin structure: a repeating unit of histones and DNA. *Science*, **184,** 868-871.

[34] van Holde, K. and Zlatonova, J. (1995) Chromatin higher order structure: Chasing a mirage? *Journal of Biological Chemistry*, **270,** 8373-8376.

J. Biomedical Science and Engineering, 2010, 3, 351-358 **JBiSE**
doi:10.4236/jbise.2010.34048 Published Online April 2010 (http://www.SciRP.org/journal/jbise/).

A phase I radiation dose escalation of stereotactic body radiotherapy for malignant lung tumors

Randi J. Cohen[1], Navesh K. Sharma[1], Jian Q. (Michael) Yu[2], Lu Wang[1], Mark K. Buyyounouski[1], Michael Unger[3], Hossein Borghaei[4], Earl King[3], Walter Scott[5], Elaine Callahan[1], Benjamin J. Movsas[6], Steven J. Feigenberg[7]

[1]Department of Radiation Oncology, Fox Chase Cancer Center, Philadelphia, USA;
[2]Department of Diagnostic Imaging, Fox Chase Cancer Center, Philadelphia, USA;
[3]Department of Pulmonary Medicine, Fox Chase Cancer Center, Philadelphia, USA;
[4]Department of Medical Oncology, Fox Chase Cancer Center, Philadelphia, USA;
[5]Department of Surgical Oncology, Fox Chase Cancer Center, Philadelphia, USA;
[6]Department of Radiation Oncology, Henry Ford Hospital, Detroit, USA;
[7]Department of Radiation Oncology, University of Maryland, Baltimore, USA.
Email: sfeigenberg@umm.edu

Received 15 January 2010; revised 25 January 2010; accepted 30 January 2010.

ABSTRACT

Objectives: This Phase I study determines the maximum tolerated dose (MTD) of stereotactic body radiotherapy (SBRT) for lung tumors. Methods: Eligible patients had biopsy proven cancer with a maximum tumor size ≤ 5 cm. Total doses were escalated from 40 to 48, then to 56 Gy, delivered in 4 equal fractions administered 2 to 3 times per week on an IRB approved protocol. SBRT was administered using 5 to 9 fixed beam arrangements with CT localization. Internal target volumes (ITV) were based on breath hold scans or 4D CT simulation. The planning target volume (PTV) was defined as the ITV with a uniform 5 mm expansion. Dose limiting toxicity (DLT) was defined as any grade 3 or higher toxicity using the Radiation Therapy Oncology Group (RTOG) common toxicity criteria (CTC). Results: Between April 2004 and February 2008, 18 patients received the prescribed treatment (40 Gy n = 6, 48 Gy n = 7, 56 Gy n = 5). Seventeen of 18 patients had non-small cell lung cancer (1 with rectal cancer), four of whom were treated for an oligometastasis. The median age of the patients was 68, while the median Karnofsky performance status was 90. The mean tumor size was 2.6 cm (range 0.9 to 4.5 cm). One grade 3 pulmonary event occurred (at 48 Gy dose level) immediately following treatment with the onset of fever and shortness of breath that responded to antibiotics. No other DLTs occurred. Conclusions: SBRT utilizing patient specific target volumes without gating appears safe. The maximum tolerated dose was not reached.

Keywords: Stereotactic Body Radiotherapy; Phase I; Dose Escalation; Prospective; Lung Cancer

1. INTRODUCTION

The standard therapy for early stage non-small cell lung cancer (NSCLC) is surgery [1]. Radiation therapy (RT) can similarly cure early stage NSCLC, but has less favorable outcomes due to competing causes of death, lack of pathologic staging and/or less efficacious treatment. With conventional radiation doses (*i.e.* 60-70 Gy) local failure is considerable and may be underestimated based on the method of follow-up with the highest failure rate reported by bronchoscopy. [2] Due to this unacceptable local failure rate, many institutions have designed trials to improve local control. [3-5] At the University of Michigan, Martel *et al*. [6] determined that the total radiation dose required to achieve a > 50% probability of local control using conventional fractionation (*i.e.* 2 Gy per fraction) was > 84 Gy and a phase I study was completed treating tumors to over 100 Gy. The major problem with this treatment strategy is the duration of therapy (2 to 2 ½ months). As an alternative, investigators have evaluated accelerating the dose of radiation through hypofractionation [7] which increases the radiobiologic effective dose by decreasing treatment time.

Stereotactic radiosurgery is an extreme version of hypofractionation that has become an established alternative to surgery for selecting brain tumors. [8] More recently, this technique has been adopted for treating tumors outside the brain. [9-18] Unlike radiosurgery for intracranial targets, stereotactic body radiotherapy (SBRT) is complicated by less precise target definition and internal organ motion, which requires a margin to ensure

coverage of the target volume. Solutions include improving immobilization (*i.e.* stereotactic body frames), reducing or monitoring internal organ motion (*i.e.* respiratory gating, active breathing control, or breath holding), reducing daily set-up uncertainties (*i.e.* Computed Tomography, CT, localization prior to treatment, electronic portal imaging with fiducial markers placed in the tumor) or fractionation. Even with all of these innovative techniques, most investigators use axial margins of at least 5 mm and a cranial-caudal margin of 5 to 10 mm around the gross tumor volume (GTV) to account for set-up error and organ motion (*i.e.* planning target volume, PTV) [9,18] with no additional margin for subclinical disease (*i.e*. clinical target volume, CTV).

When this study was developed, there were only two prospective phase I studies in the literature. Herfarth *et al*. [19] published results using SBRT in the liver in 2001. Timmerman *et al.* [16] reported their initial results at ASCO in 2002 for medically inoperable non-small cell lung cancer (NSCLC) patients with tumors < 7 cm and no evidence of lymph node involvement. The patients were treated with 3 fractions over 7 to 8 days starting at 800 cGy per fraction which was escalated to 2000 cGy per fraction. Only 2 of 36 patients developed grade 3 pulmonary toxicity (one T1 and one T2 tumor) and the maximum tolerated dose (MTD) was not reached. Patients were immobilized in a stereotactic body frame as originnally described by Blomgren and Lax, [9] who defined the PTV as an expansion of 5 mm in the axial dimension and 1 cm in the cranial caudal directions.

Fukumoto *et al*. [10] estimated the target volume by obtaining 3 CT scans during different respiratory phases, simulating a "slow CT" technique. The first scan was performed during normal respiration, while the 2nd and 3rd were obtained during maximum inhalation and exhalation, respectively. The combination of the 3 scans accurately described the gross tumor volume and its tumor specific motion. Unlike our current trial, Fukumoto *et al.*, did not use a stereotactic body frame for simulation and treatment nor did they perform imaging prior to treatment to improve daily localization and reproducibility. In their trial, the PTV was created by adding 10 mm margins to the GTV. Patients were treated with a very conformal technique to a total dose of 48 or 60 Gy in 8 fractions. This technique is ideal for a frail patient population because it limits treatment time and reduces patient discomfort.

Given the limited data in 2002, a phase I study was designed to examine the role of SBRT using 3D image guided radiotherapy and tumor specific targets motion ("slow CT"). The primary goal at the initiation of this study was to develop a treatment equivalent to approximately 70 Gy at conventional fractionation with planned dose escalations to 100 Gy (as treated in the Michigan series) with a 4 fraction regimen. The following paper describes the final results of our phase I dose escalation trial.

2. METHODS & MATERIALS

Prior to the enrollment of any patient, the protocol and consent form were reviewed and approved by an internal Research Review Committee and Institutional Research Review Board at Fox Chase Cancer Center. Patients described in this manuscript willingly participated on this prospective series. To be included in the study, patients had to have one or two tumors in the lung (primary NSCLC or metastatic) with a maximum diameter of 5 cm. Patients were required to undergo a pathologic diagnosis prior to enrollment. Local recurrences following wedge resections were allowed if biopsy-proven. Patients had to have a Karnofsky Performance Status of 60 or higher. Central tumors were not excluded. Pulmonary function tests were obtained prior to radiotherapy, although there was no restriction based on pulmonary status. Of the 18 patients, 13 were unfit for surgical treatment due to poor pulmonary function and/or other medical comorbidities and five refused surgery.

2.1. Treatment Policy

Patients were immobilized in a FDA approved stereotactic body frame (Integra Radionics, Burlington, MA, USA) that employs a rigid frame and vacuum pillow. This particular immobilization device does not use abdominal compression to limit respiratory motion. Patient initial positioning was reproduced based on tattoos at the upper and lower level of the vacuum pillow as well as at the isocenter. Planning CT scans in the stereotactic body frame were obtained to get stereotactic coordinates. For ten patients, three CT scans were obtained: one during normal respiration, one during maximum end expiration, and one during maximum end inspiration, as per Fukumoto *et al.*, [10] to obtain an accurate representation of the tumor motion (*i.e.* internal target volume, ITV) during the respiratory cycle. CT scans were fused on their bony landmarks. The last seven patients underwent a 4 dimensional CT (4DCT) simulation to generate an ITV. [13,20,21] One patient underwent both 4DCT simulation and scans using the breath holding technique. Axial images were obtained every 2.5 or 3 mm through the entire thorax. The GTV was identified on each of the axial CT imaging using pulmonary windows. Only the solid tumor component was targeted. Spiculations were not contoured.

For patient's simulated with multiphase CT scans (inspiration, expiration, and free breathing), the ITV was defined by combining the GTVs outlined in each of the three CT scans. When 4DCT was used, the ITV was defined from a reconstructed data set generated using the maximum-intensity-projection (MIP) protocol. MIP creates a 3D CT scan which represents the greatest voxel

intensity values throughout the 4D CT data-set. The CTV was defined as the ITV with no additional margin to account for subclinical disease. The PTV incorporated the ITV plus 5 mm in all directions to account for set-up error. Final patient positioning was achieved using CT localization prior to each treatment using the PRIMATOM sliding CT gantry (Siemens Medical Solutions, Concord, CA, USA) for fifteen patients and on board cone beam CT technology (Varian Medical Systems, Palo Alto, CA, USA) for three patients.

Treatment planning was delivered using the Radionics™ stereotactic planning system (Integra Radionics) using 5 to 9 coplanar or non-coplanar, non-opposing beams. No patient was treated using intensity modulation. The distance between the block edge and the PTV for each of the beams eye's view was 3 to 4 mm to ensure the 90% isodose line would cover the PTV (*i.e.* dose prescribed to 90% isodose line). This will allow a very steep fall off in the dose outside of the PTV potentially maximizing the benefit of a rapid fall off in the dose while minimizing the hot spots in the surrounding normal tissue.[22] Heterogeneity corrections were used.

As part of the dose escalation protocol, the first cohort of patients received 4000 cGy in 4 fractions with the radiation delivered on non-consecutive days either 2 or 3 times a week at 1000 cGy per fraction. This dose was chosen since it was radiobiologically equivalent to approximately 70 Gy at 2 Gy per fraction, the dose utilized off study at our institution. Biologically equivalent doses (BED) were calculated using the formula BED = nd $(1 + d/(\alpha/\beta))$, where n = number of fractions; d = daily fraction size; and $\alpha/\beta = 10$. The total treatment dose of each subsequent cohort was escalated an additional 800 cGy at 200 cGy per fraction, *i.e.*, 4800 cGy and then 5600 cGy in 4 fractions. The final dose was chosen as it is similar to the highest dose reached on the University of Michigan 3D dose escalation trial [4]. A three month period of observation after the sixth patient in each of the first two cohorts was performed prior to escalating the dose to ensure no adverse events occurred.

The primary endpoint of the study was to determine the maximum tolerated dose (MTD) for treating malignant tumors of the lung with SBRT. The secondary endpoint was to determine the response rate, local control and PET response at 3 months (for those treated definitely) for these patients undergoing SBRT.

2.2. Statistics

The dose escalation followed the method described in Babb *et al.* [23] and shown to be Bayesian-feasible, Bayesian-optimal and consistent by Zacks *et al.* [24]. The dose for each cohort was determined so that, on the basis of all available data, the probability that it exceeds the MTD is equal to a pre-specified value α. For the first cohort $\alpha = 0.25$, for the second cohort $\alpha = 0.35$, and for the third cohort $\alpha = 0.5$. A maximum of 18 patients were planned for accrual to this trial.

2.3. Follow-Up after Treatment

All patients underwent a CT scan and pulmonary function tests one month following therapy. A PET scan was obtained prior to and 3 months following treatment for patients treated with curative intent with primary NSCLC to determine the biologic response which potentially could act as an early surrogate of local failure (reported elsewhere). Subsequently, CT scans were obtained every 3 months until 2 years. Other investigations were obtained based on clinical indication. Progressive disease was defined per the RECIST criteria: [25] at least a 20% increase in the sum of longest diameter (LD) of the treated lesion taking as reference the smallest sum LD recorded since the treatment started.

3. RESULTS

Between April 2004 and February 2008, 18 patients with 19 tumors received the prescribed treatment. Patient characteristics of this cohort are described in **Table 1**. Seventeen of the 18 patients had NSCLC, while one patient had metastatic rectal cancer. The rectal cancer patient had stable extra-pulmonary disease and was treated to 2 lung metastases during the same session. Four patients with NSCLC were treated for oligometastatic disease. The median age of the patients was 68 years (range 48 to 82), while the median Karnofsky performance status was 90 (range 60 to 100). The mean tumor size was 2.0 cm (range 0.9 to 4.5 cm). Prior to SBRT, half of patients treated had received prior radiotherapy, surgery and/or chemotherapy to the lung. Six patients were on oxygen prior to SBRT. The mean pre-treatment FEV1 was 1.41 liters (range 0.49 to 2.6 L), while the mean DLCO was 52% of predicted (range 30 to 90%). The mean post-treatment pulmonary function tests were not significantly different from the pre-treatment tests (mean FEV1 = 1.25 L, mean DLCO = 50.8%).

With a median follow-up of 24 months (range 3 months to 48 months), most patients (72%) did not experience any adverse side effects during or following treatment. No patients experienced chest wall pain, rib fracture, esophageal stricture, nausea, subcutaneous fibrosis or brachial plexopathy. The most common grade 2 or higher side effect reported was fatigue, which was seen in 3 patients between one and three months following the completion of treatment. Two patients experience grade 2 erythema within the first month following treatment.

Two patients experienced pneumonitis, one that was grade 2 and one that was grade 3. Both patients had been previously treated with chemotherapy and radiation prior to SBRT for an oligometastasis. The one grade 3 event

Table 1. Patient characteristics.

Pt #	Age	Race	Gender	Total Dose	Primary Site	Tumor Location	Histology	Stage at Dx	Prior Therapy	Local Failure	Grade 3 SAE	Pre & Post Tx FEV1 (liters)		Pre& Post Tx DLCO (%)		Tumor (cm)
1	74	W	M	40 Gy	Lung	LUL	Squamous Cell Carcinoma	T4N0M0	Chemo	YES	No	0.95	0.92	44	46	1.7
2	69	W	M	40 Gy	Lung	LLL	Adenocarcinoma	T1N0M0	None	YES	No	1.06	1.28	30	31	1.5
3	52	W	F	40 Gy	Lung	LUL	Large Cell Carcinoma	T2N2M0	Surgery Radiation	No	No	1.81	1.70	54	56	1
4	79	W	F	40 Gy	Lung	RML	Bronchiolo-Alveolar Ca	T1N0M0	Surgery	No	No	0.91	0.82	59	62	2
5	71	W	M	40 Gy	Lung	RUL	Adenocarcinoma	T1N0M0	Radiation	No	No	2.26	X	43	X	1
6	61	W	F	40 Gy	Lung	LUL	Adenocarcinoma	T1N0M0	None	No	No	1.14	1.18	38	35	2
7	48	W	F	48 Gy	Lung	RUL	Squamous Cell Carcinoma	T1N0M0	Surgery, Radiation, Chemo	YES	YES	1.41	1.22	42	52	1.4
8	57	W	M	48 Gy	Lung	RUL	Adenocarcinoma	T2N1M0	Surgery, Radiation, Chemo	YES	No	2.6	X	64	X	2.1
9	69	W	F	48 Gy	Lung	RUL	Adenocarcinoma	T1N0M0	None	YES	No	0.94	1.05	40	49	1.5
10	80	W	M	48 Gy	Lung	RUL	Squamous Cell Carcinoma	T1N0M0	None	No	No	1.62	1.73	68	75	2.3
11	65	W	F	48 Gy	Rectum	2 lesions in LUL	Adenocarcinoma	T3N0M0	Surgery	No	No	0.69	0.68	43	39	3.1, 1.5
12	78	W	M	48 Gy	Lung	LUL	Squamous Cell Carcinoma	T1N0M0	None	No	No	1.99	X	90	X	1.1
13	82	W	M	48 Gy	Lung	RLL	Squamous Cell Carcinoma	T1N0M0	None	No	No	0.71	X	67	X	2.7
14	68	W	M	56 Gy	Lung	RLL	Squamous Cell Carcinoma	T2N0M0	Surgery	YES	No	2.4	2.38	70	67	2.5
15	74	B	M	56 Gy	Lung	RUL	Bronchiolo-Alveolar Ca	T2N0M0	None	No	No	1.47	X	52	X	4.5
16	59	B	F	56 Gy	Lung	RUL	Adenocarcinoma	T1N0M0	None	No	No	0.49	0.51	33	24	1.7
17	68	W	M	56 Gy	Lung	LLL	Squamous Cell Carcinoma	T1N0M0	None	No	No	1.8	1.59	64	57	1.2
18	69	W	F	56 Gy	Lung	RLL	Non-Small Cell NOS	T1N0M0	Surgery	No	No	1.13	1.18	46	68	3.1

W: White
B: Black
X: One month post-SBRT PFTs not performed
LUL: Left Upper Lobe
LLL: Left Lower Lobe
RML: Right Middle Lobe
RUL: Right Upper Lobe
RLL: Righe Lower Lobe

was previously treated for an advanced non-small lung cancer requiring induction chemotherapy and radiation followed by left sided pneumonectomy. She developed a second primary versus an oligometastasis in the contralateral right upper lobe that was treated with a wedge resection. She had a biopsy-proven local recurrence in the staple line, which was treated to 4800 cGy (see **Figure 1** which illustrates the dose distribution). A fever developed

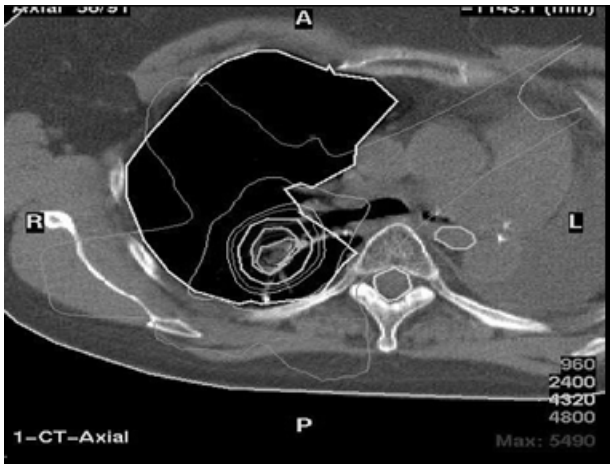

Figure 1. This is an axial CT image from the patient's simulation illustrating the prescription isodose line (48 Gy), as well as 90%, 50% and 20% of the prescription. This patient had prior induction chemoradiation followed by a pneumonectomy. She subsequently developed a second primary in the right upper lobe. This was treated with a wedge resection, which recurred locally. Her centrally-located, biopsy-proven local recurrence in the staple line was treated to 48 Gy.

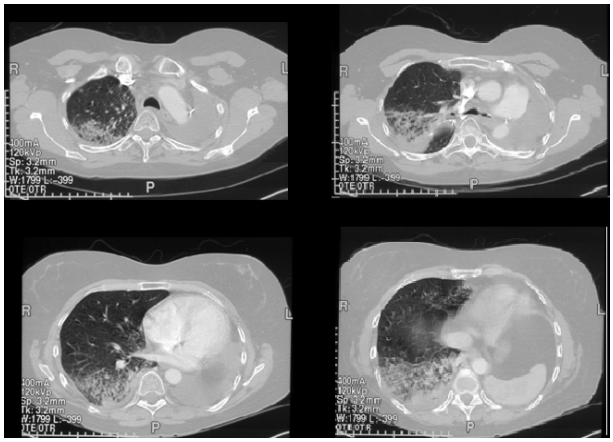

Figure 2. These CT slices were obtained one week following admission to the hospital which was required due to the development of fever of 103°F and shortness of breath one day following SBRT while on oral antibiotics. These images demonstrate the trilobar pneumonia.

after the first fraction. She was empirically treated with oral antibiotics and the fever resolved. The day after the final fraction, she developed a fever up to 103°F with increasing shortness of breath. She required admission to the hospital and a stay in the ICU for a tri-lobar pneumonia (see **Figure 2**). She remained hospitalized for a week and responded to intravenous antibiotics and supportive care. Her respiratory function continued to improve over time, although she remained intermittently oxygen dependent 16 months following treatment. Unfortunately, she developed a failure on the staple line 2 cm from the site treated.

No patient who received 56 Gy developed a symptomatic pulmonary injury, although one patient developed asymptomatic distal atelectasis for a peripherally treated tumor six months following radiation.

3.1. Local Control

Six patients developed a local failure. There were no marginal failures outside of the original PTV. Only two of the local failures were biopsy proven. One of the patients was treated for a gross recurrence following a wedge resection and developed a recurrence on the staple line 2 cm from the treated lesion. The second biopsy-proven failure occurred in patient number 1, who had very poor pulmonary function and presented with 2 tumors in the same lobe (*i.e.* T4). That individual was initially treated palliatively with chemotherapy alone (six cycles of carboplatin and paclitaxel). The smaller tumor resolved and the larger tumor shrank from 4 to 2 cm. The post-chemotherapy volume of the larger tumor was treated on study. Six months following this second treatment, an area of nodularity developed outside the original PTV, but retrospectly was in the original pre-chemotherapy GTV. The tumor that initially resolved on chemotherapy returned 14 months later. That lesion was treated off-study with SBRT.

4. DISCUSSION

There are many reports on SBRT in the literature although there are very few prospective trials. The morbidity results in our study are lower than recently published trials and seem more impressive in light of this heavily pretreated population. One could argue that the only grade 3 event described in this trial may not relate to the radiotherapy.

Baumann *et al.* [26] reported a 21% incidence of grade 3 toxicities of the 60 patients treated at the Karolinska University Hospital in Sweden. They prescribed 45 Gy in 3 fractions to the 67% isodose line (19 Gy when corrected to 80%) [26,27]. Fakiris *et al.* [28] updated the Indiana University phase II trial demonstrating an 11.4% rate of grade 3 to 5 events occurring in peripherally located tumors and 27.3% in their centrally located patients. The dose in the Indiana experience was 60 Gy in 3 fractions prescribed to the 80% isodose line. However, since heterogeneity corrections were not used, the actual prescribed dose has now been reported to be closer to 18 Gy per fraction. [16]

Nagata *et al.* [14] reported a phase I/II study using 48 Gy in 4 fractions in 45 patients with no grade 3 or higher pulmonary events and excellent local control. In the largest series reported, Onishi *et al.* [29,30] reported a 2.4% incidence of grade 3 and 4 pneumonitis and no grade 5 events. In fact, there have been only 14 (0.6%) reported grade 5 events from a Japanese National Survey out of 2104 patients treated (personal communication) compared to 5 of 70 treated on the phase II experience

from Indiana.

Other possible morbidities following SBRT are chest wall pain and rib fracture. Onishi *et al.* [29] described the multi-institutional Japanese experience and reported a 0.8% incidence of rib fractures. The Princess Margaret group [31] demonstrated a 48% incidence of rib fracture in peripheral lesions treated with 54-60 Gy in 3 fractions. Ribs in the areas of the fracture generally received 43 Gy and the tumor was less than 5 mm from the rib. The Colorado and Virginia groups [32] combined their experience of peripheral tumors less than 1.5 cm from the chest wall. The risk of chest wall pain and/or fracture correlated with the volume of chest wall receiving more than 30 Gy. The incidence was 0% (0/4), 33% (2/6), 46% (6/13) and 63% (5/8) for < 10 cc, 10.1-40 cc, 40.1-120 cc and > 120.cc, respectively. The author recommended the use of 48 Gy in 4 fractions when the tumor was adjacent to the rib. None of the patients treated on this trial developed rib fracture or chest wall pain.

The Cleveland Clinic [33] reported the most compelling study that evaluated two different fractionation schemas (50 Gy in 5 fractions versus 60 Gy in 3 fractions). When their program started, a 5 fraction regimen was used. In 2000, after the RTOG study was opened, the Timmerman approach (60 Gy in 3 fractions) was followed. With short follow-up, local control was similar between the two schemas (97% versus 100%) although the chest wall toxicity was significantly more with 60 Gy. The incidence of chest wall pain was 4% (2/56) for 50 Gy and 18% (7/38) for 60 Gy, $p = 0.028$. Also, given the median follow-up of only 9 months in the 60 Gy cohorts, the morbidity is likely to increase with further follow-up.

Brachial plexopathy (BP) is a rare event following SBRT. The Indiana University [34] experience described seven brachial plexus injuries. Four patients had grade 2, two patients had grade 3 and one had grade 4 BP. The authors tried to determine dose volume relation of apical tumors, which they defined as being located superior to the arch of the aorta (37 of 273 cases). Using the subclavian and axillary vessels as a surrogate for the brachial plexus dose, when the dose was greater than the median dose (26 Gy over 3 fractions) the 2 year incidence of BP was 46% versus 8% ($p = 0.038$) for lower doses. There were no brachial plexus injuries in our study.

Currently, there are 2 predominant fractionation schemas for SBRT of malignant lung tumors: the Japanese approach (12 Gy × 4) [14] and the RTOG approach developed by Timmerman (20 Gy × 3). [16,20,35] The biologic effective dose (BED) between the 2 schemas are drastically different (105.6 versus 180 Gy), but there are no clear differences in local control (85% versus 88%). The calculation of the BED from conventional to hyopfractionated radiation schedules, however, may be flawed. [36]

Our local control appears similar to what others describe although two of the failures are important to comment on. The tumors of patients treated in the post-operative or post-chemotherapy setting may be difficult to delineate. Therefore, these patients may not be ideal candidates for SBRT. Such is the case for the two previously described patients who had biopsy-proven local failures-the first being the patient who had a local recurrence along a wedge resection staple line and the second being the patient who had a recurrence in the pre-chemotherapy volume, although the post-chemotherapy volume was treated. Determining appropriate target volumes may be more difficult after either surgical intervention or chemotherapy. Unfortunately, the larger volumes necessary to cover all these areas of subclinical disease may increase morbidity. [37] Therefore, in post-surgical and post-chemotherapy settings, care must be taken to weigh the risks and benefits of this treatment following prior treatment.

In conclusion, SBRT utilizing patient specific target volumes without gating appears safe. In our study, patient simulation was carefully performed to create an ITV. A stereotactic body frame was utilized and imaging was obtained prior to each treatment to verify patient position. One grade 3 pulmonary event occurred at the 48 Gy dose levels, which may be related to radiotherapy. No other dose limiting toxicities occurred. There was no significant decrement in pulmonary function tests following SBRT. The maximum tolerated dose in this study was not reached.

REFERENCES

[1] Mountain, C.F. (1997) Revisions in the international system for staging lung cancer. *Chest*, **111**, 1710-1717.

[2] LeChevalier, T. *et al*. (1991) Radiotherapy alone versus combined chemotherapy and radiotherapy in nonresectable non-small-cell lung cancer: First analysis of a randomized trial in 353 Patients. *Journal of the National Cancer Institute*, **83**, 417-423.

[3] Bradley, J., Graham, M.V., Winter, K., Purdy, J.A., Komaki, R., Roa, W.H., Ryu, J.K., Bosch, W. and Emami, B. (2005) Toxicity and outcome results of RTOG 9311: A phase I-II dose-escalation study using three-dimensional conformal radiotherapy in patients with inoperable non-small-cell lung carcinoma. *International Journal of Radiation Oncology Biology Physics*, **61**, 318-328.

[4] Narayan, S., Henning, G.T., Ten Haken, R.K., Sullivan, M.A., Martel, M.K. and Hayman, J.A. (2004) Results following treatment to doses of 92.4 or 102.9 Gy on a phase I dose escalation study for non-small cell lung cancer. *Lung Cancer*, **44**, 79-88.

[5] Rosenzweig, K.E., Fox, J.L., Yorke, E., Amols, H., Jackson, A., Rusch, V., Kris, M.G., Ling, C.C. and Leibel, S.A. (2005) Results of a phase I dose-escalation study using three-dimensional conformal radiotherapy in the treatment of inoperable nonsmall cell lung carcinoma. *Cancer*,

103, 2118-2127.

[6] Martel, M.K., Ten Haken, R.K., Hazuka, M.B., Kessler, M.L., Strawderman, M., Turrisi, A.T., Lawrence, T.S., Fraass, B.A. and Lichter, A.S. (1999) Estimation of tumor control probability model parameters from 3-D dose distributions of non-small cell lung cancer patients. *Lung Cancer*, **24**, 31-37.

[7] Mehta, M., Scrimger, R., Mackie, R., Paliwal, B., Chappell, R. and Fowler, J. (2001) A new approach to dose escalation in non-small-cell lung cancer. *International Journal of Radiation Oncology Biology Physics*, **49**, 23-33.

[8] Andrews, D.W., Scott, C.B., Sperduto, P.W., Flanders, A.E., Gaspar, L.E., Schell, M.C., Werner-Wasik, M., Demas, W., Ryu, J., Bahary, J.P., Souhami, L., Rotman, M., Mehta, M.P. and Curran, W.J.Jr. (2004) Whole brain radiation therapy with or without stereotactic radiosurgery boost for patients with one to three brain metastases: phase III results of the RTOG 9508 randomised trial. *Lancet*, **363**, 1665-1672.

[9] Blomgren, H., Lax, I., Naslund, I. and Svanstrom, R. (1995) Stereotactic high dose fraction radiation therapy of extracranial tumors using an accelerator. Clinical experience of the first thirty-one patients. *Acta Oncologica*, **34**, 861-870.

[10] Fukumoto, S., Shirato, H., Shimzu, S., Ogura, S., Onimaru, R., Kitamura, K., Yamazaki, K., Miyasaka, K., Nishimura, M. and Dosaka-Akita, H. (2002) Small-volume image-guided radiotherapy using hypofractionated, coplanar, and noncoplanar multiple fields for patients with inoperable Stage I nonsmall cell lung carcinomas. *Cancer*, **95**, 1546-1553.

[11] Hara, R., Itami, J., Kondo, T., Aruga, T., Abe, Y., Ito, M., Fuse, M., Shinohara, D., Nagaoka, T. and Kobiki, T. (2002) Stereotactic single high dose irradiation of lung tumors under respiratory gating. *Radiotherapy and Oncology*, **63**, 159-163.

[12] Harada, T., Shirato, H., Ogura, S., Oizumi, S., Yamazaki, K., Shimizu, S., Onimaru, R., Miyasaka, K., Nishimura, M. and Dosaka-Akita, H. (2002) Real-time tumor-tracking radiation therapy for lung carcinoma by the aid of insertion of a gold marker using bronchofiberscopy. *Cancer*, **95**, 1720-1727.

[13] Herfarth, K.K., Debus, J., Lohr, F., Bahner, M.L., Fritz, P., Hoss, A., Schlegel, W. and Wannenmacher, M.F. (2000) Extracranial stereotactic radiation therapy: Set-up accuracy of patients treated for liver metastases. *International Journal of Radiation Oncology Biology Physics*, **46**, 329-335.

[14] Nagata, Y., Takayama, K., Matsuo, Y., Norihisa, Y., Mizowaki, T., Sakamoto, T., Sakamoto, M., Mitsumori, M., Shibuya, K., Araki, N., Yano, S. and Hiraoka, M. (2005) Clinical outcomes of a phase I/II study of 48 Gy of stereotactic body radiotherapy in 4 fractions for primary lung cancer using a stereotactic body frame. *International Journal of Radiation Oncology Biology Physics*, **63**, 1427-1431.

[15] Negoro, Y., Nagata, Y., Aoki, T., Mizowaki, T., Araki, N., Takayama, K., Kokubo, M., Yano, S., Koga, S., Sasai, K., Shibamoto, Y. and Hiraoka, M. (2001) The effectiveness of an immobilization device in conformal radiotherapy for lung tumor: reduction of respiratory tumor movement and evaluation of the daily setup accuracy. *International Journal of Radiation Oncology Biology Physics*, **50**, 889-898.

[16] Timmerman, R., Papiez, L., McGarry, R., Likes, L., DesRosiers, C., Frost, S. and Williams, M. (2003) Extracranial stereotactic radioablation: Results of a phase I study in medically inoperable stage I non-small cell lung cancer. *Chest*, **124**, 1946-1955.

[17] Uematsu, M., Shioda, A., Tahara, K., Fukui, T., Yamamoto, F., Tsumatori, G., Ozeki, Y., Aoki, T., Watanabe, M. and Kusano, S. (1998) Focal, high dose, and fractionated modified stereotactic radiation therapy for lung carcinoma patients: A preliminary experience. *Cancer*, **82**, 1062-1070.

[18] Wulf, J., Hadinger, U., Oppitz, U., Olshausen, B. and Flentje, M. (2000) Stereotactic radiotherapy of extracranial targets: CT-simulation and accuracy of treatment in the stereotactic body frame. *Radiotherapy and Oncology*, **57**, 225- 236.

[19] Herfarth, K.K., Debus, J., Lohr, F., Bahner, M.L., Rhein, B., Fritz, P., Hoss, A., Schlegel, W. and Wannenmacher, M.F. (2001) Stereotactic single-dose radiation therapy of liver tumors: Results of a phase I/II trial. *Journal of Clinical Oncology*, **19**, 164-170.

[20] Wang, L., Feigenberg, S., Chen, L., Pasklev, K. and Ma, C.C. (2006) Benefit of three-dimensional image-guided stereotactic localization in the hypofractionated treatment of lung cancer. *International Journal of Radiation Oncology Biology Physics*, **66**, 738-747.

[21] Wang, L., Hayes, S., Paskalev, K., Jin, L., Buyyounouski, M.K., Ma, C.C. and Feigenberg, S. (2008) Dosimetric comparison of stereotactic body radiotherapy using 4D CT and multiphase CT images for treatment planning of lung cancer: Evaluation of the impact on daily dose coverage. *Radiotherapy and Oncology*, **91**, 314-324.

[22] Jin, L., Wang, L., Li, J., Luo, W., Feigenberg, S.J. and Ma, C.M. (2007) Investigation of optimal beam margins for stereotactic radiotherapy of lung-cancer using Monte Carlo dose calculations. *Physics in Medicine and Biology*, **52**, 3549-3561.

[23] Babb, J., Rogatko, A. and Zacks, S. (1998) Cancer phase I clinical trials: Efficient dose escalation with overdose control. *Statistics in Medicine*, **17**, 1103-1120.

[24] Zacks, S., Rogatko, A. and Babb, J. (1998) Optimal bayesian-feasible dose escalation for cancer phase I trials. *Statistics & probability letters*, **38**, 215-220.

[25] Therasse, P., Arbuck, S.G., Eisenhauer, E.A., Wanders, J., Kaplan, R.S., Rubinstein, L., Verweij, J., Van Glabbeke, M., van Oosterom, A.T., Christian, M.C. and Gwyther, S.G. (2000) New guidelines to evaluate the response to treatment in solid tumors. *Journal of the National Cancer Institute*, **92**, 205-216.

[26] Baumann, P., Nyman, J., Hoyer, M., Gagliardi, G., Lax, I., Wennberg, B., Drugge, N., Ekberg, L., Friesland, S., Johansson, K.A., Lund, J.S., Morhed, E., Nilsson, K., Levin, N., Paludan, M., Sederholm, C., Traberg, A., Wittgren, L. and Lewensohn, R. (2008) Stereotactic body radiotherapy for medically inoperable patients with stage I non-small cell lung cancer - a first report of toxicity related to COPD/CVD in a non-randomized prospective phase II study. *Radiotherapy and Oncology*, **88**, 359-367.

[27] Baumann, P., Nyman, J., Hoyer, M., Wennberg, B.,

Gagliardi, G., Lax, I., Drugge, N., Ekberg, L., Friesland, S., Johansson, K.A., Lund, J.A., Morhed, E., Nilsson, K., Levin, N., Paludan, M., Sederholm, C., Traberg, A., Wittgren, L. and Lewensohn, R. (2009) Outcome in a prospective phase II trial of medically inoperable stage I non-small-cell lung cancer patients treated with stereotactic body radiotherapy. *Journal of Clinical Oncology*, **27**, 3290-3296.

[28] Fakiris, A.J., McGarry, R.C., Yiannoutsos, C.T., Papiez, L., Williams, M., Henderson, M.A. and Timmerman, R. (2009) Stereotactic body radiation therapy for early-stage non-small-cell lung carcinoma: Four-year results of a prospective phase II study. *International Journal of Radiation Oncology Bilolgy Physics*, **75**, 677-682.

[29] Onishi, H., Araki, T., Shirato, H., Nagata, Y., Hiraoka, M., Gomi, K., Yamashita, T., Niibe, Y., Karasawa, K., Hayakawa, K., Takai, Y., Kimura, T., Hirokawa, Y., Takeda, A., Ouchi, A., Hareyama, M., Kokubo, M., Hara, R., Itami, J. and Yamada, K. (2004) Stereotactic hypofractionated high-dose irradiation for stage I nonsmall cell lung carcinoma: clinical outcomes in 245 subjects in a Japanese multiinstitutional study. *Cancer*, **101**, 1623-1631.

[30] Onishi, H., Shirato, H., Nagata, Y., Hiraoka, M., Fujino, M., Gomi, K., Niibe, Y., Karasawa, K., Hayakawa, K., Takai, Y., Kimura, T., Takeda, A., Ouchi, A., Hareyama, M., Kokubo, M., Hara, R., Itami, J., Yamada, K. and Araki, T. (2007) Hypofractionated stereotactic radiotherapy (HypoFXSRT) for stage I non-small cell lung cancer: Updated results of 257 patients in a Japanese multi-institutional study. *Journal of Thoracic Oncology*, **2**, S94-100.

[31] Voroney, J.P.J. *et al*. (2008) Pain and rib fracture after stereotactic radiotherapy for peripheral non-small cell lung cancer. *International Journal of Radiation Oncology Biology Physics*, **72**, S35-36.

[32] Dunlap, N.E. *et al*. (2008) Chest wall volume receiving more than 30 Gy predicts risk of severe pain and/or rib fracture following lung SBRT. *International Journal of Radiation Oncology Biology Physics*, **72**, S36.

[33] Stephens, K.L. *et al*. (2008) A comparison of Stereotactic Body Radiation (SBRT) fractionation schedules for stage I non-small cell lung cancer (NSCLC): The cleveland clinic experience. *International Journal of Radiation Oncology Biology Physics*, **72**, S38-39.

[34] Forquer, J.A. *et al*. (2008) Brachial Plexopathy (BP) from Stereotactic Body Radiotherapy (SBRT) in early-stage NSCLC: Dose-limiting toxicity in apical tumor sites. *International Journal of Radiation Oncology Biology Physics*, **72**, S36.

[35] Timmerman, R., Paulus, R., Galvin, J.M., Michalski, J., Straube, W.L., Bradley, J., Fakiris, A., Bezjak, A., Videtic, G. and Choy, H. (2007) Toxicity analysis of RTOG 0236 using stereotactic body radiation therapy to treat medically inoperable early stage lung cancer patients. *International Journal of Radiation Oncology Bilolgy Physics*, **69**, S86.

[36] Guerrero, M. and Li, X.A. (2004) Extending the linear-quadratic model for large fraction doses pertinent to stereotactic radiotherapy. *Physics in Medicine and Biology*, **49**, 4825-4835.

[37] Nataf, F., Schlienger, M., Liu, Z., Foulquier, J.N., Gres, B., Orthuon, A., Vannetzel, J.M., Escudier, B., Meder, J.F., Roux, F.X. and Touboul, E. (2008) Radiosurgery with or without A 2-mm margin for 93 single brain metastases. *International Journal of Radiation Oncology Bilolgy Physics*, **70**, 766-772.

J. Biomedical Science and Engineering, 2010, 3, 359-360 **JBiSE**
doi:10.4236/jbise.2010.34049 Published Online April 2010 (http://www.SciRP.org/journal/jbise/).

Femoral notch cleaning in anterior cruciate ligament reconstruction: a new instrument

Miroslav Z. Milankov[1], Natasa Miljkovic[2], Zoran Gojkovic[1]

[1]Department of Orthopaedic Surgery and Traumatology, Clinical Centre Vojvodina, Medical School, University of Novi Sad, Novi Sad, Serbia;
[2]Plastic Surgery Research Laboratory, University of Pittsburgh, Pittsburgh, United State.
Email: milankom@eunet.rs; miljkovicnd@upmc.edu

Received 30 November 2009; revised 28 December 2009; accepted 2 January 2010.

ABSTRACT

This article describes using of this new, improvised instrument that enables better removal of ACL remnants, increased visibility of the intercondylar notch, precise location of the femoral tunnel and by doing this shor- tens the operative time. Also, the use of this instrument is cost beneficial, because it decreases the number of disposable shaver tips used and can decrease the cost of the procedure which is important for countries with poor economies.

Keywords: Anterior Cruciate Reconstruction; Femoral Notch Cleaning; Improvised Instrument

1. INTRODUCTION

Optimal anatomical replacement of anterior cruciate ligament (ACL) is essential for achieving knee stability. The most frequent surgical error causing ACL reconstruction failure is anterior and more vertical femoral tunnel placement [1,2]. One potential reason for this is failure to accurately identify the true over-the-back position on the femur in the posterior aspect of the notch. Debridement of soft tissue in the notch using radiofrequency energy, shaver or different type of rasps is necessary in ACL reconstruction of the knee. In order to simplify and speed up the removal of the ACL remnants at the femoral insertion, a new, improvised instrument for ligament remnants removal has been developed.

2. TECHNICAL NOTE

An all-inside arthroscopical procedure for ACL reconstruction was used. After the autograft had been harvested, arthroscopic examination of the knee was performed. The ACL remnants in close contact with the PCL were removed using a shaver (**Figure 1**). Using a medial portal, a special instrument for the removal of the ACL ligament remnants at the femoral insertion, was introduced into the knee. The instrument comprised of a 10 cm long, headless, cancellous screw with 9-10th-reads at its distal end and a proximal end fitted to a holder (**Figure 2**). The instrument was placed in close contact with the superior and lateral part of the intercondylar roof and by moving it from the anterior to posterior, the ACL remnants were removed from the intercondylar roof and medial part of the lateral femoral condyle. The small rest of the remnants were removed using a shaver (**Figure 3**). Afterwards, the procedure was continued in the usual fashion.

3. DISCUSSION

Accurate and anatomic tunnel placements are essential to the success of reconstruction of the anterior cruciate ligament (ACL). On the femoral side, ideal tunnel placement in the sagittal plane is in the posterior quartile [3]. In the coronal plane, the common goal is to place the tunnel between the 1 and 2 o'clock position on the left and between 10 and 11 o'clock position on the right [4].

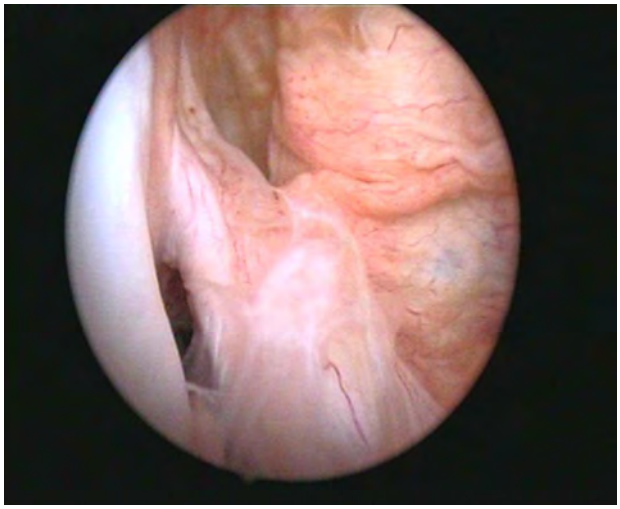

Figure 1. Arthroscopic view of the right knee from the anterolateral portal, ACL remnants.

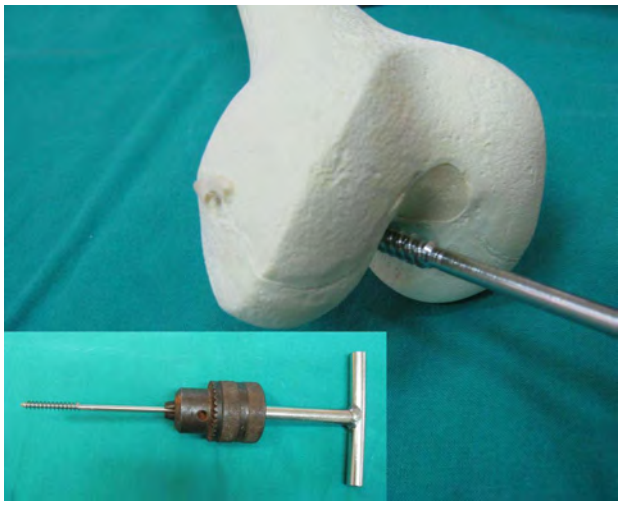

Figure 2. New, improvised instrument for ACL remnants removal. The instrument comprised of a 10 cm long, headless, cancellous screw with 9-10 threads at its distal end and a proximal end fitted to a holder.

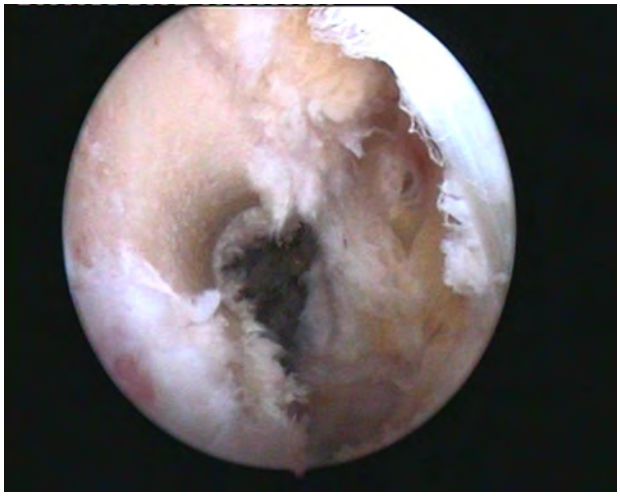

Figure 3. Arthroscopic view of the right knee from the anterolateral portal after using instrument. ACL remnants were removed from the intercondylar roof and medial part of the lateral femoral condyle. The notch doesn't have ACL remnants.

Tunnel placement based on lateral intercondylar ridge and lateral bifurcate ridge, is a more reliable approach [5-8]. The lateral intercondylar ridge is the superior border of the ACL with the knee in 90° of flexion, and the anterior border of the ACL with the knee in full extension [6,7]. The lateral bifurcate ridge separates the femoral attachment of the AM and PL bundles [6,7]. The visualization of these landmarks requires meticulous remnant removal. Failure to recognize these bone landmarks, leads to nonanatomic placement of the femoral tunnel and, therefore, premature failure of reconstructions. In older patients with poor bone quality, one has to be very careful not to overdo with the ACL remnant removal, since this can result in a significant bone indentation. Up till now, we have used this instrument in over 200 arthroscopic ACL reconstruction procedures without any difficulty or complications.

4. CONCLUSIONS

The use of this new, improvised instrument enables better removal of ACL remnants, increased visibility of the intercondylar notch and precise location of the femoral tunnel and by doing this shortens the operative time. Also, the use of this instrument is cost beneficial, because it decreases the number of disposable shaver tips used and can decrease the cost of the procedure which is important for countries with poor economies.

REFERENCES

[1] Carson, E.W., Simonian, P.T., Wickiewicz, T.L. and Warren, R.F. (1998) Revision anterior cruciate ligament reconstruction. *Instructional Course Lectures*, **47**, 361-368.

[2] Sommer, C., Friederich, N.F. and Müller, W. (2000) Improperly placed anterior cruciate ligament grafts: Correlation between radiological parameters and clinical results. *The Journal* of *Knee Surgery*, **8**, 207-213.

[3] Bernard, M., Hertel, P., Hornung, H. and Cierpinski, Th. (1997) Femoral insertion of the ACL, radiographic quadrant method. *American Journal of Knee Surgery*, **10**, 14-22.

[4] Loh, J.C., Fukuda, Y., Tsuda, E., Steadman, R.J., Fu, F.H. and Woo, S.L.Y. (2003) Knee stability and graft function following anterior cruciate ligament reconstruction: Comparison between 11 o'clock and 10 o'clock femoral tunnel placement. *Arthroscopy*, **19**, 297-304.

[5] Farrow, L.D., Chen, M.R., Cooperman, D.R., Victoroff, B.N. and Goodfellow, D.B. (2007) Morphology of the femoral intercondylar notch. *The Journal of Bone and Joint Surgery* (*American*), **89**, 2150-2155.

[6] Ferretti, M., Ekdahl, M., Shen, W. and Fu, F.H. (2007) Osseous landmarks of the femoral attachment of the anterior cruciate ligament: An anatomic study. *Arthroscopy*, **23**, 1218-1225.

[7] Fu, F.H. and Jordan, S.S. (2007) The lateral intercondylar ridge—a key to anatomic anterior cruciate ligament reconstruction. *The Journal of Bone and Joint Surgery* (*American*), **89**, 2103-2104.

[8] Hutchinson, M.R. and Ash, S.A. (2003) Resident's ridge: Assessing the cortical thickness of the lateral wall and roof of the intercondylar notch. *Arthroscopy*, **19**, 931-935.

J. Biomedical Science and Engineering, 2010, 3, 361-366 **JBiSE**
doi:10.4236/jbise.2010.34050 Published Online April 2010 (http://www.SciRP.org/journal/jbise/).

Wrist blood flow signal-based computerized pulse diagnosis using spatial and spectrum features

Dong-Yu Zhang[1], Wang-Meng Zuo[1], David Zhang[2], Hong-Zhi Zhang[1], Nai-Min Li[1]

[1]School of Computer Science and Technology Harbin Institute of Technology, Harbin, China;
[2]Biometrics Research Centre, Department of Computing the Hong Kong Polytechnic University, Hong Kong, China.
Email: cswmzuo@gmail.com

Received 4 January 2010; revised 11 January 2010; accepted 22 January 2010.

ABSTRACT

Current computerized pulse diagnosis is mainly based on pressure and photoelectric signal. Considering the richness and complication of pulse diagnosis information, it is valuable to explore the feasibility of novel types of signal and to develop appropriate feature representation for diagnosis. In this paper, we present a study on computerized pulse diagnosis based on blood flow velocity signal. First, the blood flow velocity signal is collected using Doppler ultrasound device and preprocessed. Then, by locating the fiducial points, we extract the spatial features of blood flow velocity signal, and further present a Hilbert-Huang transform-based method for spectrum feature extraction. Finally, support vector machine is applied for computerized pulse diagnosis. Experiment results show that the proposed method is effective and promising in distinguishing healthy people from patients with cholecystitis or nephritis.

Keywords: Pulse Diagnosis; Blood Flow Velocity; Hilbert-Huang Transform; Support Vector Machine

1. INTRODUCTION

Pulse diagnosis, one of the most important diagnostic methods in Traditional Chinese Medicine (TCM), has been used in disease examination and in guiding medicine selection for thousands of years [1]. In traditional Chinese pulse diagnosis (TCPD) theory [1], the wrist radial pulse signals, which caused by the fluctuation of blood flow in radial artery, contain rich and critical information which can reflect the state of human viscus, *i.e.* gallbladder, kidneys, stomach, lungs and so on [2]. That is the pathologic change of these internal organs can be reflected from the variations of rhythm, velocity, strength of radial pulse by which an experienced practitioners can tell a person's healthy condition. Moreover, TCPD is noninvasive and convenient for effective diagnosis.

The diagnostic results of TCPD, however, sincerely depend on the practitioner's subjective analysis and sometimes may be unreliable and inconsistent. Therefore, it is necessary to develop computerized pulse signal analysis techniques to make TCPD standard and objective. In recent years, techniques developed for measuring, processing, and analyzing the physiological signals [3-5] are considered in computerized pulse signal research [6-8]. A series of pulse signal acquisition systems [9,10] have recently been developed and a number of methods have been proposed to analyze the digitized pulse signals [11-15].

By far, considerable achievements have been obtained in the development of computerized pulse diagnosis based on the analysis of pulse signal acquired by pressure [9] or photoelectric sensors [10]. Since the information utilized in TCPD is comprehensive and complicated, photoelectric or pressure sensors cannot acquire all the necessary information for pulse diagnosis. Thus it is necessary to develop new types of sensors, to develop appropriate feature extraction methods, and to test the feasibility of other types of pulse signal.

Doppler ultrasonic blood flow inspection and measurement [16] is widely used as a noninvasive clinical check technique to evaluate the dynamic characteristics of peripheral artery. Thus, the effectiveness of Doppler ultrasonic blood flow signal for computerized pulse diagnosis has been recognized and preliminarily investigated [17-19]. In this paper, we systematically investigates the acquisition, pre-processing, feature extraction and classification of Doppler ultrasonic blood flow signal, and propose to use both spatial and spectrum features for computerized pulse diagnosis.

Generally speaking, as shown in **Figure 1**, the proposed scheme involves three major modules: data collection and preprocessing, feature extraction, and classification. In the first module, blood flow signal of the wrist radial artery is first collected by Doppler ultrasound device and then denoised using empirical mode decomposition (EMD)-based method [18]. In the feature

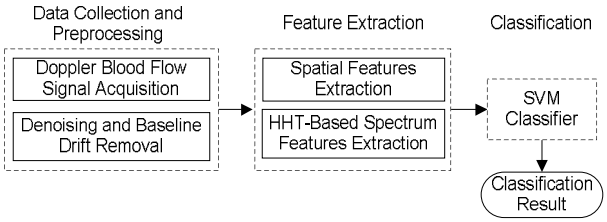

Figure 1. Schematic diagram of the proposed computerized pulse diagnosis method.

extraction module, spatial features are first extracted and then a Hilbert-Huang transform (HHT)-based method is adopted to extract the spectrum features. Finally, in the classification module, the support vector machine (SVM) classifier is used to distinguish healthy person from patients with two typical visceral diseases, cholecystitis and nephritis.

The remainder of this paper is organized as follows. Section 2 describes the procedure of data acquisition and preprocessing. In Section 3, we first extract the spatial features of blood flow signal, and then a HHT-based method is proposed to effectively extract the spectrum features. The classification results are described in Section 4. Finally, Section 5 concludes this paper.

2. DATA ACQUISITION AND PREPROCESSING

In our scheme, blood flow signals of the wrist radial artery are collect by a Doppler ultrasonic acquisition device. At the beginning of signal acquisition, operator uses his/her finger to feel the fluctuation of pulse at the patient's styloid process of radius to figure out a rough area where the ultrasound probe is then put on and moved around carefully until the most significant signal is detected. Then, a stable signal segment with 30 seconds is recorded and stored. The raw data acquired is represented in the form of Doppler spectrogram (see **Figure 2(a)**), of which the up envelope corresponds to the blood flow velocity signal.

In the preprocessing, the blood flow velocity signal is first extracted, and is then further processed to remove the noise and the baseline drift. An EMD-based method described in our former work [18] is adopted for denoising. To address the baseline drift problem, the wavelet-based cascade adaptive filter method [20] is adopted. As an example, **Figure 2(b)** shows an extracted blood flow velocity signal, and **Figure 2(c)** shows the result of blood flow velocity signal after denoising and baseline drift removal.

3. FEATURE EXTRACTION

This section describes the feature extraction methods used in our scheme. First, the spatial features of blood flow velocity signals are extracted. Then we discuss how

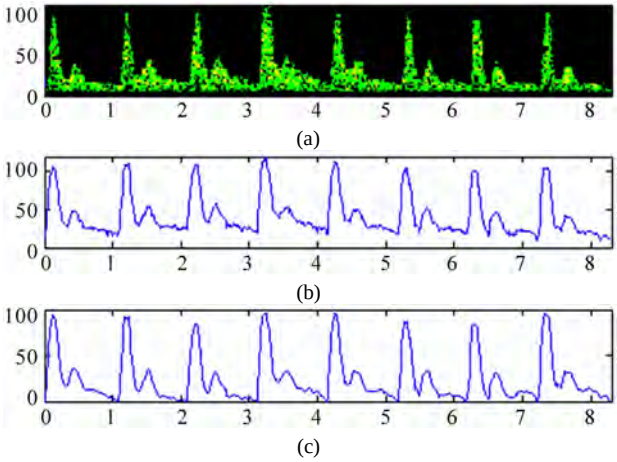

Figure 2. An illustration of the preprocessing of wrist blood flow signal, where: (a) is a typical Doppler spectrogram of blood flow signal; (b) is the blood flow velocity signal extracted from Doppler spectrogram; (c) is the blood flow signal after denoising and baseline drift removal.

to utilize the Hilbert-Huang transform (HHT), which includes empirical mode decomposition (EMD) and Hilbert transform, for spectrum feature extraction.

3.1. Spatial Feature Extraction of Blood Flow Velocity Signal

Blood flow velocity signal is a semi-periodic signal where each period signal is constructed by a primary wave, a secondary wave, and a dicrotic notch (see **Figure 3**). As shown in **Figure 3**, we define several fiducial points, and the meanings (of a, b, c, d, a') are explained in **Table 1**.

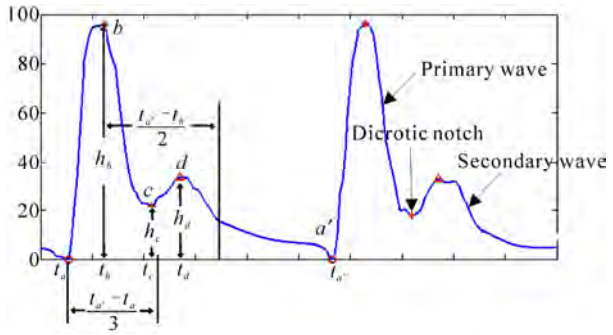

Figure 3. An illustration of the fiducial points of blood flow velocity signal.

Table 1. Fiducial points of blood velocity signal.

Points	Feature Meaning
a	Onset of one period
b	Peak point of primary wave
c	Dicrotic notch
d	Peak point of secondary wave
a'	Onset of the next period

The procedure of fiducial point location is described as follows

1) Find the onsets of each period using the method described in [20], and then locate the points *a* and *a'*, and their corresponding time labels are t_a and $t_{a'}$.

2) Detect the peak point *b* of the primary wave in $[t_a, t_a + (t_{a'} - t_a)/3]$, and obtain the time label t_b and the amplitude h_b corresponding to *b*.

3) Detect the subsequent peak point *d* within the time interval $[t_b, t_b + (t_{a'} - t_b)/2]$, and obtain its corresponding time label t_d and amplitude h_d.

4) Detect the dicrotic notch point *c* within time interval [t_b, t_d], and obtain its time labels t_c and amplitude h_c.

5) Calculate the parameters in this period by

$$\left.\begin{aligned} T &= t_{a'} - t_a \\ T_{ba} &= t_b - t_a \\ T_{cb} &= t_c - t_b \\ T_{dc} &= t_d - t_c \\ T_{a'b} &= t_{a'} - t_b \end{aligned}\right\}. \quad (1)$$

6) Repeat Step 1-Step 5 until all the fiducial points of blood flow velocity signal is detected.

After all the fiducial points are detected, we extract six spatial features from blood flow velocity signal, as listed in **Table 2**. We adopt the mean of relative ratios between different fiducial point information as spatial features because they are more stable.

3.2. EMD-Based Spectrum Feature Extraction

In this subsection, we first introduce the Hilbert-Huang transform (HHT), and then discuss how to utilize HHT for spectrum feature extraction of blood flow velocity signals.

3.2.1. Hilbert-Huang Transform

Hilbert-Huang transform (HHT) [21] is an adaptive signal processing method for analyzing non-linear and non-stationary signals. In HHT, Hilbert spectrum, a time-frequency-energy spectrum of a signal is generated for signal analysis. The cores of HHT are empirical mode decomposition and Hilbert transform.

Table 2. Meanings of spatial features.

Features	Meanings
T_{ba}/T	Ratio of time of ascent part of primary wave to the period
T_{cb}/T	Ratio of time of decent part of primary wave to the period
T_{dc}/T	Ratio of time of ascent part of secondary wave to the period
$T_{a'b}/T_{ba}$	Ratio of time of ascent part to decent part of waveform
h_c/h_b	Ratio of amplitude of dicrotic notch to that of primary peak
h_d/h_b	Ratio of amplitude of secondary peak to that of primary peak

1) *Empirical Mode Decomposition:*

Empirical Mode Decomposition (EMD) is a successful method used to generate a decomposition of signal into several individual components, intrinsic mode functions (IMFs) [21]. An IMF must satisfy the following two criteria: (1) the numbers of extrema and the number of zero-crossings of an IMF are equal or differ at most by one; (2) at any point, the mean value of the envelope defined by the local maxima and the envelope defined by the local minima is zero.

With EMD, a signal $S(t)$ is decomposed into a series of $IMF_n(t)$ and a residue $r(t)$. For expression convenience, the residue $r(t)$ is treated as the last IMF. Consequently, the original signal $S(t)$ can be reconstructed by IMFs:

$$S(t) = \sum_{n=1}^{N} IMF_n(t), \quad (2)$$

where *N* is the numbers of IMFs.

2) *Hilbert Transform*

Hilbert transform of $IMF_n(t)$ is defined as:

$$Y_n(t) = \frac{1}{p} P \int_{-\infty}^{\infty} \frac{IMF_n(t)}{t - t} dt, \quad (3)$$

where P denotes the Cauchy principal value [21].

With Hilbert transform, an analytic signal $Z_n(t)$ can be generated using $IMF_n(t)$ and the corresponding $Y_n(t)$, forming a complex conjugate pair defined as

$$Z_n(t) = IMF_n(t) + iY_n(t) = a_n(t)e^{jf_n(t)} \quad (4)$$

where $a_n(t)$ and $f_n(t)$ are instantaneous amplitude and phase defined as:

$$a_n(t) = \sqrt{(IMF_n(t))^2 + (Y_n(t))^2}, \quad (5)$$

$$f_n(t) = \arctan\left(Y_n(t) \Big/ IMF_n(t)\right), \quad (6)$$

respectively. Furthermore, the frequency of $Z_n(t)$ could be calculated as

$$f_n(t) = \frac{1}{2p} \frac{df_n(t)}{dt} \quad (7)$$

3.2.2. Feature Extraction by Hilbert-Huang Transform

The procedure to use HHT for blood flow velocity signal feature extraction is described as follows:

For each blood velocity signal $S(t)$, EMD is applied to decompose it into a series of *IMF*s which satisfy

$$S(t) = \sum_{n=1}^{N} IMF_n(t) \quad t = 1, 2, \mathbf{K}, m, \quad (8)$$

where *N* is the number of *IMF*s and *m* is the length of $S(t)$.

For each $IMF_n(t)$, we extract $a_n(t)$ and $f_n(t)$ using **Eq.5**

and **Eq.7**, and then define the average amplitude $\bar{h}_n$ and the average frequency $\bar{w}_n$ of each $IMF_n(t)$ as

$$\bar{h}_n = \sum_{t=1}^{m} a_n(t)/m, \quad (9)$$

$$\bar{w}_n = \sum_{t=1}^{m} a_n(t) f_n(t) \Big/ \sum_{t=1}^{m} a_n(t). \quad (10)$$

We define the energy P_n of $IMF_n(t)$ as

$$P_n = \frac{\sum_{t=1}^{m} \left| IMF_n(t) \right|^2}{\sqrt{\sum_{n=1}^{N} \sum_{t=1}^{m} \left| IMF_n(t) \right|^2}}. \quad (11)$$

Using **Eqs.9-11**, for each blood flow velocity signal $S(t)$, we extract $3 \times N$ parameters $\{\bar{h}_n, \bar{w}_n, P_n\}$, which form a vector to be used for blood flow velocity signal classification.

4. EXPERIMENTAL RESULT AND DISCUSSION

In this section, the extracted features by methods described in the Section 3 are tested on our blood flow velocity dataset. The dataset includes 33 healthy persons, 25 nephritis patients, and 25 cholecystitis patients. All of the data were collected at Harbin 211st Hospital using our Doppler ultrasonic analyzer. Before the classification, all the blood flow velocity signals are segmented to have the same length with the result that each has 2060 points.

For the HHT-based feature extraction method, all the 2060 points of data are used. **Figure 4** and **Figure 5** show the EMD of a healthy person and a nephritis patient. EMD is an adaptive signal processing method. For different signals the numbers of their *IMF*s may not be the same. For blood flow velocity signal, the typical numbers of *IMF*s are between 7 and 9. Since the number of *IMF*s differs in different signals, the feature vectors extracted from different signal are not guaranteed to have the same feature dimension. For each blood velocity signal, there is less oscillation in the higher order of *IMF*s, which means that these *IMF*s contain the direct-current component of the original signal. So, we discard the higher order *IMF*s and use the first five lower order *IMF*s (IMF_1 to IMF_5) for feature extraction. Then a 15-dimensional vector is extracted as

$$E = \left\{ \bar{h}_n, \bar{w}_n, P_n \mid n \in [1, \mathbf{K}, 5] \right\} \quad (12)$$

For the spatial feature extraction method, since we have fixed the length of blood flow velocity signal and the periods of different signals are not the same, there may be a span at the end of each segmented data which could not cover a complete period and some spatial feature could not be extracted in that span of signal (see **Figure 6**). Thus we discard that span and only use the remained part for spatial feature extraction. Using the method described in Subsection 3.1, we form a vector,

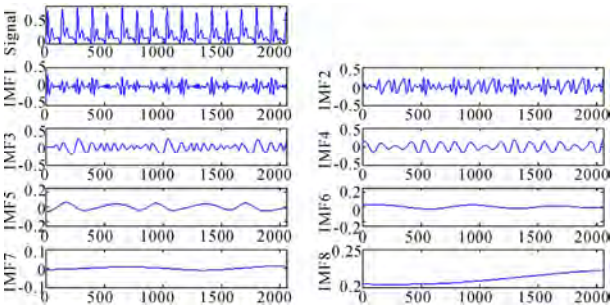

Figure 4. EMD of blood flow velocity signal of a healthy person.

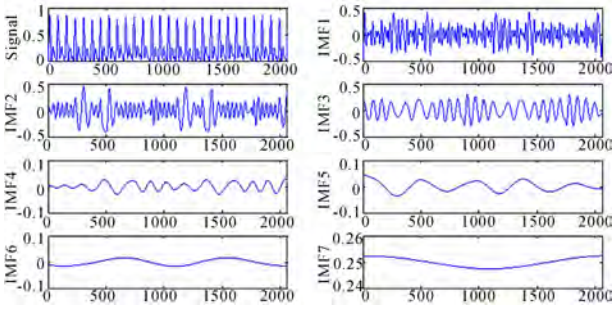

Figure 5. EMD of blood flow velocity signal of a nephritis patient.

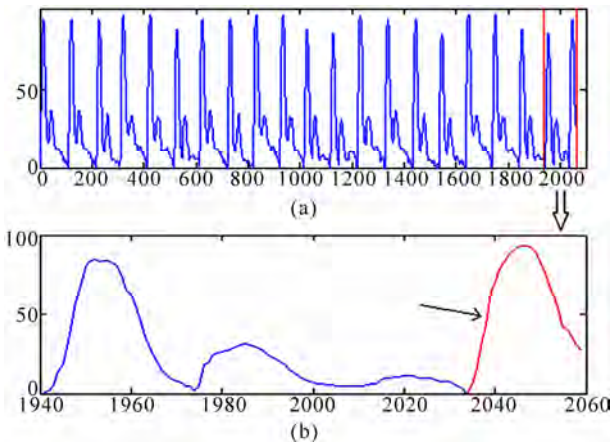

Figure 6. Data processing for spatial feature extraction: (a) is an example of segmented data with the incomplete last span of data; (b) is partial enlarged of (a).

$$S = \left\{ \frac{\bar{T}_{ba}}{\bar{T}}, \frac{\bar{T}_{cb}}{\bar{T}}, \frac{\bar{T}_{dc}}{\bar{T}}, \frac{\bar{T}_{a'b}}{\bar{T}_{ba}}, \frac{\bar{h}_c}{\bar{h}_b}, \frac{\bar{h}_d}{\bar{h}_b} \right\} \quad (13)$$

where "¯" denotes the mean value of parameters.

Using both spatial and spectrum feature extraction, we extract two vectors ***E*** and ***S*** for each blood flow velocity signal, and formulize them into a new vector ***T*** = {***E***, ***S***} for effective pulse classification.

In our experiments, we adopt support vector machine (SVM) [22] with Gaussian RBF kernel for that it has good generalization on small dataset. Our experiments were done under the MATLAB environment by using

the SVM-KM toolbox [23]. In SVM, we should determine the values of two hyper-parameters, C and s. **Figure 7** shows the influence of the two parameters on the classification error rate. According to the result shows in **Figure 7**, we choose C = 20 and s = 25. In order to reduce the bias, we adopt 10 runs of 3-folder cross-validation, and the classification results are listed in **Table 3**.

Table 3 shows that the proposed method achieves the highest accuracy, 92%, in the classification of the nephritis patients group, and the lowest accuracy, 56%, in the cholecystitis patients group. For all the three groups, the experiment achieves an acceptable accuracy of 75.9% in average.

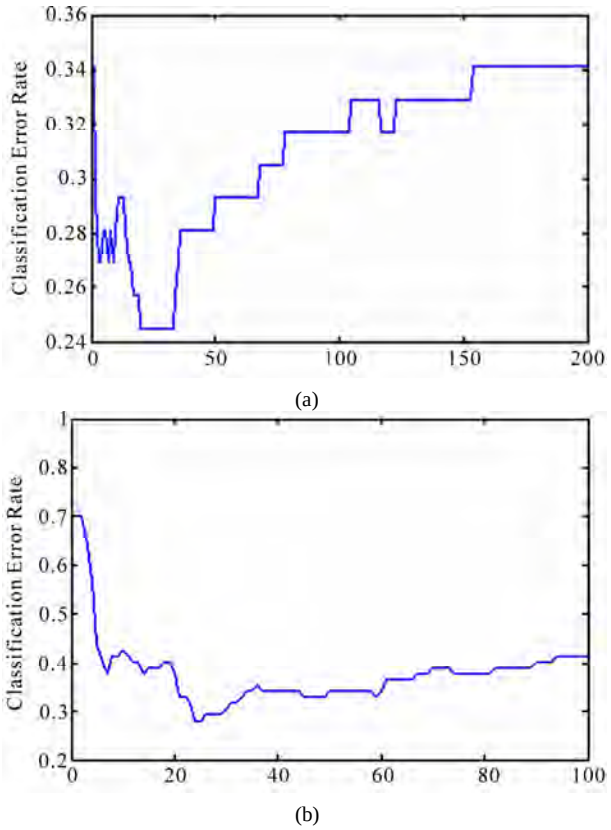

Figure 7. The influence of C and s on the classification error rate: (a) s is fixed to 10 and C varies from 0.5 to 200; (b) C is fixed to 10 and s varies from 0.5 to 100.

Table 3. Classification results using support vector machine.

Sample Class	Samples	Classification Results	Accuracy	
Cholecystitis Patients	25	14	56%	
Nephritis Patients	25	23	92%	75.9%
Healthy People	33	26	79%	

The similar work of adopting pulse signals to classify healthy people from patient with nephritis and cholecystitis were reported in [24], where the pulse signals were acquired by a typical pressure sensor. The size of data set used in [24] is comparable with that of this paper. Compared with the results of [24], our works get a promotion in discriminating nephritis patients from the other two classes where the accuracy was equal to 92%. This result shows that the Doppler spectrogram is superior to pressure sensor in nephritis diagnosis and thus may contain valuable complementary information for pulse diagnosis.

5. CONCLUSIONS

The wrist pulse signal of a person contains important information about the pathologic changes of the person's body condition. In this paper, we establish a systematic approach for computerized pulse diagnosis by studying the quantitative features of blood flow velocity signal of radial artery. First, the spatial features were extracted by locating several fiducial points of the blood flow velocity signal. Then, a HHT-based feature extraction method was proposed and a series of spectrum features were extracted. Experimental results show that blood flow velocity signal carries important information for computerized pulse diagnosis, and the proposed method achieves an accuracy of over 75% in classifying the healthy person from the patients with cholecystitis and nephritis. In the future, we will build large scale dataset with more kinds of diseases to further verify this new computerized pulse diagnosis approach, and analyze the heterogeneity and complementarities of blood flow velocity signal and other types of pulse signal.

6. ACKNOWLEDGEMENTS

This work is partially supported by the CERG fund from the HKSAR Government, the central fund from Hong Kong Polytechnic University, and the NSFC/SZHK-innovation funds of China under Contract Nos. 60620160097, 60871033, 60602038, and SG200810100003A.

REFERENCES

[1] Li, S.Z. (1985) Pulse diagnosis. Hoc Ku Huyuh and G Seifert, Sydney.

[2] Bob, F. (1995) The secret of Chinese pulse diagnosis. Blue Poppy Press, Boulder.

[3] Mahesh, V., Kandaswamy, A., Vimal, C. and Sathish, B. (2009) ECG arrhythmia classification based on logistic model tree. *Journal of Biomedical Science and Engineering*, **2**, 405-411.

[4] Dickhaus, H. and Heinrich, H. (1996) Classifying biosignals with wavelet networks: A method for noninvasive diagnosis. *IEEE Engineering in Medicine and Biology Magazine*, **15**, 103-111.

[5] McGuirk, S.P., Ewert, D., Barron, D.J. and Coote, J.H. (2009) Electrocardiographic interference and conductance volume measurements. *Journal of Biomedical Science and Engineering*, **2**, 491-498.

[6] Fei, Z.F. (2003) Contemporary sphygmology in traditional Chinese medicine. People's Medical Publishing House, Beijing.

[7] Wang, H. and Cheng, Y. (2005) A quantitative system for pulse diagnosis in traditional Chinese medicine. *Proceedings of the 27th Annual Conference on Engineering in Medicine and Biology Society*, **6**, 5676-5679.

[8] Fu, S.E. and Lai, S.P. (1989) A system for pulse measurement and analysis of Chinese medicine. *Proceedings of the 11th Annual International Conference on Engineering in Medicine and Biology Society*, **5**, 1695-1696.

[9] Tyan, C.C., Liu, S.H., Chen, J.Y., Chen, J.J. and Liang, W.M. (2008) A novel noninvasive measurement technique for analyzing the pressure pulse waveform of the radial artery. *IEEE Transactions on Biomedical Engineering*, **55**, 288-297.

[10] Hertzman, A.B. (1938) The blood supply of various skin areas as estimated by the photoelectric plethysmograph. *American Journal Physiology*, **124**, 328-340.

[11] Chun, T.L. and Ling, Y.W. (1983) Spectrum analysis of human pulse. *IEEE Transactions on Biomedical Engineering*, **30**, 348-352.

[12] Lu, W.A., Lin Wang, Y.Y. and Wang, W.K. (1999) Pulse analysis of patients with severe liver problems: Studying pulse spectrums to determine the effects on other organs. *IEEE Engineering in Medicine and Biology Magazine*, **18**, 73-75.

[13] Zhu, L., Yan, J., Tang, Q. and Li, Q. (2006) Recent progress in computerization of TCM. *Journal of Communication and Computer*, **3**, 78-81.

[14] Chen, C.Y., Wang, W.K., Kao, T., Yu, B.C. and Chiang, B.C. (1993) Spectral analysis of radial pulse in patients with acute uncomplicated myocardial infarction. *Japanese Heart Journal*, **34**, 131-143.

[15] Yu, G.L., Lin Wang, Y. Y. and Wang, W.K. (1994) Resonance in the kidney system of rats. *American Journal Physiology Heart and Circulatory Physiology*, **267**, 1544-1548.

[16] Sigel, B. (1998) A brief history of Doppler ultrasound in the diagnosis of peripheral vascular disease. *Ultrasound in Medicine and Biology*, **24**, 169-176.

[17] Zhang, D.Y., Zhang, L., Zhang, D. and Zheng, Y. (2008) Wavelet based analysis of Doppler ultrasonic wrist pulse signals. *Proceedings of the IEEE International Conference on Biomedical Engineering and Informatics*, **2**, 539-543.

[18] Zhang, D.Y., Wang, K.X., Wu, X.Q., Huang, B. and Li, N.M. (2009) Hilbert-Huang transform based Doppler blood flow signals analysis. *Proceedings of the IEEE International Conference on Biomedical Engineering and Informatics*, 1-5.

[19] Lee, Y.J., Lee, J. and Kim, J.Y. (2008) A study on characteristics of radial arteries through ultrasonic waves. *Proceedings of the 30th Annual International Conference on Engineering in Medicine and Biology Society*, **2008**, 2453-2456.

[20] Xu, L.S., Zhang, D. and Wang, K.Q. (2005) Wavelet-based cascaded adaptive filter for removing baseline drift in pulse waveforms. *IEEE Transactions on Biomedical Engineering*, **52**, 1973-1975.

[21] Huang, N.E., Shen, Z., Long, S.R., Tung, C.C. and Liu, H.H. (1998) The empirical mode decomposition and the Hilbert spectrum for nonlinear and non-stationary time series analysis. *Proceedings of the Royal Society*, **454**, 903-995.

[22] Burges, C.J.C. (1998) A tutorial on support vector machines for pattern recognition. *Data Mining and Knowledge Discovery*, **2**, 121-167.

[23] Canu, S., Grandvalet, Y., Guigue, V. and Rakotomamonjy, A. (2005) SVM and Kernel methods Matlab toolbox, perception systèmes et information, INSA de Rouen, Rouen, France. http://asi.insa-rouen.fr/enseignants/~arakotom/toolbox/index.html

[24] Guo, Q.L., Wang, K.Q., Zhang, D.Y. and Li, N.M. (2008) A wavelet packet based pulse waveform analysis for cholecystitis and nephrotic syndrome diagnosis. *Proceedings of the 2008 International Conference on Wavelet Analysis and Pattern Recognition*, **2**, 513-517.

J. Biomedical Science and Engineering, 2010, 3, 367-374 **JBiSE**
doi:10.4236/jbise.2010.34051 Published Online April 2010 (http://www.SciRP.org/journal/jbise/).

Transdermal drug delivery models

Grantham K. H. Pang, Da-Peng Qiao

Department of Electrical and Electronic Engineering, University of Hong Kong, Hong Kong, China.
Email: gpang@eee.hku.hk

Received 12 January 2010; revised 25 January 2010; accepted 9 February 2010.

ABSTRACT

In this paper, a preliminary study based on the different models of the skin impedance is carried out. The purpose is to examine the drug delivery method through iontophoresis, which relies on active transportation of the charged medication agent within an electric field. It is a kind of transdermal drug delivery method, and hence the method has to handle the variability in skin characteristics of a patient. This paper carries out a simulation study based on three different skin impedance models.

Keywords: Target Drug Delivery; Biomedical Engineering; Skin Impedance; Iontophoresis

1. INTRODUCTION

Nowadays, as opposed to the traditional oral intake and hypodermal injection, drug delivery to a patient can be carried out in many different ways. Transdermal drug delivery releases the medicament into the patient's body via the skin. There are various methods for transdermal drug delivery and they have been developed based on various principles. The developed methods could be based on diffusion, absorption, thermal energy, radio frequency energy, ultrasound, electrostatic force (electrophoresis) or electric field (iontophoresis). These are non-invasive methods, and recent developments also include transdermal skin patch that is placed on the skin to deliver a specific dose of medication through the skin, and then into the blood stream of the patient. The main advantage of a transdermal drug delivery is that it provides a controlled release of the medicament without serious pain to the patient.

However, all transdermal drug delivery methods have to deal with the complicated properties of the patient' skin, which is a very effective barrier, and its characteristics can vary a lot from one person to another. It is a natural barrier to foreign chemicals and biological agents. Methods that are based on the use of microneedles [1-3] have also been developed. These microneedles would physically puncture the skin but for less than 1 mm and deliver the drug without piercing blood vessels or damaging nerves, that are typically around 1 mm under the skin surface. The mechanical stability and the puncture behaviour of microneedles have been investigated experimentally [3]. In this paper, several electrical models for skin impedance are investigated and simulations have been carried out for a comparative study of the parameters for drug delivery through iontophoresis [4,5].

2. METHOD AND ANALYSIS

2.1. Introduction

Research has found that skin impedance can be modeled by typical RC (resistor-capacitor) circuits, without the need of any inductive component [6-9]. Hence, it is generally agreed that the skin impedance is made up of some amount of resistance and some form of capacitance. Different models of RC circuits can be developed to simulate current responses in actual skin.

2.2. Model A

An early skin impedance model is given in [7] and it is shown in **Figure 1**. The model is made up of a capacitor C in parallel with the resistance R_1. R_1 is modeling the resistance of the stratum corneum, which is the top layer of the epidermis. C represents the capacitance of the skin. The C-R_1 parallel combination is in series with another resistance R_2 which represents the resistance of the deeper tissues within the epidermis. Example of value for R_1 would range from around 100 Ω to 5000 kΩ cm^2, while R_2 would range from around 0.1 Ω to 1.0 kΩ cm^2.

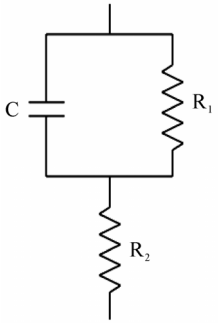

Figure 1. Skin impedance Model A.

This model is simple and can serve as an initial representation to the skin characteristics. However, a more complete representation is given in the next subsection.

2.3. Model B

Another model can also be found in [8] by Tregear which is consisted of multiple parallel RC circuits in series. This is designed to model the varying capacitance and resistance of the epidermal skin layers at different depths of the skin. This model is shown in **Figure 2** below. As mentioned in [5], this model represents the decreasing values of capacitance and resistance as individual layers of the stratum corneum are removed in experiments. The experimental result was important as it allows for the development of a more precise model of the skin impedance. Also, it has shown that the stratum corneum accounts for the major portion of the skin impedance in the skin.

2.4. Model C

Lykken [9] has proposed another model of skin impedance as shown in **Figure 3**. The model consists of several parallel paths, and each path is made up of several RC circuits, with each circuit representing a different layer of the skin. **Figure 3** provides a more distributed nature when modeling the skin impedance, and can potentially provide a more accurate model.

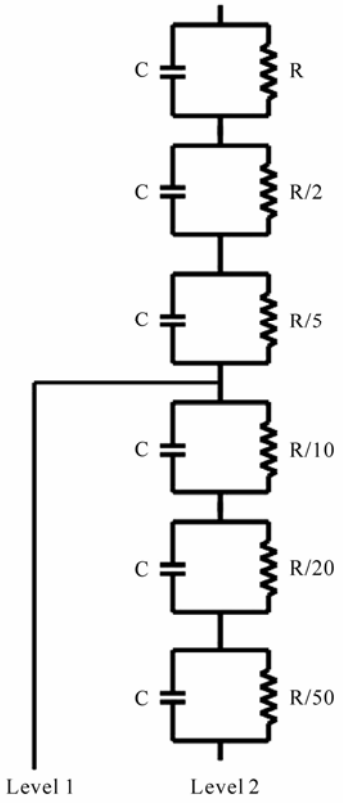

Figure 2. Skin impedance Model B.

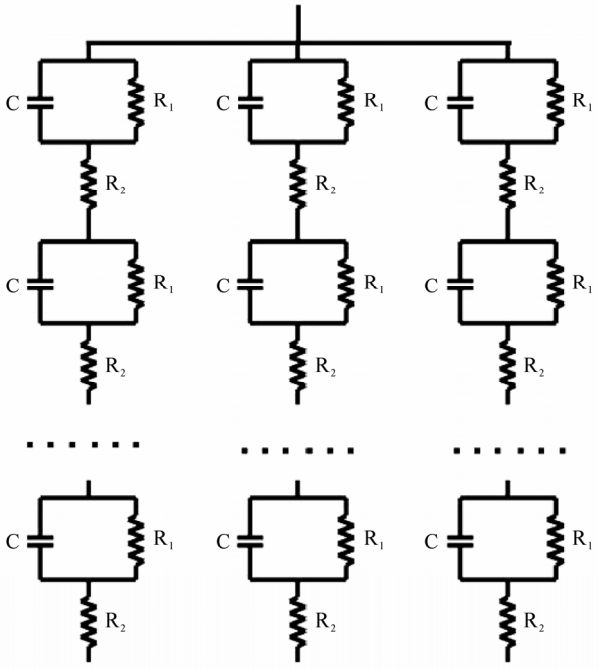

Figure 3. Skin impedance Model C.

3. RESULTS AND SIMULATION

In this section, simulations based on the three skin impedance models discussed in the previous section are presented. In these simulations, a voltage is applied at time 0.1 second and it varies linearly to 5 V at time 0.5 second.

3.1. Simulation Based on Model A

Several simulations have been carried out to examine the characteristics of the responses that may be obtained based on different parameter values. For the purpose of simulation, R_1 and R_2 have been assigned a value of 100 kΩ cm^2 and three different values of the capacitor have been used. Below are the results from the simulation:

It can be seen from the simulation that as the voltage is increased from 0.1 second to 0.5 second, the current passes through the capacitor C of Model A. At 0.5 second, the applied voltage has already reached the final value, and the current passes through R_1 and R_2.

For all the three simulations, the final steady-state current depends on the value of the two resistors. As shown in **Figures 4** to **6**, the value of the capacitor can have considerable effect on the shape of the response.

3.2. Simulation Based on Model B

In the first simulation of Model B, we will examine the response from Level 1. The capacitance value is 0.1 μF cm^2.

Figure 8 gives the current for Model B having only three sections (Level 1). This would model after three epidermal skin layers at different depths of the skin.

Figure 9 gives the current for Model B having six sections (Level 2). More sections (or skin layers) can be included for further study, but in this paper, we show the simulations of only Level 1 and 2. As shown in **Figures 8** and **10**, the current can have very different response at different point of the circuit model. In both cases, the current would settle down to its steady-state level very quickly after the voltage has been steady at 0.5 second.

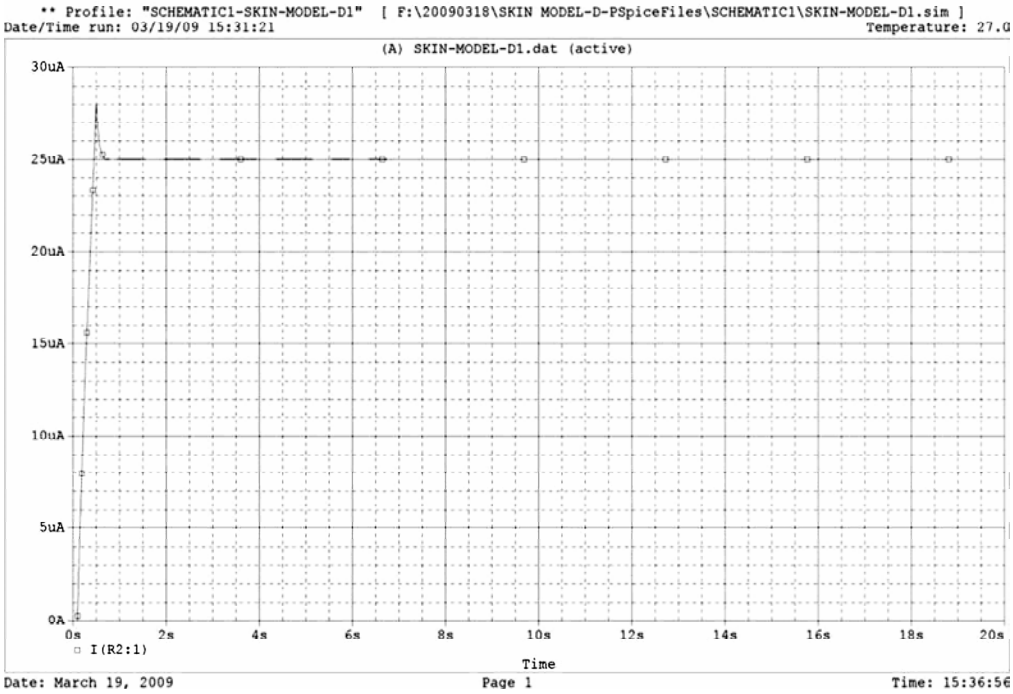

Figure 4. Model A with capacitor value 1 μF cm^2.

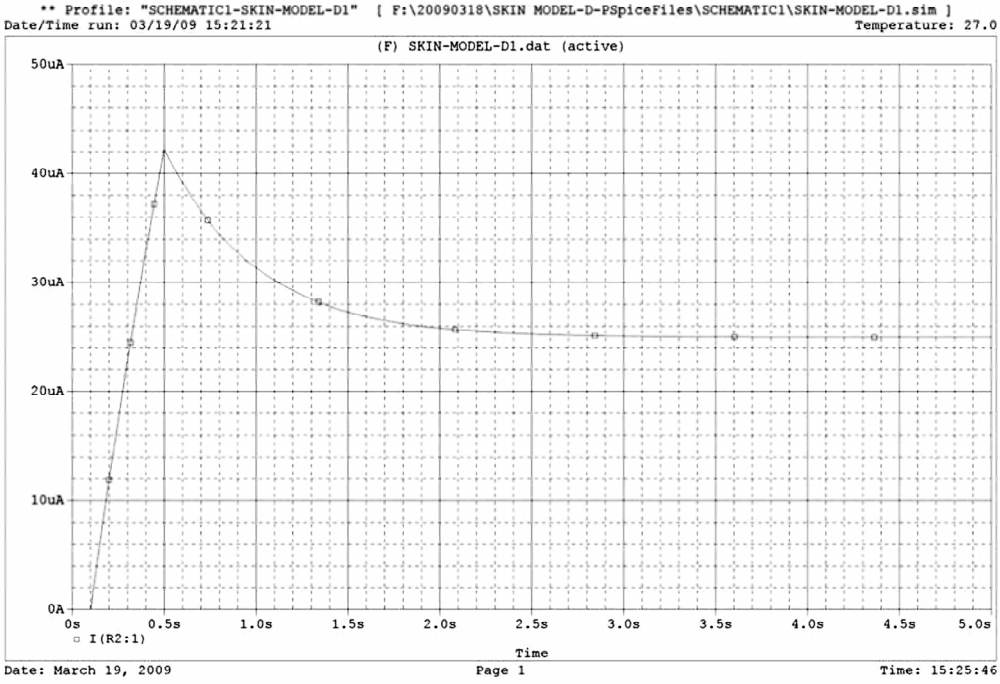

Figure 5. Model A with capacitor value 10 μF cm^2.

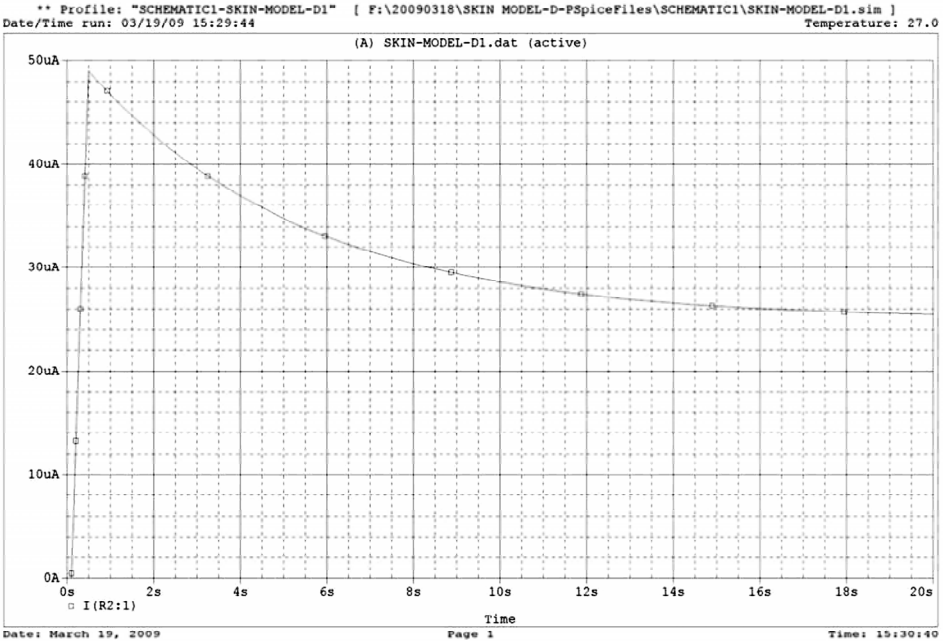

Figure 6. Model A with capacitor value 100 μF cm^2.

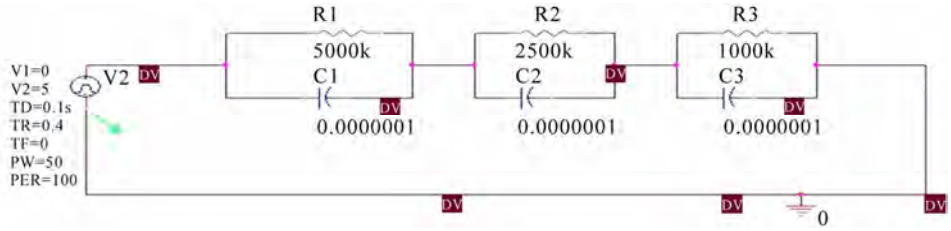

Figure 7. Level 1 of Model B.

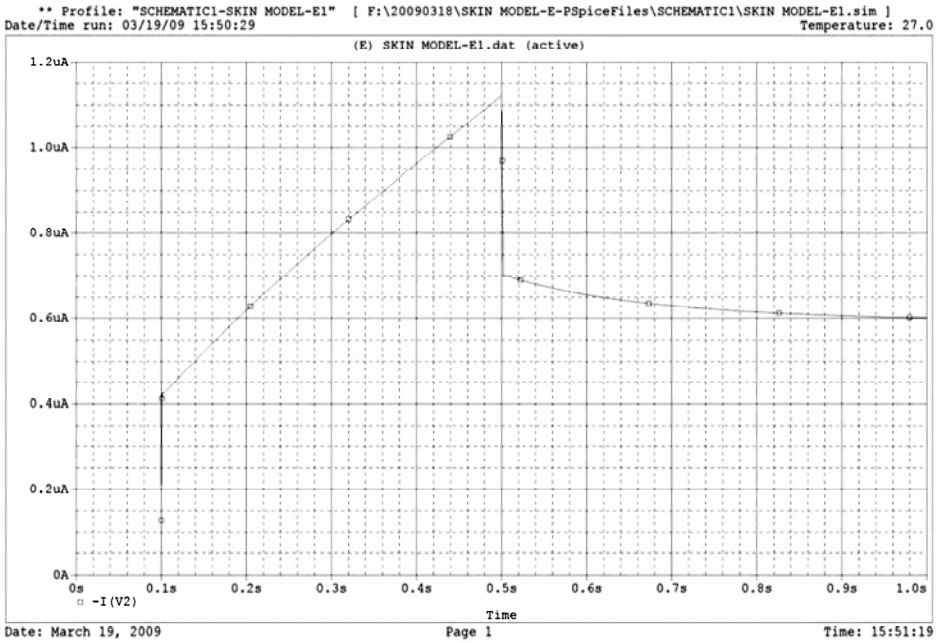

Figure 8. Model B level 1 with capacitor value 0.1 μF cm^2.

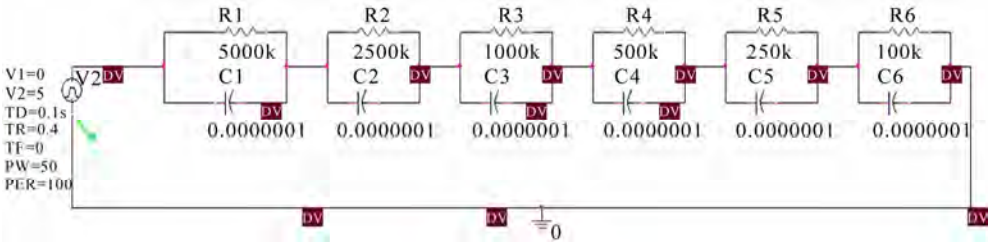

Figure 9. Level 2 of Model B.

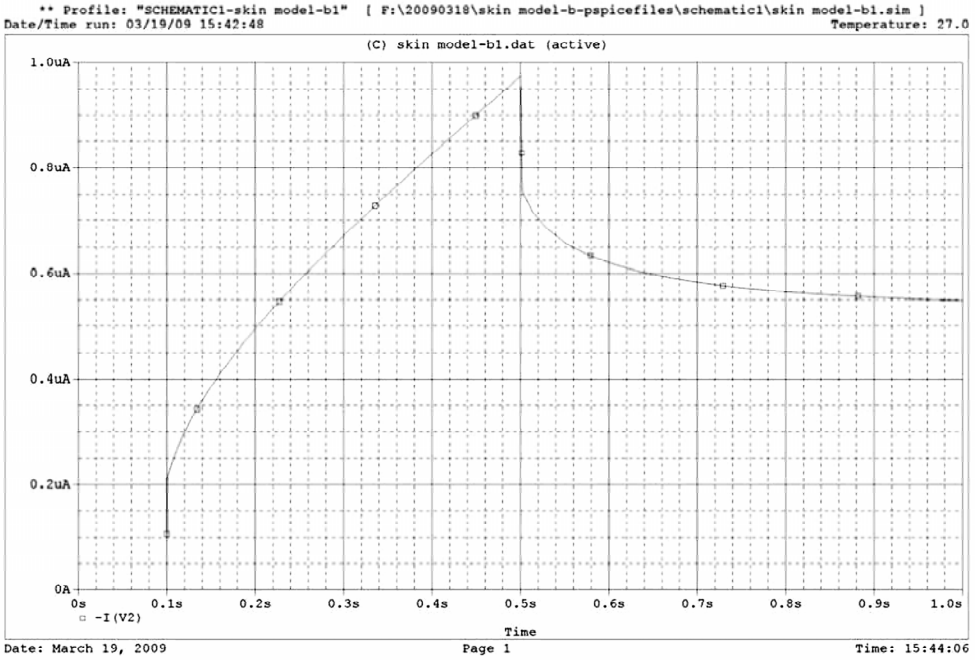

Figure 10. Model B level 2 with capacitor value 0.1 μF cm^2.

3.3. Simulation Based on Model C

In **Figure 11**, Model C with three parallel paths is shown. Each path is consisted of three sub-sections.

Figures 12 and **15** are similar in shape but differ in its vertical scale. Hence, although these two results are based on different circuit models (3 sub-section and 6 sub-section model), similar response shapes are obtained with the use of different capacitor values. The vertical scales can be aligned with a careful choice of the resistor values.

4. CONCLUSIONS

The three-element circuit of Model A is a very simple model of the skin impedance. Considering the different characteristics to the different layer of the epidermis, the model seems not too accurate in its representation. The Model B by Tregear captures the effects of capacitance for the different layers of the epidermis. However, it is not clear how many stages should best represent the skin

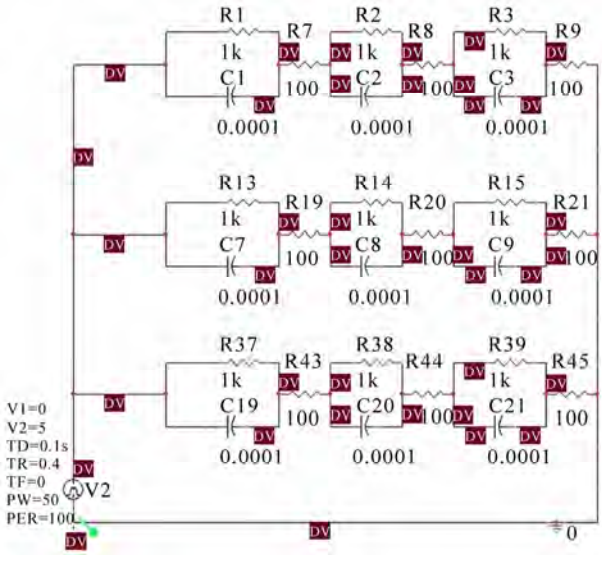

Figure 11. Model C with three parallel paths, each with three sub-sections.

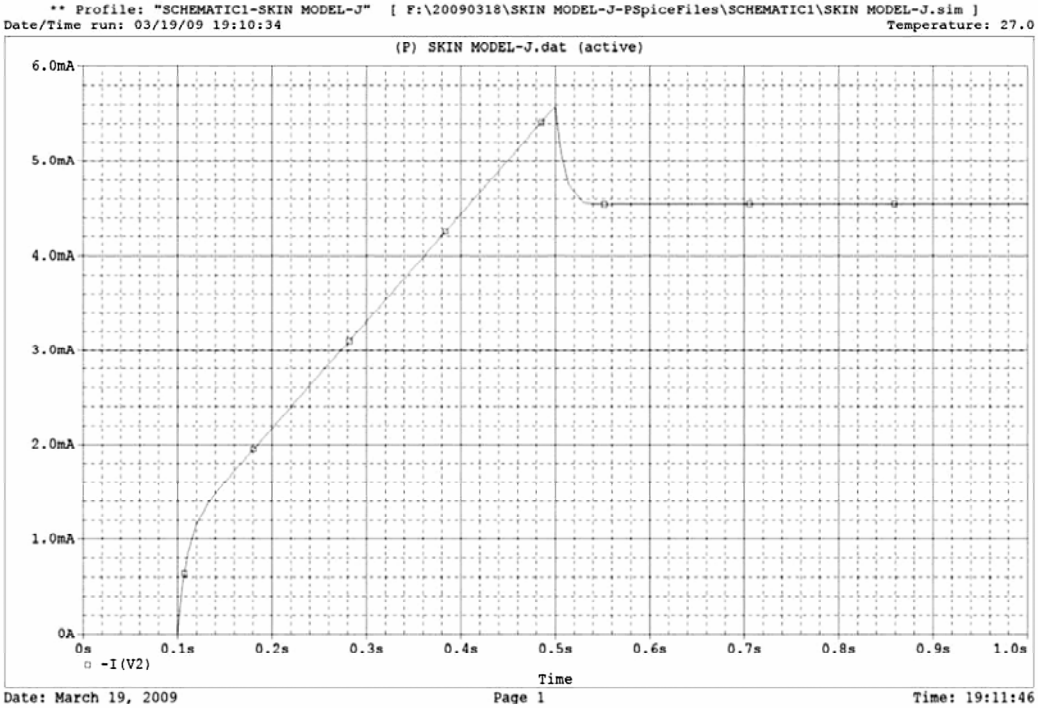

Figure 12. Simulation result of Model C with three parallel paths, each with three sub-sections, with capacitor value 100 μF cm^2, R_1 = 1000 Ω cm^2, R_2 = 100 Ω cm^2.

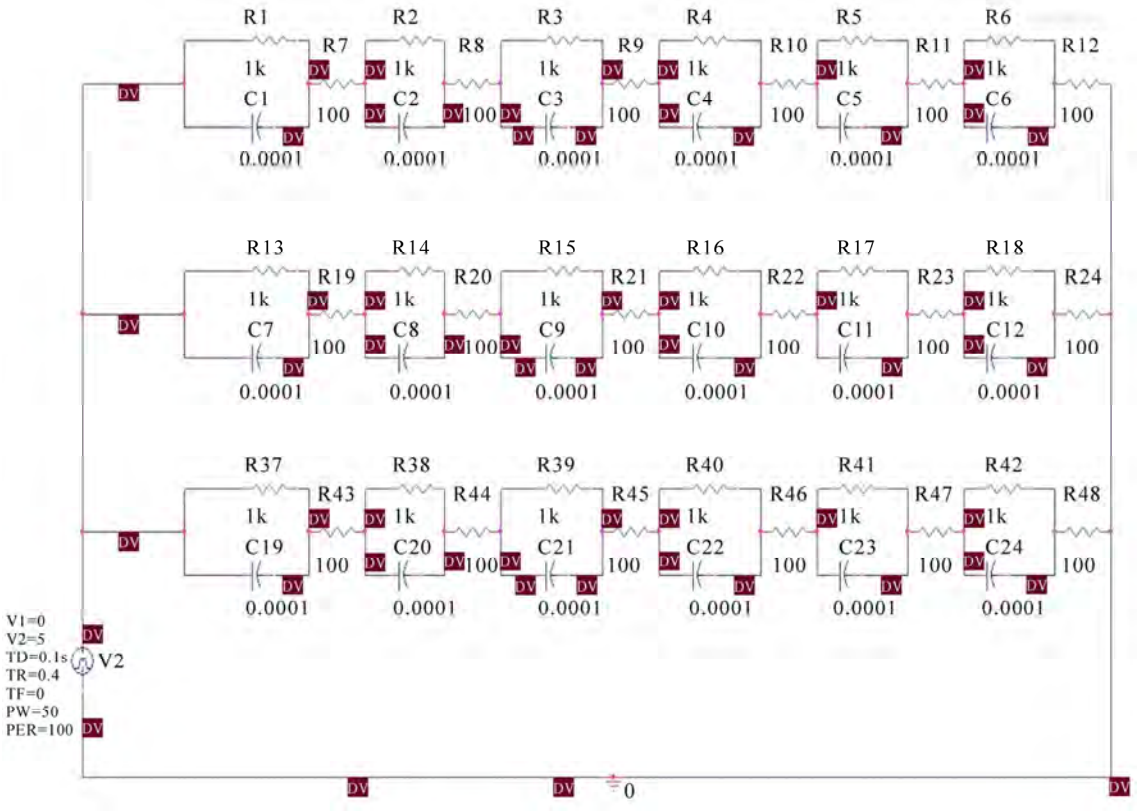

Figure 13. Model C with three parallel paths, each with six sub-sections.

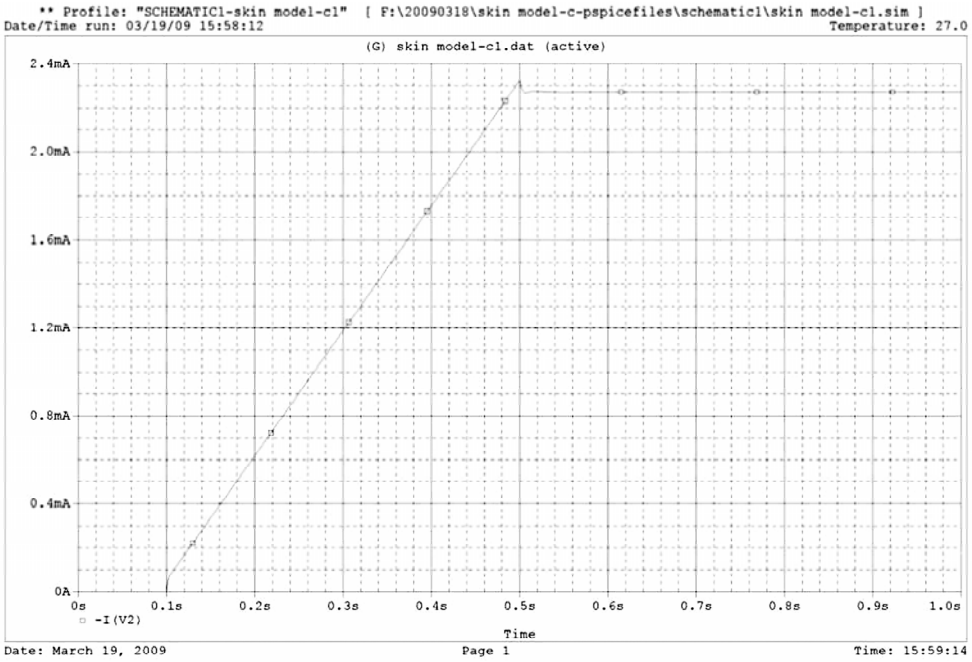

Figure 14. Simulation result of Model C with three parallel paths, each with six sub-sections, with capacitor value 10 μF cm^2, R_1 = 1000 Ω cm^2, R_2 = 100 Ω cm^2.

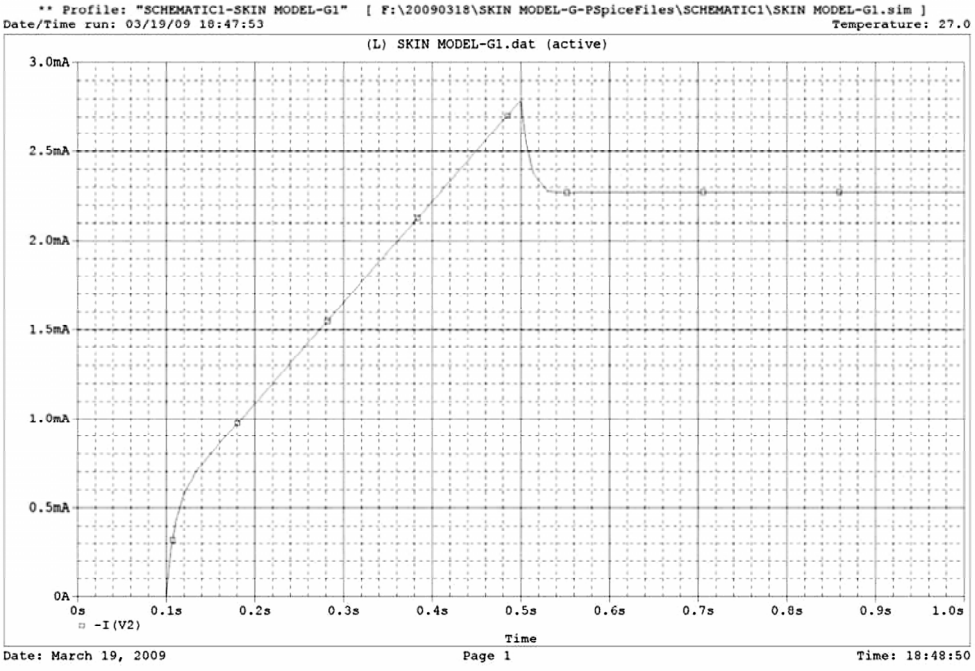

Figure 15. Simulation result of Model C with three parallel paths, each with six sub-sections, with capacitor value 100 μF cm^2, R_1 = 1000 Ω cm^2, R_2 = 100 Ω cm^2.

impedance for a certain depth of the epidermis. The Model C by Lykken has added another resistance in between the different stage, which is used to represent deep tissue resistance. This would provide a more complete model to the skin impedance. Yet, the great variability of the parameters in the model exists and experimentally study is needed for a more complete understanding of the impedance characteristics of the

skin.

5. ACKNOWLEDGEMENTS

This research is supported by a Small Project Funding grant (10400021) by the Committee on Research and Conference Grants of The University of Hong Kong.

REFERENCES

[1] Stoebar, B. and Liepmann, D. (2005) Array of hollow out-of-plane microneedles for drug delivery. *Journal of MEMS*, **14(3)**, 474-479.

[2] Ji, J., Tay, F.E.H., Miao, J. and Iliescu, C. (2006) Microfabricated microneedles with porous tip for drug delivery. *Journal of Micromechanics and Microengineering*, **16**, 958-964.

[3] Lam, D.C.C., Lee, Y.H., Shek, K.T. and Pang, G. (2008) Puncture depth and the mechanical stability of microneedles. *International Joint Conference on Biomedical Engineering Systems and Technologies*, **2**, 291-296.

[4] Coston, A.F. and Li, J.K.-J. (2001) Iontophoresis: Modelling, methodology, and evaluation. *Cardiovascular Engineering*, **1**, 127-136.

[5] Coston, A.F. and Li, J.K.-J. (2003) Transdermal drug delivery: A comparative analysis of skin impedance models and parameters. *Proceedings of IEEE Engineering in Medicine and Biology*, **3**, 2982-2985.

[6] Lawler, J.C., Davis, M.J. and Griffith, E.C. (1960) Electrical characteristics of the skin: The impedance of the surface sheath and deep tissues. *Journal of Investigative Dermatology*, **34**, 301-308.

[7] Edelberg, R. (1971) Electrical properties of skin. In Elden, H.R. Ed., Biophysical properties of the skin, John Wiley & Sons, Inc, New York.

[8] Tregear, R.T. (1966) Physical functions of the skin. Academic Press, New York.

[9] Lykken, D.T. (1970) Square-wave analysis of skin impedance. *Psychophysiology*, **7(2)**, 262-275.

J. Biomedical Science and Engineering, 2010, 3, 375-379 **JBiSE**
doi:10.4236/jbise.2010.34052 Published Online April 2010 (http://www.SciRP.org/journal/jbise/).

Heart pacemaker wear life model based on frequent properties and life distribution*

Qiao-Ling Tong[1], Xue-Cheng Zou[1], Jin Tang[2], Heng-Qing Tong[2]

[1]Department of Electronic Science & Technology, Huazhong University of Science & Technology, Wuhan, China;
[2]Department of Mathematics, Wuhan University of Technology, Wuhan, China.
Email: qltong@gmail.com

Received 4 January 2010; revised 20 January 2010; accepted 25 January 2010.

ABSTRACT

The lifetime of heart pacemaker is important for patient and researcher. To forecast the lifetime of heart pacemakers we must determine its distribution regularity. In this paper, a heart pacemaker wear life model is introduced by using frequency property, and a life distribution is presented. The parametric properties of the density are studied. The moment estimator with negative order is used, which is just the maximum likelihood estimator. A new method of parameter estimate, *F* estimate of parameter, is proposed. This method is suitable to both truncated samples and complete samples, whether or not the distribution can be transformed into a standard distribution without any parameters.

Keywords: Heart Pacemaker Life Distribution; Frequency; Negative Order Moment Estimator; Maximum Likelihood Estimate; *F* Estimate

1. INTRODUCTION

The heart pacemakers (HPM) have more and more extensive clinical applications. Almost all users of HPM worry the lifetime of HPM. If some time his HPM stops work out of the blue, that will be serious trouble. Postponing or advancing to replace or to repair HPM is not suitable. So forecasting the lifetime of heart pacemaker is important for patient and researcher.

Extending HPM lifetime is the significant aim to reduce the cost of cardiac pacing [1]. The factors which impact HPM Life content: "innate" factors and "acquired" factors (such as electromagnetic fields, drugs, etc.) [2], but the former is more important. The innate factors include many aspects which will be introduced as follows. The battery capacity is decided by battery energy and battery cubage. For the same functional circuit, increasing battery capacity will enhance its capacity, decrease pacing power and prolong the HPM life. Internal faradic current is a significant, independent factors related to battery life. Low internal faradic current is an important role to save battery life [2,3]. Although there is a little literature to introduce the relativity between internal faradic current and battery life, some scholars for this study think that internal faradic current has a major impact on HPM life and maybe is greater than the battery capacity and output energy. Markewitz, etc. [3] found that decreasing the internal faradic current consumption enables to reduce overall current consumption of HPM and gain a longer life, which approves that the internal faradic current is a foremost factor of influencing HPM life. Pacing frequency also has a marked influence on HPM life, and its level of energy consumption is proportional to the HPM. HPM electrode function is the weakest link in the system, which is also the most important factors to determine the security and life of HPM system [4]. After the HPM pulse generator (Pulse generator, PG) was designed, the battery capacity and current consumption has been identified and remain constant. Improving the wire electrode function is the only way to prolong HPM lifetime. Electrodes have many factors which will affect the HPM life. According to Ohm's law, the high impedance (> 1000 ohm) can reduce the loss current, increasing the HPM life.

Lead is also necessary. The main function of electrode lead is transmitting electricity, but its mechanism capability is important for assuring the life of pacemaker. The capability mostly lies on the material of insulating surface. Silica gel may be the best choice, which has been used over past 30 years. The resistance of lead rest with its length. The length of electrode with double pole is two times compared with unipolar one. In the theory, electrode with double pole uses more energy. Inductive circuit and pacing with multi-cavity or double cavity wastes more energy than single cavity and inductive circuit.

In this paper, a new heart pacemaker life distribution is presented according to relative influence factors. The

*The research was supported by the National Natural Science Foundation of China (30570611, 60773210).

heart pacemaker may be worn or damaged after working for a long time, therefore, its vibration and frequency may be changed. The frequency of a heart pacemaker can be recorded by a frequency record meter. The heart pacemaker life and its reliability can be investigated by the analysis of the heart pacemaker frequency.

Let $A_i^+ \ i=1,\cdots,n$ be the amplitude values of the frequency of a normal heart pacemaker, $A_i \ i=1,\cdots,n$ be that of the damaged heart pacemaker. We define the frequency parameter k:

$$k=\frac{1}{n-1}\sum_{i=1}^{n}\frac{A_i}{A_i^+} \tag{1}$$

Experiments have shown that we can deduce the level of the wear or the damage of a heart pacemaker according to the analysis of the frequency parameter k. When $k>k_{\max}$, the heart pacemaker can not work normally. The value of the frequency parameter increases as the work time of a heart pacemaker increases. In general, we suppose $k=rt$, then, we will get $t=\frac{k}{r}$, where r denotes the change rate of k. It may be affected by many independent little factors such as capability of battery, the function of electrode, lead, material and so on. We suppose that r is a random variable with normal distribution with definition $r>0$:

$$f_r(r)=\frac{C}{\sqrt{2\pi}\sigma}\exp\left(-\frac{(r-\bar{r})^2}{2\sigma^2}\right),\qquad r>0 \tag{2}$$

From $\int f_r(r)dr=1$, we know $C=\frac{1}{\phi(\bar{r}/\sigma)}$, where ϕ is the distribution function of standard normal.

Let t be the heart pacemaker wear life, $T=k_{\max}/r$, then t is also a random variable. The density function of heart pacemaker wear life distribution is

$$f(r)=\frac{C}{\phi(\bar{r}/\sigma)\sqrt{2\pi}\sigma t^2}\exp\left(-\frac{(k-\bar{r}t)^2}{2\sigma^2t^2}\right),\qquad r>0 \tag{3}$$

When $k=k_{\max}$, its distribution function is

$$F(t)=\frac{1-\Phi\left(k/(\sigma t)-\bar{r}/\sigma\right)}{\Phi(\bar{r}/\sigma)} \tag{4}$$

Now, we particularly investigate statistical property of heart pacemaker wear life distribution. First, we see the graph of $f(t)$. Put $t\to 0^+$, then $f(t)\to 0^+$, because $t^2\exp\left(-\frac{(k/(\sigma t)-\mu/\sigma)^2}{2}\right)\to+\infty$, put $t\to+\infty$, $f(t)\to 0^+$. Differentiate $f(t)$, then

$$f'(t)=f(t)\left[-\frac{2}{t}+\frac{k(k/t-\bar{r})}{t^2\sigma^2}\right] \tag{5}$$

The solution of equation $f'(t)=0$ is

$$t=\frac{k}{4\sigma^2}\left(-\bar{r}\pm\sqrt{\bar{r}^2+8\sigma^2}\right) \tag{6}$$

Second, we see the change of failure rate λ.

$$\lambda(t)=\frac{f(t)}{1-F(t)}$$

$$=\frac{k\phi(\bar{r}/\sigma)}{\phi(\bar{r}/\sigma)\sqrt{2\pi}\sigma t^2}\times\frac{\exp\left(-(k/t-\bar{r})^2/(2\sigma^2)\right)}{\left[\phi(\bar{r}/\sigma)-1+\phi(k/t\sigma)-\bar{r}/\sigma\right]} \tag{7}$$

Let

$$g(t)=t^2\exp\left(\frac{1}{2\sigma^2}\left(\frac{k}{t}-\bar{r}\right)^2\right)\left[\phi\left(\frac{\bar{r}}{\sigma}\right)-1+\phi\left(\frac{k}{t\sigma}-\frac{\bar{r}}{\sigma}\right)\right] \tag{8}$$

then $\lambda(t)=c/g(t)$, where c is a constant. Because

$$\lim_{t\to 0^+}g(t)=+\infty \tag{9}$$

and

$$\lim_{t\to+\infty}g(t)=\exp\left(\frac{\bar{r}^2}{2\sigma^2}\right)\times\lim_{t\to+\infty}\frac{\phi(\bar{r}/\sigma)-1+\phi(k/t\sigma-\bar{r}/\sigma)}{t^{-2}}$$

$$=\exp\left(\frac{\bar{r}^2}{2\sigma^2}\right)\times\lim_{t\to+\infty}\left[\frac{kt}{2\sqrt{2\pi}\sigma}\exp\left(-\frac{1}{2}\left(\frac{k}{t\sigma}-\frac{\bar{r}}{\sigma}\right)^2\right)\right]$$

$$=+\infty$$

We have $\lim_{t\to 0^+}\lambda(t)=\lim_{t\to\infty}\lambda(t)=0$. The graph of $\lambda(t)$ is also located on the first quadrate. Its left limit is origin and its right asymptotic line is t axis.

2. MOMENT ESTIMATE WITH NEGATIVE ORDER FOR COMPLETE SAMPLE

When we investigate the parameter estimate of the density function $f(t)$ of heart pacemaker wear life distribution, we notice that it has two independent parameters only. Let $a=k/\sigma$, $b=\bar{r}/\sigma$, then the density function of heart pacemaker wear life distribution is

$$f(t)=\frac{a}{\sqrt{2\pi}\Phi(b)t^2}\exp\left(-\frac{1}{2}\left(\frac{a}{t}-b\right)^2\right),\quad t>0 \tag{10}$$

In **Eq.3**, $f(t)$ has three parameters $k,\sigma,\bar{r}$. They are independent in the physical process, but they are dependent in the density function. We can estimate a,b

from **Eq.10**. We need to estimate k in addition, then we can estimate $\sigma, \bar{r}$.

First, we consider moment estimator. For common moment estimator $E(t^j), j=1,2,\cdots$, we can not calculate its integration. If we make use of moment estimator with negative order $E(t^j), j=-1,-2,\cdots$, the integration can be calculated easily.

$$\begin{aligned} ET^{-1} &= \int_0^{+\infty}\left[\frac{a}{\sqrt{2\pi}\Phi(b)t^3}\exp\left(-\frac{1}{2}\left(\frac{a}{t}-b\right)^2\right)\right]dt \\ &= \frac{1}{a\Phi(b)}\int_0^{+\infty}\left[(y+b)\frac{1}{\sqrt{2\pi}}\exp\left(-\frac{1}{2}y^2\right)\right]dy \\ &= \frac{b}{a}+\frac{1}{\sqrt{2\pi}a\Phi(b)}\exp\left(-\frac{1}{2}b^2\right) \end{aligned} \quad (11)$$

$$\left(y=\frac{a}{t}-b\right)$$

$$\begin{aligned} ET^{-2} &= \int_0^{+\infty}\left[\frac{a}{\sqrt{2\pi}\Phi(b)t^4}\exp\left(-\frac{1}{2}\left(\frac{a}{t}-b\right)^2\right)\right]dt \\ &= \frac{1}{a^3\Phi(b)}\int_{-b}^{+\infty}\left[(y+b)^2\frac{1}{\sqrt{2\pi}}\exp\left(-\frac{1}{2}y^2\right)\right]dy \\ &= \frac{b^2+1}{a}+\frac{b}{\sqrt{2\pi}a^2\Phi(b)}\exp\left(-\frac{1}{2}b^2\right) \end{aligned} \quad (12)$$

Let $t_1,\cdots,t_n$ be i.i.d. sample data of the heart pacemaker wear life. We make use of the sample moment to estimate the population moment. The difference is the sign of the order of moment. From the system of equations

$$\begin{aligned} s_1 &= \frac{1}{n}\sum_{i=1}^n\frac{1}{t_i} = \frac{b}{a}+\frac{1}{\sqrt{2\pi}a\Phi(b)}\exp\left(-\frac{1}{2}b^2\right) \\ s_1 &= \frac{1}{n}\sum_{i=1}^n\frac{1}{t_i^2} = \frac{b^2+1}{a}+\frac{1}{\sqrt{2\pi}a^2\Phi(b)}\exp\left(-\frac{1}{2}b^2\right) \end{aligned} \quad (13)$$

we have

$$\begin{cases} b=\dfrac{1}{s_1}\left(as_2-\dfrac{1}{a}\right) \\ a=\dfrac{1}{s_1}\left[b+\dfrac{1}{\sqrt{2\pi}a\Phi(b)}\exp\left(-\dfrac{1}{2}b^2\right)\right] \end{cases} \quad (14)$$

Moreover we can obtain the solution $\hat{a}$ and $\hat{b}$ from **Eq.14**. They are the moment estimate of a and b.

Second, we consider the maximum likelihood estimator of parameters. The likelihood function is

$$L(a,b)=\left(\frac{a}{\sqrt{2\pi}\Phi(b)}\right)^n\frac{1}{\prod_{i=1}^n t_i^2}\exp\left(-\frac{1}{2}\left(\frac{a}{t_i}-b\right)^2\right) \quad (15)$$

Taking derivation of $L(a,b)$, we have

$$\begin{aligned} \frac{\partial L}{\partial a} &= n\left(\frac{a}{\sqrt{2\pi}\Phi(b)}\right)^{n-1}\frac{1}{\sqrt{2\pi}\Phi(b)}\frac{1}{\prod_{i=1}^n t_i^2}\exp\left(-\frac{1}{2}\sum_{i=1}^n\left(\frac{a}{t_i}-b\right)^2\right) \\ &+\left(\frac{a}{\sqrt{2\pi}\Phi(b)}\right)^n\frac{1}{\prod_{i=1}^n t_i^2}\exp\left(-\frac{1}{2}\sum_{i=1}^n\left(\frac{a}{t_i}-b\right)^2\right)\times\left[-\sum_{i=1}^n\left(\frac{a}{t_i}-b\right)^2\frac{1}{t_i}\right] \\ &=0 \end{aligned} \quad (16)$$

and

$$\begin{aligned} \frac{\partial L}{\partial b} &= n\left(\frac{a}{\sqrt{2\pi}\Phi(b)}\right)^{n-1}\frac{a\Phi'(b)}{\sqrt{2\pi}\Phi(b)}\frac{1}{\prod_{i=1}^n t_i^2}\exp\left(-\frac{1}{2}\sum_{i=1}^n\left(\frac{a}{t_i}-b\right)^2\right) \\ &+\left(\frac{a}{\sqrt{2\pi}\Phi(b)}\right)^n\frac{1}{\prod_{i=1}^n t_i^2}\exp\left(-\frac{1}{2}\sum_{i=1}^n\left(\frac{a}{t_i}-b\right)^2\right)\times\left[-\sum_{i=1}^n\left(\frac{a}{t_i}-b\right)^2\right] \\ &=0 \end{aligned} \quad (17)$$

Simplifying **Eq.16** and **Eq.17**, we have

$$\begin{cases} a^2s_2-abs_1=1 \quad\Leftrightarrow\quad b=\dfrac{1}{s_1}\left(as_2-\dfrac{1}{a}\right) \\ s_1a=b+\dfrac{\Phi'(b)}{\Phi(b)} \quad\Leftrightarrow\quad a=\dfrac{1}{s_1}\left[b+\dfrac{e^{\left(-\frac{1}{2}b^2\right)}}{\sqrt{2\pi}a\Phi(b)}\right] \end{cases} \quad (18)$$

Noting that **Eq.18** is just **Eq.19**, we know that the moment estimator with negative order of heart pacemaker wear life distribution is just its maximum likelihood estimator. It is more reasonable to take the moment estimator with negative order for heart pacemaker wear life distribution.

3. PARAMETER ESTIMATE FOR TRUNCATED TESTING

Life testing is often truncated by the given size of samples, because the time and the cost of testing are limited. Suppose n products are taken as life testing. We have observed m products which have been failures. $t_1 \le t_2 \le \cdots \le t_m$ are m preceding order statistics of products life. For exponential distribution, Weibull distribution, normal and lognormal distribution, we can give parameter estimator in truncated testing. These distributions can be transformed into standard distributions without any parameter. According to the order statistic of the standard distribution, we can compute its expectation, variance and covariance. Then, we can obtain the Best Linear Unbiased Estimation by the least square method. But we can not do it in this way for heart pacemaker wear life distribution. The reason is it can not be transformed into any standard distribution without any parameter. The maximum likelihood esti-

mate of heart pacemaker wear life distribution from the order statistics of the truncated samples is not certain to converge, because its density function does not satisfy some of the convergency conditions.

In this paper, a new statistical method, F estimate of parameter, is proposed. It is suitable to any distribution whether or not it can be transformed into a standard distribution. What is more, it has no definition of sample size. We can consider the problem in this way. For the lives of n products in life testing, we have observed m preceding lives of products. We have not observed $n-m$ late lives of products but they are existent. For the empirical distribution function of life t, we have observed $F_n(t_1)=1/n,\cdots,F_n(t_m)=m/n$. We have not observed the late values, but they also exist. From Glivenko-Cantelli Theorem, we know that empirical distribution function of random variable with probability one converges to its distribution function uniformly. That is,

$$P\left\{\lim_{n\to\infty}\left(\sup_{-\infty<t<+\infty}\left|F_n(t)-F(t)\right|\right)=0\right\}=1 \tag{19}$$

Therefore we can obtain m approximate equations $F_n(t_i)=F(t_i), i=1,\cdots,m$, *i.e.*,

$$\begin{cases} F(t_i)=\dfrac{1}{n} \\ F(t_2)=\dfrac{2}{n} \\ \cdots\cdots \\ F(t_m)=\dfrac{m}{n} \end{cases} \tag{20}$$

The parameters to be estimated are contained in the system of **Eq.20**. The problem is changed into solving a nonlinear regression model. Solving the model by the least square method, we can obtain the parameters to be estimated. We call it F estimate of parameter. Obviously, this method is reliable in theory, simple in computation and extensive in application.

From [5], we know that heart pacemaker wear life distribution is

$$F(t)=\frac{1-\Phi\left(\dfrac{a}{t}-b\right)}{\Phi(b)} \tag{21}$$

The regression equations are

$$\frac{1-\Phi\left(\dfrac{a}{t_i}-b\right)}{\Phi(b)}=\frac{i}{n},\quad i=1,\cdots,m \tag{22}$$

Making use of the least square method, we need to seek the minimum by changing parameters a,b:

$$Q(a,b)=\sum_{i=1}^{m}\left(\frac{1-\Phi\left(\dfrac{a}{t_i}-b\right)}{\Phi(b)}-\frac{i}{n}\right)^2\to\min \tag{23}$$

Or we solve the following system of equations:

$$\sum_{i=1}^{m}\left\{\left[\frac{1-\Phi\left(\dfrac{a}{t_i}-b\right)}{\Phi(b)}-\frac{i}{n}\right]\frac{1}{t_i}\exp\left(-\frac{1}{2}\left(\frac{a}{t_i}-b\right)^2\right)\right\}=0$$

$$\sum_{i=1}^{m}\left\{\left[\frac{1-\Phi\left(\dfrac{a}{t_i}-b\right)}{\Phi(b)}-\frac{i}{n}\right]\left[\Phi(b)\exp\left(-\frac{1}{2}\left(\frac{a}{t_i}-b\right)^2\right)-\left(1-\Phi\left(\frac{a}{t_i}-b\right)\right)\exp\left(-\frac{1}{2}b^2\right)\right]\right\}=0$$

Of course, this method is also suitable to complete samples, that is $m=n$.

4. COMPUTATION EXAMPLE AND COMPARISON OF PRECISION

In order to investigate the properties of heart pacemaker wear life distribution carefully, and test the new statistical method, F estimate of parameter, we compute examples on a computer. The parameters a,b are given and random numbers are generated and are sequenced in terms of **Eq.10**. Using these data, first we compute the moment estimators with negative order (and also the maximum likelihood estimators) $\hat{a}_m,\hat{b}_m$ based on **Eq.14** or **Eq.18**. Second, we compute the F estimators of parameters $\hat{a}_F,\hat{b}_F$ using **Eq.23**. Third, we take m preceding data and compute the F estimators of parameters $\hat{a}_{F1},\hat{b}_{F1}$ according to **Eq.23** also. Compared them repeatedly by changing sample size m, parameters a,b and truncated number m.

From the results of comparison, we know that it is robust to take absolute value in **Eq.23**.

$$Q(a,b)=\sum_{i=1}^{m}\left|\frac{1-\Phi\left(\dfrac{a}{t_i}-b\right)}{\Phi(b)}-\frac{i}{n}\right|\to\min \tag{24}$$

We take the Powell algorithm improved by Sargent to

compute **Eq.24** and the bisection method to compute **Eq.14**.

When data are small samples, we take sample size $n=20$, truncated number $m=10$, initial parameters $a=0.9$, $b=3.0$. The computed results are in **Table 1**. The random data are generated 5 times and computations are repeated $k=5$ times. When the random data are generated, their seeds are different. First of all, these seeds are generated as random data independently. If it is necessary to calculate a great number of random data, we can change the modules of pseudorandom data yet. Using this method, the repeated number k can be very large. We can calculate the empirical distribution function of the statistics a_m, b_m, a_F and b_F. Therefore, we can draw up the distribution function tables of the statistics for given precision according to Glivenko-Cantelli Theorem. In any case, we are satisfied with the computed results in **Table 1**, because the sample size is so small.

When data are common samples, we take sample size $n=100$, truncated number $m=50$, initial parameters also use $a=9.0$, $b=3.0$. Computed results are in **Table 2**. Of course, they are more accurate and also make us satisfied.

5. CONCLUSIONS

More and more functions are gathered in heart pacemaker. It is used more frequently along with the development ofbiomedical engineering. Extending and forecasting the lifetime of heart pacemaker is very important to user. In this paper, we introduced a heart pacemaker wear life model by making use of the frequency property, and deduced its life distribution. The parametric properties of the distribution density are interesting because its moment estimator with negative order is just its maximum likelihood estimator. We also propose an F estimate of parameter that is suitable to both truncated samples and complete samples. Through computation example and comparison of precision, we can get satisfying results. That means whether or not the distribution can be transformed into a standard distribution without any parameters, we can estimate the parameters in truncated data sample.

Table 1. Computed results with n = 20, m = 10, a = 0.9, b = 3.0.

k	a_m	b_m	a_F	b_F	a_{F1}	b_{F1}
1	9.746	3.403	8.789	3.144	6.541	2.223
2	8.295	2.711	9.853	3.228	6.067	1.804
3	8.298	2.523	7.662	2.394	7.740	2.331
4	10.675	3.712	13.032	4.629	6.980	2.223
5	9.362	3.489	9.930	3.836	6.112	2.223

Table 2. Computed results with n = 100, m = 50, a = 9.0, b = 3.0.

k	a_m	b_m	a_F	b_F	a_{F1}	b_{F1}
1	10.491	3.544	10.504	3.568	11.210	3.823
2	9.787	3.281	9.628	3.223	9.547	3.187
3	9.337	3.086	8.809	2.890	8.127	2.641
4	9.750	3.340	9.502	3.261	7.710	2.485
5	9.417	3.318	8.957	3.152	9.046	3.178

6. ACKNOWLEDGEMENTS

We would like to thank the experts who take their time to check, approve this paper and give us valuable suggestions.

REFERENCES

[1] Oham, O.J. and Danilovic, D. (1997) Improvements in pacemaker energy consumption and functional capability: Four decades of progress. *Pacing and Clinical Electrophysiology*, **20**, 2-9.

[2] Kindermann, M., Schwaab, B., Berg, M. and Fröhlig, G. (2001) Longevity of dual chamber pacemaker: Device and patient related determiants. *Pacing and Clinical Electrophysiology*, **24(5)**, 810-815.

[3] Markewitz, A., Kronski, D., Kammeyer, A., Kaulbach, H., Weinhold, C., Doering, W. and Reichart, B. (1995) Determinants of dual chamber pulse generators longevity. *Pacing and Clinical Electrophysiology*, **18(12)**, 2116-2120.

[4] Crossley, G.H., Jeffrey, A.B., Reynolds, D., William, S., Johnson, W.B., Howard, H. and Lisa, T. (1995) Steroid elution improves the stimulation threshold in an active-fixation atrial permanent pacing lead. *Circulation*, **92(10)**, 2935-2939.

[5] Rao, C.R. (1997) Linear statistical inference and its applications. Wiley & Sons, New York.

J. Biomedical Science and Engineering, 2010, 3, 380-389 **JBiSE**
doi:10.4236/jbise.2010.34053 Published Online April 2010 (http://www.SciRP.org/journal/jbise/).

Pruned fuzzy K-nearest neighbor classifier for beat classification

Muhammad Arif[1], Muhammad Usman Akram[2], Fayyaz-ul-Afsar Amir Minhas[3]

[1]Department of Computer Science and Engineering, Air University, Islamabad, Pakistan;
[2]Software Engineer, Elixir technologies Pakistan (Pvt) Ltd, Islamabad, Pakistan;
[3]Department of Computer and Information Sciences, Pakistan Institute of Engineering and Applied Sciences, Islamabad, Pakistan.
Email: arif@mail.au.edu.pk; usman.akram232@gmail.com; fayyazafsar@gmail.com

Received 18 January 2010; revised 30 January 2010; accepted 7 February 2010.

ABSTRACT

Arrhythmia beat classification is an active area of research in ECG based clinical decision support systems. In this paper, Pruned Fuzzy K-nearest neighbor (PFKNN) classifier is proposed to classify six types of beats present in the MIT-BIH Arrhythmia database. We have tested our classifier on ~ 103100 beats for six beat types present in the database. Fuzzy KNN (FKNN) can be implemented very easily but large number of training examples used for classification can be very time consuming and requires large storage space. Hence, we have proposed a time efficient Arif-Fayyaz pruning algorithm especially suitable for FKNN which can maintain good classification accuracy with appropriate retained ratio of training data. By using Arif-Fayyaz pruning algorithm with Fuzzy KNN, we have achieved a beat classification accuracy of 97% and geometric mean of sensitivity of 94.5% with only 19% of the total training examples. The accuracy and sensitivity is comparable to FKNN when all the training data is used. Principal Component Analysis is used to further reduce the dimension of feature space from eleven to six without compromising the accuracy and sensitivity. PFKNN was found to robust against noise present in the ECG data.

Keywords: Arrhythmia; ECG; K-Nearest Neighbor; Pruning; Fuzzy; Classification

1. INTRODUCTION

Arrhythmias result due to improper pacing of the cardiac muscle or any discrepancy in the electrical conduction network of the heart [1]. Detection of these pathologically significant arrhythmias is an imperative task in the diagnosis of cardiac diseases. Electrocardiograph (ECG) can be used as a non-invasive diagnostic tool for the detection of these disorders. With the development in computing and sensor technology, standalone automated ECG based decision support systems are an active area of research. A clinical decision support system includes ECG acquisition, pre-processing and noise removal (baseline variation, electronic and electromyographic noise etc.), ECG Delineation (for detection and delineation of P, QRS and T waves of ECG), feature extraction and beat classification.

A variety of methods exist in the literature for QRS delineation [2] which rely upon derivative based methods, use of digital filters and filter-banks etc. One of the most promising approaches for QRS detection and delineation has been proposed by Martínez *et al.* [3] as it offers very high detection and delineation accuracy. It uses wavelet domain analysis for performing QRS detection and delineation which is particularly suited to the ECG signal due to the non-stationary nature of the signal.

ECG beat classification, being an integral part of any ECG based automatic decision support system, has been studied by a number of researchers. Different feature extraction methods for beat classification include use of Fourier Transform [4], multi-resolution analysis [5], wavelet transform [6-9], independent component analysis [10], morphological analysis [11] etc. For the purpose of beat classification, literature reports a variety of classifiers such as Backpropagation Neural Networks [8], Learning Vector Quantization and Probabilistic Neural Networks [6], Fuzzy Inference Systems [12], Nearest Neighbor classifiers [13] etc.

In our previous work [9], we have used features extracted from two-level wavelet decomposition of an ECG signal. The wavelet decomposition was performed through algorithm a'trous using the wavelet proposed by Martínez *et al.* [3] for QRS delineation. This wavelet offers inherent noise suppression and eliminates the need of re-evaluation of wavelet coefficients for beat classifi-

cation as these are already obtained during QRS detection and delineation. A simple *K*-nearest neighbor (SKNN) classifier has been employed for the classification of 6 types of beats (Paced Beats (PB), Atrial Premature Beat (APB), Premature Ventricular Contraction (PVC), Normal (N), Left and Right Bundle Branch Blocks (LBBB & RBBB)) to give an accuracy of ~ 99.5% over selected records (23,200 beats only) from the MIT-BIH Arrhythmia database [14] with high noise tolerance and robustness against decrease in the size of the training data set.

Simple K-Nearest Neighbor (SKNN) classifier used in our previous work offers many advantages over other classifiers including simplicity and ease of parallel implementation, adaptability and online learning [15,9]. Moreover, we have demonstrated its high accuracy for beat classification in comparison to other existing approaches. SKNN classifier assigns equal weights to all of the K-nearest neighbors regardless of their distances from the query point. An improvement over the SKNN classifier is the Fuzzy K-Nearest Neighbor classifier (FKNN) [16] which uses concepts from fuzzy logic to assign degree of membership of the given query point to different classes while considering the distance of its *K*-nearest neighbors. Points closer to the query point contribute a larger value to be assigned to the membership function of their corresponding class in comparison to far away neighbors. Class with the highest membership function value is taken as the winner. Fuzzy KNN gives class memberships for a beat to be classified as compared to true or false decision by SKNN. In case of comparable class memberships for winner and runner up classes, a confidence metric can be used on the decision.

Inherent variability of the ECG signal for different individuals, variability over age, amongst different beat classes and within each beat class itself [1] requires large amount of training data for effective training of an ECG beat classification system. Therefore, an instance based classifier like SKNN or FKNN can only be efficient in terms of both time and space complexities while offering high classification accuracy when number of training examples is very large. In such a case, amount of memory required to store the training prototype set and time required for finding the distance or the nearest neighbors of the query point can be tremendous. Solution to this issue is to use a pruning algorithm on the training data removing some data points from the training dataset without greatly affecting classification accuracy. A variety of pruning algorithms exist in the literature. A very good introduction to pruning techniques for instance-based learning algorithms is given in [17]. In this paper, we have proposed a new pruning algorithm that can be integrated in FKNN and pruning time is very small as compared to other pruning methods.

In this paper, we present a beat classification algorithm which inherits its noise robustness from the use of ten wavelet domain features and the instanttaneous RR interval as used in [9]. Use of the same wavelet transform for delineation of the QRS complex through [3] eliminates the need of re-evaluation of wavelet coefficients for beat classification, thus reducing over all time complexity of the system. To reduce the space complexity the dimensionality of the feature space can be reduced using Principal Component Analysis (PCA). A Pruned Fuzzy K-nearest neighbor (PFKNN) classifier is proposed for beat classification. Training data is pruned first and fuzzy decision of this classifier is weighted with respect to a priori probabilities of different classes to handle the class imbalance problem. To further reduce time complexity of PWFKNN, an efficient nearest neighbor search called ATRIA [18] has been used.

2. ARRHYTHMIA BEAT CLASSIFICATION

Architecture of an ECG based clinical decision support system is shown in **Figure 1**. Beat classification module of the system includes feature extraction, normalization of features, dimensionality reduction if applicable and Classification. Details of each of these components are given in detail as under.

2.1. Feature Extraction

For feature extraction, we have used the same wavelet as in [3] with wavelet transform implemented through Algortihm a' trous. The wavelet is taken to be the derivative of a low pass filter which offers inherent noise suppression. This wavelet is given by,

$$\Psi(\Omega) = j\Omega\left(\frac{\sin\left(\frac{\Omega}{4}\right)}{\frac{\Omega}{4}}\right)^4 \quad (1)$$

From the implementation viewpoint, it can be implemented through FIR low pass (*H*) & high pass (*G*) filters whose frequency responses are given by:

$$H\left(e^{jw}\right) = e^{jw}\left(\cos\frac{w}{2}\right)^3 \quad (2)$$

$$G\left(e^{jw}\right) = 4je^{jw}\left(\sin\frac{w}{2}\right) \quad (3)$$

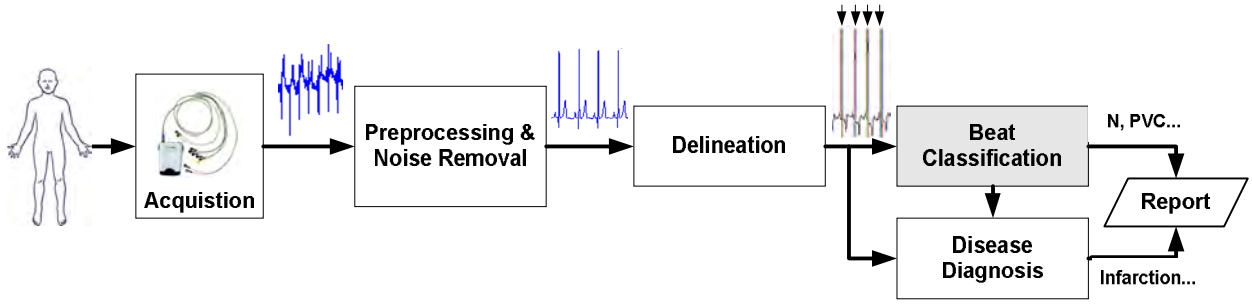

Figure 1. Architecture of a ECG based clinical decision support system.

For details, please refer to [9]. The same wavelet transform can be used for detection and delineation of the QRS complex. For the purpose of beat classification, we have used wavelet coefficients of a 64 point window centered at the QRS fiducial point, only up to scale 2^2. Following eleven features are extracted from the ECG signal:

1) Variance of the original QRS complex signal denoted by s_S^2

2) Variance in each sub-band denoted by s_{A2}^2, s_{D2}^2, s_{D1}^2

3) Variance of the autocorrelation function of wavelet coefficients in each sub-band denoted by $s_{R(A2)}^2$, $s_{R(D2)}^2$, $s_{R(D1)}^2$

4) Ratio of minimum to maximum wavelet coefficient in each sub-band denoted by r_{A2}, r_{D2}, r_{D1}

These features are combined with the instantaneous RR interval to produce a feature set given by $\left\{s_S^2, s_{D1}^2, s_{R(D1)}^2, r_{D1}, s_{D2}^2, s_{R(D2)}^2, r_{D2}, s_{A2}^2, s_{R(A2)}^2, r_{A2}, RR\right\}$ for a single beat.

2.2. Normalization

A normalization process is necessary to standardize all features to the same level. Tangent sigmoid function is used for the normalization as given below,

$$x_{ij}^{'} = \text{tansig}\left(\frac{x_{ij} - \bar{x}_j}{s_{x_j}}\right) \tag{2}$$

where $\bar{x}_j$ and s_{x_j} are the mean and the variance of the j^{th} component of the feature vector. This function will normalize the range of features to [–1,1]. The normalized feature set for the k^{th} beat is denoted by F_1^k.

2.3. Dimensionality Reduction

Features extracted from a beat except the RR interval are subjected to Principal Component Analysis (PCA) for dimension reduction. RR interval is treated separately because of its temporal nature. A covariance matrix is formed on the basis of the first ten features and its eigen-values and eigen-vectors are computed. Five of the ten eigen-vectors corresponding to the highest eigen-values are retained as they capture about 98% of energy in the features [9]. Input data is then projected onto these bases and normalized RR interval values are appended to the projected feature set that result in a 6 dimensional feature space.

2.4. Pruned Fuzzy K-Nearest Neighbor Classifier (PFKNN)

Consider a training set T and class label of a point x in the training set is denoted by $c(x)$. Fuzzy K-Nearest Neighbor search is used in training and classification of PFKNN. It is explained as follows.

2.4.1. Fuzzy K-Nearest Neighbor Search

Fuzzy KNN search is similar to simple KNN search. In simple KNN, every data point can belong to only one class which is the majority class in the K-nearest neighbor search. Whereas in fuzzy KNN, a data point can belong to multiple classes with different membership functions associated to these classes. Fuzzy KNN is described as follows,

Step 1: Find K nearest neighbor x_j, $j = 1...K$ of the given query point x using Euclidean distance from a set of stored data points using Fast nearest neighbor search through ATRIA [18].

Step 2: Evaluate the membership function value of each of the N_c classes (c_i, $i = 1... N_c$) using the following relation.

$$m_{c_i}(x) = \frac{\sum_{j=1}^{K} m_{c_i}(x_j) d_j^{-2/(m-1)}}{\sum_{j=1}^{K} d_j^{-2/(m-1)}} \tag{5}$$

where $d_j = \|x - x_j\|$ is the Euclidean Distance between x and x_j and $m_{c_i}(x_j)$ is the membership value of the point x_j for class c_i. These membership values are calculated from the stored data points. For each point, x_p, in the training set membership values for each class

are as follows,

$$m_{c_i}(x_p) = \begin{cases} 0.51 + 0.49\dfrac{k_i}{K} & if\ c(x_p) = c_i \\ 0.49\dfrac{k_i}{K} & else \end{cases} \quad (6)$$

where k_i is the number of points from the original training set among the K nearest neighbors of x_p that belong to the same class as x_p itself.

The parameter m is used to control the effective magnitude of distance of the prototype neighbors from the query point and it can be selected through cross validation along with K. If m is taken to be infinity then the classifier reduces to a SKNN classifier.

Step 3: The class label of the query point x, $c(x)$, is chosen as follows:

$$c_o(x) = \arg\max_i \left(m_{c_i}(x)\right) \quad (7)$$

2.4.2. Proposed Pruning Method

It involves pruning of the training data set T to obtain the prototype set P. Following steps explain our proposed **Arif-Fayyaz Pruning Algorithm**.

Step 1: Start with an empty prototype set, $P = f$ and training set T.

Step 2: Find K-Nearest Neighbors, x_j, j = 1...K, of each training point, x, such that $c(x_j) \neq c(x)$ and add them to the prototype set P. This gives us the border points of different clusters in the data.

Step 3: Classify each training point using the prototype set P through FKNN explained in Subsection 3.1. If the training point is misclassified, add it to the prototype set P and re-evaluate class weights and membership values of prototype set P. This is done in order to accommodate any clusters which may have been missed in Step 2.

Step 4: For each i^{th} class in the training set, Initialize a set $W(i)$, i = 1, 2,..., N^c_{Pruned}, where N^c_{Pruned} is the number of prototypes in P for i^{th} class. For each training point in the class, find the winner from the pruned set of same class. After all the training points are finished, remove the entire prototype from set P whose $W(i)$ is an empty set.

The prototype set P obtained after Step 4 will be a pruned set of prototypes obtained from the training set T. In the next step, class weights are calculated to deal with the data imbalance problem.

Incremental Policy in the Pruned Set using Arif-Fayyaz Pruning Method

Once pruned prototype is set for a certain training data points, it is very easy and efficient to include any new data points available in the later time without effecting already pruned prototype set. New training data point can become member of pruned prototype set if it is misclassified with the existing pruned prototype set.

2.4.3. Classification Using PFKNN

Classification involves calculation of the membership function values of an unknown query point using FKNN from the stored prototype training data set P obtained after pruning and assigning its class label.

3. DESCRIPTION OF DATABASE

The MIT-BIH Arrhythmia Database is used in this paper for beat classification using PFKNN. It contains two-channel ambulatory ECG recordings from 47 subjects studied by the BIH Arrhythmia Laboratory between 1975 and 1979. ECG recordings were digitized at the sampling rate of 360 Hz with 11-bit resolution. We have used the annotations of the cardiologist originally provided by the database. We have used six types of beats (Paced Beats (PB), Atrial Premature Beat (APB), Premature Ventricular Contraction (PVC), Normal (N), Left and Right Bundle Branch Blocks (LBBB & RBBB)) from the MIT-BIH Arrhythmia database. Number of beats is plotted in **Figure 2** for all six beat types. It can be seen in the figure that Normal beats dominate the database and rest of the beats are also not equally represented.

4. Results & Discussion

In this section, results of classification of the six types of cardiac rhythms are presented.

4.1. Performance Metrics

Following performance metrics are used to evaluate the performance of classifier,

1) Mean & Standard Deviation of Positive Predictive Values (PPV) of each class over five runs with ran dom selection of training and testing data. With TP_c and FP_c representing the number of true and false

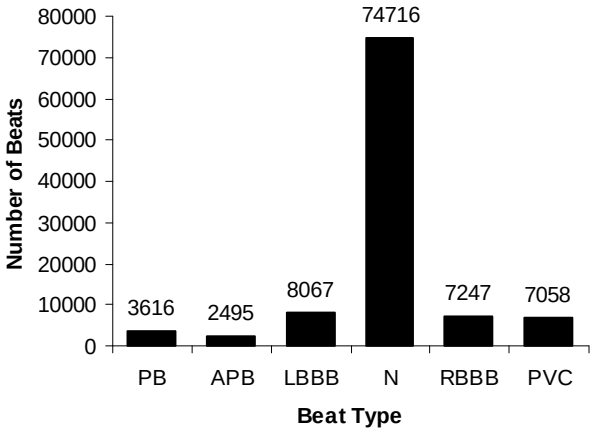

Figure 2. Distribution of beats in the database.

positives for a given class *c*, its PPV is defined by,

$$PPV_c = \frac{TP_c}{TP_c + FP_c} \quad (9)$$

2) Mean & Standard Deviation of Sensitivity Values (*Se*) of each class over five runs with random selection of training and testing data. If FN_c is the number of false negatives for a class *c* its Sensitivity is defined by,

$$Se_c = \frac{TP_c}{TP_c + FN_c} \quad (10)$$

3) Mean & Standard Deviation of Total Accuracy (*A*) of each class over five runs with random selection of training and testing data. Total Accuracy is define by,

$$A = \left(1 - \frac{N_{error}}{N_{test}}\right) \quad (11)$$

where N_{error} is the number of misclassifications and N_{test} is the total number of testing beats for all classes.

4) Mean & Standard Deviation of the Geometric Mean of Sensitivity values (*G*) over five runs with random selection of training and testing data. *G* is given by,

$$G = \left(\prod_{k=1}^{6} Se_{c_k}\right)^{1/6} \quad (12)$$

This measure is used to assess the performance of different classifiers while dealing with the class imbalance problem.

Performance measure for analyzing the performance of pruning algorithms is defined as retained ratio, *R*, given as below,

$$R = \frac{\text{No. of points in the prototype set (after pruning)}}{\text{No. of points in the training set (before pruning)}} \quad (13)$$

We have also tested noise robustness of the classification by adding uniform Gaussian noise of different intensity levels to the ECG signals and analyzed the results. The level of noise in the signal is quantized through the Signal to Noise ratio given by,

$$SNR_{dB} = 10\log\left(\frac{s_s^2}{s_e^2}\right) \quad (14)$$

where s_s^2 and s_e^2 are the power of the signal and noise respectively.

4.2. Comparison of Different Pruning Algorithms

In ECG based beat classification problem, number of training beats can grow very large and an efficient pruning method is required. Pruning of data for different classes is a difficult task when the separation boundary is nonlinear and complex and representation of classes is sparsely clustered. Checkerboard data is an example of multi-modal two class problem as shown in **Figure 3(a)** and Spiral data corresponds to two class separable problem having complex separation boundary as shown in **Figure 3(b)**. In this section, our proposed Arif-Fayyaz pruning algorithm is compared with the other pruning algorithms. We have used the implementation of Wilson *et al.* [17] of different pruning algorithms. For the comparison 10 fold cross validation results are presented with $K = 1$ and $m = \infty$ (FWKNN being used as SKNN) over two different data sets.

In **Table 1**, different pruning methods are compared with our proposed Arif-Fayyaz pruning method. The accuracy of the proposed pruning approach is comparable to other approaches over these data sets. We have compared different algorithms in terms of Pruning Time, Accuracy after pruning and Retained fraction R. All algorithms were run on PIV 2.26 GHz PC with 512 Mb RAM.

In the first row of **Table 1**, result of simple KNN is presented without any pruning. The maximum accuracy achieved in two data sets is 98.33% and 99.97% for checkerboard and spiral data respectively by retaining all the training examples. Our proposed Arif-Fayyaz pruning method has achieved the accuracy of 97.54% and 99.83% respectively while retaining only 19.86% and 7.72% training examples. Other pruning methods are

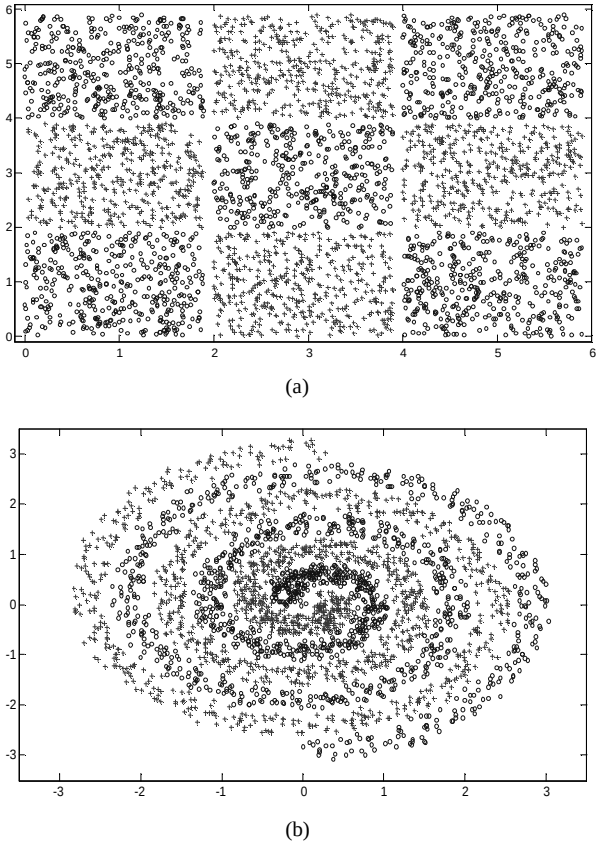

Figure 3. (a) Top: Checkerboard data; (b) Bottom: Spiral data.

Table 1. Comparison of different pruning algorithm for checkerboard and spiral data.

	Spiral (N_{total} = 2760, dimension = 2)			Checkerboard (N_{total} = 3600, dimension = 2)		
	Time (seconds)	Accuracy (%)	R × 100 (%)	Time (seconds)	Accuracy (%)	R × 100 (%)
KNN	0.95	98.33	100.00	1.61	99.97	100.00
Proposed Method	0.32	97.54	19.86	0.32	99.83	7.72
CNN [19]	0.95	95.38	8.83	1.55	98.33	3.70
SNN [20]	13.35	96.80	10.61	10.47	99.44	3.57
IB2 [21]	0.94	95.38	8.83	1.53	98.33	3.70
IB3 [21]	1.18	94.91	10.70	1.70	98.66	4.37
DEL [22]	3.13	91.71	6.64	14.16	97.49	2.24
DROP1 [22]	2.69	89.82	7.34	4.78	93.84	2.83
DROP2 [22]	2.62	96.07	15.62	12.31	99.13	5.90
DROP3 [22]	2.66	96.65	15.49	12.31	99.22	5.91
DROP4 [22]	2.65	96.47	15.54	12.32	99.22	5.91
DROP5 [22]	3.58	96.73	6.78	14.90	99.39	1.63
ENN [23]	1.02	98.00	98.59	1.62	99.94	99.95
RENN [23]	1.02	97.96	98.58	1.62	99.94	99.95
All KNN [24]	0.94	98.00	98.26	1.61	99.94	99.95
EL Grow [25]	2.20	64.04	0.45	3.69	85.54	0.32
Explore [25]	3.00	67.46	0.60	4.73	87.22	0.33
ELH [17]	2.64	91.42	5.86	4.72	96.07	2.01

better than our proposed method in retained ratio but our method outperform other methods in term of pruning time which is very important in case of large training set. Moreover, classification accuracy of Arif-Fayyaz pruning method is almost similar to simple KNN without pruning. If we look at the table, only ENN is better than Arif-Fayyaz pruning method in terms of accuracy but the retained ratio of ENN is very high (more than 98% in both cases). Explore method offers least retained ratio but its classification accuracy is very poor. Incremental policy of Arif-Fayyaz pruning algorithm is very simple and straightforward. These results clearly indicate the advantage in terms of computational complexity of using Arif-Fayyaz pruning method.

Our proposed approach offers a suitable and manageable reduction factor and faster pruning. Our proposed Arif-Fayyaz pruning method is used in the rest of paper for pruning.

4.3. Classification Results of PFKNN

Firstly, we present the result of fuzzy KNN with parameter values of k = 5 and m = 1.5. No pruning or class weights are used. We have divided total number of beats into two sets; training set include 50% of total number of beats (51600 beats) and 50% testing beats (51599 beats). Beats are selected randomly for training and testing sets.

Classification results for FKNN based classification are given in **Table 2** with 11 features as explained in Subsection 2.1. Effect of noise on classification accuracy in terms of SNR as explained in Subsection 3.1 is also illustrated in **Table 2**. Overall accuracy is dropped by only 1% for SNR equals to 20 dB. This shows good robustness of FKNN against Gaussian noise.

In PFKNN, our proposed Arif-Fayyaz pruning method is used to prune the training data set of 51600 beats and pruned feature set is used to classify the testing set of 51599 beats of six classes. Results of classification with and without noise are illustrated in **Table 3**. Overall accuracy and geometric mean of sensitivity G are given in the 9th column as A (G) and retained ration R is given in the last column of the table. It can be observed from **Table 3** that with only 19% retained ratio of the training feature set, overall accuracy is dropped by only 0.3% and geometric mean of sensitivity G is dropped by only 0.2%. Hence our proposed PFKNN method offers advantage in terms of space and computational complexity.

Principal Component Analysis (PCA) is used to reduce the number of features. Considering the eigen-values of the resultant principal components, six principal components are selected and 11-dimensional feature space is projected on six-dimensional space. **Table 4** shows overall accuracy, geometric mean of sensitivity and retained ratio considering no noise and different level of noise. It can be observed from the **Table 4** that with the same overall accuracy and geometric mean of sensitivity it can further reduce the computational complexity of the classifier.

Table 2. Beat classification using fuzzy KNN.

SNR (dB)		Effect of noise Without PCA Feature Reduction (N_{train} = 51600, N_{test} = 51599) with FKNN, k = 5, m = 1.5						
		PB	APB	LBBB	Normal	RBBB	PVC	Overall Accuracy (G)
No Noise	PPV	99.93 ± 0.05	83.11 ± 1.11	94.65 ± 0.35	98.55 ± 0.05	98.30 ± 0.14	94.58 ± 0.26	97.63 ± 0.02 (94.74)
	SEN	99.95 ± 0.00	83.47 ± 1.15	94.53 ± 0.47	98.54 ± 0.05	98.59 ± 0.19	94.36 ± 0.28	
40	PPV	99.91 ± 0.06	83.51 ± 0.68	94.45 ± 0.42	98.48 ± 0.06	98.20 ± 0.04	94.96 ± 0.44	97.59 ± 0.04 (94.56)
	SEN	99.91 ± 0.10	82.83 ± 1.30	94.48 ± 0.21	98.54 ± 0.04	98.63 ± 0.16	94.09 ± 0.49	
35	PPV	99.89 ± 0.07	82.38 ± 1.18	94.60 ± 0.31	98.47 ± 0.05	98.11 ± 0.13	94.38 ± 0.43	97.52 ± 0.06 (94.45)
	SEN	99.97 ± 0.05	82.42 ± 0.55	94.14 ± 0.20	98.48 ± 0.08	98.59 ± 0.20	94.26 ± 0.31	
30	PPV	99.82 ± 0.09	81.56 ± 1.43	93.65 ± 0.40	98.37 ± 0.08	97.99 ± 0.23	93.99 ± 0.21	97.31 ± 0.04 (94.18)
	SEN	99.95 ± 0.05	82.36 ± 0.74	93.57 ± 0.24	98.34 ± 0.09	98.47 ± 0.16	93.54 ± 0.36	
25	PPV	99.91 ± 0.06	81.38 ± 0.89	93.00 ± 0.70	98.21 ± 0.08	97.74 ± 0.22	93.65 ± 0.71	97.11 ± 0.07 (93.65)
	SEN	99.90 ± 0.05	80.79 ± 1.27	93.06 ± 0.27	98.23 ± 0.03	98.44 ± 0.18	92.90 ± 0.27	
20	PPV	99.85 ± 0.05	78.53 ± 1.23	91.55 ± 0.16	97.74 ± 0.04	96.92 ± 0.33	92.49 ± 0.37	96.45 ± 0.10 (92.27)
	SEN	99.81 ± 0.15	77.78 ± 0.64	90.12 ± 0.46	97.88 ± 0.08	97.77 ± 0.29	92.19 ± 0.21	

Table 3. Beat classification using pruned fuzzy KNN.

SNR (dB)		Effect of Noise Without PCA Feature Reduction (N_{train} = 51600, N_{test} = 51599) with PFKNN, k = 5, m = 1.5							
		PB	APB	LBBB	Normal	RBBB	PVC	A (G)	R
No Noise	PPV	99.93 ± 0.05	78.61 ± 0.68	93.66 ± 0.23	98.51 ± 0.06	97.51 ± 0.33	94.46 ± 0.52	97.32 ± 0.05 (94.58)	0.19
	SEN	99.86 ± 0.07	83.49 ± 0.98	94.60 ± 0.32	98.17 ± 0.03	98.65 ± 0.14	93.72 ± 0.50		
40	PPV	99.88 ± 0.06	78.77 ± 0.94	93.65 ± 0.52	98.54 ± 0.04	97.55 ± 0.25	94.07 ± 0.52	97.32 ± 0.06 (94.64)	0.19
	SEN	99.89 ± 0.10	83.50 ± 0.35	94.62 ± 0.27	98.12 ± 0.08	98.70 ± 0.18	94.03 ± 0.31		
35	PPV	99.91 ± 0.03	77.90 ± 1.48	93.21 ± 0.29	98.48 ± 0.04	97.51 ± 0.13	93.63 ± 0.26	97.17 ± 0.08 (94.47)	0.19
	SEN	99.94 ± 0.04	83.42 ± 0.74	94.30 ± 0.17	98.02 ± 0.08	98.49 ± 0.23	93.67 ± 0.49		
30	PPV	99.93 ± 0.06	78.12 ± 1.63	93.18 ± 0.56	98.39 ± 0.043	97.42 ± 0.14	93.63 ± 0.46	97.12 ± 0.04 (94.28)	0.19
	SEN	99.82 ± 0.08	83.35 ± 0.94	93.89 ± 0.48	98.04 ± 0.06	98.53 ± 0.07	93.07 ± 0.45		
25	PPV	99.88 ± 0.06	77.31 ± 0.95	91.83 ± 0.31	98.20 ± 0.03	97.06 ± 0.29	92.75 ± 0.38	96.76 ± 0.04 (93.79)	0.20
	SEN	99.88 ± 0.09	82.57 ± 0.55	92.44 ± 0.21	97.77 ± 0.04	98.31 ± 0.17	92.86 ± 0.21		
20	PPV	99.82 ± 0.09	74.05 ± 0.75	89.83 ± 0.23	97.79 ± 0.12	96.34 ± 0.37	91.87 ± 0.26	96.12 ± 0.09 (92.28)	0.23
	SEN	99.83 ± 0.08	78.29 ± 1.24	90.77 ± 0.55	97.40 ± 0.06	97.76 ± 0.34	91.40 ± 0.73		

Table 4. Beat classification using pruned fuzzy KNN with reduced feature space using PCA.

SNR (dB)		Effect of Noise With PCA Feature Reduction (N_{train} = 51600, N_{test} = 51599) with PCA & PFKNN							
		PB	APB	LBBB	Normal	RBBB	PVC	A (G)	R
No Noise	PPV	99.92 ± 0.05	78.88 ± 0.85	93.56 ± 0.3	98.54 ± 0.08	97.62 ± 0.21	93.92 ± 0.32	97.31 ± 0.10 (94.74)	0.19
	SEN	99.91 ± 0.08	84.46 ± 1.14	94.24 ± 0.4	98.13 ± 0.09	98.78 ± 0.14	93.78 ± 0.2		
40	PPV	99.96 ± 0.03	78.88 ± 1.98	93.39 ± 0.22	98.52 ± 0.07	97.57 ± 0.27	93.55 ± 0.56	97.29 ± 0.03 (94.53)	0.19
	SEN	99.85 ± 0.14	83.28 ± 1.25	94.70 ± 0.22	98.14 ± 0.09	98.69 ± 0.18	93.55 ± 0.56		
35	PPV	99.92 ± 0.05	78.75 ± 1.39	93.33 ± 0.23	98.52 ± 0.05	97.39 ± 0.09	93.70 ± 0.36	97.23 ± 0.05 (94.62)	0.19
	SEN	99.87 ± 0.06	83.98 ± 0.62	94.08 ± 0.25	98.06 ± 0.05	98.61 ± 0.19	94.05 ± 0.42		
30	PPV	99.91 ± 0.05	78.14 ± 1.52	92.92 ± 0.52	98.41 ± 0.07	97.49 ± 0.32	93.62 ± 0.43	97.12 ± 0.20 (94.25)	0.20
	SEN	99.91 ± 0.12	82.80 ± 1.01	93.94 ± 0.46	98.02 ± 0.08	98.51 ± 0.33	93.39 ± 0.55		
25	PPV	99.86 ± 0.06	77.02 ± 0.80	91.76 ± 0.21	98.26 ± 0.05	97.01 ± 0.32	93.11 ± 0.13	96.82 ± 0.06 (93.71)	0.21
	SEN	99.89 ± 0.07	81.49 ± 1.14	93.04 ± 0.28	97.80 ± 0.05	98.39 ± 0.21	92.90 ± 0.37		
20	PPV	99.89 ± 0.10	72.67 ± 0.63	89.89 ± 0.48	97.78 ± 0.09	96.11 ± 0.22	91.80 ± 0.65	96.04 ± 0.08 (92.28)	0.23
	SEN	99.73 ± 0.12	78.65 ± 0.86	90.36 ± 0.18	97.31 ± 0.08	97.83 ± 0.26	91.53 ± 0.75		

4.4. Analysis of Results

Main advantage of using fuzzy KNN over simple KNN is the membership value of each class for a particular query beat. Hence it gives a much more informed decision by inclusion of a higher level decision process. To accomplish this, we can first normalize the firing strengths of each class and then use the following classification rule: If the normalized firing strength of the runner-up class lies within a certain threshold of that of the winner class then we can assume the winning class label to be doubtful and take the runner-up class label in to consideration as well. Mathematically the winner class label is considered to be doubtful if,

$$\frac{m_{winner}(x) - m_{runner-up}(x)}{\sum_i m_{c_i}(x)} \leq q \qquad (15)$$

where θ is the threshold value and it is user specific. If we take winner and runner-up classes into consideration when inequality **Eq.15** is satisfied, we can consider the beat classification as correct if winner or runner-up belongs to correct class. Following this strategy, overall accuracy versus threshold value is plotted in **Figure 4**. We can observe from the figure that accuracy increases with the relaxation of threshold value.

Table 5 illustrates the time and space complexity of standard FKNN algorithm and our proposed PFKNN algorithm with fast nearest neighbor search using ATRIA. It can be seen from the table that PFKNN is very time efficient with small retained ratio. Overall accuracy and geometric mean of sensitivity of standard FKNN and PFKNN are also comparable. Hence, it highlights the effectiveness of using PFKNN.

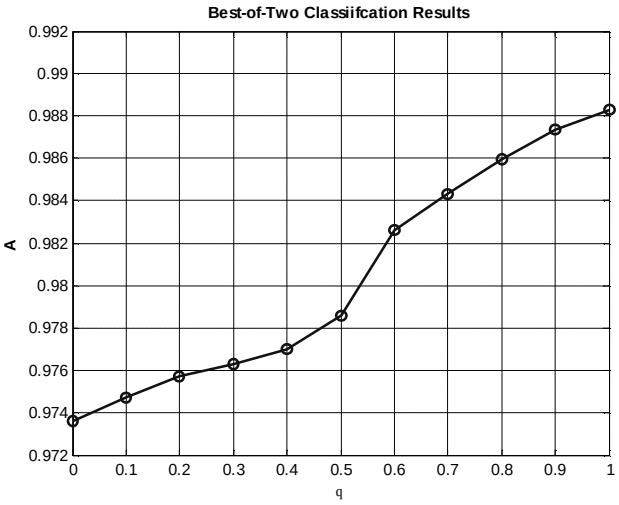

Figure 4. Plot of overall accuracy a versus threshold value.

Table 5. Time and space complexity for standard FKNN and PFKNN.

Type of Algorithm	Classification Time (Seconds)	Retained Ratio R	Overall Accuracy	Geometric Mean Sensitivity
Standard FKNN	1116	1.0	97.63	94.74
PFKNN (With 11 Features)	353	0.19	97.32	94.58
PFKNN (With 6 Features)	303	0.19	97.31	94.74

Table 6. Comparison of beat classification techniques.

Method	**Number of Beat Types**	**Number of Features**	**Database Size**	**Accuracy (%)**
Osowski *et al* [26]	7	18	7,185 Beats	96.06
Guler *et al* [27]	5	24	450 Beats	97.78
Guler *et al* [28]	4	19	450 Beats	96.94
Minami *et al* [4]	3	5	700 Beats	98
Al-Fahoum *et al* [6]	4	6	1590 Beats	97.5
Dokur *et al* [29]	5	15	1,000 Beats	97
Prasad *et al* [5]	12	25	105,423 Beats	96.77
Chen *et al* [8]	7	30	23,200 Beats	99.7
Yu *et al* [30]	6	11	23,200 Beats	99.65
Yu *et al* [31]	8	17	9,800 Beats	98.7
PFKNN (Proposed) without PCA	6	11	**23,200 Beats**	99.30
PFKNN (Proposed) with PCA	6	6	**23,200 Beats**	99.25
PFKNN (Proposed) without PCA	6	11	**104,700 Beats**	97.35 ± 0.04
PFKNN (Proposed) with PCA	6	6	**104,700 Beats**	97.30 ± 0.04

Many researchers have compared their methods with the other existing methods present in the literature. **Table 6** shows the comparison of the proposed approach with other methods in the literature. In our view, a fair comparison of methods is not possible as most of the researchers have focused on different set of beat types and tested their methods on selected number of records present in the MIT-BIH database. From the table, we can observe that accuracy of our method is comparable to other methods although we have tested our method on whole set of six beat types present in the MIT-BIH database. Moreover, our feature set is very small (only six) and exhibits good time and space complexity. While using a limited set of 23200 beats, our accuracy is dropped by only 0.5% as compared to [30].

5. CONCLUSIONS

Pruned fuzzy KNN (PFKNN) classifier is proposed for arrhythmia beat classification that can offer reduced computational complexity and simple incremental policy. A new pruning algorithm is proposed especially suited for KNN based classifiers that can prune the data efficiently in less computational time without compromising the accuracy of the classifier. PCA is used to further reduce the feature set to only six features per beat. Results have proved that PFKNN can offer better computational complexity than FKNN without compromising the classification accuracy. Hence PFKNN is a suitable option for online implementation of such clinical decision support system for Arrhythmia beat classification that demands less space and time complexity. Because of simplicity of the proposed classifier it is very easy to increment further training data of similar beat types or new beat types.

REFERENCES

[1] Garcia, T.B. and Miller, G.T. (2004) Arrhythmia recognition: The art of interpretation. Jones and Barlett Publishers, the United States of America.

[2] Kohler, B.U., Hennig, C. and Orglmeister, R. (2002) The principles of software QRS detection. *IEEE Magazine of Engineering in Medicine and Biology*, **21(1)**, 42-57.

[3] Martinez, J.P., Almeida, R., Olmos, S., Rocha, A.P. and La-guna, P. (2004) A wavelet-based ECG delineator: Evaluation on standard databases. *IEEE Transactions on Biomedical Engineering*, **51(4)**, 570-581.

[4] Minami, K., Nakajima, H. and Toyoshima, T. (1999) Real-time discrimination of ventricular tachyarrhythmia with fourier-transform neural network. *IEEE Transactions on Biomedical Engineering*, **46(2)**, 179-185.

[5] Prasad, G.K. and Sahambi, J.S. (2003) Classification of ECG arrhythmias using multi-resolution analysis and neural networks. *Conference on Convergent Technologies for Asia-Pacific region*, **1**, 227-231.

[6] Al-Fahoum, A.S. and Howitt, I. (1999) Combined wavelet transform and radial basis neural networks for the classifying life threatening cardiac arrhythmias. *Medical & Biological Engineering & Computing*, **37**, 566-573.

[7] Addison, P.S., Watson, J.N., Clegg, G.R., Holzer, M., Sterz, F. and Robertson, C.E. (2000) A Novel wavelet based analysis reveals hidden structure in ventricular fibrillation. *IEEE Engineering in Medicine and Biology*, **19(4)**, 383-392.

[8] Chen,Y.-H. and Yu, S.N. (2007) Subband features based on higher order statistics for ECG beat classification. 29*th Annual International Conference of IEEE Engineering in Medicine and Biology Society*, Lyon, January 1, 2001.

[9] Afsar, F.A. and Arif, M. (2008) Robust electrocardiogram (ECG) beat classification using discrete wavelet transform. *Physiological Measurement*, **29**, 555-570.

[10] Yu, S.N. and Chou, K.T. (2007) A switchable scheme for ECG beat classification based on independent component analysis. *Expert System Applications*, **33(4)**, 824-829.

[11] Bortolan, G., Bortolan, G., Jekova, I., Jekova, I. and Christov, I. (2005) Comparison of four methods for premature ventricular contraction and normal beat clustering. *Computers in Cardiology*, **2005**, 921-924.

[12] Exarchos, T.P., Tsipouras, M.G., Exarchos, C.P., Papaloukas, C., Fotiadis, D.I. and Michalis, L.K. (2007) A methodology for the automated creation of fuzzy expert systems for ischemic and arrhythmic beat classification based on a set of rules obtained by a decision tree. *Artificial Intelligence in Medicine*, **40**, 187-200.

[13] Christov, I., Jekova, I. and Bortolan, G. (2005) Premature ventricular contraction classification by the Kth nearest-neighbours rule. *Physiological Measurement*, **1**, 123.

[14] Mark, R. and Moody, G. (1988) MIT-BIH arrhythmia database directory. Second Edition, MIT Press, Cambridge.

[15] Duda, R., Hart, P. and Stork, D. (2001) Pattern classification. Second Edition, John Wiley and Sons, Inc, New York.

[16] Keller, J.M., Gray, M.R. and Givens, J.A. (1985) A fuzzy k-nearest neighbor algorithm. *IEEE Transactions on Systems, Man and Cybernetics*, **SMC-15(4)**, 580.

[17] Wilson, D.R. and Martinez, T.R. (2000) Reduttion techniques for instance based learning algorithms. *Machine Learning*, **38(3)**, 257-286.

[18] Merkwirth, C., Parlitz, U. and Lauterborn, W. (2000) Fast nearest-neighbor searching for nonlinear signal processing. *Physical Review E*, **62(2)**, 2089-2097.

[19] Hart, P.E. (1968) The condensed nearest neighbor rule. *IEEE Transactions on Information Theory*, **14**, 515-516.

[20] Ritter, G.L., Woodruff, H.B., Lowry, S.R. and Isenhour, T.L. (1975) An algorithm for a selective nearest neighbor decision rule. *IEEE Transactions on Information Theory*, **21(6)**, 665-669.

[21] Aha, D.W., Kibler, D. and Albert, M.K. (1991) Instance-based learning algorithms. *Machine Learning*, **6**, 37-66.

[22] Wilson, D.R. and Martinez, T.R. (1997) Improved hetero-geneous distance functions. *Journal of Artificial Intelligence Research* (*JAIR*), **6(1)**, 1-34.

[23] Wilson, D.L. (1972) Asymptotic properties of nearest neighbor rules using edited data. *IEEE Transactions on Systems, Man, and Cybernetics*, **2(3)**, 408-421.

[24] Tomek, I. (1976) An experiment with the edited nearest-neighbor rule. *IEEE Transactions on Systems, Man, and Cybernetics*, **6(6)**, 448-452.

[25] Cameron-Jones, R.M. (1995) Instance selection by en-

coding length heuristic with random mutation hill climbing. *Proceedings of the Eighth Australian Joint Conference on Artificial Intelligence*, 99-106.

[26] Osowski, S. and Tran, H.L. (2001) ECG beat recognition using fuzzy hybrid neural network. *IEEE Transactions on Biomedical Engineering*, **48(11)**, 1265-1271.

[27] Güler, İ. and Übeylı, E.D. (2005a) ECG beat classifier designed by combined neural network model. *Pattern recognition*, **38**, 199-208.

[28] Güler, İ. and Übeylı, E.D. (2005b) A modified mixture of experts network structure for ECG beats classification with diverse features. *Engineering Applied Artificial Intelligence*, **18**, 845-856.

[29] Dokur, Z., Olmez, T. and Yazgan, E. (1999) Comparison of discrete wavelet and fourier transforms for ECG beat classification. *Electronics Letters*, **35(18)**, 1502-1504.

[30] Yu, S.-N. and Chen, Y.-H. (2007) Electrocardiogram beat classification based on wavelet transformation and probabilistic neural network. *Pattern Recognition Letters*, **28(10)**, 1142-1150.

[31] Yu, S.-N. and Chou, K.-T. (2008) Selection of significant independent components for ECG beat classification. *Expert Systems with Applications*, **36(2)**, 2088-2096.

J. Biomedical Science and Engineering, 2010, 3, 390-396 **JBiSE**
doi:10.4236/jbise.2010.34054 Published Online April 2010 (http://www.SciRP.org/journal/jbise/).

Classification of human emotion from EEG using discrete wavelet transform

Murugappan Murugappan, Nagarajan Ramachandran, Yaacob Sazali

School of Mechatronic Engineering, Universiti Malaysia Perlis (UniMAP), Perlis, Malaysia.
Email: murugappan@unimap.edu.my

Received 21 November 2009; revised 28 December 2009; accepted 4 February 2010.

ABSTRACT

In this paper, we summarize the human emotion recognition using different set of electroencephalogram (EEG) channels using discrete wavelet transform. An audio-visual induction based protocol has been designed with more dynamic emotional content for inducing discrete emotions (disgust, happy, surprise, fear and neutral). EEG signals are collected using 64 electrodes from 20 subjects and are placed over the entire scalp using International 10-10 system. The raw EEG signals are preprocessed using Surface Laplacian (SL) filtering method and decomposed into three different frequency bands (alpha, beta and gamma) using Discrete Wavelet Transform (DWT). We have used "db4" wavelet function for deriving a set of conventional and modified energy based features from the EEG signals for classifying emotions. Two simple pattern classification methods, K Nearest Neighbor (KNN) and Linear Discriminant Analysis (LDA) methods are used and their performances are compared for emotional states classification. The experimental results indicate that, one of the proposed features (ALREE) gives the maximum average classification rate of 83.26% using KNN and 75.21% using LDA compared to those of conventional features. Finally, we present the average classification rate and subsets of emotions classification rate of these two different classifiers for justifying the performance of our emotion recognition system.

Keywords: EEG; Human Emotions; Discrete Wavelet Transform; KNN; LDA

1. INTRODUCTION

Emotion is one of the most important features of humans. Without the ability of emotions processing, computers and robots cannot communicate with human in natural way. It is therefore expected that computers and robots should process emotion and interact with human users in a natural way. In recent years, research efforts in Human Computer Interaction (HCI) are focused on the means to empower computers to understand human emotions. Although limited in number compared with the efforts being made towards intention-translation means, some researchers are trying to realize man-machine interfaces with an emotion understanding capability. Most of them are focused on facial expression recognition and speech signal analysis [1,2]. In these works, the emotions of the subjects are purposefully expressed and it can be more easily concealed by those of other subjects [3]. Another possible approach for emotion recognition is physiological signal analysis. We believe that this is a more natural means of emotions recognition, in that the influence of emotion on facial expression or speech can be suppressed relatively easily, and emotional status is inherently reflected in the activity of nervous system. The traditional tools for the investigation of human emotional status are based on the recording and statistical analysis of physiological signals from the both central and autonomic nervous systems. Some of the main physiological signals highly adopted for human emotion assessment are: Electromyogram (EMG), Electrocardiogram (ECG), Skin Conductive Resistance (SCR), and Blood Volume Pressure (BVP) [4,5]. Several approaches have been reported by different researchers on finding the correlation between the emotional changes and EEG signals [6-8]. The past works on emotion recognition using EEG signals are reported in [9].

One of the difficulties of categorizing emotion names is that the distinction between the emotion categories is not clear. All people express their emotions differently: it is not an easy task to judge or to model emotions. Researchers often use two different methods to model emotions [10,11]. One approach is word labels, for example, happy, sad, surprise, anger, fear, disgust, etc. Another ways is to have multiple dimensions or scales to categorize emotions. Instead of choosing discrete labels, observers can indicate their impressions of each stimulus on several continuous scales: for example, pleasant-unpleasant, attention-rejection, simple-complicated, etc. Many researchers have attempted to utilize the two dimensional

modeling of emotions due to simplicity of protocol design and signal processing techniques [12,13]. However, our work is to realize the basic emotions that are in discrete mode for developing intelligent emotion recognition system. Furthermore, the assessment of discrete mode emotions is useful to create suitable reactions in man-machine systems such as robots for disabled. Indeed, the development of human emotion recognition system is challenging in terms of developing protocol design and in terms of developing efficient machine learning algorithms for deriving the discrete emotion from the multiple complex emotions encountered by human.

In order to provide a simplified emotion recognition system, in our earlier work, we proposed asymmetric ratios based channel selection for reducing the number of channels from 62 to 8 and to 4 [14]. Since, the reduction of channels does minimize the physical burden, mental fatigue during electrode placement, computational time and complexity. The basic EEG based emotion recognition system is shown in **Figure 1**.

The rest of this paper is organized as follows. In Section 2, we summarize the research methodology by elucidating the data acquisition process, preprocessing, and feature extraction using wavelet transform, and classification of emotions by linear classifiers. Section 3 illustrates the overview of the results and discussion of this present work, and conclusions are given in Section 4.

2. RESEARCH METHODOLOGY

2.1. EEG Data Acquisitions

This section describes the acquisition of EEG signals for emotion assessment experiment. A pilot panel study is conducted on 25 university students to select any 5 video clips (trials) for each emotion from 115 emotional video clips including from the international standard emotional clips[1]. All the video clips are short in time duration and with more dynamic emotional content. The selection of video clips is based on self assessment questionnaires mentioned in [15]. The subjects who have undergone this panel study do not take part in the data collection experiment. Three females and seventeen males in the age group of 21-39 years were employed as subjects in our experiment. All these subjects are university students and do not have psychiatric or neurological disorders. All the subjects have given written consent prior to the recording. Every participant was given information about the design and purpose about the experiment. The subjects were paid and allowed to perform the experiments during their free times during working days (Monday ~ Friday).

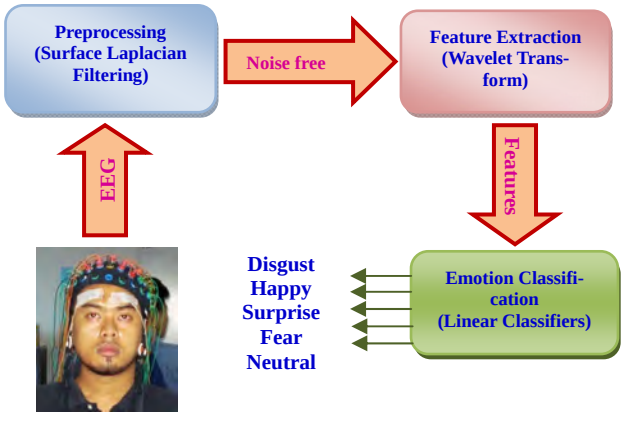

Figure 1. Basic emotion recognition system using EEG.

[1]http://psychology.stanford.edu/~psyphy/resources.html

The EEG signals were acquired using the Nevus EEG, Iceland with 64 electrodes. There are 62 active electrodes plus one electrode for reference and one electrode for ground (**Figure 2(a)**). All these electrodes are placed on the scalp according to International 10-10 system and made up of Ag/Ag-Cl. The reference electrode AFz is placed in between AF1 and AF2 electrodes and the ground electrode Oz is placed in between O1 and O2 electrodes. The impedances of the electrodes were kept below 5KΩ. The EEG signals collected from the scalp electrodes are filtered on-line (band-pass) between 0.5 Hz and 70 Hz. The sampling rate was fixed at 256 samples per second for all the channels and digitized at 16 bit. The recording of EEG signals for various emotional stimuli is carried out in an electrical and sound attenuated room while the participant was seated comfortably on the armchair.

2.2. Emotion Elicitation Method

Emotions can be induced by one of the following ways: 1) visual (images/pictures) [12]; 2) audio-visual (film clips/video clips) [13,16]; 3) recalling of past emotional events [8]; 4) audio (songs/sounds) [17]. Most of researchers are using visual stimuli for evoking emotions. In our previous work, we have used both visual and audio-visual stimuli for evoking discrete emotions. The result of this study confirms that, audio-visual stimulus performs superior in evoking emotions than visual stimulus [18].

The main advantage of this method resides in the strong correlation between induced emotional states and the physiological responses. Hence, we have designed an audio-visual induction based protocol for eliciting the discrete emotions in this present work. The complete protocol design is computerized to follow in prescribed time period. Thereby no human intervention is required to disturb the experimental session. In order to get quality data, the subjects are asked to follow a set of instruction prior to the experimental session: 1) sit back comfortably; 2) do not move until the end of the experiment session; 3) let yourself freely experience whatever emotions as much as you can; 4) do not try to hold back your feelings.

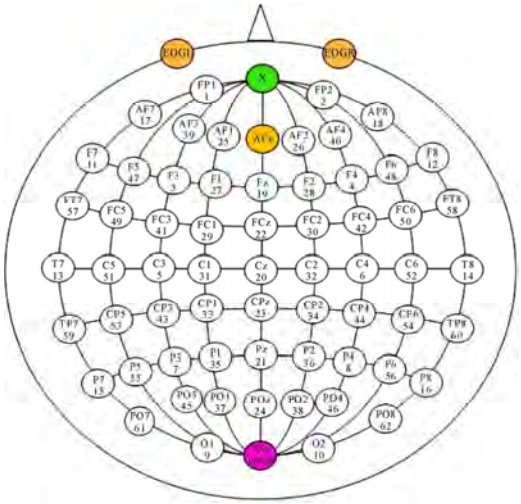

(a)

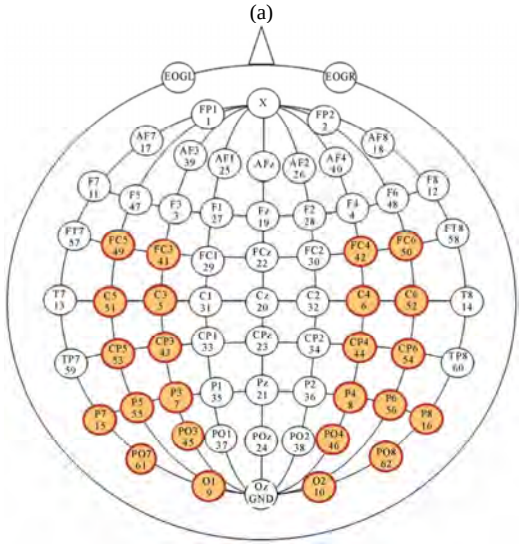

(b)

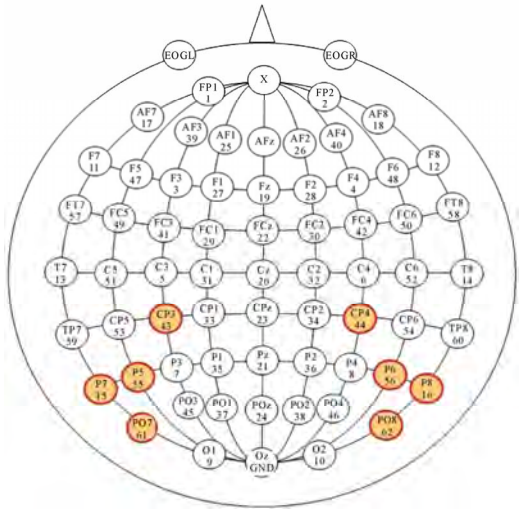

(c)

Figure 2. Electrodes diagram (a) 62 channel; (b) 24 channel; (c) 8 channel.

The audio-visual stimulus protocol for one of the trials of our experiment is shown in **Figure 3**. The orders of the emotional video clips are changed in a random manner for other trials. X1 to X5 denote time periods of selected video clips. The time duration of video clips vary from one another. In this protocol design, the current emotional state of the subjects before the experiment session is neutralized by showing a set of "natural scenes" and also playing a "soothing music" will make the subjects to feel calm with relaxed mind. Since, in most of the experimental sessions, previous researchers have tolerated the effect of current emotional state of the subjects before undergoing the emotions assessment experiment. Between each emotional stimulus (video clips), the "blank (dark) screen" is displayed for 10 second to "rest and prepare" the subject to next stimulus. Between each emotional video clips, under self assessment section, the subjects were informed to answer the emotions they have experienced [18]. Finally, 5 trials for disgust, happy and surprise emotions and 4 trials for fear and neutral emotions are considered for further analysis. All the signals are collected without imparting discomfort to the subjects.

2.3. Preprocessing

EEG signals recorded over various positions on the scalp are usually contaminated with noises and artifacts (Ocular (EoG), Muscular (EMG), Vascular (ECG) and Gloss kinetic artifacts). The complete removal of artifacts will also remove some of the useful information of EEG signals. This is one of the reasons why considerable experience is required to interpret EEGs clinically [19,20]. A couple of methods are available in the literature to avoid artifacts in EEG recordings. However, removing artifacts entirely is impossible in the existing data acquisition process.

In this work, we use of Surface Laplacian (SL) filter for removing the noises and artifacts. The SL filter is used to emphasize the electric activities that are spatially close to a recording electrode ("*i*"), filtering out those that might have an origin outside the skull. In addition, this filter also attenuates the EEG activity which is

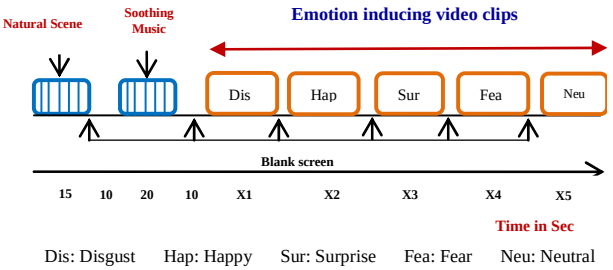

Figure 3. EEG data acquisition protocol using audio-visual stimulus.

common to all the involved channels in order to improve the spatial resolution of the recorded signal. The neural activities generated by the brain, however, contain various spatial frequencies. Potentially useful information from the middle frequencies may be filtered out by the analytical Laplacian filters. Hence, the signal "pattern" derived from SL filters is similar to "spatial distribution of source in the head".

The mathematical modeling of Surface Laplacian filter is given as

$$X_{new} = X(t) - \frac{1}{N_E}\sum_{i=1}^{N_E} X_i(t) \quad (1)$$

where X_{new}: filtered signal; $X(t)$: raw signal; N_E: number of neighbor electrodes.

2.4. Feature Extraction

In the emotion recognition research using EEG signals, the non-parametric method of feature extraction based on multi-resolution analysis of Wavelet Transform (WT) is quite new. The joint time-frequency resolution obtained by WT makes it as a good candidate for the extraction of details as well as approximations of the signal which cannot be obtained either by Fast Fourier Transform (FFT) or by Short Time Fourier Transform (STFT) [21,22]. The non-stationary nature of EEG signals is to expand them onto basis functions created by expanding, contracting and shifting a single prototype function ($\Psi_{a,b}$, the mother wavelet), specifically selected for the signal under consideration.

The mother wavelet function $\Psi_{a,b}(t)$ is given as

$$\psi_{a,b}(t) = \frac{1}{\sqrt{a}}\psi\left(\frac{t-b}{a}\right) \quad (2)$$

where $a, b \in R$, $a > 0$, and R is the wavelet space.

Parameters 'a' and 'b' are the scaling factor and shifting factor respectively. The only limitation for choosing a prototype function as mother wavelet is to satisfy the admissibility condition (**Eq.3**),

$$C_\psi = \int_{-\infty}^{\infty} \frac{|\Psi(\omega)|^2}{\omega} d\omega < \infty \quad (3)$$

where $\Psi(\omega)$ is the Fourier transform of $\Psi_{a,b}(t)$.

The time-frequency representation is performed by repeatedly filtering the signal with a pair of filters that cut the frequency domain in the middle. Specifically, the discrete wavelet transform decomposes the signal into approximation coefficients (CA) and detailed coefficients (CD). The approximation coefficient is subsequently divided into new approximation and detailed coefficients. This process is carried out iteratively producing a set of approximation coefficients and detail coefficients at different levels or scales [23] (**Table 1**).

Table 1. Decomposition of EEG signals into different frequency bands with a sampling frequency of 256 Hz.

Frequency Range (Hz)	Decomposition Level	Frequency Bands	Frequency Bandwidth (Hz)
0–4	A5	Delta	4
4–8	D5	Theta	4
8–14	**D4**	**Alpha**	**6**
14–32	**D3**	**Beta**	**18**
32–64	**D2**	**Gama**	**32**
64–128	D1	Noises	64

In this work, the multi-resolution analysis of "db4" wavelet function is used for decomposing the EEG signals into five levels and three frequency bands (alpha, beta, and gamma) that are considered for deriving the statistical features (**Table 1**). This wavelet function has been chosen due to their near optimal time-frequency localization properties. Therefore, extraction of EEG signals features are more likely to be successful [24]. In order to analyze the characteristic natures of different EEG patterns, we proposed an energy based feature called *Recoursing Energy Efficiency* (*REE*) in our earlier work [15]. In that work, we use the Fuzzy C Means (FCM) and Fuzzy K-Means (FKM) for clustering the human emotions. The equation for deriving REE for three frequency bands is given in **Eq.4**. In this present work, we used the same feature and two of its modified form namely *Logarithmic REE* (*LREE*) *and Absolute Logarithmic REE* (*ALREE*) for classifying emotions using two linear classifiers. The equations for calculating LREE and ALREE for gamma band are given in **Eq.5** and **Eq.6**; similarly the remaining frequency bands can be derived. These features are derived from the three frequency bands of EEG.

$$REE_{gamma-3b} = \frac{E_{gamma}}{E_{total-3b}} \quad (4)$$

$$LREE_{gamma-3b} = \log_{10}\left[\frac{E_{gamma}}{E_{total-3b}}\right] \quad (5)$$

$$ALREE_{gamma-3b} = abs\left(\log_{10}\left[\frac{E_{gamma}}{E_{total-3b}}\right]\right) \quad (6)$$

$$E_{total-3b} = E_{alpha} + E_{beta} + E_{gamma} \quad (7)$$

In addition, we have used a set of conventional features (power, standard deviation and variance) for classifying the emotions and comparing the efficacy of newly proposed statistical features (**Table 2**).

2.5. Emotion Classification

In this work, we have used two simple classifiers such as Linear Discriminant Analysis (LDA) and K

Table 2. Statistical features (conventional) used for emotion recognition and their description.

Features	Description
Standard Deviation	Measures the deviations of electrodes potential from the mean value
Power	Measures the amplitude of EEG signal
Variance	Measures the variability of electrodes potential

Nearest Neighbor (KNN) for classifying the discrete emotions. Among these two classifiers, LDA provides extremely fast evaluations of unknown inputs performed by distance calculations between a new sample and mean of training data samples in each class weighed by their covariance matrices. A linear discriminant analysis tries to find an optimal hyper plane to separate five classes of emotions (disgust, happy, surprise, fear and neutral).

In addition, KNN is also a simple and intuitive method of classifier used by many researchers typically for classifying the signals and images. This classifier makes a decision on comparing a new labeled sample (testing data) with the baseline data (training data). In general, for a given unlabeled time series X, the KNN rule finds the K "closest" (neighborhood) labeled time series in the training data set and assigns X to the class that appears most frequently in the neighborhood of k time series. There are two main schemes or decision rules in KNN algorithm, that is, similarity voting scheme and majority voting scheme [25]. In our work, we used the majority voting for classifying the unlabeled data. It means that, a class (category) gets one vote, for each instance, of that class in a set of K neighborhood samples. Then, the new data sample is classified to the class with the highest amount of votes. This majority voting is more commonly used because it is less sensitive to outliers. Besides the training and testing samples, LDA does not require any external parameter for classifying the discrete emotions. However, in KNN, we need to specify the value of "K" closest neighbor for emotions classification. In this experiment, we try different "K" values ranging from 2 to 6. Finally, the value of "K" is selected as 5. This gives a maximum classification performance among the other values of K.

3. RESULTS AND DISCUSSIONS

Among all twenty subjects, we sample and preprocess a total of 460 EEG epochs from five discrete emotions. The number of data points in each epoch depends on the time duration of video clips. In our experiment, the time duration of video clips vary from one another. The next stage is to train the KNN classifier with a best value of K while LDA classifier directly works for classifying the emotions. Among these two classifiers, LDA is a very simple but elegant approach to classify various emotions. The classification ability of a statistical feature set can be measured through classification accuracy by averaging five times over a 5 fold cross-validation. In order to develop a reliable and efficient emotion recognition system with less number of electrodes, we have compared the classification accuracy of the original set of channels (62) with reduced set of channels 24 channels [5] and 8 channels [21]. In [5], the reduced set of channels was obtained on the basis of localizing the frequency range of emotion over different areas of the brain though cognitive analysis.

From **Table 3**, we inferred that, KNN gives higher average classification accuracy than LDA on three different channels sets. The maximum classification accuracy of 83.26%, 79.93% and 72.68% is obtained using *ALREE* feature on 62 channels (**Figure 2(a)**), 24 channels (**Figure 2(b)**) and 8 channels (**Figure 2(c)**) respectively. Among the three different channel combination, *ALREE* performs better than the other proposed (*REE and LREE*) and conventional features. **Table 4** to **Table 6** shows the individual emotions classification rate of KNN and LDA classifiers for three different sets of channels. From **Table 4**, we found that, the 62 channel EEG data gives the maximum individual classification rate on five emotions (happy, surprise, fear and neutral) compared to other channel sets. The maximum subsets of emotions classification rate of 91.67% for disgust, 81.67% for happy and surprise, 81.25% for fear and 93.75% for neutral is achieved using 62 channels EEG signals. Hence, the 62 channel EEG performs better over other channels sets for classification of human emotion through EEG.

Table 3. Average classification accuracy (%) of proposed and conventional statistical features using KNN and LDA.

Features	62 Channels		24 Channels		8 Channels	
	KNN	LDA	KNN	LDA	KNN	LDA
Conventional Features						
Power	55.87	63.40	64.71	45.43	70.51	45.22
Std Dev	62.46	71.73	70.58	54.78	72.61	53.26
Variance	56.10	64.56	68.84	46.67	71.52	44.06
Proposed Energy Features						
REE	51.23	77.17	77.97	64.64	72.68	55.29
LREE	81.08	76.08	79.49	67.10	71.30	58.48
ALREE	**83.26**	75.21	**79.93**	66.30	**72.68**	58.12

Table 4. Subsets of emotions classification rate (%) for 62 channel EEG over conventional and modified energy features.

Features	Disgust		Happy		Surprise		Fear		Neutral	
	Conventional Features									
	KNN	LDA	KNN	LDA	KNN	LDA	KNN	LDA	KNN	LDA
Power	58.33	80	60	40	70	73.33	39.58	52.08	39.58	75
Std Dev	56.67	86.67	66.67	70	66.67	78.33	52.08	54.16	47.92	79.17
Variance	63.33	78.33	78.33	50	65	80	39.58	41.67	37.5	62.5
Proposed Energy Features										
REE	53.33	90	60	73.33	63.33	78.33	22.92	60.42	39.58	93.75
LREE	91.67	91.33	78.33	58.33	73.33	73.33	68.75	75	89.58	91.92
ALREE	**91.67**	88.33	**81.67**	60	78.33	**81.67**	**81.25**	68.75	89.58	**93.75**

Table 5. Subsets of emotions classification rate (%) for 24 channel EEG over conventional and modified energy features.

Features	Disgust		Happy		Surprise		Fear		Neutral	
	Conventional Features									
	KNN	LDA	KNN	LDA	KNN	LDA	KNN	LDA	KNN	LDA
Power	83.33	83.33	73.33	38.33	60	60	50	58.33	52.08	70.83
Std Dev	85	55	68.33	30	60	71.67	47.92	62.5	72.92	45.83
Variance	83.33	68.33	71.67	18.33	68.33	65	50	35.42	56.25	47.92
Proposed Energy Features										
REE	91.67	90	65	28.33	70	76.67	60.42	45.83	72.92	75
LREE	90	91.67	71.67	36.67	76.67	73.33	66.47	56.25	73.75	77.08
ALREE	**90**	90	**75**	40	65	**76.67**	**66.67**	52.08	**91.67**	70.08

Table 6. Subsets of emotions classification rate (%) for 8 channel over conventional and modified energy features.

Features	Disgust		Happy		Surprise		Fear		Neutral	
	Conventional Features									
	KNN	LDA	KNN	LDA	KNN	LDA	KNN	LDA	KNN	LDA
Power	90	48.33	70	40	71.67	83.33	62.5	16.67	60.42	45.83
Std Dev	86.67	70	71.67	26.68	58.33	70	64.58	39.58	77.08	39.58
Variance	83.33	50	63.33	35	61.67	86.67	62.5	14.58	77.08	20.83
Proposed Energy Features										
REE	76.67	83.33	53.33	40	65	63.33	60.42	52.08	77.08	39.58
LREE	78.33	90	63.33	40	63.33	65	70.83	50	79.17	62.5
ALREE	80	**85**	**61.67**	38.33	**70**	55	**75**	52.08	**81.25**	70.08

4. CONCLUSIONS AND FUTURE WORK

In this paper we have presented an approach to discrete emotion recognition based on the processing of EEG signals. One of the major limitations on this research is the lack of international standard data base. Hence, we have compared the efficacy of emotion classification using newly proposed energy features with conventional features. Here, the modified energy features classify the emotions better than the conventional features with higher classification rate. The newly proposed feature, *Absolute Logarithmic Recoursing Energy Efficiency* gives the maximum average classification rate over other conventional features. Therefore the extracted features successfully capture the emotional changes of the subject through their EEG signals regardless of the user's cultural background, race, and age. In addition, it also shows a significant relationship between EEG signals and emotional states experienced by the subjects during the interaction with audio-visual content. This study is ongoing to involve different classification algorithms in order to track the emotional status of brain activation during audio-visual stimuli environment. The results of this study provide a framework of methodology that can be used to elucidate the dynamical mechanism of human emotional changes underlying the brain structure. In future, we are interested to develop efficient feature extraction algorithm using different wavelet functions and with a different set of statistical features for improving

the emotion classification rate.

5. ACKNOWLEDGEMENTS

This work is supported by the two grants of Ministry of Science and Technology Innovation (MOSTI), Malaysia. Grant Code: 9005–00020 & 9005–00002.

REFERENCES

[1] Bung, H. and Furui, S. (2000) Automatic recognition and understanding of spoken languages-a first step toward natural human machine communication. *Proceedings of IEEE*, **88**, 1142-1165.

[2] Cowie, R., Douglas, E., Tsapatsoulis, N., Votsis, G., Kollias, G., Fellenz, W. and Taylor, J.G. (2001) Emotion Recognition in human-computer interaction. *IEEE Signal Processing*, **1**, 3773-3776.

[3] Takahashi, K. (2004) Remarks on emotion recognition from bio-potential signals. *The Second International Conference on Autonomous Robots and Agents*, 186-191.

[4] Picard, R.W. (2000) Toward computers that recognize and respond to user emotion. *IBM Systems Journal*, **39(3)**, 705-719.

[5] Picard, R.W. and Healey, J. (1997) Affective wearable's. *Personal Technologies*, **1(4)**, 231-240.

[6] Kim, K.H., Band, S.W. and Kim, S.B. (2004) Emotion recognition system using short-term monitoring of physiological signals. *Proceedings on Medical & Biological Engineering & Computing*, **42**, 419-427.

[7] Chanel, G., Karim, A.A. and Pun, T. (2007) Valence-arousal evaluation using physiological signals in an emotion recall paradigm. *Lecturer Notes in Computer Science*, **1**, 530-537.

[8] Chanel, G., Kronegg, J., Grandjean, D. and Pun, T. (2005) Emotion assessment: Arousal evaluation using EEG's and peripheral physiological signals. *Technical Report*, **4105**, 530-537.

[9] Murugappan, M., Rizon, M., Nagarajan, R. and Yaacob, S. (2009a) Inferring of human emotion states using multichannel EEG. *International Journal of Soft Computing and Applications* (*IJSCA*), EURO Journals, United Kingdom. (Accepted).

[10] Russell, J.A. (1980) A Circumplex model of affect. *Journal of Personality and Social Psychology*, **39(6)**, 1161-1178.

[11] Lang. P.J. (1995) The emotion probe: Studies of motivation and attention. *American Psychologist*, **50(5)**, 372-385.

[12] Danny, O.B. (2008) Automated artifact detection in brain stream. *Technical Report*, 1-8.

[13] Wang, Y. and Guan, L. (2005) Recognizing human emotion from audiovisual information. *Proceedings of the International Conference on Acoustics, Speech, and Signal Processing*, **2**, 1125-1128.

[14] Murugappan, M., Rizon, M., Nagarajan, R. and Yaacob, S. (2008) Asymmetric ratio and FCM based salient channel selection for human emotion recognition using EEG. *WSEAS Transactions on Signal Processing*, **10(4)**, 596-603.

[15] Murugappan, M., Rizon, M., Nagarajan, R., Yaacob, S., Hazry, D. and Zunaidi, I. (2008) Time-frequency analysis of EEG signals for human emotion detection. *IFMBE Proceedings*, **21**, 262-265.

[16] Takahashi, K. and Tsukaguchi, A. (2004) Remarks on emotion recognition from multi-modal bio-potential signals. *Proceedings of IEEE International Workshop on Robot and Human Interactive Communication*, 95-100.

[17] Jonghwa, K. and Elisabeth, A. (2008) Emotion recognition based on physiological changes in music listening. *IEEE Transactions on Pattern Analysis and Machine Intelligence*, **30(12)**, 1-17.

[18] Murugappan, M., Rizon, M., Nagarajan, R. and Yaacob, S. (2009) An Investigation on visual and audiovisual stimulus based emotion recognition using EEG. *Transactions on Medical Engineering and Informatics*, **1(3)**, 342-356.

[19] Jung, T. (2000) Removing electroencephalographic artifacts by blind source separation. *Journal of Psychophysiology*, **37(2)**, 163-178.

[20] Gott, P.S., Hughes, E.C. and Whipple. (1984) Voluntary control of two lateralized conscious states: Validation by electrical and behavioral studies. *Journal of Neuropsychological*, **22**, 65-72.

[21] Mallat, S.G. (1989) A theory for multi-resolution signal decomposition: The wavelet representation. *IEEE Transactions on Pattern Analysis and Machine Intelligence*, **11(7)**, 674-693.

[22] Merzagora, A.C., Bunce, S., Izzetoglu, M. and Onaral, B. (2006) Wavelet analysis for EEG feature extraction in deceptive detection. *IEEE Proceedings on EBMS*, **6**, 2434-2437.

[23] Chethan, P. and Cox, M. (2002) Frequency characteristics of wavelets. *IEEE Transactions on Power Delivery*, **17(3)**, 800-804.

[24] Charles, W.A. and Zlatko, S. (1997) Classification of EEG signals from four subjects during five mental tasks. *IEEE Proceedings on Engineering Application in Neural Networks*, 407-414.

[25] Wanpracha, A.C., Ya-ju, F. and Rajesh, C.S. (2007) On the time series k-nearest neighbor classification of abnormal brain activity. *IEEE Transactions on Systems, Man and Cybernetics–Part A*: *Systems and Humans*, **37(6)**, 1005- 1016.

J. Biomedical Science and Engineering, 2010, 3, 397-404 **JBiSE**
doi:10.4236/jbise.2010.34055 Published Online April 2010 (http://www.SciRP.org/journal/jbise/).

Prokaryotic expression, purification of a novel candidate tumor suppressor gene FUS1 and characterization of its polyclonal antibodies

Dong-Mei Zhang, Han-Shuo Yang, Xin-Yu Zhao, Wen Zhu, Zhi-Hua Feng, Yang Wan, Zhi-Wei Zhao, Ming-Hai Tang, Nong-Yu Huang, Yu-Quan Wei

State Key Laboratory of Biotherapy, West China Hospital, West China Medical School and School of Life Sciences, Sichuan University, Chengdu, China.
Email: yuquawei@vip.sina.com; zwjulia@163.com

Received 6 June 2009; revised 27 November 2009; accepted 4 December 2009.

ABSTRACT

FUS1 is a novel candidate tumor suppressor gene identified in human chromosome 3p21.3. Its expression showed significantly reduction or even loss in lung cancer and other types of cancers. In order to further investigate the biological function of FUS1 protein, FUS1 cDNA from MRC-5 cells was amplified by RT-PCR and cloned into prokaryotic expression vector pQE-30. The recombinant expression plasmids were transformed into M15 strain and grown at 20℃ or 37℃. SDS–PAGE analysis revealed that the accumulation of the recombinant protein FUS1 (rFUS1) in inclusion body forms reached maxium amount when induced with 0.5 mM IPTG for 5 h at 37℃. The inclusion bodies were solubilized in 2M urea and purified by a 6 × His tagged affinity column under denaturing condition. The purified rFUS1 was identified by electrospray ionization-mass spectrometry (ESI-MS) and tested for purity by HPLC chromatography. The purified rFUS1 proteins were then used to immunize rabbits to obtain anti-human FUS1 polyclonal antibodies, which were suitable to detect both the recombinant exogenous FUS1 and the endogenous FUS1 from tissues and cells by western blot and immunohistochemistry, Available purified rFUS1 proteins and self-prepared polyclonal antibodies against FUS1 may provide effective tools for further studies on biological function and application of FUS1.

Keywords: FUS1; Polyclonal Antibody; Prokaryotic Expression; Recombinant Protein; Tumor Suppressor Gene

1. INTRODUCTION

With a rapidly increasing incidence and a low cure rate, lung cancer has been the most common malignancy and leading cause of cancer deaths in the world [1]. Therefore, identification of new therapeutic targets and novel strategies are essential to improve the survival of patients diagnosed with this disease. FUS1 is a novel tumor-suppressor gene located on the human chromosome 3p21.3 region [2]. Genetic alterations and allelic loss of 3p21.3 are among the most frequent and earliest cancer abnormalities detected in the pathogenesis of lung cancers. This phenomenon occurs in almost 100% of small cell lung cancers (SCLCs) and more than 80% of non-small-cell lung cancers (NSCLCs) [3]. FUS1 functions as “gatekeepers” of human cancer and plays a very important role in lung cancer development [4,5]. A majority of human lung cancers have been found loss of expression, haploinsufficiency or deficiency of post-translational of FUS1 [2,6,7]. FUS1 was recently demonstrated to mediate accumulation of p53 protein, and thus led to the apoptosis and cell cycle arrest in the early stages of lung cancer progression [8,9].However, many properties of FUS1 biological functions as well as its action mechanism are not well understood and little is known about its basic structure–function relationships. Therefore, the expression and the preparation of recombinant protein FUS1 and its polyclonal antibody should provide effective experimental tools for further identifying its mechanism and biological functions against cancers.

In the present study, the full length FUS1 with six histidine (6 × His) residues was expressed in *Escherichia coli* M15. The recombinant protein was purified by urea and identified by electrospray ionization-mass spectrometry analysis (ESI-MS). The polyclonal antibodies against FUS1 were prepared which were suitable to detect the presence of both the exogenous and endogenous FUS1 efficiently by western blot and immunohistochemistry. The self-prepared polyclonal antibodies may be applied as the effective tools for investigating the further molecular mechanisms of FUS1.

2. MATERIALS AND METHODS

2.1. Materials

Escherichia coli strain JM109 and M15 were maintained by our Lab. The human non-small-cell lung cancer (NSCLC) cell line A549 and normal human lung fibroblast cell line MRC-5 were obtained from ATCC and were maintained in RPMI 1640 or DMEM supplemented with 10% FCS respectively. pQE-30 plasmid was purchased from Qiagen (Germany). Human paracancerous normal lung tissues and lung cancer tissues were obtained from Department of Thoracic and Cardiovascular Surgery, West China Hospital, Sichuan University. Restriction endonucleases, T4 DNA ligase and prestained low range protein molecular weight marker were products of MBI Fermentas (Lithuania). The High Fidelity PrimeScript™ RT-PCR Kit was purchased from TaKaRa (Dalian, China). All PCR products used for cloning were confirmed by sequencing at Invitrogen Biotechnology Co., Ltd (Shanghai, China). pVITRO2-FUS1 plasmid was constructed by our Lab.

2.2. Total RNA Isolation

Total RNA was isolated from MRC-5 cells using a standard Trizol RNA isolation protocol. Prior to use, RNA concentration was spectrophotometrically determined, and RNA integrity was verified by electrophoresis.

2.3. RT-PCR Amplification of FUS1 cDNA

The cDNA of full length FUS1 was prepared using a High Fidelity PrimeScript™ RT-PCR Kit according to the manufacturer instructions. Based on the FUS1 cDNA sequence (GenBank accession No. **AF055479**), a pair of primers was designed as follows: 5'-CGCGGATCCATGGGCGCCAGCGGGTCCAAAG-3'(sense) and 5'-CCGGTCGACTCACACCTCATAGAG GATCACAG-3'(anti-sense). The sense and anti-sense primers were introduced *BamHI* and *SalI* restriction sites (underlined) respectively.

2.4. Plasmid Construction and Identification

The amplified FUS1 cDNA and expression vector pQE-30 were digested with restriction enzymes *BamHI/SalI* respectively. The digested products were separated on a 1% agarose gel and the bands were extracted. The purified FUS1 cDNA and the linear vector were ligated overnight at 16℃ with T4 DNA ligase followed by transformed into *E.coli* JM109 competent cells. The transformation mixture was plated on to LB agar plates containing ampicillin (100 μg/ml). The plates were incubated for 16h at 37℃. The desired recombinant plasmid pQE-30-FUS1 was confirmed by PCR and restriction enzyme digestion with *BamHI/SalI* and DNA sequencing (Invitrogen).

2.5. Expression of Fusion Proteins

E. coli M15 cells were transformed with recombinant plasmid pQE-30-FUS1 extracted from JM 109. The bacteria cells were cultured at 37℃ in 5 ml LB liquid medium with 100 μg/ml ampicillin for 4-6 h at 220 rpm till to an absorbance of 0.6 at 600 nm. Expression of the fusion protein was induced by isopropyl-β-D-thiogalactopyranoside (IPTG) with a final concentration of 0.5 mM for 5 h at 37℃. A time and temperature course of expression and solubility to determine the optimal induction conditions for maximum expression of protein was measured by taking aliquots of cells at 1, 2, 3, 4 and 5 h after induction with IPTG at 37℃ and 20℃ These samples were harvested by centrifugation at 13,000 rpm for 1min. The pellets were resuspended in PBS (pH 8.0) and sonicated for 6 × 10 s with 10 s pauses at 20 W on ice. The total lysate induced with IPTG was divided into soluble and insoluble fractions by centrifugation at 15,000 rpm for 2 min at 4℃. The expression and solubility of FUS1 protein were then analyzed in parallel by 15% SDS–PAGE followed by staining with Coomassie Brilliant Blue R-250. The protein extracts of cells transformed with the uninduced bacteria were used as the control.

2.6. Extraction of Fusion Proteins

For large scale expression and purification, M15 strain was transformed with the plasmid and cultured in 1 L of LB medium at 37℃ until to an absorbance of 0.6 at 600 nm followed by induction of 0.5 mM IPTG at 37℃ for an additional 5 h before harvested. The cells were harvested by centrifugation at 4,000 rpm for 20 min at 4℃. The pellet was resuspended in PBS (20mM PB, 500 mM NaCl, pH 8.0). Extraction was performed using a French Pressure Cell Press (APU Co., 04010008) at an internal pressure of 800 psi [10]. The remaining pellet was then harvested by centrifugation at 15,000 rpm for 30 min at 4℃. The supernatant (soluble fraction) was collected for analysis later. The inclusion bodies were weighted and solution buffer (20 mM PB, 500 mM NaCl, 2 M urea, Ph 8.0) were pulled to suspend the cells, then the supernatant were collected by centrifugation at 15000 rpm for 30 min at 4℃. The purified recombinant protein was confirmed by SDS-PAGE and Western blotting using anti-His monoclonal antibody conjugate to HRP. The concentration of the protein was determined according to Bradford [11].

2.7. rFUS1 Identification by ESI-MS Analysis

The presence of purified rFUS1 in the eluted fractions was separated on 15% SDS–PAGE and identified by electrospray ionization (ESI)-mass spectrometry (MS). The gel band stained with Coomassie brilliant blue R-250 was excised minced, reduced, alkylated with io-

doacetamide, In-gel digestion of proteins was carried out with 12.5 ng/μl mass spectrometry grade Trypsin Gold (Promega) for 12-16 h at 37℃ [12]. The tryptic peptides were extracted twice with the buffer containing 50% ACN /0.1% TFA for 15 min, and the solutions were combined together. Mass spectra were acquired using an ESI-Q-TOF mass spectrometer (Micromass, Manchester, UK) with 15 μl of tryptic peptides solution. The MS/MS data were acquired by the software of MassLynx (Micromass) and converted to PKL files by the software of ProteinLynx 2.2.5 (Waters) were then analyzed using °MASCOT search engine (http://www.matrixscience. com).

2.8. Preparation, Purification of rFUS1 Polyclonal Antibodies

The purified rFUS1 was used to prepare antibodies in New Zealand white rabbit. The rabbit was first immunized subcutaneously with rFUS1 (200 μg) in complete Freund's adjuvant. Two booster injections were given in incomplete Freund's adjuvant every week. The serum was collected 7 days after the 3rd immunization to determine the antibody titer by enzymelinked immunosorbent analysis (ELISA). The last immunization was performed one week later, and the antiserum was collected through heart after 7 days. The rabbit IgG fraction was precipitated from the immune serum with 50% saturated $(NH_4)_2SO_4$ and purified by DEAE-Sepharose column chromatography.

2.9. Specificity Analysis of the Polyclonal Antibodies by Western Blot

The specificity of the antiserum was tested by western blot analysis using the total proteins of MRC-5 cells and those of A549 cells transfected with FUS1 constructs. rFUS1 and the total proteins of A549 cells untransfected were used as control. The cells were harvested and lysed in lysis buffer [10 mM Tris/HCl, pH 8.0, 150 mM NaCl, 1% Triton X-100 and 1 mM DTT supplemented with protease and phosphatase inhibitors (2 mM sodium orthovanadate, 100 nM okadaic acid, 1 mM NaF, 1 mM β-glycerophosphate and cocktail (Sigma)] according to the related methods [13]. The protein samples were separated on 15% SDS-PAGE and electrophoretically transferred onto PVDF (polyvinyllidenefluoride) membrane. After blocking overnight in 5% (w/v) non-fat milk, the PVDF membranes were incubated with serum at a dilution of 1:1000 for 2 h. The membranes were washed three times with TBST buffer and then incubated in goat anti-rabbit IgG conjugated with HRP at a dilution of 1:10000 for 1 h at 37℃.After washing two times with TBST buffer, one time with TBS then analyzed using the enhanced chemiluminescence detection system and exposed to Kodak BioMax X-ray film for 2-5 min.

2.10. Cell and Tissue Immunohistochemistry

In order to further confirm that the polyclonal antibodies against rFUS1 are suitable for application in recognizing the innate FUS1 proteins from cells or tissues, immunohistochemistry was performed in A549 cells transfected with FUS1 constructs and normal lung tissue respectively. A549 cells were seeded onto coverslips and cultured in RPMI-1640 with 10% (v/v) FBS (fetal bovine serum) at 37℃ in 5% CO2. The cells were transfected with recombinant plasmid pVITRO2-FUS1 and vector pVITRO2 when cell confluence reached 60%. Hoechst 33258 staining was used to identify apoptosis induced by FUS1 expression in A549 cells. At 48 h post-transfection, cells were fixed with fresh Carnoy's fixative, stained with Hoechst 33258 for 30 min at the concentration of 0.5 μg/ml. Stained nuclei were detected after washing twice with distilled water and observed under a fluorescence microscope. At the same time, the coverslips transfected with pVITRO2-FUS1 was immersed in ice-cold acetone to fix for 20 min on ice. The cell was permeabilized with 0.2% Triton X-100 for 10 min after washing two times with deionized water, the slips were blocked with goat serum albumin at 37℃ for 15 min, the anti-rFUS1 polyclonal serum was used as the primary antibody (1:750). The second antibody was a biotinylated goat anti-rabbit IgG. The cells were then stained with HRP–streptavidin reagents (Dako) and DAB. Brown staining was considered positive.

As for tissue immunohistochemical analysis, normal lung tissues were fixed in 10% buffered neutral formalin and embedded in paraffin. Then, indirect immunostaining for FUS1 was performed on paraffin-embedded tissues by using the LSAB (labelled streptavidin–biotin) method to visualize antibody response as described above.

3. RESULTS AND DISCUSSION

3.1. Construction and Identification of Expression Plasmid pQE-30-FUS1

For amplification of FUS1 cDNA, RT–PCR was performed with total RNA from MRC-5 cell as the template, using gene-specific primers containing a *Bam*H I site or a *Sal* I site to facilitate cloning into expression plasmid pQE-30. A DNA fragment, approximate 350 bp in length, was obtained as shown (**Figure 1(a)**), which is consistent with the FUS1 cDNA 333 bp in length.

The amplified FUS1 cDNA was inserted into the sites of *Bam*H I and *Sal* I in the expression plasmid pQE-30. The recombinant plasmid pQE-30-FUS1 was verified by PCR using FUS1-specific primer and restriction endonuclease digestion with *Bam*H I/*Sal* I (**Figure 1(b)**) and DNA sequencing (data not shown).

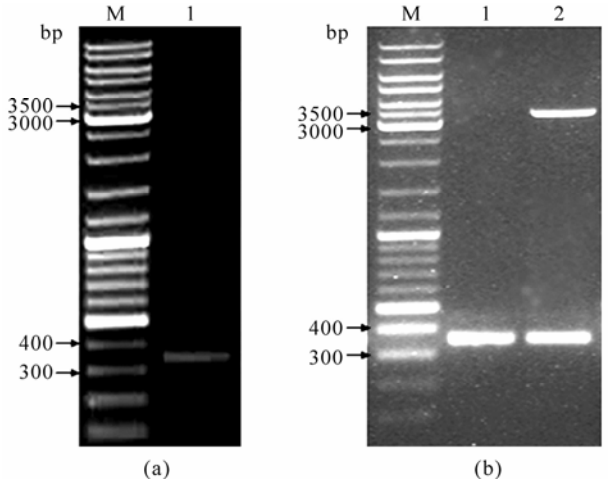

Figure 1. Cloning of FUS1 cDNA and identification of recombinant plasmid pQE-30-FUS1. (a) FUS1 cDNA was amplified from the total RNA of MRC-5 cell by RT-PCR. M: DNA marker; lane 1: FUS1 cDNA fragment. (b) Recombinant plasmid pQE-30-FUS1 was identified by PCR and *Bam*H I/*Sal* I digestion. M: DNA marker; lane 1: FUS1 cDNA fragment obtained by PCR using FUS1-specific primers with recombinant plasmid as template; lane 2: DNA fragments obtained by *Bam*H I/*Sal* I digestion.

3.2. Expression and Solubility Identification of pQE-30-FUS1

The rFUS1 was produced in *E. coli* M15 as a fusion protein with 6 × His tag at the N-terminus. The expressed protein was approximate 16 kDa. The *E. coli* cells containing recombinant plasmid pQE-30-FUS1 were cultured in 5 ml of LB medium by adding IPTG at a final concentration of 0.5 mM. The solubility of FUS1 protein was examined by varying induction temperature from 20℃ to 37℃. No observable difference was observed in the expression form of the rFUS1. SDS-PAGE analysis revealed that the expression of FUS1 in *E.coli* was mainly in insoluble form (**Figure 2**). In addition, we also constructed recombinant plasmid pET-32a (+) -FUS1. When it was expressed in *E. coli*, no significant difference in the solubility of the rFUS1 was observed, except that there was more hybridprotein in inclusion bodies which enhanced the difficulty of the purify of recombinant protein than plasmid pQE-30-FUS1 (data not shown). Therefore, in the present study, FUS1 expression from pQE-30-FUS1 was induced with 0.5 mM IPTG for 5 h at 37℃ for further experiments.

In order to determine the optimal induction time for maximum expression of the protein, the cells were incubated for 1 to 5 h after IPTG was added. The rFUS1 protein showed expression at 1 h post-induction and the maximum protein amount could be achieved at the fifth hour at 37℃ (**Figure 2(a)**), while its synthesis rate was low at 20℃ (**Figure 2(b)**).

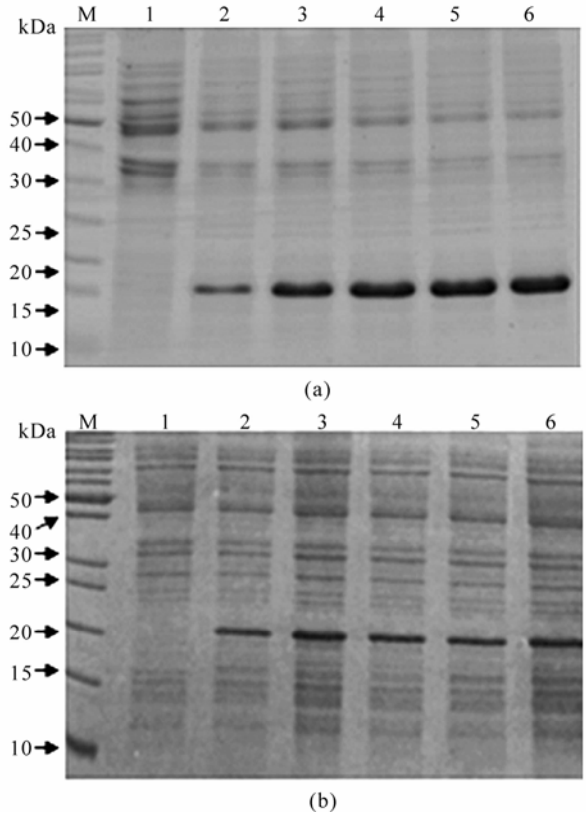

Figure 2. SDS-PAGE analysis of recombinant protein FUS1 produced in *E. coli* M15 by induced with 0.5 mM IPTG at 37℃ (a) and 20℃ (b) from 1 to 5 hours. The cell lysates were analyzed every one hour after IPTG induction. M: protein molecular marker; lane 1: total bacterial protein without IPTG induction; lane 2-6: total bacterial protein at the established time ends.

3.3. Purification of rFUS1

15% SDS-PAGE analysis revealed that the expression of rFUS1 in *E. coli* M15 was nearly 100% in insoluble forms at 37℃ for 5 h (**Figure 3(a)**). For purification of the recombinant protein FUS1, cells collected from 1 liter LB culture were pressured by a French Pressure Cell Press. The inclusion bodies were harvested by centrifugation at 15,000 rpm for 30 min at 4℃. The pellet was washed by gradient urea from 1 M to 8 M [14]. The inclusion bodies began to dissolve in 2M urea buffer. More rFUS1 were dissolved to a gradually increasing concentration of urea with more hybrid proteins. So the inclusion bodies were dissolved in 2 M urea buffer. After purification, rFUS1 were analyzed by 15% SDS-PAGE and showed a single band at the expected molecular mass (16 kD) on SDS-PAGE (**Figure 3(b)**). The purity of the rFUS1 protein was proved to be higher than 90% by HPLC chromatography (data not shown) and the protein concentration was determined using Bradford reagent.

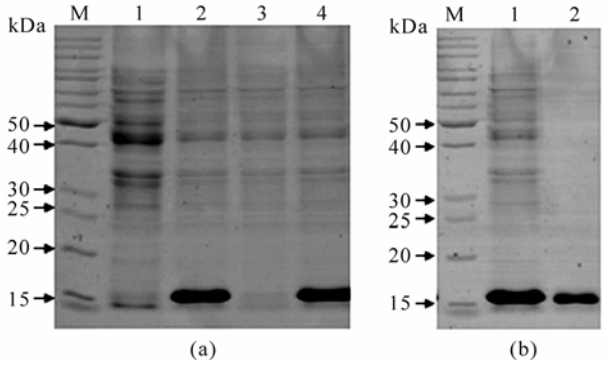

Figure 3. Solubility identification and purification of rFUS1 in E. coli M15. (a) the M15 cells were cultured at 37℃ , induced with 0.5 mM IPTG for 5 h and assayed by SDS-PAGE analysis. Lane 1: total bacterial protein without IPTG induction; lane 2: total bacterial protein with IPTG induction; lane 3: supernatant with IPTG induction; lane 4: precipitate with IPTG induction; (b) Purification of rFUS1.Lane 1: The precipitate of total bacterial protein containing rFUS1 with IPTG induction. Lane 2: purified rFUS1; M: protein molecular marker.

3.4. Western Blot Anlysis of the Purified rFUS1

After SDS–PAGE, rFUS1 was transferred to a nitrocellulose membrane. The membrane was incubated with blocking buffer [0.1% Tween and 5% non-fat milk in Tris-buffered saline (TBS)] overnight at 4℃ and then with the anti-His-tag monoclonal antibody conjugate HRP diluted 1:1000. The membrane was washed 3 times with washing solution (Tween 0.1% in TBS) and incubated with an antimouse peroxidase-conjugated antibody (KPL) diluted 1:5000. After washed 3 times with washing solution, the membrane was treated with SuperSignal West Pico Chemiluminescent Substrate (Pierce) for 5 min, then exposed to HyperWlm (Amersham Biosciences) for 5 min and visualized. The purified rFUS1 was verified successfully using Western-blot analysis through anti-His-tag mAb (**Figure 4**).

3.5. rFUS1 Identification by ESI-MS Analysis

The purified recombinant FUS1 proteins were further validated by ESI-MS analysis. The result from MS data suggested that the identified protein exactly matched with human FUS1 protein, which had a Mascot score 1018. MS/MS analysis revealed that seven unique peptide unambiguously matched to the target FUS1 protein (**Figure 5(a)**). For example, MS/MS spectrum of parent ion 861.7737 and the result of peptide sequence query were shown in **Figure 5(b)**. All matched peptides were shown in **Figure 5(c)** (underlined), which indicated that the purified recombinant protein FUS1 were completely correct. A sufficient amount of purified FUS1 protein would make it possible to prepare polyclonal antibodies against FUS1 and to further analyze its interacting proteins or structure by X-ray crystallography.

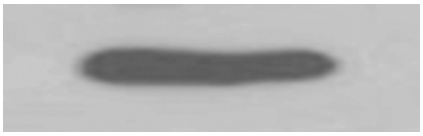

Figure 4. Analysis of purified rFUS1 by Western blot. The purified recombinant protein FUS1 was separated on 15% SDS-PAGE and probed by with anti-His tag mAb conjugated with HRP (1:10000). Chemiluminescence immunoassay was used for color development.

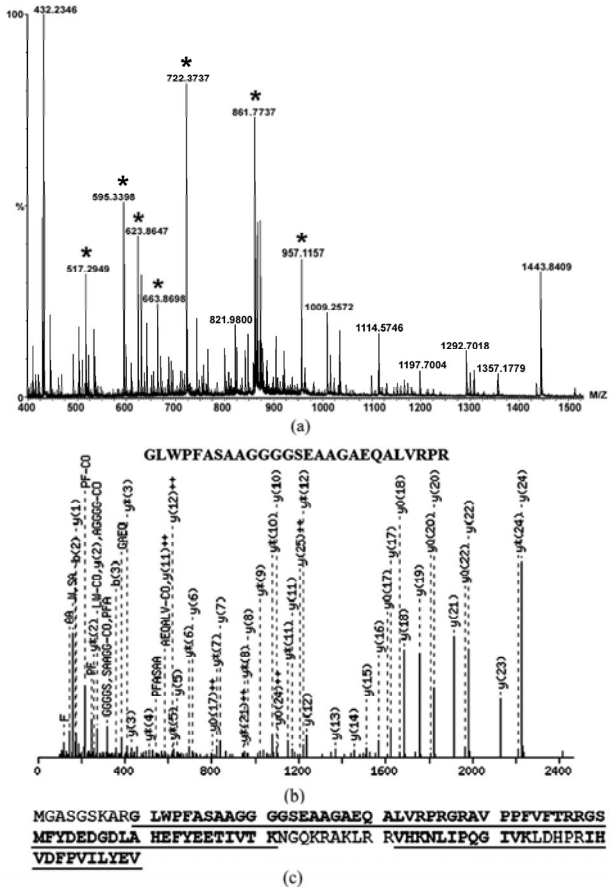

Figure 5. ESI–MS/MS identification of tryptic peptides from the purified recombinant protein. (a) mass spectrogram of tryptic peptides from purified FUS1 protein. Totally 7 unique peptides were matched to target protein; (b) MS/MS spectrum of parent ion 861.7737 as an example. Data base search indicated its peptide sequence was GLWPFASAAGGGGSEAAGAEQALVRPR, which was a part of the sequence of FUS1; (c) matched peptides (underlined).

3.6. Characteristics of Antiserum Against FUS1

The specificity of the antiserum from rabbit against purified rFUS1 and total proteins extracted from MRC-5 was checked by Western blot analysis. FUS1 has been proved no protein level expression in A549 cells though FUS1

mRNA was detectable [3,6]. Therefore, total proteins from A549 cells transfected with expression plasmid pVITRO2-FUS1 was also used in Western blot. The result indicated that the antiserum from rabbit can recognize both exogenous recombinant FUS1 and endogenous FUS1 effectively. There were positive bands at the position of approximately 16 kDa (**Figure 6**). However, non-immunized serum was negative (data not shown).

The FUS1 protein is proved to be indeed present in the cytoplasm and may have a role in signal transduction [8]. In the present study, FUS1-negative A549 cells were stained with Hoechst 33258 after 24 h transient transfection with pVITRO2-FUS1. More hypercondensed nuclei and apoptotic bodies appeared in the transfected A549 cells (brightly stained; **Figure 7(c)**) comparing with that in the control cells (**Figure 7(a)** and **(b)**). The result of FUS1 inducing apoptosis consisted with the findings reported previously by Ji *et al.* and Ito *et al.* [8,15] FUS1-mediated apoptosis is proved to be associated with the accumulation of p53 protein, the down-regulating expression of MDM2 and the activation of Apaf1-drivened mitochondrial apoptotic pathway [9]. However, the exact mechanism of inactivation of FUS1 in human tumorigenesis and its role in FUS1-mediated tumor suppression are still unclear and need to be investigated in detail.

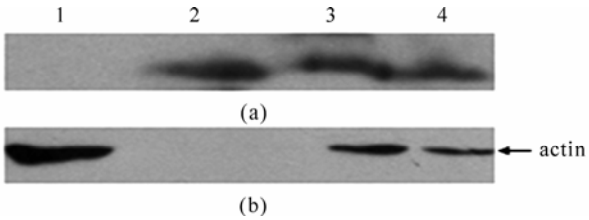

Figure 6. Western-blot analysis of FUS1 expression using the rabbit antiserum (1:1000). (a) the total protein from A549 (lane 1), purified rFUS1 (lane 2), the total protein from MRC-5 cells (lane 3) and the total protein from A549 cells after transient transfection with FUS1 constructs (line 4) were loaded. Horse radish peroxidase-conjugated goat anti-rabbit IgG (1:10000) and enchanced chemiluminescence were used for color development; (b) the same blots were probed by β-actin as control.

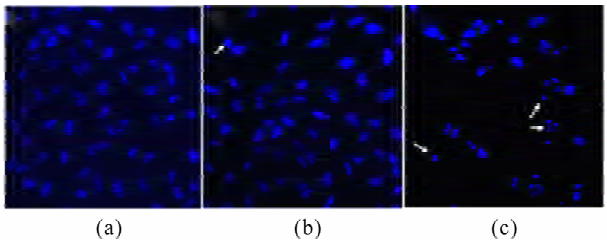

Figure 7. Induction of apoptosis in A549 cells by the expression of FUS1. (a) the untreated A549 cells as negative control; (b) A549 cells transfected with pVITRO2; (c) A549 cells transfected with pVITRO2-FUS1. At 24 h post-transfection, the cells were stained with Hoechst 33258. The arrows indicated the representatives of apoptotic cell. Original magnification, × 200.

To further elucidate the relationship between FUS1 expression and apoptosis, the self-prepared anti-rFUS1 polyclonal antibodies were used for immunostaining in A549 cells transfected with pVITRO2-FUS1 and untreated cells. At the same time, immunohistochemistry was also performed in paracancerous normal lung tissues and lung cancer tissues. There were strong brown staining in the cytoplasm of A549 cells transfected with FUS1 constructs and that of paracancerous normal lung tissues (**Figure 8(a)** and **(c)**). However, no immunostaining was observed in the cytoplasm of non-transfected A549 cells and that of lung cancer tissues (**Figure 8(b)** and **(d)**). These results are consistent with previous findings and provide further evidence that FUS1 plays important roles in tumor-suppression function and lung cancer development. The similar results were obtained in liver, stomach,

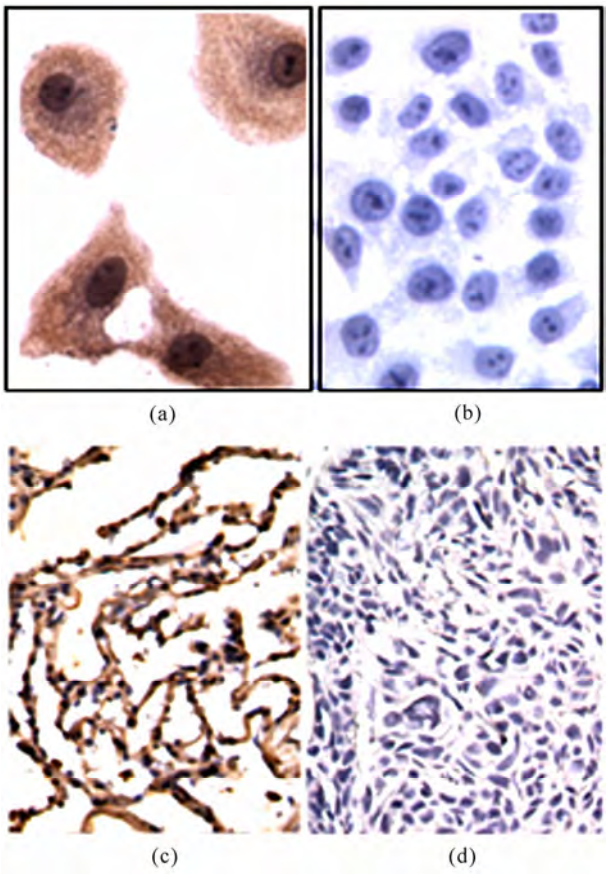

Figure 8. Analysis of FUS1 expression using the self-prepared rabbit anti-human rFUS1 polyclonal antibodies (1:750). Immunostaining was performed in A549 cells transfected with pVITRO2-FUS1 or not (a and b) and paracancerous normal lung tissues and lung cancer tissues (c and d). The anti-FUS1 polyclonal antibodies (1:750) can recognize the FUS1 protein in the cytoplasm of A549 cells transfected with FUS1 constructs and that of paracancerous normal lung tissues (a and c) comparing with the corresponding controls (b and d). Brown staining showed the positive results. Haematoxylin staining showed the cell nuclei. Original magnification, × 200.

cervix, endometrial and ovarian carcinomas when using the self-prepared anti-FUS1 polyclonal antibodies (data not shown).

4. CONCLUSIONS

FUS1 is a novel tumor-suppressor gene located on human chromosome 3p21.3 that is frequently deleted in human lung and breast cancers. But there is no commercial antibody against full-length FUS1 until now. In the present work, human full-length FUS1 cDNA was cloned and expressed as a fusion protein with six histidine (6 × His) tag in *E. coli*. The purified recombinant protein was identified by ESI–MS (electrospray ionization MS) analysis. Furthermore, the specific and sensitive polyclonal antibodies against full-length FUS1 were raised, which were suitable to detect both the recombinant exogenous FUS1 and the endogenous FUS1 from tissues and cells by western blot and immunohistochemistry. To our knowledge, this is the first report of soluble expression and purification of rFUS1 protein and generation of antifull-length FUS1 polyclonal antibodies so far. The purified rFUS1 proteins and self-prepared polyclonal antibodies against FUS1 may provide effective tools for further studies on biological function and mechanism of FUS1 in pathogenesis of lung and other carcinomas in the future.

FUS1 protein expression rarely existed in human primary lung cancer tissue using the self-prepared polyclonal antibodies, while it can be detected in cytoplasm of normal lung tissues. The similar result was also testified in A549 cells transfected with or without FUS1 constructs. These results are consistent with previous findings and provide further evidence that FUS1 plays important roles in tumor-suppression function and lung cancer development.

5. ACKNOWLEDGEMENTS

This work was supported by the grant from the National Key Research Program for New Drug Development (2009ZX09301-004).

REFERENCES

[1] Jemal, A., Siegel, R., Ward, E., Hao, Y., Xu, J., Murray, T. and Thun, M.J. (2008) Cancer statistics. *A Cancer Journal for Clinicians*, **58**, 71-96.

[2] Kondo, M., Ji, L., Kamibayashi, C., Tomizawa, Y., Randle, D., Sekido, Y., Yokota, J., Kashuba, V., Zabarovsky, E., Kuzmin, I., Lerman, M., Roth, J. and Minna, J.D. (2001) Overexpression of candidate tumor suppressor gene FUS1 isolated from the 3p21.3 homozygous deletion region leads to G1 arrest and growth inhibition of lung cancer cells. *Oncogene*, **20**, 6258-6262.

[3] Lerman, M.I., Glenn, G.M., Daniel, L., Latif, F., Hosoe, S., Brauch, H., Hampsch, K., Delisio, J., Orcutt, M. and Zbar, B. (1990) A new polymorphic probe on chromosome 3p: Lambda LIB28-77 (D3S169E). *Nucleic Acids Research*, **18**, 205.

[4] Lerman, M.I. and Minna, J.D. (2000) The 630-kb lung cancer homozygous deletion region on human chromosome 3p21.3: Identification and evaluation of the resident candidate tumor suppressor genes. The International Lung Cancer Chromosome 3p21.3 Tumor Suppressor Gene Consortium. *Cancer Research*, **60**, 6116-6133.

[5] Zabarovsky, E.R., Lerman, M.I. and Minna, J.D. (2002) Tumor suppressor genes on chromosome 3p involved in the pathogenesis of lung and other cancers. *Oncogene*, **21**, 6915-6935.

[6] Uno, F., Sasaki, J., Nishizaki, M., Carboni, G., Xu, K., Atkinson, E.N., Kondo, M., Minna, J.D., Roth, J.A. and Ji, L. (2004) Myristoylation of the FUS1 protein is required for tumor suppression in human lung cancer cells. *Cancer Research*, **64**, 2969-2976.

[7] Prudkin, L., Behrens, C., Liu, D.D., Zhou, X., Ozburn, N.C., Bekele, B.N., Minna, J.D., Moran, C., Roth, J.A., Ji, L. and Wistuba, L.L. (2008) Loss and reduction of FUS1 protein expression is a frequent phenomenon in the pathogenesis of lung cancer. *Clinical Cancer Research*, **14**, 41-47.

[8] Ito, I., Ji, L., Tanaka, F., Saito, Y., Gopalan, B., Branch, C.D., Xu, K., Atkinson, E.N., Bekele, B.N., Stephens, L.C., Minna, J.D., Roth, J.A. and Ramesh, R. (2004) Liposomal vector mediated delivery of the 3p FUS1 gene demonstrates potent antitumor activity against human lung cancer in vivo. *Cancer Gene Therapy*, **11**, 733-739.

[9] Deng, W.G., Kawashima, H., Wu, G., Jayachandran, G., Xu, K., Minna, J.D., Roth, J.A. and Ji, L. (2007) Synergistic tumor suppression by coexpression of FUS1 and p53 is associated with down-regulation of murine double minute-2 and activation of the apoptotic protease-activating factor 1-dependent apoptotic pathway in human non-small cell lung cancer cells. *Cancer Research*, **67**, 709-717.

[10] Tsukamoto, H., Fukudome, K., Kohara, J., Nakatake, H. and Kimoto, M. (2007) Preparation of recombinant murine tumor necrosis factor-alpha in Escherichia coli: A rapid method to remove tags from fusion proteins by thrombin-cleavage and ion-exchange chromatography. *Protein Expression and Purification*, **56**, 138-144.

[11] Bradford, M.M. (1976) A rapid and sensitive method for the quantitation of microgram quantities of protein utilizing the principle of protein-dye binding. *Analytical Biochemistry*, **72**, 248-254.

[12] Zhao, X.Y., Li, H.X., Liang, S.F., Yuan, Z., Yan, F., Ruan, X.Z., You, J., Xiong, S.Q., Tang, M.H. and Wei, Y.Q. (2008) Soluble expression of human DRR1 (down-regulated in renal cell carcinoma 1) in Escherichia coli and preparation of its polyclonal antibodies. *Biotechnology and Appied Biochemistry*, **49**, 17-23.

[13] Benzinger, A., Muster, N., Koch, H.B., Yates, J.R. and Hermeking, H. (2005) Targeted proteomic analysis of 14-3-3 sigma, a p53 effector commonly silenced in cancer. *Molecular & Cellular Proteomics*, **4**, 785-795.

[14] Wilkinson, R.J., Elliott, P., Carragher, J.F. and Francis, G. (2004) Expression, purification, and in vitro characterization of recombinant salmon insulin-like growth factor-II. *Protein Expression and Purification*, **35**, 334-343.

[15] Ji, L., Nishizaki, M., Gao, B., Burbee, D., Kondo, M., Kamibayashi, C., Xu, K., Yen, N., Atkinson, E.N., Fang, B., Lerman, M.I., Roth, J.A. and Minna, J.D. (2002) Ex-

pression of several genes in the human chromosome 3p21.3 homozygous deletion region by an adenovirus vector results in tumor suppressor activities in vitro and in vivo. *Cancer Research*, **62**, 2715-2720.

J. Biomedical Science and Engineering, 2010, 3, 405-414 **JBiSE**
doi:10.4236/jbise.2010.34056 Published Online April 2010 (http://www.SciRP.org/journal/jbise/).

Detection and analysis of the effects of heat stress on EEG using wavelet transform
——EEG analysis under heat stress

Prabhat Kumar Upadhyay[1], Rakesh Kumar Sinha[2], Bhuwan Mohan Karan[1]

[1]Department of Electrical and Electronics Engineering Birla Institute of Technology, Birla, India;
[2]Department of Biomedical Instrumentation Birla Institute of Technology, Birla, India.
Email: uprabhat@rediffmail.com

Received 25 October 2009; revised 17 November 2009; accepted 6 December 2009.

ABSTRACT

Continuous wavelet transform (CWT) method has been applied to capture localized time-frequency information of rat electroencephalogram (EEG) in different vigilance states and analyze alterations in transients during awake, slow wave sleep (SWS), and rapid eye movement (REM) sleep stages due to exposure to high environmental heat. Rats were divided in three group (i) acute heat stress-subjected to a single exposure for four hours in the Biological Oxygen Demand (BOD) incubator at 38°C; (ii) chronic heat stress-exposed for 21 days daily for one hour in the incubator at 38°C, and (iii) handling control groups. After two hours long EEG recordings from young healthy rats, EEG data representing three sleep states was visually selected and further subdivided into 2 seconds long epoch. Powers of wavelet spectra corresponding to delta, theta, alpha, and beta bands at all scales and locations were computed and variation in their states investigated. The wavelet analysis of EEG signals following exposure to high environmental heat revealed that powers of subband frequencies vary with time unlike Fourier technique. Changes in higher frequency components (beta) were significant in all sleep-wake states following both acute and chronic heat stress conditions. Percentage power of different components of the four bands was always found to be varying at different intervals of time in the same signal of analysis.

Keywords: Electroencephalogram; Rat; Sleep; Wavelet transform

1. INTRODUCTION

Environmental heat is one of the well-known stressor to the mankind. Although, the problems of heat-afflicted illness are receiving increased importance in view of the current estimates of global warming and its impact on biological systems, the etiological factors that lead to heat exhaustion and heat stroke have not been well established. Review of literature revealed that the afflictions and damages to the central nervous system (CNS) and alterations in brain cortical potentials or electroencephalogram (EEG) [1] imposed by high environmental temperature have largely been ignored as the likely cause of heat induced mortality, although it is well known that neurochemical and cellular mechanisms of neural tissues are highly temperature sensitive [2].

Over the years, various signal processing techniques have been applied to the analysis of clinical EEG signals which are inherently dynamic, non-linear, stochastic and non-stationary [3-6]. Statistical pattern recognition was one of the first methods used for sleep-EEG analysis [7]. Following this method, quantitative features in terms of intervals were extracted from EEG and optimized [8]. A piece-wise segmentation and clustering techniques had also been developed, that was based on the assumption that an EEG consists of finite number of elementary patterns, which may be determined by dividing the signals a priori into segments of one second each [9]. Among several signal-processing techniques applied for EEG analysis, power spectrum analysis using the fast Fourier transform (FFT) was one of the most popular methods to estimate frequency and amplitude changes [10-13] in different pathological and psychological states. However, this approach considers the EEG signal as a stationary process, which assumption is not satisfied in practice, hence restricting the actual confidence on results. In contrary, the wavelet transform analysis enables to provide time-frequency information simultaneously, and effectively used in many biomedical signal analysis [14-17].

As time-frequency signal's analysis methods offer simultaneous interpretation of the signal in both time and frequency which allows local, transients or intermittent components to be elucidated [18,19]. Many of the ideas

behind wavelet transforms have been in existence for a long time. A strong mathematical framework was built around the basic wavelet idea and is documented in the recent book by Mayer [20], which also shows the connections to earlier results in operator theory. Wavelet transform analysis has now been applied to a wide variety of biomedical signals including the electromyogram (EMG), EEG, clinical sounds, respiratory patterns and blood pressure trends [21].

Application of wavelet transform is found to be very much useful in automated analysis of medical signals and other signal processing tasks [22-27], automatic recognition of vigilance state, where prediction of the level of drowsiness was examined and delta, theta, alpha, and beta sub-frequencies of the EEG signals were extracted by using the wavelet transform technique [14]. In near past, variation of component powers in different frequency bands of rat electroencephalogram under slow wave sleep was also studied using wavelet transform [17]. Dynamic state recognition and event-prediction are fundamental tasks in biomedical signal processing. Therefore, motivated by adaptive time frequency patterns and data compression capabilities of wavelet transforms, a system has been made to identify the changes in sleep EEG spectral patterns due to exposure to high environmental heat.

2. MATERIALS AND METHODS

2.1. Subjects and Electrode Implantation

The experiments were carried out with male Charles Foster rats of age 12-14 weeks and weight around 180-200 grams at the beginning of the experiment. The rats were individually housed in polypropylene cages (30 cm × 20 cm × 15 cm) with drinking water and food (Hindustan Liver Limited, India) *ad libitum*. All rats were kept in an ambient environment temperature of 23 ± 1 °C from birth and the animal room was artificially illuminated with 12:12 hours Light: Dark cycle, changed at 07.00 hours and 19:00 hours Indian Standard Time (IST).

For the common grounding, midline Frontal stainless steel screw electrode, 1 mm in diameter, and two other similar screw electrodes were used for cortical EEG. Four stainless steel loop electrodes, insulated, except at the tip (two for electrooculogram (EOG) and two for EMG), were also used. Their socket contacts had earlier been prepared to a seven-pin amphitronic connector. Screw and loop electrodes were connected and soldered to the free pins of the connector, connected with thin flexible wires. The EEG and grounding screw electrodes were kept free; however, four pins of EOG and EMG electrodes were fixed in the amphitronics connector with the help of dental acrylic, well before implantation. Screw electrodes were connected and fixed to the socket contact by dental acrylic after fixing them on the skull. Such separate connectors were used for each of the experimental animals for the recording of electrophysiological signals.

2.2. Heat Stress Model

The stress was produced in the rats, by subjecting them in the Biological Oxygen Demand (BOD) incubator (Oceania, India) at preset temperature of 38 ± 1°C and relative humidity 45-50% [33], simulated with the environmental conditions of Varanasi (India) in the months of May and June.

***Acute heat stress*:** Rats were subjected to the incubator for continuous four hours of heat exposure from 8.00 a.m. to 12.00 p.m. for a single day, just before the recording of electrophysiological signals.

***Chronic heat stress*:** Rats were subjected to the incubator for one hour daily for 21 days of chronic heat exposure from 8.00 a.m. to 9.00 a.m. and electrophysiological signals were recorded on 22nd day.

***Control*:** Respective control groups of rats were placed in the incubator at room temperature (23 ± 1°C) and whole procedure was followed exactly similar to that of their stressed groups.

2.3. Electrophysiological Recordings

The test chamber (35 cm × 25 cm × 30 cm) was constructed entirely of perspex and was located in a constantly illuminated (500-600 Lux white light), sound insulated chamber (300 cm × 180 cm × 240 cm). Holes at regular distances were made on the walls of test chamber for proper ventilation. The continuous four hours of recordings of EEG, EOG and EMG were performed from 12.00 hour to 16.00 hours IST on the recording day through the 8 channels Electroencephalograph (EEG-8, Recorders & Medicare Systems, India). The paper recordings were performed with standard amplifier setup (Sinha, 2004) and at the chart speed of 7.5 mm/sec. The digitized data was collected, stored and processed with the help of data acquisition system (AD-LiNK, 8112HG, NuDAQ, Taiwan) and processing software (Visual Lab.-M, Version 2.0c, Blue Pearl Laboratory, USA). The recordings were done with the sampling frequency of 256 Hz and selected data were stored in hard disk in small segments (approximately 2 minutes) in separate data files. Further, for ease of wavelet processing, recorded signals for all three states were split into an epoch of two seconds length.

2.4. EEG Signal Processing with Wavelet

Having acquired the digital data for sleep staging from different subjects, wavelet technique, which is based on multiresolution analysis (MRA), was applied on each signal. The data representing three sleep states such as AWAKE, rapid eye movement (REM) sleep and slow wave sleep (SWS) were selected from the raw EEG data

recorded using VLM software and they were further subdivided into two seconds long epoch. Since the sampling frequency being 256 Hz, one epoch comprises 512 data points. Using Matlab-7 (The Mathworks Inc.), all the epochs were loaded individually on Matlab's editor and converted to MAT files in Matlab's workspace.

Matlab codes calculate all the coefficients for each scale (1 to 128) and for each epoch containing 512 sample points, hence producing a matrix of size [128,512]. Daubechies order-4 wavelet was applied to AWAKE, REM, and SWS sleep EEG data of size [512,1] over scales 1:128, which gives coefficients as a function of time and scale. In order to know the frequency information contained in the signal instead of scales [16], following formula has been used: $F_a = \frac{F_c}{\Delta \cdot a}$.

where, F_a is the pseudo frequency corresponding to scale 'a' (in Hz), F_c is the center frequency or dominant frequency of a wavelet in Hz, defined as the frequency with the highest amplitude in the Fourier transform of the wavelet function, and Δ is the sampling period. Given below are the frequencies corresponding to different levels of decomposition for db-4 wavelet on scales over 1 to 128.

Pseudo frequencies in (Hz)	3.7	7.9	16.6	30.4
Corresponding scales	46	23	11	6

Depending upon the desired frequency information, signals were grouped together into delta (0.5-4 Hz), theta (4-8 Hz), alpha (8-14 Hz), and beta (14-30 Hz) range. After extracting frequency information from the time domain signal and categorizing into delta, theta, alpha, and beta frequency bands, powers of all the four bands of AWAKE, REM and SWS were computed for each subject.

2.5. Body Temperature

Core body temperature was recorded as stress markers for both acute and chronic stress group of rats through the thermistor probe connected to 6-channel telethermometer. The marked probe at 4 cm was inserted to the rectum of the animal and kept static for 1 minute to record the body temperature. For acute stress group, body temperature was recorded before and after the heat exposure. While for the chronic stress group, the body temperature was recorded on every third day just before putting them into the incubator for chronic heat stress.

3. RESULTS

Variation of power in three vigilance states of sleep-EEG under chronic stressed condition has been observed as follows:

***AWAKE*:** It is evident from **Figure 1(a)** that the wavelet coefficients posses considerably larger values between time instants 200-250 and about 475, for which scale vector spans 8-20. The respective frequency band lies between 22.8 Hz to 9.13 Hz. Here, the dominant frequency component that occurs at time instant 480 is 16.6 Hz, which is further followed by 12.2 Hz and other lower frequencies on their respective scales. Between 300 and 430, high frequency components disappear but delta and theta are easily detectable, where delta is found to be most dominant in this interval of time. The powers of delta, theta, alpha, and beta frequency bands of AWAKE state have been plotted as functions of time (samples) and frequency as shown in **Figure 2(a)**, where subject belongs to its respective control group. Powers of all the frequency bands except beta were initially found to be almost equal (from higher to lower order of frequency in

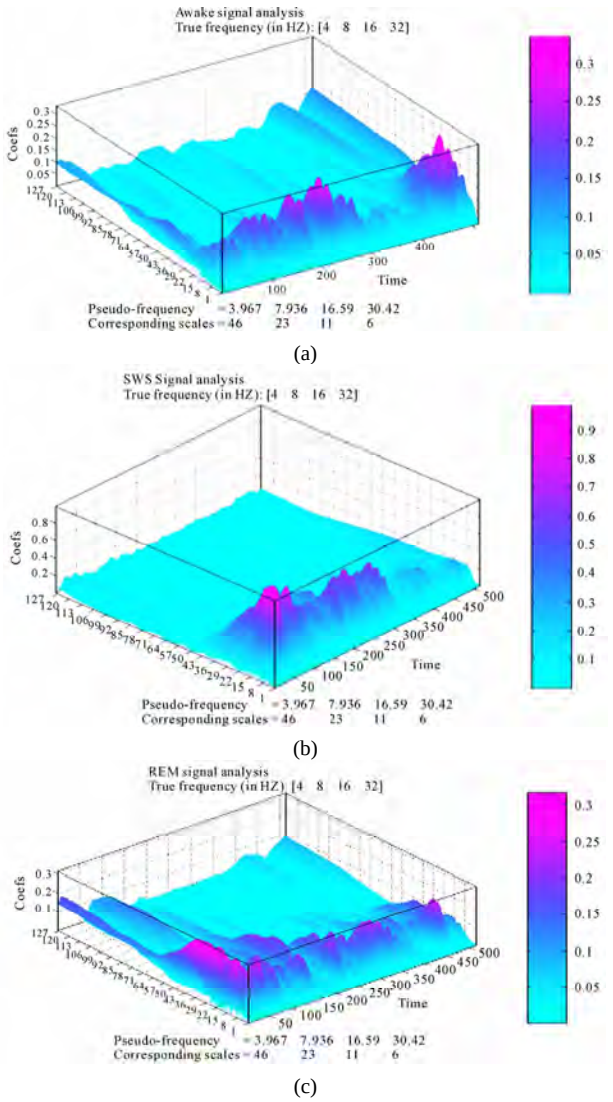

Figure 1. wavelet coefficients calculated and plotted over scales 1:512 (one epoch) for (a) AWAKE; (b) SWS; (c) REM signals subjected to chronic heat stress.

the respective four bands), but for delta and theta bands, the lower frequency components posses more power than the components in the higher frequency side. It may also be seen that more than 40% of the durations, delta and theta bands have negligible power, however theta shows dominating spectrum than delta. It is quite obvious from the plot that power spectrum of AWAKE state shows both alpha and beta to be prominent bands for longer duration but higher frequencies of beta were found to have less power as compared to the lower one, whereas it reverses for alpha band. In the very beginning (between 0-50), theta seemed to have highest power. To study the variation in power, when subject is exposed to chronic heat stress, powers of different bands were plotted as shown in **Figure 2(b)**. Some change in the powers of delta and beta components have been observed, however no change in powers of theta and beta was noted. Powers of the frequency components of delta band appeared to have decreased, whereas for beta band it has increased.

***SWS*:** A plot of wavelet coefficients versus scale and time as shown in **Figure 1(b)** reveals time and frequency information regarding SWS signal taken from control group of chronic heat stress. From scales 1-20 and time interval 50-100, values of the wavelet coefficients are very high, which further showed decreasing trend. For delta, theta, and alpha bands, these values were very low after time instant 300. From **Figure 3(a)**, it is clear that out of the three peaks lying in the time interval 50-100 and scales 15-22, the middle one, which corresponds to frequency 10.2 Hz holds highest power, whereas the other two frequency components (13 Hz and 8.3 Hz) holds almost same power. The appearance of beta waves twice between time instants 150-200 and scales 7-10 has also been noted but found to have least power. During times 30-50 and 170-210, theta was seen in abundance. At many other places on higher scales, delta is present but its power is small. The plot investigating the changes in powers of four frequency bands of SWS signal recorded from subject under chronic heat stress has been shown in **Figure 3(b)**. The effect of stress is not evident for theta and beta bands but variation in power can be seen for delta and alpha bands, which suggests that power of delta has increased in little and power of alpha being reduced. In this case, so far as power is concerned, delta and alpha happen to be the leading frequency bands. Any other remarkable change was not noticed for this epoch. The result reveals that for some periods, where delta has very small power, the other higher frequencies such as alpha and beta show significant amount of power. This analysis is also indicative of the fact that powers of frequencies in different frequency bands varied with time. In addition to this, powers of delta, theta, were very much less in more than quarter of EEG.

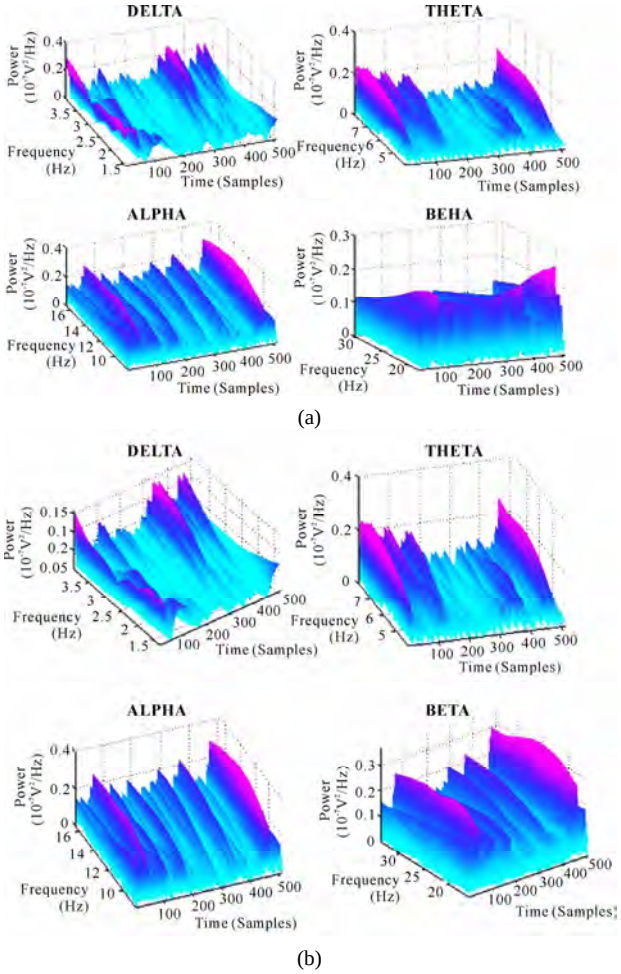

Figure 2. 3-D plots of power against time and frequency of delta, theta, alpha and beta bands of AWAKE signals under exposure to chronic heat stress. (a) control group, (b) respective chronic stressed group.

***REM*: Figure 1(c)** depicts time and scale localization of frequency components of REM signals under chronic heat stress. Coefficient's values were found to be large between scales 7-67 and times 1-50 that covers all frequencies between 26-27 Hz, while, within times 50-512, mostly faster waves were found to have larger values of the wavelet coefficients. At around 200, these coefficients for theta, alpha, and beta bands are quite insignificant but for delta, it is large. As regards the estimation of powers of the components of four bands in respective control group as shown in **Figure 4(a)**, alpha is spread over almost the entire epoch with larger magnitude, all frequency components of beta band were initially found to be present with noticeable power but only the higher frequencies of delta band were seen in the beginning of the epoch with largest power. Components of delta showed poor presence except in the beginning of the epoch where, their powers for few components are comparable to alpha. When heat stress was given to the

subject, the changes in powers of different bands have been shown in **Figure 4(b)**. These changes can undoubtedly be seen for delta and beta bands. In case of stress, the overall power of delta band was found to be decreased, and for beta it has increased. No significant change in the powers of theta and alpha components were noticed. Powers of all the bands showed variations in time nonlinearly.

3.1. Variation of Power Following Acute Heat Stress

After the subjects were exposed to acute heat stress, the effect caused significant change in the powers of some frequency bands, whereas insignificant change in powers of other frequency bands was observed. Reports on the variation of powers of frequency components of delta, theta, alpha and beta bands in AWAKE, SWS and RAM states of sleep-EEG have been presented herein.

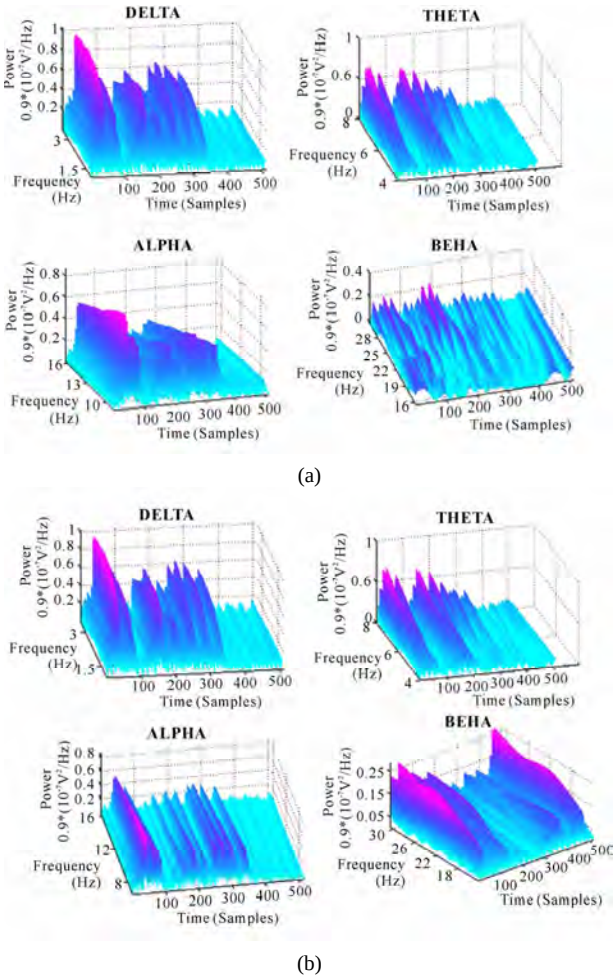

Figure 3. 3-D plots of power against time and frequency of delta, theta, alpha and beta bands of SWS signals under exposure to chronic heat stress. (a) control group; (b) respective chronic stress group.

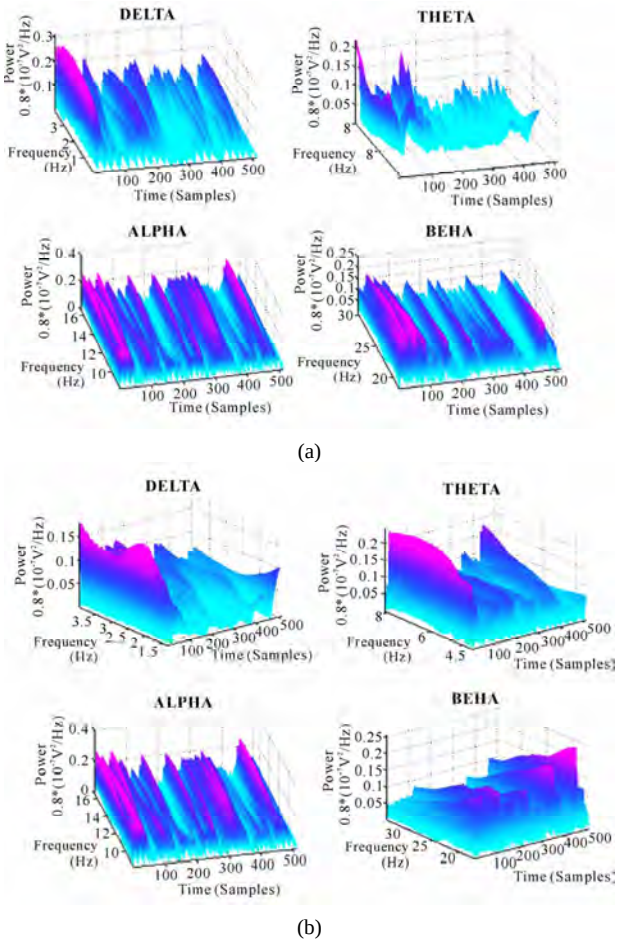

Figure 4. 3-D plots of power against time and frequency of delta, theta, alpha and beta bands of REM signals under exposure to chronic heat stress. (a) control group; (b) respective chronic stressed group.

***AWAKE*:** Wavelet power spectrum as shown in **Figure 5(a)** suggest that higher frequency components of delta in the beginning of the epoch was seen to be higher and for the lower frequencies it gradually decreased. At the end of the epoch, change in this trend has been observed *i.e.*, lower components of delta were high as compared to the upper one. In the middle of the epoch, delta's power was about half of the maximum power. Most of the time, theta components appeared to have greater power than delta and around the time instant 450, two major peaks were found whose powers were almost double the delta's power but on the other hand, in quarter of EEG, it remained very small for all frequencies of theta. All frequencies of alpha greater than 12 Hz acquired larger powers during time 100-250 and at the end too. Components of alpha and to some extent beta with considerable power were seen to exist for longer duration as compared to others. It was also witnessed that for the period, where power of delta was small, alpha band possessed large power. Frequent peaks of beta were no-

ticed during times 100-300 in which lower components of beta were seen to hold more powers than the upper frequencies of the band. At time-480, powers of all the components were roughly equal and large (but less than alpha). So far as change in powers due to exposure of heat stress is concerned, delta, theta, and alpha bands showed negligible change, whereas the power of beta went up **Figure 5(b)**.

***SWS*:** As depicted in **Figure 6(a)**, powers of higher frequencies of delta band among all the bands were found to be largest at time 50 *i.e.*, at the start of the epoch, which further showed decreasing tendency over all the scales till the end of the epoch. Between times 300-512, it had drastically reduced but at the same time faster waves reported their existence with small powers. Next dominant frequency components belonged to theta band for which the highest component of the band held largest power. Theta too, did not show noticeable power during time 300-500. The plot of alpha implies that lower frequencies of alpha, which lies on scale 16-22 (8.3 Hz-11.4 Hz) seemed to have more power and it slightly decreases for the higher frequencies of the same band. Between 220 and 340, many lower frequencies reported their presence with reduced power. After time 340, powers of all frequency components were not worth mentioning. In beta band, two peaks were observed on scale-7 (26.1 Hz) during time 150-170 with equal power, which was quarter of delta power on scale-44. **Figure 6(b)** shows the power spectrum of respective stressed subjects. When subject undergoes exposure of acute heat stress, change in power over all scales was investigated for the three bands-delta, alpha, and beta. Increase in the powers of delta components were noticed at many places in the epoch but on the other hand, powers of alpha and beta components went down, indicating reciprocal relationship between changes in the powers of slow and fast waves.

***REM*:** Having examined the power spectrum of all the four bands as shown in **Figure 7(a)**, it may be noted that there existed more than 60% of time duration in which powers of faster waves (high frequencies of alpha band and low frequencies of beta band) were most significant. In the time interval 140-380 and scale 13-15 (12.2 Hz-14 Hz), powers of all the components were found to be

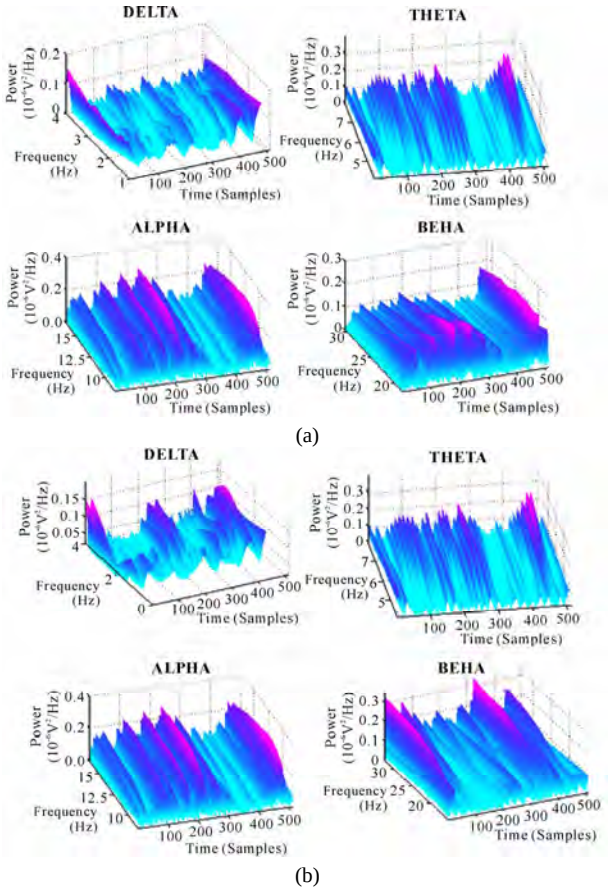

Figure 5. 3-D plots of power against time and frequenc of delta, theta, alpha and beta bands of AWAKE signals under exposure to acute heat stress. (a) control group; (b) respective acute stressed group.

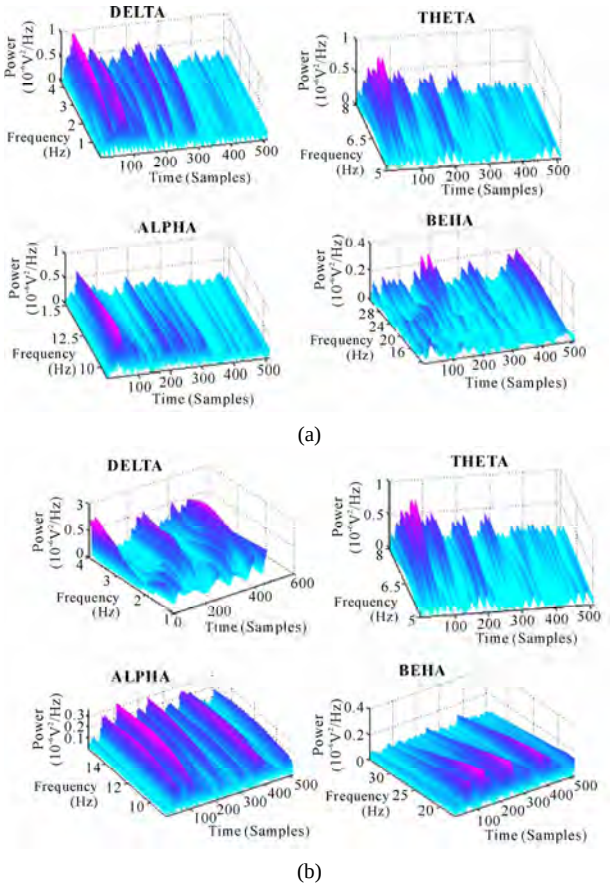

Figure 6. 3-D plots of power against time and frequency of delta, theta, alpha and beta bands of SWS signals under exposure to acute heat stress. (a) control group; (b) respective acute stressed group.

large, which suddenly vanished for all the scales of the band after time instant 400. The same happened with beta too, but it did not agree with the power decay trend followed by the alpha components. Many peaks can clearly be seen between times 80-390 over all scales whose powers remained consistent. Like alpha band, sudden fall in powers of all the components were observed after time-390. Lot of inconsistency in variation of powers of delta components for all scales and time were marked. Up to time-200, increase in powers of frequency components from lower to higher order in delta band followed a gradual and unusual shift in time. In this band, powers of different components were found to be smaller than others. At time-220 and 300, two major peaks were obtained whose powers were seen to be at par with the average power of the alpha components. Over all scales, higher frequencies of theta contained more power than the lower one and decay in power was found to be almost uniform. The way acute heat stress alters the wavelet power spectra can unambiguously be seen in **Figure 7(b)**. The alpha components witnessed a normal increase in the amount of power; meanwhile powers of beta components were significantly enhanced. Delta and theta components seemed to have nearly no change in their powers.

Similar computations by means of program written in Matlab were carried out for all the signals and analyses were performed for both the subjects stressed as well as their respective controls.

3.2. Analysis of Changes in Body Temperature

The results showed that acute heat exposure significantly increased the body temperature of rats. It was also observed that the increased body temperature of the animals returned to the control level after four to five hours of the incubation. The mean rectal temperatures recorded just before the incubation, for three weeks of chronically heat stressed rats were measured on every third day, just before daily exposure to 38 ± 1°C for one hour. No change in body temperature was recorded during chronic stress till 3rd day. The body temperature was found increased in young rats from 6th day onwards. The analyses of results suggest significant increase in the mean rectal temperature of rats till 21st day of chronic heat stress.

4. Discussion

The increase in body temperature is one of the main characteristics of the stress, induced by acute exposure of the high environmental heat. The body temperature of rats was significantly increased by acute heat stress similar to the findings of Menon *et al* [28], Sharma [29] and Sinha [34]. The review of literatures suggests that the immediate rise in the body temperature following acute heat stress plays essential role in the stimulation of

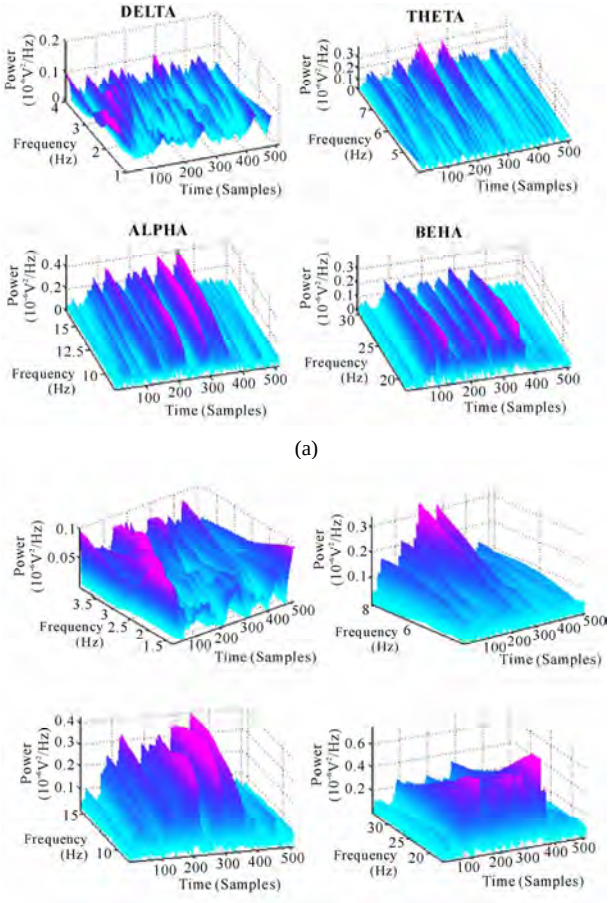

Figure 7. 3-D plots of power against time and frequency of delta, theta, alpha and beta bands of REM signals under exposure to acute heat stress. (a) control group; (b) respective acute stressed group.

the mechanisms necessary for heat dissipation. However, following the 21 days of chronic exposure of the high environmental heat, the body temperature of the rats was found to set at the higher temperature similar to the results obtained by Dey [30,31].

Wavelet analysis was performed to find out the dominant frequency components present in all bands- delta, theta, alpha, and beta for the subjects undergoing two types of heat stresses-acute and chronic and then the same was repeated for their respective control groups. Subsequent to the exposure of heat stress, all changes induced in frequency and power were investigated. Unlike other conventional techniques, the present study suggested that all the three sleep-stages–AWAKE, SWS and REM exhibited common characteristics regarding presence of leading frequency components in all four bands, which never remained constant at all times. Percentage power of different components of the four bands was always found to be varying at different intervals of time in the same signal of analysis. Thus, distribution of

frequency and powers in these three vigilance states before and after the heat stress was applied, has been observed to be highly nonlinear and so comparative analysis is done every where instead of showing the results in exact figures. For all subjects when exposed to chronic heat stress, variation in the power of theta components were least observed, whereas changes in delta, alpha and beta were frequently observed for acutely exposed subjects. Effect of acute heat stress caused significant change in the powers of alpha and beta at many time intervals for REM state, but this change was noticed mostly for the lower frequency components of beta and higher components of alpha. The change induced was more noticeable (increased) for beta than that of alpha. For the same state, power of beta at some time instants was smaller than others. In AWAKE state, only beta components showed increase in power, however this change was smaller than what was seen for REM. Quantitatively, insignificant rise and fall of powers in other three bands-delta, theta, and alpha were observed. With regard to percentage power of theta, it seemed to hold more compared to delta. The analysis reflected that chronic heat stress caused power of frequency component of delta to decrease in AWAKE and REM states, whereas the least change in theta and alpha was noticed.

No report has come to light on the study of brain cortical electrical activity with the similar model of acute or chronic heat stress using wavelet analysis. However, it is evident that the changes found in the EEG activities following acute heat stress are similar to the earlier report [32]. It has been supposed that acute heat stress alters the EEG frequencies that may have occurred due to neuronal and non-neuronal changes in the CNS [32,33]. In the present work, the quantitative changes in EEG for four defined EEG frequency bands were done and it was found that even though the EEG power spectrum showed the recovery in four hours of EEG recording following acute heat exposure, the quantitative analysis of EEG still showed significant changes in EEG signals in all the three sleep-wake states. Conversely, the chronic heat stress showed similar irreversible changes in EEG power spectra as reported in the previous work. The quantitative EEG changes following chronic heat exposure has also been found to be strikingly similar to those reported by Sarbadhikari *et al.* [12] in their study on exercise stress. They showed that the chronic exercise stress increases beta activities and decreases delta activity in AWAKE state. In SWS, the beta activities were also found to have increased. Like the chronic exercise stress, long-term exposure to high environmental heat also increased the beta activities in all subjects and decreased the delta activity in AWAKE condition. The increased beta activities in SWS were also found to exist. These changes in EEG activities following chronic heat exposure seemed to be due to adaptations of animal's physiological systems to the new ambient environmental conditions [34].

Dubois *et al.* [32] reported an initial increase in EEG frequency with increase in body temperature either by spontaneous or artificially induced fever. If the elevation of body temperature was maintained long enough or above 41-42^{o}C, a major transient reduction in EEG activity was observed. They also showed that as cooling was resumed; these changes in EEG frequencies were usually totally reversible. Rarely, the changed EEG frequencies did not return to the control level and that may occur due to CNS damage, which attributed to anorexia, dehydration, metabolic imbalance, energy failure or cellular changes following heat stress [32,33]. Similar to this report, our findings showed changes in the beta frequency components after acute heat stress that returned to the control level in four hours of cooling at room temperature except in AWAKE state. However, beta and alpha frequency components in SWS did not return to the control level, which might reflect the neuronal and non-neuronal changes in the brain due to acute heat stress [32,33]. On the other hand, 21 days of chronic heat exposure significantly decreases the beta frequencies in AWAKE state in all four hours of EEG recording. The EEG recordings also indicate that the beta frequency components were decreased in second hour of SWS and third hour in REM sleep. It has been supposed that the changed EEG activity were recorded due to adaptations of animals physiological systems to the new ambient environmental conditions similarly as suggested by Sarbadhikari and his co-workers [12] in their study on chronic exercise stress. In the present study, it has been found that the changes in EEG components in three sleep-wake states in generalization are observed to be sensitive to hot environment and found dependent upon the different sleep-wake states, both acute and chronic heat stress conditions in all three sleep-wake cycle in all experimental groups of rats. Further, the results demonstrate that the wavelet analysis of long term EEG recordings can be used for obtaining useful results in analyzing heat induced changes in electrophysiological activities of cerebral cortex.

Several research works have been reported in the area of EEG signal analysis using wavelet transform as a preprocessor such as sleep spindles detection, spike detection, sleep EEG analysis, event related potentials, epileptic seizures, but no work has been reported so far which investigated the changes in frequency and powers of EEG due to heat stress, with the help of wavelet transform. However, with this existing model no work has been reported except by Sinha and Ray [34], and Sinha [1], who investigated these changes by applying Fourier transform to the time domain EEG signals. Since Fourier transform has got some limitations due to which the analysis contains only globally averaged information. Transients EEG phenomena, which occur for short dura-

tion were not detected. In the earlier works, it has only been shown what the dominant frequency components in these sleep-states are, and how they change after heat stress. It was also shown that four frequency subbands for any particular epoch show constant behavior. In the present study, it has been clearly demonstrated the presence of different components with their varying powers in their separate bands with time of their occurrence. Information regarding frequency and time are very much localized. This study in the time-frequency domain separates the signal's power in different frequency bands with respect to time and frequency. Hence, wavelet technique provides superior resolution on data analyses at a lower time scale and thus can provide more refined data analyses on sleep EEG data compared to traditional Fourier analysis. This paper provides an example applying this technique to physiological data. Hope this technique can have broader application in sleep state transition analyses.

REFERENCES

[1] Sinha, R.K. (2004) Electro-encephalogram disturbances in different sleep-wake states following exposure to high environmental heat. *Medical & Biological Engineering & Computing*, **42**, 282-287.

[2] Sinha, R.K. (2007) Study of changes in some pathophysiological stress markers in different age groups of an animal model of acute and chronic heat stress. *Iranian Biomedical Journal*, **11**, 101-111.

[3] Guler, I., Kiymik, M.K., Akin, M. and Alkan, A. (2001) AR spectral analysis of EEG signals by using maximum likelihood estimation. *Computers in Biology and Medicine*, **31**, 441-450.

[4] Herrmann, C.S., Arnold, T., Visbeck, A., Hundemer, H.P. and Hopf, H.C. (2001) Adaptive frequency decomposition of EEG with subsequent expert system analysis. *Computers in Biology and Medicine*, **31**, 407-427.

[5] Peters, B.O., Pfurtscheller, G. and Flyvbjerg, H. (2001) Automatic differentiation of multichannel EEG analysis. *IEEE transactions on Biomedical Engineering*, **48**, 111–116.

[6] Vuckovick, A., Radivojevic, V., Chen A.C.N. and Popovic, D. (2002) Automatic recognition of alertness and drowsiness from EEG by an artificial neural network. *Medical Engineering and Physics*, **24**, 349-360.

[7] McKeon, M.J., Humphries, C., Achermann, P., Borbely, A.A. and Sejnowski, T.J. (1997) Anew method for detecting state changes in EEG: Exploratory application to sleep data. *Journal of Sleep Research*, **7**, 48-56.

[8] Dement, W.C. and Kleitman, N. (1957) Cyclic variations in EEG during sleep and their relation to eye movements, body motility and dreaming. *Electroencephalography and Clinical Neurophysiology*, **9**, 673-690.

[9] Jansen, B.H., Hasman, A. and Lenten, R. (1981) Piecewise EEG analysis: An objective evaluation, *International Journal of Bio-Medical Computing*, **12**, 17-27.

[10] Al-Nashash, H.A.M. (1995) A dynamic Fourier series for the compression of ECG using FFT and adaptive coefficient estimate. *Medical Engineering and Physics*, **17**, 197-203.

[11] Sinha, R.K. (2003) Artificial neural network detects changes in electro-encephalogram power spectrum of different sleep-wake states in an animal model of heat stress. *Medical & Biological Engineering & Computing*, **41**, 595-600.

[12] Sarbadhikari, S.N., Dey, S., Ray, A.K. (1996) Chronic exercise alters EEG power spectra in an animal model of depression. *Indian Journal of Physiology and Pharmacology*, **40**, 47-57.

[13] Jung, T.P., Makeig, S., Stensmo, M. and Sejnowski, T.J. (1997) Estimating alertness from the EEG power spectrum. *IEEE Transactions on Biomedical Engineering*, **44**, 60-69.

[14] Subasi, A. (2005) Automatic recognition of alertness level from EEG by using neural network and wavelet coefficients. *Expert Systems with Applications*, **28**, 701-711.

[15] Adeli, H. *et al*. (2007) A wavelet-chaos methodology for analysis of EEGs and EEG Subbands to detect seizure and epilepsy. *IEEE Transactions on Biomedical Engineering*, **54(2)**, 205-211.

[16] Adeli, H., Zhou, Z. and Dadmehr, N. (2003) Analysis of EEG records in an epileptic patient using wavelet transform. *Journal of Neuroscience Methods*, **123**, 69-87.

[17] Feng, Z. and Xu, Z. (2002) Analysis of rat electroencephalogram under slow wave sleep using wavelet transform. *Proceedings of the Second Joint EMBS/BMES Conference Houston*, TX, USA.

[18] Daubechies, I. (1990) The Wavelet transform time-frequency localization and signal analysis. *IEEE Transactions on Information Technology*, **36(5)**, 961-1005.

[19] Mallat, S. (1989) A theory for multiresolution signal decomposition: The wavelet representation. *IEEE Transactions on Pattern Analysis and Machine Intelligence*, **11(7)**, 674-693.

[20] Meyer, Y. (1989) Orthonormal wavelets in Wavelets, Time-Frequency Methods and Phase Space (Lecture Notes on IPTI), J. M. Combes *et al*., Ed., New Work: Springer-Veriag.

[21] Bianchi, A.M., Mainardi, L.T. and Cerutti, S. (2000) Time-frequency analysis of biomedical signals. *Transactions of the Institute of Measurement and Control*, **22**, 321-336.

[22] Kalayci, T. and Ozdamar, O. (1995) Wavelet preprocessing for automated neural network detection of EEG spikes. *IEEE Engineering in Medicine and Biology Magazine*, **14**, 160-166.

[23] Farge, M. (1992) Wavelet transforms and their applications to turbulence. *Annual Review of Fluid Mechanics*, **24**, 395-457.

[24] Sakkalis, V. *et al*. (2006) Significant EEG features involved in mathematical reasoning: Evidence from wavelet analysis. *Brain Topography*, **19(1/2)**, 53-60.

[25] Shen, M., Sun, L. and Chan, F.H.Y. (2001) Method of extracting time-varying rhythms of electroencephalography via wavelet packet analysis. *IEE Proceedings-Science, Measurement and Technology*, **148**.

[26] Ting, W. *et al.* (2007) EEG feature extraction based on wavelet packet decomposition for brain computer interface. *Meaurement.*

[27] Unser, M. and Aldroubi, A. (1996) A review of wavelets in biomedical applications. *Proceedings of the IEEE*,

84(4), 626-638.

[28] Menon, M.K. and Dandiya, P.C. (1969) Behavioural and brain neurohormonal changes produced by acute heat stress in rats: Influence of psychopharmacological agents. *European Journal of Pharmacology*, **8**, 284-291.

[29] Sharma, H.S. (1982) Blood-brain barrier (BBB) in stress. Ph. D. Thesis, Zoology, Banaras Hindu University.

[30] Dey, P.K. (1998) Modification of dopamine receptor agonist mediated behavioral responses in rats following exposure to chronic heat stress. *Biomedicine*, **18**, 41-47.

[31] Dey, P.K. (2000) Involvement of endogenous opiates in heat stress. *Biomedicine*, **20**, 143-148.

[32] Dubois, M., Sato, S., Lees, D.E., Bull, J.M., Smith, R., White, B.G., Moore, H. and Macnamara, T.E. (1980) Electroencephalographic changes during whole body hyperthermia in humans. *Electroencephalography and Clinical Neurophysiology*, **50**, 486-495.

[33] Sharma, H.S., Westman, J. and Nyberg, F. (1998) Pathophysiology of brain edema and cell changes following hyperthermic brain injury: Progress in Brain Research. Elsevier, Amsterdam, **115**, 351-412.

[34] Sinha, R.K. and Ray, A.K. (2004) An assessment of changes in open-field and elevated plus-maze behavior following heat stress in rats. *Iranian Biomedical Journal*, **8**, 127-133.

J. Biomedical Science and Engineering, 2010, 3, 415-421 **JBiSE**
doi:10.4236/jbise.2010.34057 Published Online April 2010 (http://www.SciRP.org/journal/jbise/).

Insilico structural analysis of parasporin 2 protein sequences of non-toxic bacillus thuringiensis

Ayyasamy Mahalakshmi, Rajaiah Shenbagarathai

PG Research Department of Zoology and Biotechnology, Lady Doak College, Madurai-2, Tamilnadu, India.
Email: shenbagarathai@rediffmail.com

Received 17 September 2009; revised 5 December 2009; accepted 7 December 2009.

ABSTRACT

The unusual and remarkable property of parasporin 2 of non-insecticidal *Bacillus thuringiensis* is specifically recognizing and selectively targeting human leukemic cell lines. The 37-kDa inactive nascent protein is proteolytically cleaved to the 30-kDa active form that loses both the N-terminal and the C-terminal segments. Accumulated cytological and biochemical observations on parasporin-2 imply that the protein is a pore-forming toxin. To confirm the hypothesis, *insilico* analysis was performed using homology modeling. The resulting model of parasporin 2 protein is unusually elongated and mainly comprises long β-strands aligned with its long axis. It is similar to aerolysin-type β-pore-forming toxins, which strongly reinforce the pore-forming hypothesis. The molecule can be divided into three domains. Domain 1, comprising a small β-sheet sandwiched by short α-helices, is probably the target-binding module. Two other domains are both β-sandwiches and thought to be involved in oligomerization and pore formation. Domain 2 has a putative channel-forming β-hairpin characteristic of aerolysin-type toxins. The surface of the protein has an extensive track of exposed side chains of serine and threonine residues. The track might orient the molecule on the cell membrane when domain 1 binds to the target until oligomerization and pore formation are initiated. The β-hairpin has such a tight structure that it seems unlikely to reform as postulated in a recent model of pore formation developed for aerolysin-type toxins. Parasporin 2 (Accession no: BAD35170) protein sequence analysis indicated two different domains namely, aerolysin toxin and clostridium toxin domain based on different database searches (CDD and Pfam). It showed a close similarity with the available PDB template (PDB id: 2ZTB) of parasporin which has cytocidal activity against MOLT-4, HL60 and Jurkat cell lines. Based on the PSI Blast analysis, 3D structures of the domains were predicted by using Swiss model server. Accuracy of the prediction of 3D structure of different domains of parasporin protein was further validated by Ramachandran plot and PROCHECK (G-value). The structure is dominated by β-strands (67%, S1-12), most of which are remarkably extensive, running all or most of the longer axis of the molecule. This study helped to elucidate the 3D structure of parasporin 2 (Acc. No. BAD35170) which might enable to probe further its specific mechanism of action. Though the similarity is observed in the domain architecture, there is variation in the regions of the domains even among the same group of parasporin 2. Docking of this model structure and experimental structure with specific receptors of the cancer cells will facilitate to explore mechanism of parasporin 2 action and also provide information about its evolutionary relationship with toxic Cry proteins.

Keywords: Parasporin; Homology Model; Non-Toxic; *Bacillus thuringiensis*; Cell Lines

1. BACKGROUND

Since the incidence of new cancer patients is increasing annually due to altered food habits and life styles, efforts are being made worldwide to identify new molecular markers and therapeutic agents for the purpose of diagnosis and treatment of the same. The existing chemotherapeutics not only affect tumor cells but also normal cells. Hence, search for compounds which can specifically target the cancer cells will overcome the existing problem [1].

At present, four genealogically different parasporins are identified as parasporin-1 to parasporin-4 that has the ability to specifically act against cancer cells [2]. This area of research is still under exploration, since a very few of the literature is available related to parasporin structure and mechanism of action. Parasporin 2 is known to interact with GP-I protein and the cell death induced by parasporin-2 is non-apoptotic, although the apoptotic process occurs when the cell damage proceeded slowly.

Parasporin-2 increases the plasma membrane permeability of the target cells as it binds to a detergent-resistant membrane, the so-called "lipid raft" in a plasma membrane, and then forms the SDS-resistant oligomer embedded in the membrane. This toxin binds GPI-proteins in lipid raft, and then seems to form the oligomer that can permeabilize the plasma membrane. This is followed by the formation of oligomers (> 200 kDa) of PS2Aa1 in plasma membranes, leading to pore formation and cell lysis. The oligomerization occurs in the presence of membrane proteins, lipid bilayer and cholesterols [3].

Only two experimentally determined structures (PDB: 2ZTB, 2D42) are available till date as confirmed in the PDB. Hence, alternative strategies are being applied to develop theoretical models of protein structure of parasporin 2 (Accession no: BAD35170) when X-ray diffraction or NMR structures are not available, aiming to bridge the structure-knowledge gap. Higher resolution models, derived from relationships with better than about 30% sequence identity or refined from lower resolution starting models, are very helpful in assigning detailed aspects of molecular function [4].

2. RESULTS AND DISCUSSION

2.1. Domain identification

The complete sequence of parasporin protein (*Bacillus thuringiensis*) available from NCBI till date revealed the aerolysin toxin and clostridium toxin domain (**Table 1**). Domains present one of the most useful levels at which to understand protein function and the domain family-based analysis has had a profound impact on the study of individual proteins [5].

2.2. Template Identification by Fold-Recognition Servers

Two approaches are employed to identify the potential templates by submitting a multiple sequence alignment (MSA) of all the parasporin sequences and submitting each of the parasporin sequences individually. Thus, in order to identify a template structure for modeling of parasporin protein sequences, we used the comparative modeling approach (match of secondary structure elements, compatibility of residue-residue contacts, etc.). In the former, MSA for the entire sequence from N-to C-terminus (**Figure 1**) was submitted to the FUGUE server; the template 2ZTB was identified [10] with very high confidence levels (Z-score for the top hit = 31.32; certain). Even the GeneSilico metaserver identified 2ZTB template with reliable confidence levels (3D-Jury score for the top hit = 133; *reliable*). In view of these, both the servers identified 2ZTB as the top hit (Z-score = 31.3.2; certain and 3DJury score = 133; *reliable*).

In the second approach, complete sequence of the parasporin was used separately as query to search for homologs in the PDB database using BLAST and PSI-BLAST. The fold-recognition servers, GeneSilico metaserver, FUGUE and SAM-T02 identified 2ZTB as the possible template only for parasporin sequence (Acc. No. BAD35170) with a high level of confidence (**Table 2**). Despite the scores reported by the individual threading methods were hardly significant, the consensus server Pcons5 [11] assigned a significant score (1.35) to the 2ZTB structure as a potential modeling template as evident in its sequence alignment (**Figure 2**).

2.3. Modeling 3-D Structure and Stereochemical Evaluation of the Predicted Models

The 3-D structure of parasporin sequence at 2.38 °A resolution (PDB id: 2ZTB, A chain) is the main template for modeling only one parasporin sequence (Acc. No. BAD35170) with 88% identity, since, all other parasporin sequences had less than 26% identity with its corre-

Table 1. Domains of parasporin protein sequence as suggested by Pfam-A search and conserved domain database search (http://pfam.sanger.ac.uk/search; http://www.ncbi.nlm.nih.gov/).

S.no	Accession no	Significant Domains identified	Sequence		Bit score	E-value
			start	end		
1	BAD35170	-------	-----	----	----	-----
2	BAE44986	delta endotoxin, N-terminal domain	114	363	33.1	9.2e-11
3	BAE44985	delta endotoxin, N-terminal domain	95	344	32.9	9.4e-11
4	BAE44984	delta endotoxin, N-terminal domain	114	363	36.3	5.8e-11
5	BAE44983	delta endotoxin, N-terminal domain	114	363	32.5	1e-10
6	BAE79808	delta endotoxin, N-terminal domain	147	396	33.1	9.2e-11
7	BAE79809	delta endotoxin, N-terminal domain	147	396	32.9	9.4e-11
8	BAB11757	delta endotoxin, N-terminal domain	147	396	33.1	9.2e-11

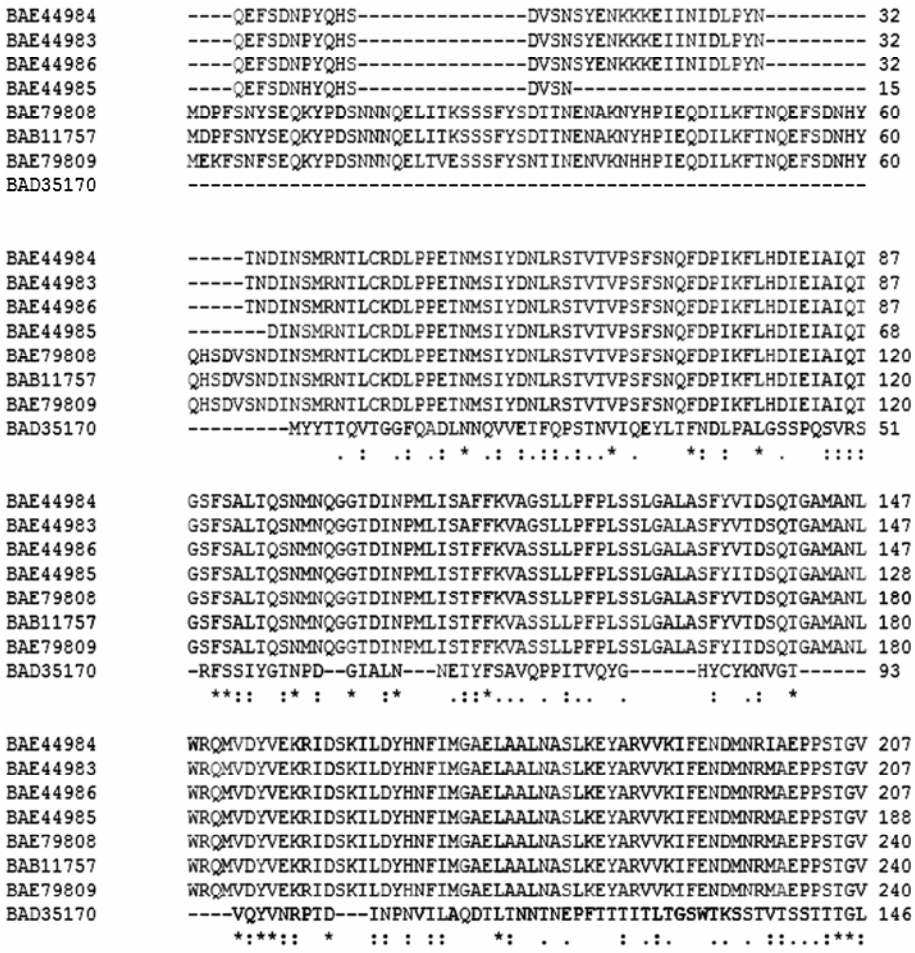

Figure 1. Multiple sequence alignment of parasporin protein residues *-conserved residues.

Table 2. Summary of the best template sequence profile that was generated at the end of 3rd iteration of PSI Blast analysis using the parasporin protein sequence of *B.thuringiensis* as query. Threshold PSI-BLAST E-value = 0.001.

S.no	Accession no	Query region	Template sequence id	Region of template seq aligned	% identity	Gap (%)	E-value	Annotation of the template
1	BAD35170	28-278	2ZTB	2-252	88	0	2e-114	Parasporin 2 crystal structure of *Bacillus thuringiensis*
2	BAE44986	119-383	1DLC	18-251	26	15	1e-12	Crystal Structure Of Insecticidal Delta-endotoxin.
3	BAE44985	101-364	1DLC	19-251	26	15		Crystal Structure Of Insecticidal Delta-endotoxin.
4	BAE44984	109-383	1DLC	5-251	26	16	6e-13	Crystal Structure Of Insecticidal Delta-endotoxin.
5	BAE44983	109-383	1DLC	5-251	26	16	1e-12	Crystal Structure Of Insecticidal Delta-Endotoxin
6	BAE79808	153-416	1DLC	19-251	25	15	2e-12	Crystal Structure Of Insecticidal Delta-Endotoxin
7	BAE79809	153-416	1DLC	19-251	26	15	2e-12	Crystal Structure Of Insecticidal Delta-Endotoxin
8	BAB11757	153-416	1DLC	19-251	25	15	2e-12	Crystal Structure Of Insecticidal Delta-Endotoxin


```
BAD35170        MYYTTQVTGGFQADLNNQVVETFQPSTNVIQEYLTFNDLPALGSSPQSVRSRFSSIYGTN 60
2ZTB_A          -------------------------MDVIREYLMFNELSALSSSPESVRSRFSSIYGTN 34
                                         :**:*** **:*.**.***:**************

BAD35170        PDGIALNNETYFSAVQPPITVQYGHYCYKNVGTVQYVNRPTDINPNVILAQDTLTNNTNE 120
2ZTB_A          PDGIALNNETYFNAVKPPITAQYGYYCYKNVGTVQYVNRPTDINPNVILAQDTLTNNTNE 94
                ************.**:****.***:**********************************

BAD35170        PFTTTITLTGSWTKSSTVTSSTTTGLKITTKLSIKKVFEIGGEVSFSTTIGSSEATSETF 180
2ZTB_A          PFTTTITITGSFTNTSTVTSSTTTGFKFTSKLSIKKVFEIGGEVSFSTTIGTSETTTETI 154
                *******:***:*::**********:*:*:*********************:**:*:**:

BAD35170        TVSKAVTVTVPAQSRRNIQLTAKIARESADFSAPITVDGYFGANFPRRVGPGGHYFWFNP 240
2ZTB_A          TVSKSVTVTVPAQSRRTIQLTAKIAKESADFSAPITVDGYFGANFPKRVGPGGHYFWFNP 214
                ****:***********.********:*******************:*************

BAD35170        ARDVLNATSGTLRGTVTNVSSFDFQTVVQPAYSLLAEQQEALESAISGDPSEEQLKQIQQ 300
2ZTB_A          ARDVLNTTSGTLRGTVTNVSSFDFQTIVQPARSLLDEQ---------------------- 252
                ******:*******************:**** *** **

BAD35170        TIGL 304
2ZTB_A          ----
```

Figure 2. Sequence alignment of the parasporin protein (Acc. No. BAD35170) with its template (PDB id: 2ZTB-A chain).

sponding template (**Figure 3**). The final averaged and optimized model passed all the tests implemented in the stereochemistry-evaluating WHATCHECK suite [12-15] and in the VERIFY3D program, which uses contact potentials to assess whether the modeled amino acid residues occur in the environment typical for globular proteins with hydrophobic core and solvent-exposed surface (Eisenberg *et al*., 1997). Moreover, the reasonable energies are rarely observed for misfolded structures. Thus, the scores reported for our model by WHATCHECK (*Z*-score-4.1) and VERIFY3D (average score 0.3, no regions scored lower than 0) suggest that both its three-dimensional fold and the conformation of individual residues are reasonable.

The selected model, the value of the objective function, reported as current energy is in the same range as that if the template is aligned with its own sequence. On an average, 99.1% of the residues are found in the allowed region of Ramachandran map, PROCHECK considers the model to be very good if it has 90% of the residues in the most favored region. The inter-atomic distances are within acceptable range. Verify3D score is greater than zero for the entire model (1 to 274 residues). The models were also evaluated using Colorado3D server, which facilitates the change of amino acid window size when calculating the overall score. Two window sizes, 5 and 21, were used to calculate the average Verify3D and ProsaII score per residue for the model [12,13]. The scores calculated using these two window sizes were found to be very similar. The template and target models were rendered with the residues color-coded based on ProsaII and Verify3D scores. With ProsaII score-based coloring, most of the residues are green and yellow (*i.e*., average score) in both the target and template proteins. Z-score of a model is a measure of compatibility between its sequence and structure, the model Z-score should be comparable to that of the template. With Verify3D score-based coloring, even the template proteins has residues in red color (*i.e*., bad score) although the number of such residues are more in the targets.

2.4. Description of the Model

The structure is dominated by β-strands (67%, S1–12), most of which are remarkably extensive, running all or most of the longer axis of the molecule (**Figure 3**). The longest strand (S8), comprising 21 residues, runs the whole length of the molecule; three others (S11, S12, S14) span two-thirds of the molecule's length. The molecule can be divided into three domains: domain 1 (Val29-His85, Gly145-Ser173), domain 2 (Ile36-Pro53, Ala81-Asp138, Glu160-Ser175, Gly211-Gln236), and domain 3 (Val54-Asn80, Phe139-Leu159, Thr237-Ala250). Domain 1 is composed of a short N-terminal β-strand

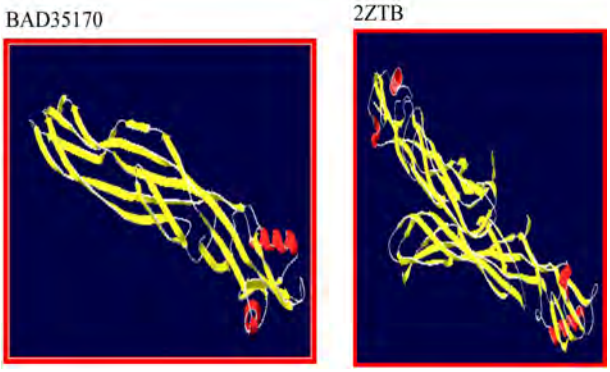

Figure 3. Homology model of the parasporin protein sequence (Acc.No. BAD35170).

(S1: 30-34), a α/β structure (H1 and S2: 46-66), a β-hairpin (S9 and S10: 152-168), and a α-helix (H2: 79 -83). α-Helices are found only in this domain. The two α-helices, H1 and H2, are close together and short, occupying only 8.9% of the molecule. Domains 2 and 3 are both β-sandwiches: the former is made of a two-stranded β-hairpin (S6 and S7) and a curled anti-parallel five stranded β-sheet including S3, S9, S12, S5 and S8; and the latter is of antiparallel three-stranded and two-stranded β-sheets (S4, S9 and S12; S5 and S8). These results (**Figure 3**, **Table 3**) are consistent with earlier reports [14]. This model is expected to yield insight into the molecular function and mechanism of parasporin action [15].

3. CONCLUSIONS

The initial step in cytocidal action of PS2Aa1 is the specific binding of this cytotoxin to a putative receptor located in the lipid rafts, followed by its oligomerization and pore formation in plasma membrane.Secondary structures observed in the model (Accession No: BAD 35170) are organized virtually in the same way as the experimentally determined parasporin-2 protein (PDb id: 2ZTB). Even though 2ZTB and 2D42 belong to the parasporin type 2 protein sequence, BAD35170 bears greater similarity to 2ZTB in its domain organization.

4. METHODS

4.1. Databases

The amino acid sequences of the experimentally characterized parasporin sequences (**Table 4**) were retrieved from the protein sequence database at NCBI http://www.ncbi.nlm.nih.gov. The 3-D structures of proteins were obtained from the protein data bank [16]. The fold classification of proteins is from the SCOP database [17].

Table 3. Structural superposition report of the model generated for BAD35170 with its corresponding template, 2ZTB.

Local RMSD

	Alpha Carbons	Back Bone	Heavy	All
RMSD	0.07	0.10	0.53	0.53
Atoms	238	729	1536	1536

Structure	Residues
PDBA	28-265
2ZTB chain 'A'	52-289

Global RMSD

	Alpha Carbons	Back Bone	Heavy	All
RMSD	0.07	0.10	0.53	0.53
Atoms	238	729	1536	1536

Structure	Residues
PDBA	28-265
2ZTB chain 'A'	52-289

Table 4. List of parasporin sequences retrieved from NCBI database.

S.no	Accession no	Type of protein
1	BAD35170	Parasporin 2 Ab cytotoxic Crystal protein (*Bacillus thuringiensis*)
2	BAE44986	Putative uncharacterized protein 1 (*Bacillus thuringiensis*)
3	BAE44985	Putative uncharacterized protein 2 (*Bacillus thuringiensis*)
4	BAE44984	Putative uncharacterized protein 3 (*Bacillus thuringiensis*)
5	BAE44983	Putative uncharacterized protein 4 (*Bacillus thuringiensis*)
6	BAE79808	81-k da leukemia protein (*Bacillus thuringiensis)*
7	BAE79809	Cry 31-like 82-k da protein (*Bacillus thuringiensis*)
8	BAB11757	81-k da leukemia toxin (*Bacillus thuringiensis*)

4.2. Servers

Protein sequence databases were searched using PSI-BLAST [18] servers at NCBI, PHYRE (successor of 3D-PSSM) [19], SAM-T02 [20] and GeneSilico Metaserver [21] were used for fold-recognition. Multiple sequence alignments were obtained using the CLUSTALW server [22]. Verify3D [13] and Colorado3D [23] were used to evaluate the models. All the servers were used with default values for the various parameters, except where mentioned otherwise.

4.3. Software and Hardware

SwissPDBviewer [24] was used for visualization and/or rendering. The stereochemical quality of the generated model was assessed using PROCHECK [10]. Default values were used for all the parameters, unless specified otherwise.

4.4. Template-Target Sequence Alignment

The parasporin sequences were submitted for structure prediction using comparative modeling technique. The preliminary models were obtained using unrefined pairwise alignments reported by PSI-BLAST [25]. Energy minimization was carried out using GROMOS96 [26] until all inconsistencies in geometry were rectified and all the short contacts were relieved. The stereochemical and energetic properties of modeling intermediates and of the final model were evaluated using WHATCHECK [27] and VERIFY3D [28]. Semi-automated and manual manipulations with protein structures and sequence–structure alignments were conducted using SWISS-PDB VIEWER [24]. All the servers provide alignment of the submitted

parasporin sequence (target) with the sequence of the potential hits (templates).

4.5. Validation of Predicted 3-D Structures

The stereochemical properties of predicted 3-D structures were assessed by PROCHECK and the residue environments by Verify3D and Colorado3D. Regions that are found by these servers as poorly modeled were improved by manual adjustment of alignments and re-modeling.

5. ACKNOWLEDGEMENTS

The authors acknowledge N.Lavanya Roselin for acquisition of data. Authors express their heartfelt thanks for DBT-BIF in providing the necessary infrastructure facility in the collection, analysis, and interpretation of data; in the writing of the manuscript; and in the decision to submit the manuscript for publication.

BLAST server: http://www.ncbi.nlm.nih.gov/BLAST/
Colorado3D: http://asia.genesilico.pl/colorado3d/
FUGUE: http://www-cryst.bioc.cam.ac.uk/fugue/
GeneSilico Metaserver: http://genesilico.pl/meta
PDB: http://www.rcsb.org
PHYRE: http://www.sbg.bio.ic.ac.uk/~phyre
PROCHECK: http://www.biochem.ucl.ac.uk/~roman/procheck/procheck.html
SCOP database: http://scop.mrc-lmb.cam.ac.uk/scop/
SwissPDBviewer: http://ca.expasy.org/spdbv/
Verify_3D: http://nihserver.mbi.ucla.edu/Verify_3D/

REFERENCES

[1] Mizuki, E., Ohba, M., Akao, T., Yamashita, S., Saitoh, H. and Park, Y.S. (1999) Unique activity associated with non-insecticidal Bacillus thuringiensis parasporal inclusions: In vitro cell-killing action on human cancer cells. *Journal of Applied Microbiology*, **86**, 477-86.

[2] Katayama, H., Yokota, H., Akao, T., Nakamura, O., Ohba, M., Mekada, E. and Mizuki, E. (2005) Parasporin-1, a novel cytotoxic protein to human cells from non-insecticidal parasporal inclusions of Bacillus thuringiensis. *Biochemistry*, **137**, 17-25.

[3] Abe, Y., Shimada, H. and Kitada, S. (2008) Raft-targeting and oligomerization of parasporin-2, a Bacillus thuringiensis crystal protein with Anti-Tumour activity. *Biochemistry*, **143(2)**, 269-275.

[4] Murray, D. and Honig, B. (2002) Electrostatic control of the membrane targeting of C2 domains. *Molecular Cell*, **9**, 145-154.

[5] Copley, R.R., Doerks, T., Letunic, I. and Bork, P. (2002) Protein domain analysis in the era of complete genomes. *FEBS Letters*, **20**, 129-134.

[6] Godzik, A. (2003) Fold recognition methods. *Methods of Biochemical Analysis*, **44**, 525-546.

[7] Kurowski, M.A., Bujnicki, J.M. (2003) GeneSilico protein structure prediction meta-server. *Nucleic Acids Research*, **31**, 3305-3307.

[8] Akiba, T., Abe, Y., Kitada, S., Kusaka, Y., Ito, A., Ichimatsu, T., Katayama, H., Akao, T., Higuchi, K., Mizuki, E., Ohba, M., Kanai, R. and Harata, K. (2009) Crystal structure of the parasporin-2 of Bacillus thuringiensis toxin that recognizes cancer cells. *Journal of Molecular Biology*, **386**, 121-133.

[9] Lundstrom, J., Rychlewski, L., Bujnicki, J.M. and Elofsson, A. (2001) Pcons: A neural-network-based consensus predictor that improves fold recognition. *Protein Science*, **10**, 2354-2362.

[10] Laskowski, R.A., MacArthur, M.W., Moss, D.S. and Thornton, J.M. (1993) PROCHECK: A program to check the stereochemical quality of protein structures. *J Appl Cryst*, **26**, 283-291.

[11] Hooft, R.W.W., Vriend, G., Sander, C. and Abola, E.E. (1996) Errors in protein structures. *Nature*, **381,** 272-272.

[12] Sippl, J. (1993) Recognition of errors in three dimensional structures of proteins. *Proteins*, **17**, 355-362.

[13] Lüthy, R., Bowie, J.U. and Eisenberg, D. (1992) Assessment of protein models with three-dimensional profiles. *Nature*, **5**, 83-5.

[14] Brenner, S.E. (2001) A tour of structural genomics. *Nature Reviews Genetics*, **2**, 801-809.

[15] Berman, H.M., Westbrook, J., Feng, Z., Gilliland, G., Bhat, T.N., Weissig, H., Shindyalov, I.N. and Bourne, P.E. (2000) The protein data bank. *Nucleic Acids Research*, **28**, 235-242.

[16] Andreeva, A., Howorth, D., Brenner, S.E., Hubbard, T.J., Chothia, C. and Murzin A.G. (2004) SCOP database in 2004: Refinements integrate structure and sequence family data. *Nucleic Acids Research*, **32**, 226-229.

[17] Altschul, S.F., Madden, T.L., Schaffer, A.A., Zhang, J., Zhang, Z., Miller, W. and Lipman, D.J. (1997) Gapped BLAST and PSI-BLAST: A new generation of protein database search programs. *Nucleic Acids Research*, **25**, 3389-3402.

[18] Shi, J., Blundell, T.L. and Mizuguchi, K. (2001) FUGUE: sequence-structure homology recognition using environment-specific substitution tables and structure-dependent gap penalties. *Journal of Molecular Biology*, **29**, 243-57.

[19] Kelley, L.A., MacCallum, R.M., Sternberg, M.J.E. (2000) Enhanced genome annotation using structural profiles in the program 3D-PSSM. *Journal of Molecular Biology*, **299**, 499-520.

[20] Karplus, K., Karchin, R., Draper, J., Casper, J., Mandel-Gutfreund, Y., Diekhans, M. and Hughey, R. (2003) Combining local-structure, fold-recognition, and new fold methods for protein structure prediction. *Proteins*, **53,** 491-496.

[21] Kurowski, M.A. and Bujnicki, J.M. (2003) GeneSilico protein structure prediction meta-server. *Nucleic Acids Research*, **31**, 3305-3307.

[22] Thompson, J.D., Higgins, D.G. and Gibson, T.J. (1994) CLUSTAL W: Improving the sensitivity of progressive multiple sequence alignment through sequence weighting, position-specific gap penalties and weight matrix choice. *Nucleic Acids Research*, **22**, 4673-4680.

[23] Sasin, M. and Bujnicki, J.M. (2004) COLORADO3D, a web server for the visual analysis of protein structures. *Nucleic Acids Research*, **32**, 586-589.

[24] Guex, N. and Peitsch, M.C. (1997) SWISS-MODEL and the Swiss-PdbViewer: An environment for comparative protein modeling. *Electrophoresis*, **18**, 2714-2723.

[25] Altschul, S.F, Madden, T.L., Schäffer, A.A., Zhang, J., Zhang, Z., Miller, W. and Lipman, D.J. (1997) Gapped blast and PSI-blast: A new generation of protein database search programs. *Nucleic Acids Research*, **25(17)**, 3389-3402.

[26] van Gunsteren, W.F., Billeter, S.R., Eising, A.A., Hünenberger, P.H., Krüger, P., Mark, A.E., Scott, W.R.P. and Tironi, I.G. (1996) Biomolecular simulation. *The GROMOS*96 *Manual and User Guide*, Zürich, Groningen.

[27] Hooft, R.W.W., Vriend, G., Sander, C. and Abola, E.E. (1996) Errors in protein structures. *Nature*, **381**, 272-272.

[28] Eisenberg, D., Lüthy, R. and Bowie, J.U. (1997) VERIFY3D: Assessment of protein models with three-dimensional profiles. *Methods Enzymol*, **277**, 396-404.

J. Biomedical Science and Engineering, 2010, 3, 422-429 **JBiSE**
doi:10.4236/jbise.2010.34058 Published Online April 2010 (http://www.SciRP.org/journal/jbise/).

The opinion and experience of surgeons with laparoscopic bowel grasper haptics

Eleonora P. Westebring-van der Putten[1], Margriet C. J. Berben[1], Richard H. M. Goossens[1], Jack J. Jakimowicz[1,2], Jenny Dankelman[3]

[1]Department of Applied Ergonomics and Design, Faculty of Industrial Design Engineering, Delft University of Technology, Delft, the Netherlands;
[2]Department of Surgery, Catharina Hospital, Eindhoven, the Netherlands;
[3]Department of Biomechanical Engineering, Faculty of Mechanical, Maritime and Materials Sciences, Delft University of Technology, Delft, the Netherlands.
Email: e.p.westebring-vanderputten@tudelft.nl

Received 17 December 2009; revised 28 December 2009; accepted 12 January 2010.

ABSTRACT

Background: In order to develop new and better laparoscopic bowel instruments, which reduces patient risks, the opinions and experience that surgeons have with current laparoscopic bowel grasper haptics is important. In this study we explored this by means of a questionnaire. Method: A total of 386 online-questionnaires, were sent to laparoscopic surgeons working in European hospitals. They were all members of the European Association of Endoscopic Surgery and perform laparoscopic obesities or bowel surgery. Surgeons where divided into different age and experience groups. Results: A total of 174 completely filled out forms were analyzed. In total, 16% of the surgeons cannot prevent damage when they pinch too hard, although they (10%) might have seen or felt it. Seven percent of the respondents were not able to see or feel tissue slippage. Whereas 31% can see or feel slippage they cannot do anything to prevent it. Overall, most of the respondents would appreciate technical changes in the laparoscopic bowel graspers to reduce tissue damage. Of all the respondents, 79% maintain that it is necessary to have a new laparoscopic grasper with augmented feedback. The majority of the respondents (77%) would like to have tactile feedback as an indication of the level of pinch force. There are not many differences in the opinions of surgeons at different skill levels. Conclusion: From the results of the questionnaire and the other comments made by respondents it is evident that research and developments in the field of new laparoscopic graspers should continue.

Keywords: Laparoscopy; Vision and Experience; Bowel Graspers; Questionnaire; Haptic Feedback

1. INTRODUCTION

Laparoscopic surgery has many benefits for the patient, such as fewer traumas, shorter hospital stays and reduced recovery times [1-5]. However, this technique gives rise to difficulties for the surgeon such as reduced haptics and indirect vision [6], which in turn may lead to a higher rate of adverse events [7]. During laparoscopic bowel surgery stress injury, which leads to tissue damage (*e.g.* perforation), pathological scar tissue formation, bleeding, adhesions, and loss of bowel motility may occur when the instrument is pinched with excessive force or when tissue slips from the grasper [8,9].

Many studies are currently being performed to establish the best way of reducing tissue damage during laparoscopic procedures (for a review of this see [10]). One of our own projects concerns laparoscopic grasp control. There we are trying to determine whether augmented feedback in relation to excessive pinch force and tissue slippage during laparoscopic grasping may improve performance. Preliminary tests with augmented feedback containing grasp force information have shown that the accuracy/level of grasping forces has indeed increased. The main aim of the project is thus to find the best kind of augmented feedback in relation to grasp force during laparoscopic grasping. Laparoscopic obesities and bowel surgery is chosen as the applicable field, as the tissue of the bowel is very delicate. Good grasp control is therefore a prerequisite in the correct performance of bowel surgery.

Apart from gaining results from experiments, we are interested in surgeons' opinions and experience with the current laparoscopic graspers during bowel surgery. This way researcher can develop instruments that fulfill the demands and wishes of the surgeons who are going to use the instruments. Current literature does not provide

us with information retrieved from large groups of surgeons. Individual surgeons are asked to provide research groups with their opinion and experiences, although, these opinions are useful they might not represent the opinion of the whole user group. The amount of research done in the field of improving haptics sugges that this need is obvious, however, this has not been confirmed by large user groups. To collect this information, we compiled a questionnaire, which was first approved by the technical committee of the European Association for Endoscopic Surgery (EAES). The questionnaire was distributed to surgeons who use laparoscopic techniques. It included questions on laparoscopic surgery in general, laparoscopic bowel surgery, (augmented) feedback on pinch force information during laparoscopic grasping, involvement in hospital innovation and awareness and participation in research projects devoted to augmented feedback. This article will present the findings of that questionnaire.

2. METHODS

In total, 386 surgeons from different European hospitals (members of the EAES who perform laparoscopic bowel and obesities surgery), were approached by email and asked to fill in a questionnaire via the Internet (developed using NETQuestionnaires 6.0).

Apart from the overall opinions of the whole group we were also interested to see whether there were differences in the answers given by surgeons of different ages or levels of experience. We therefore distinguished three categories based on experience in terms of number of operations, experience in terms of years and age. All the surgeons were divided into one of the four levels given within each category (see **Table 1** in the Result section).

Table 1. Devision in groups of the 174 respondents.

		Respondents (%)
Experience (no. of operations)	< 500	30
	500-1000	17
	1000-2000	20
	> 2000	33
Experience (years)	< 5	9
	5-10	22
	10-15	28
	15-20	41
Age (years)	< 40	6
	40-50	26
	50-60	40
	> 60	28

The collected data was exported and processed into SPSS 16.0 for Microsoft Windows XP. The questions asked can be found in the appendix. Most questions had a one-answer option. Questions 6, 7, 8 and 10 allowed several answers. With each question it was possible to give additional comment.

To make sure that each respondent used the same definitions, we used the following explanation for tactile and proprioceptive feedback. Tactile perception relates to the perception of pressure, vibration, and texture (also sometimes called discriminative touch or cutaneous sense), and relies on different receptors in the skin (cutaneous mechanoreceptors). Proprioception (haptics) concerns the perception of posture and the position of the limbs, body and head in space and their positioning relative to each other, including the vestibular system, cutaneous sense and kinesthesia [11].

3. RESULTS AND DISCUSSION

A total of 281 surgeons responded. Of the 281 respondents, 174 submitted a completely filled-in questionnaire. This resulted in a completely filled out rate of 45%. The experience level of the surgeons ranged from 80 to more than 10.000 operations and from < 5 to 15-20 years of experience. The age of the surgeons ranged from 29 to 69 years. The amount of surgeons that responded is enough to make rough conclusions about their opinion. Although, each new development in this field should check its specific need with the user group. The results can be biased, as it is possible that the surgeons that did not fill the questionnaire are indifference for the topic.

3.1. Results from the Complete Group of Respondents

Forty-six percent of the respondents use grasper 1 to grasp bowel tissue, followed by 24% who use grasper 2. Graspers 3, 4 and 5 where used by 10, 10 and 3% of the respondents respectively and only 7% of the respondents reported using another type of grasper. Grasper 1 was used in our previous studies [9,12,13]. The answers to this question confirmed that this choice of bowel grasper was suitable for representing the bowel graspers used in practice.

From **Figure 2** it can been seen that 51% of the respondents can feel when they apply excessive pinch force to the tissue and are able to adjust the pinch force to prevent damage. In total, 33% of the respondents can see when they apply excessive pinch force and are able to prevent damage. Six percent of the respondents cannot see or feel when they apply excessive pinch force to the tissue. Finally 16% of the surgeons cannot prevent damage although 10% might see or feel it.

Figures 3 shows that 32% of the respondents can feel, 30% can see tissue slippage and are able to prevent it. In total, seven percent of the respondents can not

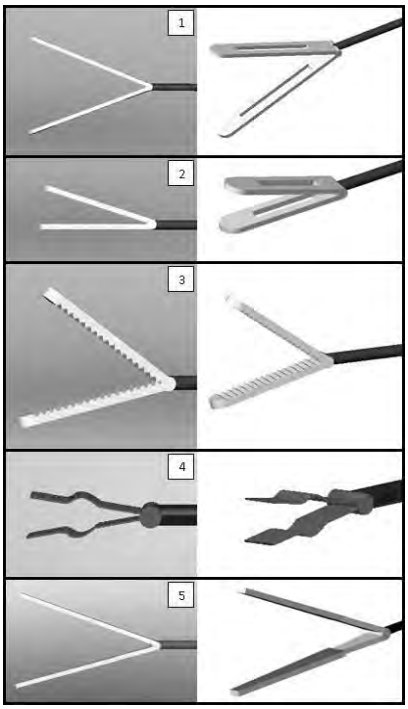

Figure 1. Images of laparoscopic graspers (see question 2).

see or feel when tissue is about to slip. Some 31% of the respondents can see or feel slippage but they cannot do anything to prevent it. The results state that 94% of the respondents indicate that they notice tissue slippage, however, 38% of the respondents indicate that they cannot prevent it. These results show that there is a high percentage of the surgeons who cannot prevent tissue damage through slip. Heijnsdijk *et al.* [8] discovered during a study carried out during 10 laparoscopic colectomies and 15 cholecystectomics conducted by experienced surgeons that the bowel slipped out of the grasper in 7% of the grasp actions, whereas the gallbladder slipped out in 17% of cases. Thus, it seems that even experienced surgeons have difficulty maintaining an accurate pinch force.

In total, 32% of the respondents are aware of the existence of research projects linked to augmented feedback on pinch force information within laparoscopy and the respondents this questionnaire was the first time they heard anything about it. This could indicate that surgeons are not concerned about this issue. However, if we look at the questionnaire response rate, we see that surgeons are concerned. Further research into this topic is therefore important. In addition, the results of these studies should be made easily accessible to surgeons.

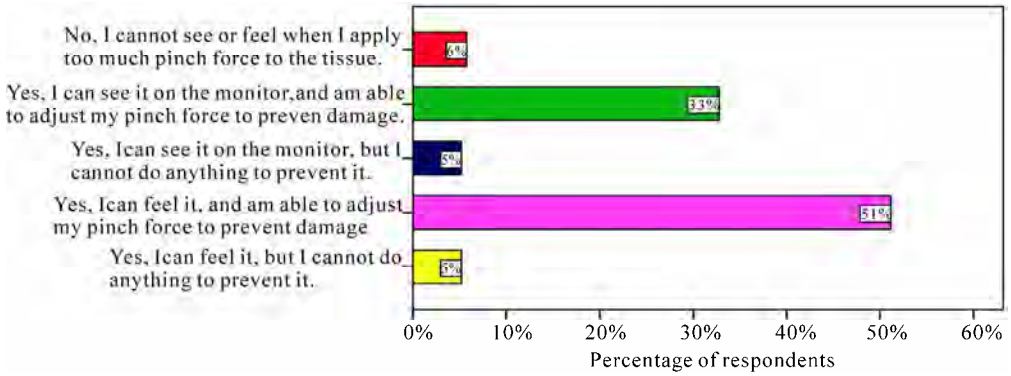

Figure 2. Respondent awareness of excessive pinch force usage. Answer on question 3. "Do you notice when you are about to apply too much pinch force on the tissue?"

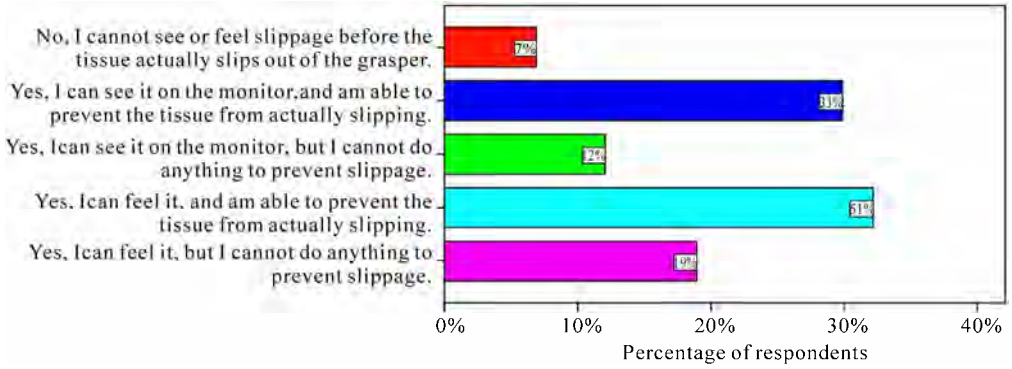

Figure 3. Respondent awareness of tissue slippage. Answer on question 4. "Do you notice when tissue is about to slip?"

Ultimately 12% of the respondents had experience with some form of augmented feedback regarding pinch force within laparoscopy. **Table 3** shows which form of augmented feedback these surgeons had experience with. Some respondents had experience with more than one form of augmented feedback. The majority used visual (95%) or tactile feedback (81%).

In total, 18% of the respondents had used a form of augmented feedback on pinch force information, during their virtual reality training. **Table 4** shows the form of augmented feedback that the respondents used during virtual reality training. Some respondents had had experience with various forms of augmented feedback during their virtual reality training. However, the majority used visual or tactile feedback.

The results of questions six and seven show that tactile and visual augmented feedback is used in research much more frequently than audible and proprioceptive feedback. This can be explained by the fact that additional audible signals in the operating room will distract the surgeon, as there are so many other sounds already. Augmented proprioceptive feedback is technically more difficult to implement and it will be hard for the surgeon to interpret unless a natural reaction is provoked.

The questionnaire gave the respondents the opportunity to indicate their preferred augmented feedback form as an indication of the levels of pinch force. **Figure 4** shows the preferences of the respondents. Most of the respondents would prefer to use tactile feedback as an indication of the level of pinch force (77%), followed by visual feedback (39%). Only 7% of the respondents do not like to use augmented feedback as an indication of the level of pinch force.

Table 3. The form of augmented feedback regarding pinch force that respondents had experienced within laparoscopy.

Form of additional feedback	Number of respondents*	% of respondents
Visual feedback	20	95
Audible feedback	0	0
Tactile feedback	17	81
Proprioceptive feedback	7	33
Otherwise, (open response)	0	0

*Twelve percent of the total number or respondents answered question 6 with 'yes'. The number and percentage of respondents out of this twelve percent who used this form of augmented feedback during laparoscopy is indicated.
Note that some respondents had experienced multiple forms of augmented feedback.

Table 4. The form of augmented feedback regarding pinch force that respondents had experienced during virtual reality training.

Form of augmented feedback	Number of respondents*	% of respondents
Visual feedback	19	61
Audible feedback	6	19
Tactile feedback	19	61
Proprioceptive feedback	5	16
Otherwise, (open response)	2	6

*Eighteen percent of the total number or respondents answered question 6 with 'yes'. The number and percentage of respondents out of this eighteen percent who used this form of augmented feedback during laparoscopy is indicated.
Note that some respondents had experienced multiple forms of augmented feedback.

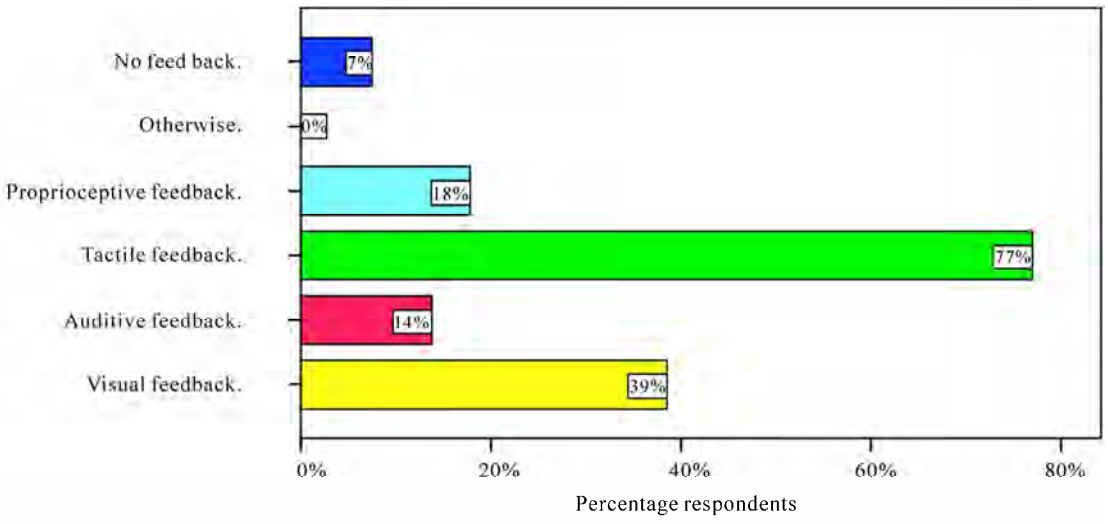

Figure 4. Preferred form of augmented feedback as indication of the levels of applied pinch force. Answer on question 8. "Which form of feedback would you like to use as an indication of the levels of pinch force ?"

During laparoscopic procedures, 64% of the respondents do not look at their hands while performing laparoscopic surgery, while 7% do look several times, 9% look frequently and 20% regularly look at their hands. When the respondents look at their hands, 30% (n = 19) of them look at the hand position on the handle, 24% (n = 15) look at the fingers on the handle, 49% (n = 31) look at the position of the handle and 21% (n = 13) look at other things, for example the hand position relative to the abdomen, angle of instrument to the abdomen and the open or closed position of the handle. These results show that the handle is not the most suitable place to position a visual augmented feedback display but that it might be appropriate to have a tactile or proprioceptive display on the handle.

Twenty-one percent of the respondents have taken part in the modification and/or development of laparoscopic instruments. Twenty surgeons of that group (56%) initiated the innovations themselves, and 25% (9) of them indicated that a colleague instigated the developments. Manufactures were cited in 19% (7) of cases as being responsible for the modification and/or development of laparoscopic instruments. None of the modifications or developments was enforced by the hospitals. This means that surgeons will use/develop new instruments when they are convinced of the added value with respect to the old instrument.

The respondents were asked if a new atraumatic grasper with additional haptic feedback is necessary. This question was answered with a 'yes' by 79% of the respondents. In their reply the respondents emphasized the safety of the grasper and the fact that it will prevent damage. The respondents who indicated that a new atraumatic grasper is not necessary are satisfied with the current laparoscopic instruments. Even though some of the respondents indicated that they notice when tissue is about to slip and that they can prevent it happening, 93 percent would like to have a laparoscopic instrument that provides some form of augmented feedback for slipping tissue. The conclusion therefore is that a new atraumatic grasper with augmented haptic feedback might help to reduce tissue damage.

Finally, 99% of the respondents are open to technical changes in the field of laparoscopic instruments; only 1% of the respondents were not open to changes and indicated that the current laparoscopic instruments are fine. Should this research be continued, 95% of the respondents declared themselves willing to participate in follow-up studies. This could mean that when a new laparoscopic instrument is introduced which contains augmented haptic feedback, a high proportion of the surgeons will want to use it.

3.2. Results of the Categories

There were no major differences in the response between the twelve groups (4 levels in each category). However, there were some minor differences and these are listed below.

Experienced surgeons (1000-2000 operations), use grasper 1 (62%) more frequently than the less experienced ones (33%). More experienced surgeons (> 2000 operations or 15-20 years of experience) indicate more frequently (63 and 61% respectively) than surgeons with less than 5 years of experience (19%) that they can feel when they are applying excessive pinch force to the tissue. Regarding the use of visual verification to determine whether they are about to apply excessive pinch force, the difference between these categories is minimal. Less experienced surgeons find it more difficult to prevent tissue damage than experienced surgeons (> 2000 operations, 15-20 years experience and > 60 age). This means that experience leads to a better interpretation of the task-intrinsic feedback. However, the learning curve for laparoscopic grasp control is long and even experienced surgeons do have difficulty using task-intrinsic feedback.

Surgeons of 60 years and older are not always the persons with the most experience in laparoscopic procedures. In contrast to the others, the category over the age of 60 does not have experience (0%) with virtual reality training regarding augmented feedback on pinch force. This is probably due to the fact that these techniques did not exist when they where being educated. In addition, this category of surgeons looks more to their hands during any given procedure (50% in this category as opposed to 30% in the categories > 2000 operations or with 15-20 years of experience). The last minor difference is that less experienced surgeons (< 500 operations, < 5 years experience or < 40 years) indicate not having been involved in new developments compared to the other categories. This is obviously attributable to the fact that less experienced surgeons might think they do not have enough experience to innovate change.

4. CONCLUSIONS

The aim of this study was to estimate the opinions and experiences of surgeons with the use of laparoscopic bowel graspers from the point of view of haptics, Thanks to the large number of respondent's research and development of new instruments can now address the needs of the surgeons themselves.

In 38% of the cases the damage, according to the respondents, emanates from slip and in 16% of cases damage is attributable to excessive pinch force. This kind of tissue damage has to be reduced, possibly by using a laparoscopic instrument with augmented feedback on the levels of pinch force. The outcome of this study indicates a clear need for research and for the development of a new instrument with augmented feedback on force information and slippage.

REFERENCES

[1] Cuschieri, A. (1995) Whither minimal access surgery: Tribulations and expectations. *American Journal of Surgery*, **169**, 9-19.

[2] Moreno-Egea, A., Torralba, J., Morales, G., Fernandez, T., Guzman, P., Hita, G., Girela, E., Corral, M., Campillo, A. and Aguayo, J. (2005) Laparoscopic repair of secondary lumbar hernias: Open vs. laparoscopic surgery. A prospective, nonrandomized study. *Cirugia Espanola*, **77**, 159-162.

[3] Dedemadi, G., Sgourakis, G., Karaliotas, C., Christofides, T., Kouraklis, G. and Karaliotas, C. (2006) Comparison of laparoscopic and open tension-free repair of recurrent inguinal hernias: A prospective randomized study. *Surgical Endoscopy*, **20**, 1099-1104.

[4] Roumm, A., Pizzi, L., Goldfarb, N. and Cohn, H. (2005) Minimally invasive: Minimally reimbursed? An examination of six laparoscopic surgical procedures. *Surgical Innovations*, **12**, 261-287.

[5] Stefanoni, M., Casciola, L., Ceccarelli, G., Spaziani, A., Conti, D., Bartoli, A., Zitti, L.D., Bellocchi, R. and Valeri, R. (2006) The biliopancreatic diversion. A comparison of laparoscopic and laparotomic techniques. *Minerva Chirurgica*, **61**, 205-213.

[6] Stassen, H.G., Dankelman, J., Grimbergen, C.A. and Meijer, D.W. (2001) Man-machine aspects of minimally invasive surgery. *Annual Reviews in Control*, **25**, 111-122.

[7] Dankelman, J., Wentink, M. and Stassen, H.G. and Gouma, D.J. (2003) Human reliability and training in minimally invasive surgery. *Minimally Invasive Therapy and Allied Technologies*, **12**, 129-135.

[8] Heijnsdijk, E.A.M., Dankelman, J. and Gouma, D.J. (2002) Effectiveness of grasping and duration of clamping using laparoscopic graspers. *Surgical Endoscopy*, **16**, 1329-1331.

[9] Westebring-van der Putten, E.P., van den Dobbelsteen, J.J., Goossens, R.H., Jakimowicz, J.J. and Dankelman, J. (2009) Force feedback requirements for efficient laparoscopic grasp control. *Ergonomics*, **52**, 1055-1066.

[10] Westebring-van der Putten, E.P., Goossens, R.H.M., Jakimowicz, J.J. and Dankelman, J. (2008) Haptics in minimally invasive surgery-a review. *Minimally Invasive Therapy and Allied Technologies*, **17**, 3-16.

[11] Widmaier, E.P., Hershel, R. and Strang, K.T. (2004) Vander, Sherman, and Lucano's Human Physiology, The mechanisms of body function, 9th Edition, McGraw-Hill, 207-266.

[12] Westebring-van der Putten, E.P., van den Dobbelsteen, J.J., Goossens, R.H.M., Jakimowicz, J.J. and Dankelman, J. (2009) Effect of laparoscopic grasper force transmission ratio on grasp control. *Surgical Endoscopy*, **23**, 818-824.

[13] Westebring-van der Putten, E.P., Lysen, W.W., Hensen, V.D., Koopmans, N., Goossen, R.H.M., van den Dobbelsteen, J.J., Dankelman, J. and Jakimowicz, J.J. (2009) Tactile Feedback exceeds visual feedback to display tissue slippage in a laparoscopic grasper, Ios Press, **142**, 420-425.

Appendix: Questionaire

Laparoscopic operations in general

1. How many years have you been using laparoscopic surgery?
2. Which of the pictures below best represents the laparoscopic grasper you use to grasp bowel tissue ? The pictures are presented in **Figure 1**.
3. Do you notice when you are about to apply too much pinch force on the tissue?
   - *Yes, I can feel it, but I cannot do anything to prevent it.*
   - *Yes, I can feel it, and am able to adjust my pinch force to prevent damage.*
   - *Yes, I can see it on the monitor, but I cannot do anything to prevent it.*
   - *Yes, I can see it on the monitor, and am able to adjust my pinch force to prevent damage.*
   - *No, I cannot see or feel it when I apply too much pinch force to the tissue.*
4. Do you notice when tissue is about to slip?
   - *Yes, I can feel it, but I cannot do anything to prevent slippage.*
   - *Yes I can feel it, and am able to prevent the tissue from actually slipping.*
   - *Yes, I can see it on the monitor, but I cannot do anything to prevent slippage.*
   - *Yes, I can see it on the monitor, and am able to prevent the tissue from actually slipping.*
   - *No, I cannot see or feel slippage before the tissue is actually out of the grasper.*

Laparoscopic surgery and augmented feedback

5. Are you well informed on research into augmented feedback on pinch force information within laparoscopy?
   - *Yes, I have read studies.*
   - *Yes, I take/took part in similar research.*
   - *Yes, (open response).*
   - *No, (open response).*

The following definitions are used in questions 6 ,7 and 8: Tactile perception relates to the perception of pressure, vibration, and texture (also sometimes called discriminative touch or cutaneous sense), and relies on different receptors in the skin (cutaneous mechanoreceptors). Proprioception (haptics) concerns the perception of posture and the position of the limbs, body and head in space and their positioning relative to each other, including the vestibular system, cutaneous sense and kinesthesia

6. Do you have experience with a form of additional feedback regarding pinch force within laparoscopy?
   - *Yes, from another research project. This research is about:*
   - *Visual feedback.*
   - *Auditive feedback.*
   - *Tactile feedback.*
   - *Proprioceptive feedback.*
   - *Otherwise, (open response).*
   - *No.*
7. Have you used a form of additional/alternative feedback on pinch force information, during a virtual reality training exercise?
   - *Yes, what kind of feedback have you used?*
   - *Visual feedback.*
   - *Auditive feedback.*
   - *Tactile feedback.*
   - *Proprioceptive feedback.*
   - *Otherwise, (open response).*
   - *No.*
8. Which form of feedback would you like to use as an indication of the levels of pinch force?
   - *Visual feedback.*
   - *Auditive feedback.*
   - *Tactile feedback.*
   - *Proprioceptive feedback*
   - *Otherwise, (open response).*
   - *No feedback.*
9. Do you look at your hands while performing laparoscopic surgery?
   - *Yes, several times (once or twice every 10 minutes) during surgery.*
   - *Yes, frequently (once or twice during every surgical procedure).*
   - *Yes, regularly (but not during every surgical procedure).*
   - *No, never.*

10. When you look at your hands what do you look at?
    - *My hand position on the handle.*
    - *My fingers on the handle.*
    - *The position of the handle.*
    - *Otherwise, (open response).*

Laparoscopic surgery and involvement

11. Have you taken part in the modification/development in laparoscopic instruments?
    - *Yes.*
    - *No.*
12. Who was responsible for the initiation of these changes?
    - *Self initiated.*
    - *Instigated by a colleague.*
    - *Enforced by the hospital.*
    - *Enforced by the manufacturer.*
13. Do you think a new atraumatic grasper with additional haptic feedback is necessary?
    - *Yes, because (open response).*
    - *No, because (open response).*
14. Are you open to technical changes in the field of laparoscopic instrumentation?
    - *Yes, I am open to changes and their applications.*
    - *Yes, I am open to changes, will probably continue to use the current laparoscopic instruments.*
    - *Yes, (open response).*
    - *No, I am not open to changes, the current laparoscopic instruments are working fine.*
    - *No, (open response).*
15. Are you willing to take part in follow-up research, possibly including a test with a prototype?
    - *Yes, you may contact me in the future.*
    - *No, I am not interested.*

J. Biomedical Science and Engineering, 2010, 3, 430-438 **JBiSE**
doi:10.4236/jbise.2010.34059 Published Online April 2010 (http://www.SciRP.org/journal/jbise/).

Fermentation process modeling of exopolysaccharide using neural networks and fuzzy systems with entropy criterion

Zuo-Ping Tan[1,2,3], Shi-Tong Wang[1], Zhao-Hong Deng[1], Guo-Cheng Du[2]

[1]School of Information Engineering, Jiangnan University, Wuxi, china;
[2]Key Laboratory of Industrial Biotechnology, Ministry of Education, Jiangnan University, Wuxi, China;
[3]Jiangsu Province Key Laboratory of Information Technology at Suzhou University, Suzhou, China.
Email: wxwangst@yahoo.com.cn

Received 17 December 2009; revised 28 December 2009; accepted 12 January 2010.
.

ABSTRACT

The prediction accuracy and generalization of fermentation process modeling on exopolysaccharide (EPS) production from Lactobacillus are often deteriorated by noise existing in the corresponding experimental data. In order to circumvent this problem, a novel entropy-based criterion is proposed as the objective function of several commonly used modeling methods, *i.e.* Multi-Layer Perceptron (MLP) network, Radial Basis Function (RBF) neural network, Takagi-Sugeno-Kang (TSK) fuzzy system, for fermentation process model in this study. Quite different from the traditional Mean Square Error (MSE) based criterion, the novel entropy-based criterion can be used to train the parameters of the adopted modeling methods from the whole distribution structure of the training data set, which results in the fact that the adopted modeling methods can have global approximation capability. Compared with the MSE-criterion, the advantage of this novel criterion exists in that the parameter learning can effectively avoid the over-fitting phenomenon, therefore the proposed criterion based modeling methods have much better generalization ability and robustness. Our experimental results confirm the above virtues of the proposed entropy-criterion based modeling methods.

Keywords: Relative Entropy; MSE-Criterion Based Modeling; Robustness; Parzen Window; TSK Fuzzy System

1. INTRODUCTION

Polysaccharides are produced by plants, algae and bacteria, which are used in pharmaceutical, chemical, pesticide and oil exploitation. Some microorganisms such as the lactic acid producers are known to synthesize exopolysaccharides (EPS), which can be used commercially as food additives and have health stimulating properties such as immunity stimulation, anti-ulcer activity and cholesterol reduction. However, as we may know well, EPS's fermentation mechanism is very complex because it refers to the growth and reproduction of microorganisms [1]. In view of control, fermentation process contains high non-linearity, high time-varying and uncertainty. Meanwhile the lack of biosensor and the interaction of coupled parameters also bring much difficulty for the fermentation process modeling [2]. In the last decade, artificial neural networks (ANNs) have been proved to be able to model nonlinear systems and successfully applied in various chemical and biological models [3]. Especially they have emerged as an attractive tool for predicting and approximating the parameters in fermentation process [4], and demonstrated their powers in the factorial design [5]. More examples include one ANNs-based model for amino acid composition and optimum pH in G/11 xylanase [6], and another ANNs-based model for optimization of fermentation media for exopolysaccharide production from Lactobacillus plantarum [7]. In recent years, fuzzy systems and/or fuzzy neural networks researchers have paid particular attention on industrial fermentation process modeling [8]. For instance, fuzzy neural network has been used for dissolved Oxygen predictive control of fermentation process [9], and Takagi-Sugeno-Kang (TSK) fuzzy system has been used for biochemical variable estimation of fermentation process [10]. In addition, an application of fuzzy control in citric acid fermentation process has been adopted to maximize the biomass quantities [11]. However, when MSE-criterion based objective function is used for model parameter learning, the above methods have the so-called over-fitting drawback, that is to say, MSE-criterion based modeling methods may over-fit each training sample such that the whole distribution of the training set is errously estimated and the generalization ability can not be assured.

In this study, in order to overcome the weaknesses

mentioned above, the new criterion is proposed as the objective function for fermentation process modeling. This new criterion, called the entropy criterion, is based on the probability density estimation for the whole training set and relative entropy [12]. And then the proposed criterion is used in the classical Multi- Layer Perceptron (MLP) network modeling, Radial Basis Function (RBF) neural network modeling and Takagi-Sugeno-Kang (TSK) fuzzy system modeling, for the EPS fermentation process modeling.

2. MATERIALS AND METHODS

The data we used in this study was derived from the reference [7]. This project was conducted in 2004-2006 by Mumbai University of Food Engineering, in Mumbai, India.

2.1. Bacterial Strain

Lactobacilli strain is isolated from the Indian fermented food ragi. This isolation is characterized as Lactobacillus plantarum using biochemical tests.

2.2. Medium

The medium contain lactose, casine hydrolysate, triammonium citrate, beef extract and proteose peptone, along with sodium acetate: 1 g/l, Mg-sulfate: 1 g/l, manganese sulfate: 0.5 g/l and calcium chloride: 0.25 g/l. The medium are autoclaved at 110℃ for 10 min; lactose is autoclaved separately.

2.3. Fermentation Conditions

The batch fermentation is carried in a 250 ml shake flask for 24 h at 150 rpm and 35℃. The pH of the fermentation medium is adjusted to 6.5 ± 0.3 with the addition of 1N NaOH/1N HCL. Flasks at the end of fermentation are analyzed for EPS production.

2.4. Analysis

The cells are separated by centrifugation(10,000 rpm, 10℃, 15 min) and the crude EPS is precipitated from the broth at 4 by the addition of two volumes of cold ethanol (95%). The resulting precipitate is collected by centrifugation and re-dissolved in water. The crude EPS solution is dialyzed at 4℃ to estimate the yield.

2.5. MSE-Criterion Based Fermentation Process Modeling

In most of current modeling methods, the MSE-criterion based objective function is often used for training model parameters. The MSE-criterion can be formulated as

$$E_1 = \frac{1}{2N}\sum_{i=1}^{N}(y_i - y_{di})^2 \qquad (1)$$

where y_i, y_{di} are the predicted and desired output for ith sample , respectively.

From **Eq.1**, we can see that the MSE-criterion based model parameter learning is just a local approximation process and does not consider the whole distribution of the training set [13,14], thus the generalization and robustness of the model will not be ensured and the over-fitting often occurs, especially when there are noises in the training data.

3. ENTROPY-CRITERION BASED FERMENTATION PROCESS MODELING

3.1. Relative Entropy and Jeffreys-Divergence Entropy

Entropy is a measurement of uncertainty in information theory, which is a function of the probability density distribution. The concept of relative entropy can be introduced to measure the difference between certain probability density distribution $f_1(x_i)$ and a given probability density distribution $f_2(x_i)$, which may be written as follows [12,15],

$$V(f_1, f_2) = -\sum f_1(x_i)\log[f_1(x_i)/f_2(x_i)] \le 0 \qquad (2)$$

where the smaller value of relative entropy is, the larger difference between the two density distributions is. Meanwhile, when certain probability density distribution is equal to the given distribution, the relative entropy will reach its maximum (equal to zero). It is well known that relative entropy is additive and non-symmetrical. To obtain a symmetrical measure, Jeffreys-divergence entropy (J-divergence entropy) can be used. It is also called symmetrical relative entropy which can measure the difference between two densities $f_1(x_i)$ and $f_2(x_i)$.

$$\begin{aligned} W(f_1, f_2) &= V(f_1, f_2) + V(f_2, f_1) \\ &= -\sum f_1(x_i)\log[f_1(x_i)/f_2(x_i)] \\ &\quad -\sum f_2(x_i)\log[f_2(x_i)/f_1(x_i)] \\ &= -\sum f_1(x_i)\log[f_1(x_i)] - \sum f_2(x_i)\log[f_2(x_i)] \\ &\quad +\sum f_1(x_i)\log[f_2(x_i)] + \sum f_2(x_i)\log[f_1(x_i)] \end{aligned} \qquad (3)$$

According to the above J-divergence entropy, a novel objective function based on entropy-criterion will be illustrated in the next subsection.

3.2. Relative Entropy Based Objective Function

For a given training sample set $\left\{(\mathbf{x}_i, y_{di}) \middle| \mathbf{x}_i \in R^d,\ y_{di} \in R,\ i = 1, 2, ..., N\right\}$, we can reconstruct two new sets, *i.e.*, one contains the sample inputs and the sample outputs, $S_1 = \{\mathbf{z}_i' \middle| \mathbf{z}_i' = (\mathbf{x}_i, y_{di})\}$,

$\mathbf{z}_i^{'} \in R^{d'}$ ($d^{'} = d+1$), and the other contains the sample inputs and the model predicted outputs, $S_2 = \{\mathbf{z}_i^{"} \,|\, \mathbf{z}_i^{"} = (\mathbf{x}_i, y_i)\}$, $\mathbf{z}_i^{"} \in R^{d'}$.

For the above sample set $\{\mathbf{x}_i \,|\, \mathbf{x}_i \in R^d,\ i = 1,2,...,N\}$, its probability density can be estimated with the following parzen window density estimator,

$$f(\mathbf{x},\sigma) = \frac{1}{N}\sum_{i=1}^{N}(\sqrt{2\pi}\sigma)^{-d} e^{-\frac{\|\mathbf{x}-\mathbf{x}_i\|}{2\sigma^2}} \quad (4)$$

where σ represents the window width. For a given data, it is constant and can be used to effectively estimate the corresponding density distribution. Here with maximum likelihood estimation (MLE), it is determined through cross-validation (CV) method, and the value resulting in the max magnitude is chosen [16].

For the above two data sets S_1 and S_2, their probability density distribution functions, $f_1(\mathbf{z},\sigma)$ and $f_2(\mathbf{z},\sigma)$, can be formulated as

$$f_1(\mathbf{z},\sigma) = \frac{1}{N}\sum_{i=1}^{N}(\sqrt{2\pi}\sigma)^{-d'} e^{-\frac{\|\mathbf{z}-\mathbf{z}_i^{'}\|}{2\sigma^2}} \quad (5)$$

$$f_2(\mathbf{z},\sigma) = \frac{1}{N}\sum_{i=1}^{N}(\sqrt{2\pi}\sigma)^{-d'} e^{-\frac{\|\mathbf{z}-\mathbf{z}_i^{"}\|}{2\sigma^2}} \quad (6)$$

Suppose $G(\mathbf{z}-\mathbf{z}^{'},\sigma^2) = e^{-\frac{\|\mathbf{z}-\mathbf{z}_i\|}{2\sigma^2}}$, then we get,

$$f_1(\mathbf{z},\sigma) = \frac{(\sqrt{2\pi}\sigma)^{-d'}}{N}\sum_{t_1=1}^{N} G(\mathbf{z}-\mathbf{z}^{'},\sigma^2) \quad (7)$$

$$f_2(\mathbf{z},\sigma) = \frac{(\sqrt{2\pi}\sigma)^{-d'}}{N}\sum_{t_2=1}^{N} G(\mathbf{z}-\mathbf{z}^{"},\sigma^2) \quad (8)$$

By using the properties of relative entropy, the bigger the value of relative entropy is, the smaller the difference between two probability densities is, as aforementioned. When the relative entropy reaches its maximal value, the two density functions will absolutely be the same, *i.e.*, $f_2(\mathbf{z},\sigma)$ is equal to $f_1(\mathbf{z},\sigma)$. In other words, in this case the predicted output y_i of the model approximates the sample output y_{di} in the training set well. Consequently the novel objective function may be defined as

$$\begin{aligned} E_2 &= -W(f_1, f_2) \\ &= -\left[V(f_1, f_2) + V(f_2, f_1)\right] \\ &= \int f_1(\mathbf{z}) \log f_1(\mathbf{z}) / f_2(\mathbf{z})\, dz + \int f_2(\mathbf{z}) \log f_2(\mathbf{z}) / f_1(\mathbf{z})\, dz \\ &= \int \{ f_1(\mathbf{z})\left[\log f_1(\mathbf{z}) - \log f_2(\mathbf{z})\right] \\ &\quad + f_2(\mathbf{z})\left[\log f_2(\mathbf{z}) - \log f_1(\mathbf{z})\right]\} d\mathbf{z} \end{aligned} \quad (9)$$

From **Eq.4-Eq.6**, we can see that f(z) is obtained by Parzen window estimator , thus its value ranges from 0 to 1. According to the properties of Taylor's expansion, when $f(\mathbf{z})$ is small, we can just keep the linear parts of $\log f(\mathbf{z})$, that is to say, $\log f(\mathbf{z})$ can be simplified as follows,

$$\log f(\mathbf{z}) = \log\left[1 + (f(\mathbf{z}) - 1)\right] \approx f(\mathbf{z}) - 1 \quad (10)$$

Therefore, submitting **Eq.10** into **Eq.9**, we get,

Please note, Erhan and Jose [17] have strictly inferred the following formulas,

$$\int f_1^2(\mathbf{z})\, d\mathbf{z} = \frac{\left(\sqrt{2\pi}\sqrt{2}\sigma\right)^{-d'}}{N^2}\sum_{t_1=1}^{N}\sum_{t_2=1}^{N} G\left(\mathbf{z}_{t_1}^{'} - \mathbf{z}_{t_2}^{'}, 2\sigma^2\right) \quad (12)$$

$$\int f_2^2(\mathbf{z})\, d\mathbf{z} = \frac{\left(\sqrt{2\pi}\sqrt{2}\sigma\right)^{-d'}}{N^2}\sum_{t_1=1}^{N}\sum_{t_2=1}^{N} G\left(\mathbf{z}_{t_1}^{"} - \mathbf{z}_{t_2}^{"}, 2\sigma^2\right) \quad (13)$$

$$\int f_1(\mathbf{z})\, f_2(\mathbf{z})\, d\mathbf{z} = \frac{\left(\sqrt{2\pi}\sqrt{2}\sigma\right)^{-d'}}{N^2}\sum_{t_1=1}^{N}\sum_{t_2=1}^{N} G\left(\mathbf{z}_{t_1}^{'} - \mathbf{z}_{t_2}^{"}, 2\sigma^2\right) \quad (14)$$

Thus, submitting **Eqs.12**,**13**, and **14** into **Eq.11**, we can immediately derive the novel objective function as follows

$$\begin{aligned} E_2 = \frac{\left(\sqrt{2\pi}\sqrt{2}\sigma\right)^{-d'}}{N^2}\Bigg[&\sum_{t_1=1}^{N}\sum_{t_2=1}^{N} G\left(\mathbf{z}_{t_1}^{'} - \mathbf{z}_{t_2}^{'}, 2\sigma^2\right) \\ &+ \sum_{t_1=1}^{N}\sum_{t_2=1}^{N} G\left(\mathbf{z}_{t_1}^{"} - \mathbf{z}_{t_2}^{"}, 2\sigma^2\right) - 2\sum_{t_1=1}^{N}\sum_{t_2=1}^{N} G\left(\mathbf{z}_{t_1}^{'} - \mathbf{z}_{t_2}^{"}, 2\sigma^2\right)\Bigg] \end{aligned} \quad (15)$$

Since **Eq.15** actually originates from the Parzen window desity estimator and relative entropy for the sampling set and roots at the whole distribution of the training sample set, this novel objective function has the following virtues: since the new criterion is based on the density probability and not the local data points, this corresponding model parameter learning can effectively avoid the over-fitting drawback and show a less sensitivity to noise in the noisy environment. Our experimental results in this study will confirm these virtues.

3.3. Entropy-Criterion Based Parameter Learning

For a given modeling model, with the commonly used gradient descent procedure [18], we can easily get the following model parameter's learning rule,

$$p(t+1) = p(t) - r\frac{\partial E_2}{\partial p} \quad (16)$$

where p denotes the model parameter; t denotes the iteration number and r is the learning rate.

4. RESULTS

In this section, we will illustrate the performance of the proposed entropy-criterion based fermentation process modeling on EPS production from Lactobacillus.

4.1. Performance Index

In order to do the comparative study for the performances of different modeling methods with MSE-criterion and entropy-criterion, we adopt the following performance index to evaluate different modeling methods [19,20].

$$J = \sqrt{\frac{\sum_{l=1}^{N}\left(y_l - y_l^d\right)^2}{\sum_{l=1}^{N}\left(y_l^d - \bar{y}\right)^2}} \tag{17}$$

where $\bar{y} = \frac{1}{N}\sum_{l=1}^{N} y_l^d$; N denotes the number of the testing samples; y_l^d is the l th desired output in the testing set; y_l is the predicted output of the model in testing set. Here, the smaller the value of J is, the better the performance of the corresponding training model is.

4.2. Results

In our experiments, we take three modeling methods: MLP network model, RBF network model and TSK fuzzy system model. All three models have four input nodes representing the four influential process variables (concentrations of lactose, casein hydrolysate and triammonium citrate, and inoculum size) and one output node representing the EPS yield (g/l) at the end of batch. The process data for modeling are generated by carrying out a number of fermentation runs under various input conditions. Here we collect 54 sample data as shown in **Table 1**, each sample data represents a pair of model inputs (fermentation conditions) and a single output (EPS concentration). For MLP network model, RBF neural network model and TSK fuzzy system model, these 54 sample data will be partitioned into a training set (45 samples) and a testing set (9 samples) [7]. The training set is utilized to adjust the parameters of all three models and the testing set is used to evaluate the prediction accuracy. The EPS yield comparisons of the sample data and predicted ones in the testing set obtained by using MSE-criterion based models and entropy-criterion based models are illustrated in **Figures 2-4**. a L, T, C and I in the table represented for Lactose/(g/l), Triammonium citrate/(g/l), Casein hydrolysate/(g/l), Inoculum size/(vol%), respectively.

In fact, due to the extremely complexity of both the fermentation mechanism and the limitation of the experimental condition, experimental data may inevitably contain noise. Hence, how to enhance robustness of the fermentation process modeling is very important. In order to compare the robustness between MSE-criterion based models and entropy-criterion based models, we add Gaussian white noise (G(0, σ_1)) to the training sample set, where $\sigma_1 \in (0, 0.20)$ [8]. In **Tables 2-4**, we list the corresponding performance index for the testing set with 11 different Gaussian white noises.

4.3. MLP Network Modeling

Multi-Layer Perceptron (MLP) network [21] is one of the most widely utilized paradigms in the fermentation process modeling, because it is very simple, general and matured. In the network training procedure, the tangent sigmoid activation function and linear combination function are used for computing the outputs of the hidden and output nodes, respectively. When developing an appropriate MLP model, we must carefully select the number of hidden nodes and then use Back- propagation procedure (BP procedure) [22] to adjust the model parameters. Here the MLP network model contains 15 hidden nodes, and its architecture is illustrated in **Figure 1(a)**. The experimental results about EPS fermentation data from Lactobacillus are illustrated in **Table 2**.

4.4. RBF Network Modeling

Another widely utilized modeling method is Radial Basis Function (RBF) neural network [23], Just like MLP network, RBF network is essentially a feed-forward network. However, RBF network utilizes radial basis functions as its activation functions in the hidden layer. In our experiments, the number of hidden nodes is fixed to be 13, and the RBF network's architecture can be seen in **Figure 1(b)**. The experimental results about EPS fermentation data are illustrated in **Table 3**.

4.5. TSK Fuzzy System Modeling

Takagi-Sugeno-Kang (TSK) fuzzy system [24] has been widely applied, due to its strong capability in learning, universal approximation and handling with matural linguistics with fuzzy rules acquried from the skilled worker and/or experts. In our experiments, the number of the fuzzy rules is fixed to be 8, and the architecture of the TSK fuzzy system can be seen in **Figure 1(c)**. The experimental results about EPS fermentation data are illustrated in **Table 4**.

As it can be seen from **Tables 2**, **3** and **4**, the prediction accuracies of these three modeling methods with the proposed entropy-criterion based objective function are obviously higher than these methods with MSE-criterion based objective function. This fact means that the proposed objective function is very suitable for the EPS fermentation process modeling.

Figures 5-7 are generated from **Tables 2-4**. In **Figures 5-7**, X-axis denotes the added noise corresponded (see the second column in **Tables 2-4**), and Y-axis denotes the testing performance index. Dotted lines correspond to the testing performance indices of MSE-based criterion (see the third column in **Tables 2-4**), while real lines correspond to the testing performance indices of these modeling methods with entropy-based criterion (see the fourth column in **Tables 2-4**).

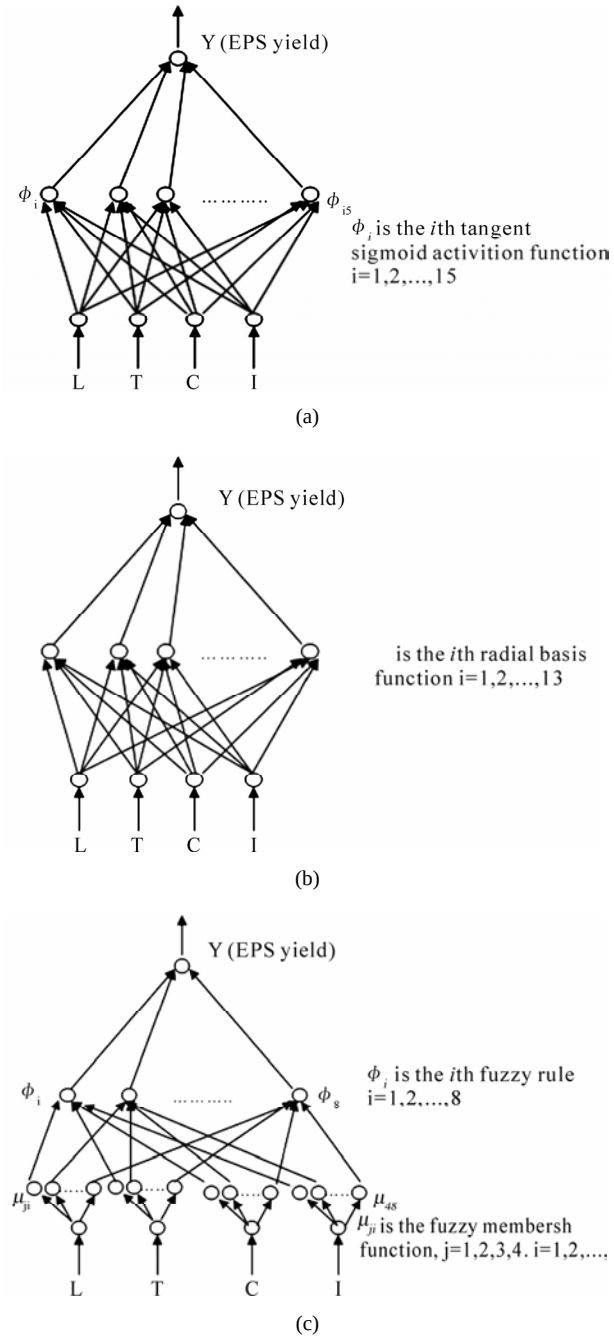

Figure 1. (a) Architecture of MLP network; (b) Architecture of RBF neural $\mu_n$etwork; (c) Architecture of TSK fuzzy system.

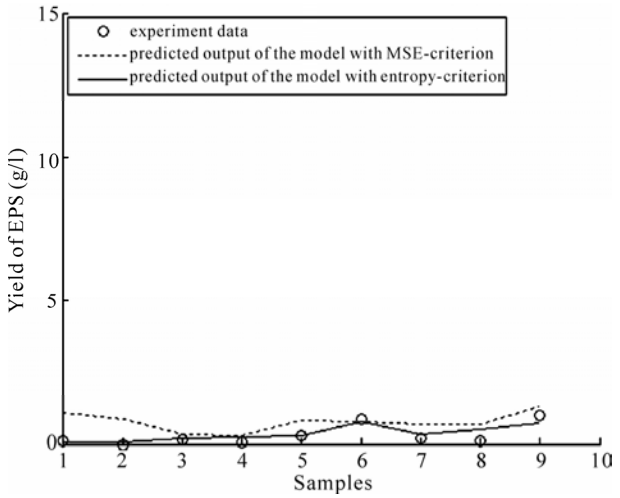

Figure 2. Comparison of EPS yield prediction using MLP network model.

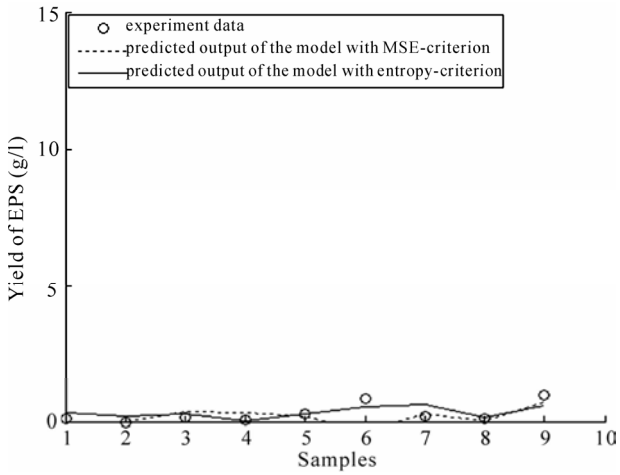

Figure 3. Comparison of EPS yield prediction using RBF model.

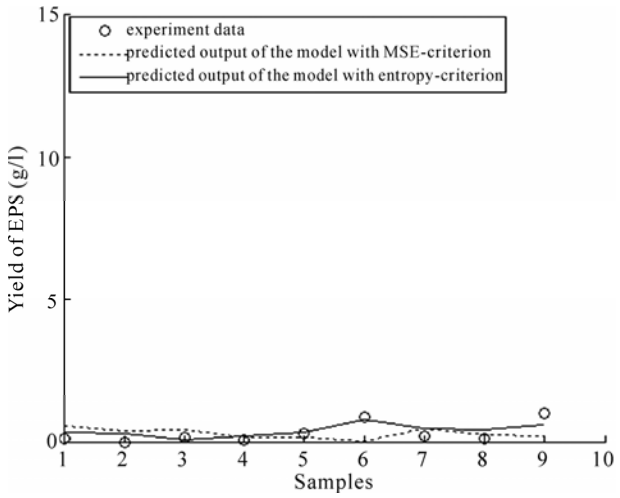

Figure 4. Comparison of EPS yield prediction using fuzzy system model.

Table 1. EPS fermentation data.

No.	Factors and levels				EPS	No.	Factors and levels				EPS
	L	T	C	I			L	T	C	I	
1	8	0	2	1.5	2.29 ± 0.41	28	20	0.3	5	1	1.90 ± 0.44
2	8	0.2	8	3.5	3.43 ± 0.12	29	8	0.2	4	3.5	2.68 ± 0.42
3	25	0	4	1.5	5.16 ± 0.73	30	8	0	4	2	2.65 ± 0.45
4	8	0.2	2	2	2.38 ± 0.62	31	8	0.2	2	1.5	2.51 ± 0.66
5	25	0.2	2	2	4.51 ± 0.37	32	4	0.2	8	2	1.99 ± 0.07
6	25	0.2	8	2	5.32 ± 0.12	33	25	0	4	3.5	5.04 ± 0.16
7	20	0.2	8	1	1.64 ± 0.18	34	40	0.2	4	1	1.88 ± 0.05
8	4	0.2	4	1.5	1.54 ± 0.04	35	2	0.2	4	1	0.65 ± 0.46
9	25	0.2	4	2	5.20 ± 0.24	36	8	0.2	8	2	3.55 ± 0.40
10	25	0	8	1.5	5.66 ± 0.76	37	8	0.2	4	1	1.20 ± 0.05
11	8	0	4	1.5	2.80 ± 0.01	38	20	0.2	4	1	1.70 ± 0.18
12	20	0.1	5	1	1.80 ± 0.50	39	25	0	2	3.5	4.61 ± 0.73
13	10	0.2	4	1	1.35 ± 0.64	40	4	0	8	1.5	2.26 ± 0.48
14	4	0	4	1.5	1.43 ± 0.15	41	4	0.2	8	3.5	2.17 ± 0.39
15	25	0.2	4	1.5	5.22 ± 0.57	42	20	0.2	1	1	0.80 ± 0.69
16	4	0	2	2	0.98 ± 0.58	43	4	0	2	3.5	1.02 ± 0.34
17	8	0.2	4	1.5	2.91 ± 0.32	44	25	0	2	2	4.90 ± 0.57
18	8	0.2	8	1.5	3.79 ± 0.53	45	4	0.2	2	3.5	1.11 ± 0.21
19	4	0.2	2	1.5	1.08 ± 0.42	46	20	0.2	5	1	1.95 ± 0.26
20	4	0.2	4	1	0.80 ± 0.51	47	20	0.2	3	1	1.40 ± 0.13
21	25	0	4	2	5.40 ± 0.12	48	4	0.2	8	1.5	1.98 ± 0.79
22	4	0	4	2	1.59 ± 0.34	49	4	0.2	4	2	1.60 ± 0.73
23	25	0	8	3.5	5.13 ± 0.30	50	4	0.2	4	3.5	2.53 ± 0.28
24	8	0	2	2	2.59 ± 0.59	51	25	0.2	2	3.5	5.04 ± 0.69
25	8	0	4	3.5	2.87 ± 0.47	52	4	0	8	3.5	2.25 ± 0.12
26	8	0	8	3.5	3.78 ± 0.52	53	20	0.4	5	1	1.86 ± 0.26
27	4	0	8	2	2.21 ± 0.71	54	25	0	8	2	5.64 ± 0.66

Table 2. The results about MLP network modeling with MSE-criterion and entropy-criterion.

No.	Noise	Performance index J	
		MSE-criterion	Entropy-criterion
1	0.00	0.8621	0.7730
2	0.02	0.9101	0.8160
3	0.04	0.9940	0.7988
4	0.06	1.1855	0.8487
5	0.08	1.0616	0.8502
6	0.10	1.2130	0.8501
7	0.12	1.3540	0.8511
8	0.14	1.4107	0.8565
9	0.16	1.3558	0.8676
10	0.18	1.5425	0.9117
11	0.20	1.5924	0.9188

Table 3. The results about RBF network modeling with MSE-criterion and entropy-criterion.

No.	Noise	Performance index J	
		MSE-criterion	Entropy-criterion
1	0.00	0.8724	0.7223
2	0.02	0.9279	0.7291
3	0.04	0.9375	0.7441
4	0.06	0.9637	0.7572
5	0.08	0.9970	0.7522
6	0.10	0.9718	0.7779
7	0.12	1.0933	0.7753
8	0.14	1.1369	0.7868
9	0.16	1.1793	0.7914
10	0.18	1.2189	0.7999
11	0.20	1.2413	0.8051

Table 4. The results about fuzzy system modeling with MSE-criterion and entropy-criterion.

No.	Noise	Performance index J	
		MSE-criterion	Entropy-criterion
1	0.00	0.8810	0.6889
2	0.02	1.0852	0.7446
3	0.04	1.1616	0.7641
4	0.06	1.2195	0.8051
5	0.08	1.2237	0.8170
6	0.10	1.2531	0.8124
7	0.12	1.2330	0.8235
8	0.14	1.2689	0.8201
9	0.16	1.2680	0.8390
10	0.18	1.2798	0.8771
11	0.20	1.3141	0.8733

From **Figures 5-7**, it is easy to observe that the three curves corresponding to these three modeling methods with MSE-criterion objective function are always respectively over the curves of these three modeling methods with entropy-criterion based objective function. In addition, with the increases of the noise, the curves of predicted performance indices in **Figures 5-7**, corresponding to the MSE-criterion based modeling methods, have dramatic changes, which mean that the prediction accuracy is deteriorated greatly with the increasing of noise, while the curves corresponding to entropy-criterion based modeling methods in these figures are very smooth. Therefore the experimental results obviously demonstrate that the entropy-criterion based modeling methods have a better generalization and robustness than the MSE-criterion based modeling methods in the EPS fermentation process modeling.

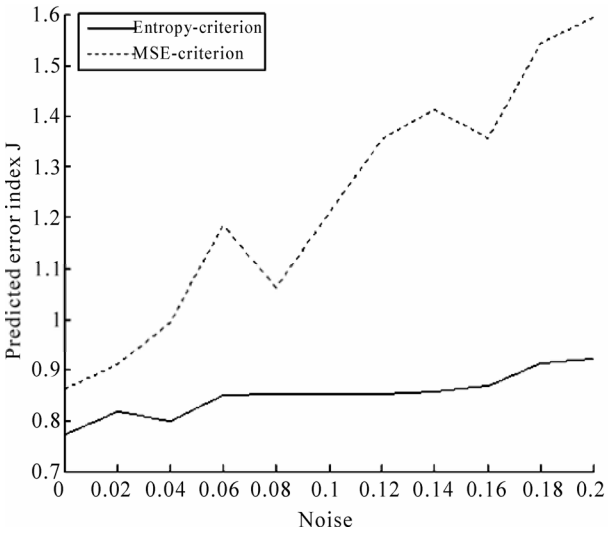

Figure 5. Comparison of testing performance indices of MSE-criterion and entropy-criterion based MLP network modeling method.

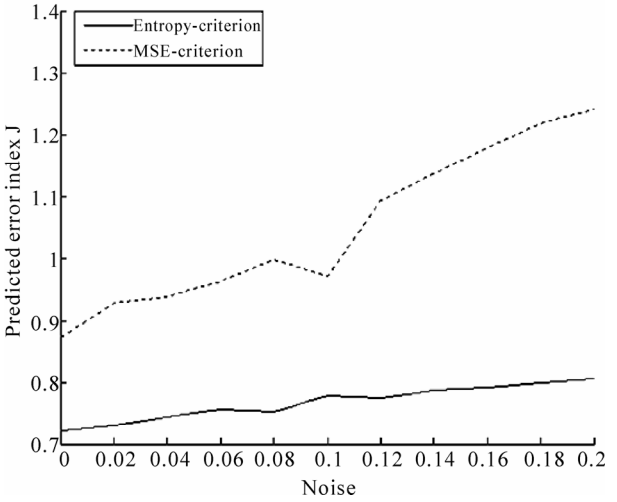

Figure 6. Comparison of testing performance indices of MSE-criterion and entropy-criterion based RBF modeling method.

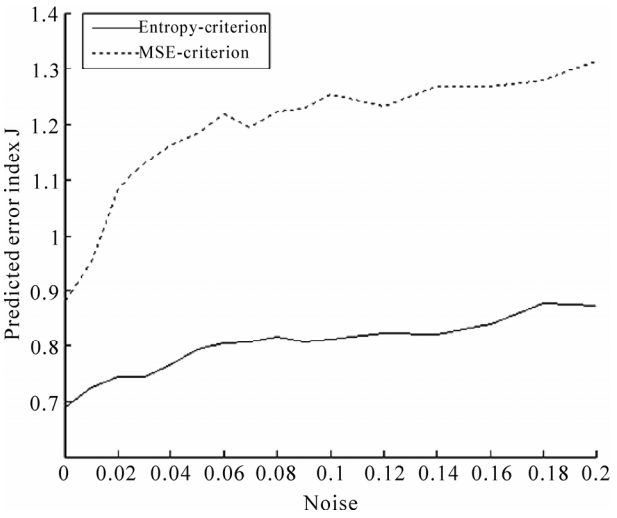

Figure 7. Comparison of testing performance indices of MSE-criterion and entropy-criterion based fuzzy system modeling method.

4.6. Statistical Results for the Obtained Performance Indices

In view of the mean and standard variance of EPS production obtained from the above experiments as the output of the training samples, we can see from **Table 1** that the standard variance is not little, therefore, it is necessary for us to observe the performance of the above three modeling methods from the statistical viewpoint.

In this experiment, we keep the same inputs in the training set as above, however, add noise to the corresponding outputs. The added noise has the mean zero and the same standard variance as derived from the experimental data. In order to keep the experimental results fair, we run each sample data 50 times, and then take their means and standard variances of the performance indices J for the corresponding modeling methods. **Table 5** lists the obtained results.

We can clearly see from **Table 5** that, both the means and standard variances of the outputs of these three modeling methods with entropy-criterion are always lower than the ones with MSE-criterion. This fact confirms our claims again that the proposed entropy- criterion based modeling methods possess the favorable capability in approximation, generalization and robustness.

5. DISCUSSION

When studying fermentation process modeling of EPS from Lactobacillus, we must consider two factors. One is the collected data corrupted by noise, due to the shortage of apparatus and the limitation of experimental conditions. The other is the comparatively weak generalization and robustness capability of current MSE-criterion based modeling methods. In this work, the EPS fermentation process modeling methods with entropy-criterion based objective function are addressed. When it is used in MLP network modeling, RBF modeling and TSK fuzzy system modeling for EPS fermentation from Lactobacillus, our experimental results demonstrate that three modeling methods with entropy-criterion are less sensitive to noise and have better generalization abilities and robustnesses than three modeling methods with MSE-criterion. Because the proposed objective function is derived from the Parzen window desity estimator and relative entropy, and considers the whole distribution structure of the training set in the parameter's learning process, which is different from previous study. The results obtained in this study are very useful in modeling EPS fermentation process, and the entropy- criterion based modeling methods can also be efficiently applied to other fermentation processes.

Table 5. Statistical results of the performance index J of three modeling methods.

Modeling methods	J of MLP network	J of RBF network	J of TSK fuzzy system
MSE-criterion	1.3663 ± 0.2577	1.3893 ± 0.1684	1.1197 ± 0.1807
Entropy-criterion	1.1165 ± 0.1363	0.9998 ± 0.1119	0.9240 ± 0.1210

6. ACKNOWLEDGEMENTS

This work was supported by 863 project of china (grant No.2007AA1Z158, 2006AA10Z313), National Science Foundation of China (grant No. 60773206/F020106，60704047/F030304), The Project Innovation of Graduate Students of Jiangsu Province of China 2008, New century Outstanding Young Scholar Grant of Ministry of Education of China (NCET-04-0496), 2006 Outstanding Young Scholar Grant at JiangSu Province, Grants from the National KeySoft Lab. at Nanjing University and from Jiangsu Province Key Lab. of Information Technologies at Suzhou university.

REFERENCES

[1] Du, F., Lei, M. and Liu, Q. (2004) Advanced control in fermentation process. *Chinese Journal of Information Technology in Construction*, **33**, 314-317.

[2] Gao, X.J., Wang, P., Sun, C.Z., Zhang, Y.T., Zhang, H.Q. and Fan, Q.W. (2006) Modeling and optimization control for the microbial fermentation process. *Chinese Journal of Control Science and Engineering*, **13**, 152-153.

[3] Lee, M.W., Hong, S.H., Choi, H., Kim, J.H., Lee, D.S. and Park, J.M. (2008) Real-time remote monitoring of small-scaled biological wastewater treatment plants by a multivariate statistical process control and neural network-based software sensors. *Process Biochemistry*, **43**, 1107-1113.

[4] Desai, K.M., Vaidya, B.K., Singhal, R.S. and Bhagwat, S.S. (2005) Use of an artificial neural network in modeling yeast biomass and yield of b-glucan. *Process Biochemistry*, **40**, 1617-26.

[5] Kennedy, M.J., Prapulla, S.G. and Thakur, M.S. (1992) A comparison of neural networks to factorial design. *Biotechnology Techniques*, **6**, 293-299.

[6] Zhang, G.Y. and Fang, B.S. (2005) A model for amino acid composition and optimum pH in G/11 xylanase based on neural networks. *Chinese Journal of Biotechnology*, **21(4)**, 658-661.

[7] Desai, K.M., Akolkar, S.K., Badhe, Y.P., Tambe, S.S. and Lele, S.S. (2006) Optimization of fermentation media for exopolysaccharide production from Lactobacillus plantarum using artificial intelligence based techniques. *Process Biochemistry*, **41**, 1842-1848.

[8] Tan, Z.P., Wang, S.T. and Du, G.C. (2008) Glutathione Fermentation Process Modeling based on CCTSK Fuzzy Neural Network. *Journal of Biotechnology*, **7**, 73-79.

[9] Yin, M., Zhang, X.H. and Dai, X.Z. (2000) Dissolved oxygen predictive control based on fuzzy neural networks for fermentation process. *Chinese Journal of Control and Decide*, **15**, 523-526.

[10] Feng, B. and Xu, W.B. (2006) Biochemical variable estimation model based on TSK fuzzy system. *Chinese Journal of Applied Chemistry*, **23**, 343-346.

[11] Meng, H., Fu, X.M. and Cao, G.P. (1999) Neural network fuzzy control of critric acid fermentation process. *Chinese Hebei Journal of Industrial Science & Technology*, **16**, 53-55.

[12] Bian, Z.Q., Zhang, X.G., Yan, P.F., Zhao, N.Y. and Zhang, C.S. (1999) Pattern recognition. Press of Tsing-hua University, Beijing.

[13] Deng, Z.H. and Wang, S.T. (2004) RBF regression modeling based on visual system theory and weber law.

Journal of Southern Yangtze University (Natural Science Edition), **3**, 25-29.

[14] Wang, S.H., Chung, F.L., Xu, M., Deng, Z.H. and Hu, D.W. (2007) A visual system theoretic cost criterion and its application to clustering. *Information Technology Journal*, **6**, 310-324.

[15] Kullback, S. (1968) Information theory and statistics. Dover Publications, New York.

[16] Girolami, M. and He, C. (2003) Probability density estimation from optimally condensed data samples. *IEEE Transactions on Pattern Analysis and Machine Intelligence*, **25**, 1253-1264.

[17] Erhan, G. and Jose, C.P. (2002) Information theoretic clustering. *IEEE Transactions on Pattern Analysis and Machine Intelligence*, **24**, 158-171.

[18] Gardner, W.A. (1984) Learning characteristics of stochastic-gradient-descent algorithms: A general study, analysis and critique. *Signal Processing*, **6**, 113-133.

[19] Jang, J.S.R., Sun, C.T. and Mizutani, E. (1997) A computational approach to learning and machine intelligence. *Neuro-Fuzzy and Soft Computing*, Upper Saddle River, NJ: Prentice-Hall.

[20] Chung, F.L., Wang, S.T., Deng, Z.H. and Hu, D.W. (2006) CATSMLP: Towards a robust and interpretable multilayer perceptron with sigmoid activation functions. *IEEE Transactions on Systems, Man, and Cybernetics-Part B*, **36**, 1319-1331.

[21] Arena, P.L., Fortuna, R.R. and Xibilia, M.G. (1995) Multilayer perceptrons to approximate comples valued functions. *International Journal of Neural Systems*, **6**, 435-446.

[22] Chen, D.S. and Jain, R.C. (1994) A robust backpropagation learning algorithm for function approximation. *IEEE Transactions on Neural Networks*, **5**, 467-479.

[23] Park, J. and Sandberg, I.W. (1991) Universal approximation using radial-basis-function networks. *Neural Computation*, **3**, 246-257.

[24] Sugeno, M. and Yasukawa, T. (1993) A fuzzy-logic-based approach to qualitative modeling. *IEEE Transactions on Fuzzy Systems*, **1**, 7-31.

J. Biomedical Science and Engineering, 2010, 3, 439-441 **JBiSE**
doi:10.4236/jbise.2010.34060 Published Online April 2010 (http://www.SciRP.org/journal/jbise/).

Estimation of the galanthamine using derivative spectrophotometry in bulk drug and formulation

Karan Mittal[1], Ramni Kaushal[1], Rajashree Mashru[2], Arti Thakkar[1]

[1]I. S. F. College of Pharmacy, Ferozepur Road, Ghal Kalan, Moga, Punjab, India;
[2]Center of Relevance and Excellence in Novel Drug Delivery Systems, Pharmacy Department, G.H. Patel Building, The Maharaja Sayajirao University of Baroda, Vadodara, India.
Email: artirthakkar@gmail.com

Received 8 January 2010; revised 20 January 2010; accepted 23 January 2010.

ABSTRACT

Two simple, rapid, accurate, precise, reliable and economical spectrophotometric methods have been proposed for the determination of galanthamine hydrobromide (GH) in bulk and pharmaceutical formulation. First method is zero order UV spectrophotometry and second is 1st derivative zero crossing spectrophotometry. The developed methods have shown best results in terms of linearity, accuracy, precision, LOD and LOQ for bulk drugs and marketed formulations. Absorbance was measured at 287 nm for zero order and 277.4 nm for first derivative. It obeyed Lambert-Beer's law in the range of 30-80 μg mL-1. Both methods have good linearity (r2 = 0.9997) and accuracy found to be 100.5% and 101.2% for both methods respectively.

Keywords: Galanthamine Hydrobromide (GH); Zero Order UV-Spectrophotometry; First Derivative Zero Crossing Spectrophotometry

1. INTRODUCTION

Figure 1 is the structure of galanthamine hydrobromide (GH), which is (4a*S*,6*R*,8a*S*)-5, 6, 9, 10, 11, 12-hexahydro-3-methoxy-11-methyl-4a*H*-[1] benzofuro [3a,3,2-*ef*] [2] benzazepin-6-ol [1,2]. It is used for the treatment of mild to moderate Alzheimer's disease and various memory impairments [3,4]. The molecular weight of GH is 368.27 and melting point is 258-264°C. GH is very soluble in water [5].

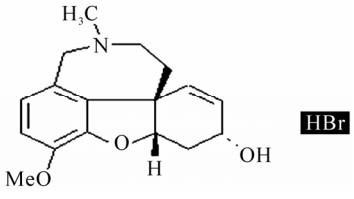

Figure 1. Structure of GH.

The official monograph of USP [6] describes assay method for GH using HPLC but compare to that spectrophotometric methods are more economic and simple. Under computer-controlled instrumentation, derivative spectrophotemetry is playing a very important role in the analysis of drugs by giving more resolved spectra than the zero order spectra [7,8].

The aim of the present work is to investigate utility of derivative spectrophotometry and to develop reliable spectrophotometric procedure for determination of GH either in bulk and marketed formulation.

2. MATERIALS AND METHODS

2.1. Instruments and Reagents

Spectrophotometric measurements were made on a Shimadzu 1700 double beam UV-VIS spectrophotometer with a fix slit width of 1 nm coupled with computer loaded with Shimadzu UV PC software (UV probe) version 2.31. Double distilled water was used and pure GH was obtained from Alembic Pharmaceuticals Ltd. Vadodara, India. The marketed formulation of GH was obtained commercially from Sun Pharmaceuticals Ltd (Galmer-40 tablets labeled 4 mg of pure drug, Batch Number-GK 90964).

2.2. Standard and Test Solutions

Stock solution of 1 mg mL-1 of pure GH and its formulation was freshly prepared in double distilled water. Test solution of GH was tested for stability in solution during the actual analysis. The behaviour of GH was found to be stable over the period of 24 hr from their preparation at room temperature.

2.2.1. Zero Order UV-Spectrophotemetry (Method 1)

The working solutions were prepared by accurately diluting aliquots of the standard solution with water to obtain the concentration in range of 30-80 μg mL-1. The absorption spectra of the samples were recorded between 200-400 nm against double distilled water using a 1.0 cm

quartz cell. Zero order spectra of pure drug GH were stored individually within mentioned concentration ranges and absorbance was measured at 280 nm.

2.2.2. First Derivative Zero Crossing Spectrophotometry (Method 2)

The zero order absorption spectra of GH were derivatized in first order using delta lambda 4 and scaling factor 10. The first derivative amplitudes were recorded at 277.4 nm.

3. RESULTS AND DISCUSSION

The absorption spectra of the GH were recorded at wavelength 287 nm for zero order UV-spectrophotometry and 1st derivative was measured at 277.4 nm. It is observed from the spectra that GH shows a good linearity in the range of 30-80 μg mL-1. **Figure 2** explains the zero order spectra of GH. While, **Figure 3** describes first derivative spectra of GH which showed more resolution than zero order spectra. Both methods were validated, all the validation parameters were in limit as per the ICH guidelines [9]. **Table 1** exhibits the detailed validation parameters for both the methods. **Table 2** represents results of recovery studies of both methods and **Table 3** explains the statistical comparison of results of both the validated methods.

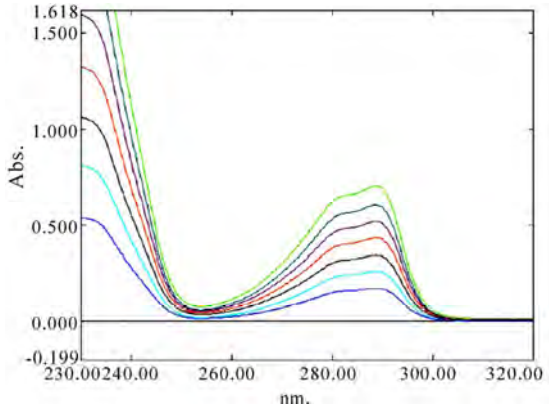

Figure 2. The zero order spectra of GH of 30-80 μg mL^{-1}.

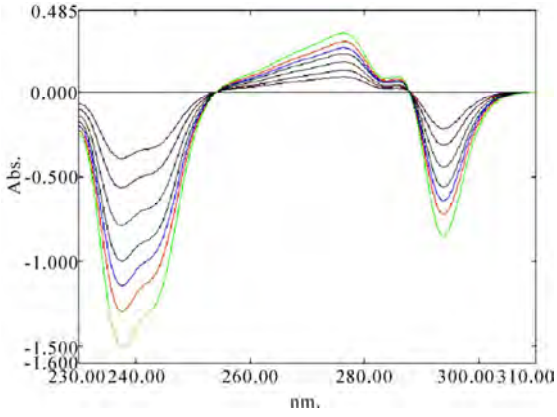

Figure 3. The first derivative spectra of GH of 30-80 μg mL^{-1}.

Table 1. Validation parameters obtained by method 1 and method 2.

Parameters	Method-1	Method-2
Linearity	0.9996	0.9997
Range (μg mL^{-1})	30-80	30-80
Accuracy	100.5 ± 2.39	101.2 ± 1.63
Precision	% R.S.D-0.8315	% R.S.D-1.7052
LOD (μg mL^{-1})	1.46	0.72
LOQ (μg mL^{-1})	4.45	2.19
Assay (%Purity)	98.02	99.94

Table 2. The results of recovery studies of the method 1 and method 2.

Amt added (μg mL^{-1})	% Recovery Method 1	% Recovery Method 2
16	99.25	101.6
20	99.05	99.4
24	103.3	102.6
Mean recovery	100.5	101.2
SD	2.39	1.63

Table 3. The statistical comparison of the results of validated methods.

t-Test	F-Test
$t_{calculated}$ = 0.419	$F_{calculated}$ = 2.14
$t_{theoretical}$ = 3.52	$F_{theoretical}$ = 19.0

The results obtained were compared statistically by Student *t*-test and by the variance ratio *F*-test with those obtained by each method. The calculated values of the Student *t*-values at 95% confidence level and the variance ratio *F*-values did not exceed the theoretical values indicating that there were no significant differences among the results of the developed two methods.

4. CONCLUSIONS

The developed spectrophotometric methods for determination of GH are simple, specific, accurate, precise, rapid and economical which indicates its adequacy for routine pharmaceutical analysis. It is concluded that derivative spectrophotometry is successfully utilized for the estimation of GH.

5. ACKNOWLEDGEMENT

The authors express their sincere thanks to Mr Bhagirath Patel, F & D Division, Alembic Pharmaceuticals Ltd. Vadodara, India for supplying

gift samples of pure Galanthamine hydrobromide and also I.S.F College of Pharmacy, Moga for providing facilities to carry out the research.

REFERENCES

[1] Ping, J., Rong, S., Jing, Z., Liang, F., Qiaojun, H. and Yongzhou, H. (2008) Design, synthesis and evaluation of galanthamine derivatives as acetylcholinesterase inhibitors. *European Journal of Medicinal Chemistry*, **44 (12)**, 772-784.

[2] Traykova, M., Traykov, T., Hadjimitova, V., Krikorian, K. and Bojadgieva, N. (2003) Antioxidant Properties of Galantamine Hydrobromide. *Zeitschrift für Naturforschung*, **58c**, 361-365.

[3] Heinrich, M. and Teoh, H.L. (2004) Galanthamine from snowdrop-the development of a modern drug against Alzheimer's disease from local Caucasian knowledge. *Journal of Ethno pharmacology*, **92**, 147-162.

[4] Scott, L.J. and Goa, K.L. (2000**)** Galantha mine: A review of its use in Alzheimer's disease. *Adis Review*, **60(5)**, 1095-122.

[5] Novikova, I.Y. and Tulaganov, A.A. (2002) Physicochemical methods for the analysis of galanthamine (review). *Pharmaceutical Chemistry Journal*, **36(11)**, 623-627.

Call for Papers

Journal of Biomedical Science and Engineering (JBiSE)

www.scirp.org/journal/jbise

JBiSE, an international journal, publishes research and review articles in all important aspects of biology, medicine, engineering, and their intersection. Both experimental and theoretical papers are acceptable provided they report important findings, novel insights, or useful techniques in these areas. All manuscripts must be prepared in English, and are subject to a rigorous and fair peer-review process. Accepted papers will immediately appear online followed by printed in hard copy.

Subject Coverage

- Bioelectrical and neural engineering
- Bioinformatics and Computational Biology
- Biomedical modeling
- Biomedical imaging, image processing and visualization
- Clinical engineering, wearable and real-time health monitoring systems
- Biomechanics and biotransport
- Software, tools and application in medical engineering
- Biomaterials
- Physiological signal processing
- Biomedical devices, sensors, artificial organs and nano technologies
- NMR/CT/ECG technologies and electromagnetic field simulation
- Structure-based drug design

Editor-in-Chief

Editorial Board

Notes for Intending Authors

Submitted papers should not have been previously published nor be currently under consideration for publication elsewhere. Paper submission will be handled electronically through the website. All papers are refereed through a peer review process. For more details about the submissions, please access the website.

Website and E-Mail

www. scirp. org/journal/jbise
Email: jbise@scirp.org

ISSN 1937-6871 (Print), 1937-688X (Online)

Journal of Biomedical Science and Engineering, 2010, 3.
Published Online April 2010 in SciRes (http://www.scirp.org/journal/jbise).

TABLE OF CONTENTS

Volume 3, Number 4, April 2010

